

Utah State University

DigitalCommons@USU

---

All Graduate Theses and Dissertations

Graduate Studies

---

5-2017

## Design and Characterization of a Time-of-Flight Mass Spectrometer for Composition Measurements in the Upper Atmosphere

E. Addison Everett  
*Utah State University*

Follow this and additional works at: <https://digitalcommons.usu.edu/etd>



Part of the [Atmospheric Sciences Commons](#), and the [Physics Commons](#)

---

### Recommended Citation

Everett, E. Addison, "Design and Characterization of a Time-of-Flight Mass Spectrometer for Composition Measurements in the Upper Atmosphere" (2017). *All Graduate Theses and Dissertations*. 5698.  
<https://digitalcommons.usu.edu/etd/5698>

This Dissertation is brought to you for free and open access by the Graduate Studies at DigitalCommons@USU. It has been accepted for inclusion in All Graduate Theses and Dissertations by an authorized administrator of DigitalCommons@USU. For more information, please contact [digitalcommons@usu.edu](mailto:digitalcommons@usu.edu).



DESIGN AND CHARACTERIZATION OF A TIME-OF-FLIGHT MASS  
SPECTROMETER FOR COMPOSITION MEASUREMENTS

IN THE UPPER ATMOSPHERE

by

E. Addison Everett

A dissertation submitted in partial fulfillment  
of the requirements for the degree

of

DOCTOR OF PHILOSOPHY

in

Physics

Approved:

---

Michael J. Taylor  
Major Professor

---

Erik A. Syrstad  
Committee Member

---

JR Dennison  
Committee Member

---

Ludger Scherliess  
Committee Member

---

Charles M. Swenson  
Committee Member

---

Mark R. McLellan  
Vice President for Research and  
Dean of the School of Graduate Studies

UTAH STATE UNIVERSITY  
Logan, Utah

2017

Copyright © Edward Addison Everett 2017

All Rights Reserved

## ABSTRACT

Design and Characterization of a Time-of-Flight Mass Spectrometer  
for Composition Measurements in the Upper Atmosphere

by

E. Addison Everett, Doctor of Philosophy

Utah State University, 2017

Major Professor: Dr. Michael J. Taylor  
Department: Physics

*In-situ* composition measurements of the mesosphere/lower thermosphere (MLT) are challenging; this region is only accessible via high-speed sounding rockets, ambient pressures extend into the  $10^{-3}$  Torr range, and particles of interest range in mass from electrons to meteoric smoke and dust particles. Time-of-flight mass spectrometers (TOF-MS) are capable of making fast, accurate measurements over a wide mass range. However, since they rely on pressure-sensitive microchannel plate (MCP) detectors and high voltages, they have rarely been applied at these altitudes. A new TOF-MS for making *in-situ* composition measurements in the MLT has been developed at the Space Dynamics Laboratory. This instrument employs modest acceleration potentials and a pressure-tolerant MCP detector. A Bradbury-Nielsen gate is used to produce short, well-defined ion pulses to reduce the temporal and spatial uncertainty of sampled ions. A prototype TOF-MS was constructed and used to demonstrate TOF-MS technology under conditions relevant to *in-situ* MLT measurements. Operational boundaries and capabilities of this new instrument were identified through laboratory experiments combined with computer modeling. The prototype instrument achieved a maximum resolution of 100 at  $m/z$  40 (Ar), sufficient to resolve major atmospheric species of interest. During experiments at elevated pressures, the MCP detector maintained low background count rates ( $<10$  /second) at pressures as high as  $10^{-3}$  Torr.

A novel getter-based vacuum system was evaluated for use with the new TOF-MS, and a computer model was developed to simulate instrument pressure during a rocket flight. Results from these experiments suggest that when combined with an appropriately sized sampling aperture, this pumping system can extend the measurement range of the instrument to lower altitudes by 10 – 20 km, compared to an unpumped instrument. A computer model was developed to study the effects of critical operating parameters on instrument performance; the most important factor affecting resolution was found to be the initial energy spread of sampled ions. Sensitivity and number density measurement analyses suggest the new instrument will measure major species in the MLT at better than 10% uncertainty. Composition measurements made with the new TOF-MS will contribute to a better understanding of the MLT.

(292 pages)

Design and Characterization of a Time-of-Flight Mass Spectrometer  
for Composition Measurements in the Upper Atmosphere

E. Addison Everett

The mesosphere/lower thermosphere (MLT) is perhaps the least understood region of Earth's atmosphere. Too high for balloons and winged aircraft, yet too low for satellites, direct access to the MLT to make *in-situ* measurements is via high-speed sounding rockets for brief periods of at most a few minutes. Mass spectrometers have previously been used to make composition measurements in this region. But, mass spectrometry in the MLT is difficult, mainly due to the ambient pressures here and also the high speeds and short flight durations of sounding rocket missions. Time-of-flight mass spectrometers (TOF-MS) are capable of making fast, accurate measurements over a wide mass range. However, due to its dependence on microchannel plate (MCP) detectors and high acceleration voltages, this technique has rarely been applied in the MLT.

A new TOF-MS for making composition measurements of both charged and neutral particles in the upper atmosphere has been developed at the Space Dynamics Laboratory. This instrument employs modest acceleration potentials and a pressure-tolerant MCP detector. A prototype instrument was constructed and used to demonstrate TOF-MS technology under conditions relevant to *in-situ* MLT research. Laboratory experiments with this instrument also demonstrated its ability to resolve major atmospheric species of interest. A novel vacuum system for the new TOF-MS was evaluated. Results from these experiments were incorporated in a computer model to simulate instrument pressure during a sounding rocket flight. A computer model was also developed to evaluate the effects of critical operating parameters on instrument performance; the initial energy spread of sampled particles was found to have the greatest impact on mass resolution. Composition measurements made with the new TOF-MS will advance our understanding of the MLT.

For Camille et al.

## ACKNOWLEDGMENTS

Special thanks go to the members of my graduate committee: Mike Taylor, Erik Syrstad, JR Dennison, Ludger Scherliess, and Charles Swenson. Each one has taken time to meet with me and has offered important insight and advice during the course of this project. I especially thank Erik Syrstad for taking me on as a student and allowing me to be a major participant in the development of this new mass spectrometer. Erik spent much time and effort guiding and teaching me over the course of this project. His insight, in particular, has been invaluable, and he has allowed me space to learn and grow. Mike Taylor also deserves special thanks for serving as the chair of my graduate committee, even though the project I worked on was not his. His encouragement kept me going on several occasions when I did not see a path forward.

This work was funded by NASA (grant # NNX09AH97G) and carried out at the Space Dynamics Laboratory. Jim Dyer's expertise was very helpful on multiple occasions. I have also appreciated his encouragement. I had the privilege of working closely with Scott Schicker in the laboratory. Scott, an "old sergeant" (his words), was very patient with me and from him I learned some very important lessons on laboratory experimentation, instrument assembly, and life in general.

I have had great professors throughout my time as a student at USU. I would like to especially acknowledge Haeyeon Yang, who first taught me how to be a physicist. I would also like to thank Eric Held for his encouragement, support, and advice throughout my educational journey. Karalee Ransom, the department advisor, also deserves my special thanks for her encouragement, advice, and guidance. In my opinion she is the best departmental advisor on campus. Many thanks go to Sharon Pappas, for her help and encouragement. My fellow graduate students, David, Kripa and Kausik have been good friends and helped me stay sane. I also gratefully acknowledge the Keith Taylor Summer Fellowship, which supported me for a summer.

My warmest, deepest, most sincere thanks and appreciation are reserved for my family. Camille has been a special help and support; she has gone without and sacrificed much in order for me to finish my schooling. Abby, Caden, and Maren have also gone without and sacrificed much; but they have also provided much joy and happiness, and many smiles and giggles, which are very important. My parents and siblings have encouraged and supported me every step along the way. My in-laws have been a second family to me and have also been very supportive.

Thank you, all.

Edward Addison Everett

## CONTENTS

	Page
ABSTRACT .....	iii
PUBLIC ABSTRACT .....	v
DEDICATION .....	vi
ACKNOWLEDGMENTS .....	vii
LIST OF TABLES .....	xi
LIST OF FIGURES .....	xii
LIST OF ABBREVIATIONS .....	xx
CHAPTER	
1. INTRODUCTION .....	1
1.1. Remote Sensing of the MLT .....	1
1.2. In-Situ Sensing of the MLT .....	4
1.3. Introduction to Time-of-Flight Mass Spectrometry .....	13
1.4. A New Time-of-Flight Mass Spectrometer for the MLT .....	22
2. ION OPTICS DESIGN .....	27
2.1. Ion Optics Simulation Methods .....	27
2.2. Ion Behavior, Beam-on State .....	29
2.3. Ion Behavior, Beam-off State .....	34
2.4. Conclusions .....	42
3. ELECTRICAL AND MECHANICAL DESIGN .....	44
3.1. Electrical Design .....	44
3.2. Mechanical Design .....	54
3.3. Vacuum Design .....	62
4. HIGH PRESSURE MICROCHANNEL PLATE TESTING .....	65
4.1. Experiment Description .....	66
4.2. Results .....	74
4.3. Discussion .....	88
4.4. Conclusions .....	94

	x
5. EXPERIMENTAL TESTS OF A GETTER-BASED PUMPING SYSTEM .....	96
5.1. Experimental Setup and Procedures .....	97
5.2. Data Analysis .....	102
5.3. Results .....	108
5.4. Discussion and Conclusions .....	114
6. BOW SHOCK AND INSTRUMENT PRESSURE MODELING .....	120
6.1. Methods .....	122
6.2. Results .....	130
6.3. Discussion .....	142
6.4. Conclusions .....	148
7. LABORATORY EXPERIMENTS WITH THE PROTOTYPE TOF-MS .....	150
7.1. Equipment and Methods .....	150
7.2. Results and Discussion .....	153
7.3. Conclusions .....	171
8. INSTRUMENT PERFORMANCE MODELING: MASS RESOLUTION .....	173
8.1. Mass Resolution for TOF-MS in General .....	173
8.2. Resolution Simulations for the SDL TOF-MS .....	179
8.3. Simulations of the SDL Instrument Operating <i>In-Situ</i> in the MLT .....	189
8.4. Conclusions .....	194
9. PREDICTED PERFORMANCE: SENSITIVITY AND ACCURACY .....	196
9.1. Sensitivity Analysis .....	196
9.2. Number Density Accuracy .....	201
9.3. Conclusions .....	220
10. SUMMARY, CONCLUSIONS, AND FUTURE WORK .....	222
10.1. Summary and Conclusions .....	222
10.2. Future Work .....	225
REFERENCES .....	227
APPENDICES .....	245
A. TG EXPERIMENT VOLUME CALCULATIONS .....	246
B. TG EXPERIMENTS: SUPPLEMENTAL FIGURES .....	260
C. PERMISSION TO INCLUDE FIGURE .....	267
CURRICULUM VITAE .....	268

## LIST OF TABLES

Table	Page
1.1. Challenges to Performing TOF-MS in the MLT, and Corresponding Solutions Incorporated in the SDL Instrument . . . . .	23
1.2. Factors that Contribute to Peak Broadening, and Corresponding Solutions Incorporated in the SDL TOF-MS . . . . .	25
4.1. Characteristics of the AP-TOF MCP Detector Used in the EDU . . . . .	67
4.2. Ionization Energies for Molecular Nitrogen, Molecular Oxygen, and Argon [ <i>Linstrom and Mallard, 2001</i> ] . . . . .	85
9.1. Dissociation Fractions of Molecules Used in the Neutral Number Density Accuracy Analysis [ <i>Linstrom and Mallard, 2001</i> ] . . . . .	213
9.2. Electron Ionization Cross Sections Used in the Neutral Number Density Accuracy Analysis [ <i>Sorokin et al., 2000; Linstrom and Mallard, 2001; Jorshipura et al., 2001</i> ] . . . . .	213
9.3. Contributors to Different $m/z$ Peaks in a Mass Spectrum of Neutral Particles in the Upper Atmosphere . . . . .	214
A.1. Dimensions for the Cylindrical Portions of the Conical Adapter . . . . .	248

## LIST OF FIGURES

Figure	Page
1.1. Relative abundance of major atmospheric species in the MLT . . . . .	2
1.2. Representative densities and temperatures in the MLT . . . . .	5
1.3. Rocket velocities in the MLT for ballistic apogees between 100 and 180 km . . . . .	7
1.4. Mean energies of major atmospheric species at 1000 m/s (typical rocket speed) and 7000 m/s (typical satellite speed in LEO) . . . . .	8
1.5. Velocity variance $\left(\sqrt{k_B T/m}\right)$ for H, O, and Ar in the MLT . . . . .	9
1.6. Principal of operation for a TOF-MS instrument . . . . .	15
1.7. Instrument concept for the SDL TOF-MS . . . . .	24
2.1. SIMION <sup>®</sup> model of the SDL instrument . . . . .	33
2.2. Ion collection efficiency, beam-on state . . . . .	33
2.3. Illustration representing axial and side views of a BNG for both beam-on and beam-off states . . . . .	35
2.4. BNG simulation using SIMION <sup>®</sup> . . . . .	37
2.5. Deflection angles resulting from SIMION <sup>®</sup> simulations of ions passing through a BNG for $V_{\text{acc}}/V_{\text{def}}$ ratios ranging from 4 to 10 . . . . .	38
2.6. Fitting coefficients $a_1$ , $a_2$ , $a_3$ , and $a_4$ for equation 2.16, plotted against the ratio $V_{\text{acc}}/V_{\text{def}}$ . . . . .	40
2.7. Comparison of BNG deflection efficiency simulations, based on simulated and theoretically calculated BNG deflection angles. . . . .	42
2.8. Comparison of simulated BNG performance with experimental results . . . . .	43
3.1. Electronics schematic for the EDU, showing the three functional subassem- blies of the electrical system. . . . .	45
3.2. Ionizer drawing and wiring diagram . . . . .	46
3.3. Ratio of Faraday cup current to the ionizer cathode emission current with the cathode floating at -100 V . . . . .	46
3.4. SIMION <sup>®</sup> simulation of ionizing electron and ion trajectories in neutral mode, for acceleration potentials that were expected to be used . . . . .	47

3.5. SIMION <sup>®</sup> simulation of ionizing electron trajectories in neutral mode, for acceleration potentials that were actually used . . . . .	48
3.6. MCP detector wiring diagram . . . . .	49
3.7. BNG modulation drive board . . . . .	50
3.8. Initial waveforms from the BNG modulation driver board . . . . .	52
3.9. MDB waveforms after placing a 150 $\Omega$ resistor in series with each BNG channel . . . . .	53
3.10. SDL TOF-MS electronics overview . . . . .	54
3.11. Solid model of the EDU, showing the arrangement of major instrument components . . . . .	55
3.12. Solid model of the EDU front assembly . . . . .	56
3.13. Examples of electrical isolation in the EDU . . . . .	57
3.14. Acceleration grid fabrication . . . . .	57
3.15. Front (a) and back (b) views of the BNG, as built . . . . .	59
3.16. BNG mounted on CMM for measuring wire spacing and planarity . . . . .	60
3.17. Fully assembled prototype time-of-flight mass spectrometer, with mounting frame attached . . . . .	61
3.18. Solid model showing potential TG arrangement for pumping the SDL instrument . . . . .	62
3.19. Solid model of a reflectron version of the SDL TOF-MS mounted inside a dewar of liquid helium . . . . .	63
4.1. Background count rate as a function of laboratory air backfill pressure for a 5 $\mu\text{m}$ pore MCP detector from PHOTONIS USA, Inc . . . . .	66
4.2. Experimental setup for the MCP pressure experiments . . . . .	70
4.3. Experimental setup for MCP humidity experiments . . . . .	72
4.4. Detector gain during the second scrub of the MCP used in the EDU . . . . .	75
4.5. MCP background count rates under N <sub>2</sub> backfill . . . . .	76
4.6. MCP background count rates under Ar backfill . . . . .	77
4.7. MCP background count rates under laboratory air backfill . . . . .	78
4.8. MCP background count rates under He backfill . . . . .	78

4.9. Prescrub background count rates for laboratory air, argon, helium, and nitrogen, with the MCP operating at -1900 V . . . . .	79
4.10. Gain-matched postscrub MCP background count rates for laboratory air, nitrogen, and argon . . . . .	80
4.11. Voltage-matched postscrub MCP background count rates for laboratory air, nitrogen, and argon . . . . .	80
4.12. Effect of humidity on MCP background count rates for nitrogen backfill . . . .	81
4.13. Effect of humidity on MCP background count rates for laboratory air backfill . . . . .	81
4.14. Prescrub MCP discharge events under nitrogen, argon, and laboratory air backfills . . . . .	83
4.15. MCP discharge events measured after the first scrub, under nitrogen, laboratory air, and oxygen backfills . . . . .	84
4.16. Postscrub discharge events for the MCP detector under nitrogen, argon, and laboratory air backfills . . . . .	84
4.17. Pressures of detector discharge events at different points during the progression of the MCP scrub . . . . .	85
4.18. Detector discharge events for nitrogen backfill, for different amounts of water added to the backfill gas . . . . .	86
4.19. Detector discharge events for laboratory air backfill, for different amounts of water added to the backfill gas . . . . .	87
4.20. Mass spectrum taken with the EDU operating under argon backfill at $2 \times 10^{-4}$ Torr . . . . .	88
4.21. Comparison of prescrub and postscrub MCP arcing events . . . . .	90
5.1. Schematic of the TG experimental apparatus . . . . .	99
5.2. TG preparation for pumping experiments . . . . .	100
5.3. Pressure and temperature during the activation process for TG 10383-1 . . . .	102
5.4. Example data from backfill experiments with TG 10383-1, showing the Baratron <sup>®</sup> pressure readings for both volumes of the experimental setup . . . .	103
5.5. Range of noninert gas partial pressure and quantity of gas sorbed during backfill experiments with TG 10383-1 . . . . .	104
5.6. Gas load due to outgassing during the activation heating of TG 10383-1 . . . .	107

5.7. Pumping speed versus noninert gas partial pressure during experiments with TG 10383-1 .....	109
5.8. Pumping speed versus quantity of gas sorbed for TG 10383-1 .....	110
5.9. Pressure runs four and five for TG 10383-1, showing the scatter (at low pressures) in the experimentally calculated pumping speed .....	112
5.10. Surface fit of TG pumping speed versus noninert gas partial pressure and amount of gas sorbed for TG 10384-3 .....	113
5.11. Surface fit of pumping speed for TG 10384-3, with inconsistent data points removed .....	114
5.12. Average TG pumping speed, based on data from experiments with five TGs .....	115
5.13. Number of data points used to calculate the average TG pumping speeds shown in Figure 5.12 .....	116
5.14. Random uncertainty, shown as a percentage, in the average TG pumping speeds shown in Figure 5.12 .....	117
5.15. Average TG pumping speed versus noninert gas partial pressure for several constant amounts of gas sorbed .....	117
5.16. Average TG pumping speed versus amount of gas sorbed for several constant noninert gas partial pressures .....	118
5.17. Comparison of experimentally derived TG pumping speeds with speeds quoted by the manufacturer .....	118
6.1. Comparison of the analytic solution (equation 6.7) of the pumping equation to the numerical approximation (equation 6.5) used in the IPM .....	126
6.2. Convergence of the IPM, based on the initial pressure spike for time steps ranging from 1 $\mu$ s to 0.1 s .....	129
6.3. Computation time required to run the IPM at different time step sizes, assuming aperture open at 70 km .....	129
6.4. Bow shock number density, from DSMC simulations of the SDL TOF-MS for an apogee of 160 km .....	132
6.5. Bow shock temperatures, from DSMC simulations of the SDL TOF-MS for an apogee of 160 km .....	133
6.6. Bow shock enhancement factors for number density and temperature due to high speed rocket flight through the MLT .....	134
6.7. Particle flux for a 160 km apogee .....	134

6.8. Particle transmission through the bow shock (i.e., fraction of ambient particles that pass through the bow shock without experiencing collisions) . . . . .	135
6.9. Altitude vs. time for a 160 km ballistic trajectory . . . . .	136
6.10. IPM simulation pressure curves for an SDL TOF-MS with no active pumping, opening the sampling aperture at 90 km, assuming an apogee of 160 km . . . . .	137
6.11. IPM simulation pressure curves for an SDL TOF-MS with no pumping, pumping via eight TGs, and pumping provided by a miniature turbo pump (constant speed of 4 L/s), for an aperture diameter of 0.1 mm and an opening altitude of 90 km . . . . .	138
6.12. IPM simulation pressure curves for an SDL TOF-MS with no pumping, pumping via eight TGs, and pumping provided by a miniature turbo pump (constant speed of 4 L/s), for an aperture diameter of 1.0 mm and an opening altitude of 90 km . . . . .	139
6.13. Maximum value of the pressure spike at aperture open for the SDL instrument, with no active pumping, as simulated with the IPM . . . . .	140
6.14. Maximum value of the pressure spike at aperture open for the SDL instrument, with a miniature turbo pump (constant 4 L/s), as simulated with the IPM . . . . .	141
6.15. Maximum value of the pressure spike at aperture open for the SDL instrument, pumped with eight TGs, as simulated with the IPM . . . . .	142
6.16. Altitudes above which the pressure requirement is met, based on IPM results assuming an aperture open altitude high in the rocket trajectory . . . . .	143
6.17. Altitudes above which the mfp requirement is met, based on IPM results assuming an aperture open altitude high in the rocket trajectory . . . . .	143
7.1. Example of an ion beam produced in the SDL IOTF . . . . .	151
7.2. The EDU (facing away from camera) mounted in the 24" UHV chamber . . . . .	152
7.3. Relative count rate intensity for several BNG deflection potentials, with the EDU operating in ion mode . . . . .	154
7.4. Relative count rate intensity for $V_{\text{def}}/E_{\text{ion}}$ ratios up to 0.5, for 238 eV ions, with the EDU operating in neutral mode . . . . .	155
7.5. Count rates at increasing values of $V_{\text{def}}$ for 200 eV ions . . . . .	157
7.6. Count rates with the EDU operating in RPA mode, using 200 eV ions . . . . .	157
7.7. Count rates at increasing values of the BNG offset voltage ( $V_{\text{def}}$ ) for 238 eV neutrals . . . . .	159

7.8. Early mass spectrum recorded with the EDU .....	160
7.9. Modulation waveform most commonly used to drive the BNG during experiments with the EDU .....	160
7.10. Mass spectrum of argon taken with the EDU operating in ion mode .....	161
7.11. Mass spectrum of $^{40}\text{Ar}$ and $^{36}\text{Ar}$ , resulting from an ion beam with the velocity filter tuned between the two masses .....	162
7.12. Mass spectrum collected with the EDU operating in ion mode, using an ion gauge as the ion source .....	163
7.13. Mass spectrum produced with the EDU in neutral mode at $5 \times 10^{-7}$ Torr, under nitrogen and argon backfill .....	165
7.14. Mass spectrum produced with the EDU operating in neutral mode at $9 \times 10^{-5}$ , under argon backfill .....	166
7.15. Effect of BNG deflection offset voltage ( $V_{\text{def}}$ ) on mass resolution .....	168
7.16. Effect of BNG deflection offset voltage ( $V_{\text{def}}$ ) on mass resolution of the EDU for ion energies of 200 eV .....	168
7.17. Highest resolution mass spectrum obtained with the EDU during laboratory testing .....	169
7.18. Pressure effects on mass resolution for the EDU .....	170
8.1. Effect of pulse width on mass resolution .....	175
8.2. Effect of drift length on mass resolution .....	176
8.3. Effect of energy spread on mass resolution .....	178
8.4. Neutral mass spectrum collected with the EDU .....	180
8.5. Simulated mass spectrum, using the Monte Carlo methods described in section 8.2 .....	181
8.6. Convergence testing of the SDL instrument Monte Carlo model: average resolution .....	182
8.7. Convergence testing of the SDL instrument Monte Carlo model: standard deviation .....	183
8.8. Simulated effect of ion energy FWHM on mass resolution for the SDL instrument .....	184
8.9. Simulated effect of start pulse width on mass resolution for the SDL instrument .....	185

8.10. Simulated effect of drift length on mass resolution for the SDL instrument, for ions with a 1 eV FWHM energy spread . . . . .	186
8.11. Simulated effect of drift length on mass resolution for the SDL instrument, with a 0.5 eV FWHM energy spread . . . . .	187
8.12. Simulated effect of drift length on mass resolution for the SDL instrument for monoenergetic ions . . . . .	187
8.13. Simulated effect of ion energy (acceleration potential) on mass resolution for the SDL instrument . . . . .	189
8.14. Simulated effect of bin width on mass resolution for the SDL instrument . . .	190
8.15. Simulated spectrum for a linear TOF-MS instrument traveling at 1 km/s, sampling particles thermalized at 500 K . . . . .	191
8.16. Simulated spectrum for a linear TOF-MS instrument traveling at 7.8 km/s, sampling particles thermalized at 1000K . . . . .	192
8.17. Simulated spectrum for a reflectron TOF-MS instrument traveling at 7.8 km/s, sampling particles thermalized at 1000 K. . . . .	194
9.1. Volume emission rates for 120.0 and 149.3 nm photons above Poker Flat, AK, consistent with a class IBC III aurora . . . . .	202
9.2. The UV background emission cone extends in front of the instrument, with its apex located at the instrument aperture . . . . .	203
9.3. Estimated background count rate for the SDL TOF-MS at altitudes from 70 - 160 km, due to background UV airglow emissions . . . . .	206
9.4. Ion densities used in the ion number density accuracy analysis . . . . .	207
9.5. Modeled number density accuracy for ions . . . . .	208
9.6. Densities used in the neutral number density accuracy analysis . . . . .	212
9.7. Results from the neutral number density accuracy analysis for a 202 $\mu\text{m}$ diameter instrument aperture and an integration distance of 1 km . . . . .	215
9.8. Results from the neutral number density accuracy analysis for the SDL TOF-MS operating in saturation mode, for a 1600 $\mu\text{m}$ diameter instrument aperture and an integration distance of 1 km . . . . .	216
9.9. Results from the neutral number density accuracy analysis for the SDL TOF-MS operating in saturation mode, for a 1600 $\mu\text{m}$ diameter instrument aperture and an integration distance of 5 km . . . . .	217
A.1. Diagram for calculating the volume of the conical adapter . . . . .	250

B.1. Range of noninert gas partial pressure and quantity of gas sorbed during backfill experiments with TG 10382-6 .....	260
B.2. Range of noninert gas partial pressure and quantity of gas sorbed during backfill experiments with TG 10384-1 .....	261
B.3. Range of noninert gas partial pressure and quantity of gas sorbed during backfill experiments with TG 10384-2 .....	261
B.4. Range of noninert gas partial pressure and quantity of gas sorbed during backfill experiments with TG 10384-3 .....	262
B.5. Pumping speed versus noninert gas partial pressure during experiments with TG 10382-6 .....	262
B.6. Pumping speed versus noninert gas partial pressure during experiments with TG 10384-1 .....	263
B.7. Pumping speed versus noninert gas partial pressure during experiments with TG 10384-2 .....	263
B.8. Pumping speed versus noninert gas partial pressure during experiments with TG 10384-3 .....	264
B.9. Pumping speed versus quantity of gas sorbed for TG 10382-6 .....	264
B.10. Pumping speed versus quantity of gas sorbed for TG 10384-1 .....	265
B.11. Pumping speed versus quantity of gas sorbed for TG 10384-2 .....	265
B.12. Pumping speed versus quantity of gas sorbed for TG 10384-3 .....	266

## LIST OF ABBREVIATIONS

A/TD	Amplifier/Timing Discriminator
AIM	Aeronomy of Ice in the Mesosphere
BNG	Bradbury-Nielsen gate
CEM	Channel Electron Multiplier
CF	ConFlat™
CMM	Coordinate Measuring Machine
DSMC	Direct Simulation Monte Carlo
EDU	Engineering Demonstration Unit
EI	Electron Impact
FWHM	Full Width at Half Maximum
HT	Hadamard Transform
ICON	Ionospheric Connection Explorer
IG	Ionization Gauge
IOTF	Ion Optics Test Facility
IPA	Isopropyl Alcohol
IPM	Instrument Pressure Model
Kn	Knudsen number
LEO	Low Earth Orbit
LUT	Lookup Table
MCP	Microchannel Plate
MDB	Modulation Driver Board
mfp	mean free path
MLT	Mesosphere/Lower Thermosphere
MSIS	Mass Spectrometer and Incoherent Scatter radar
NEG	Nonevaporable Getter

PEEK	Polyether Ether Ketone
PRBS	Pseudorandom Binary Sequence
RH	Relative Humidity
RPA	Retarding Potential Analyzer
RTOF-MS	Reflectron Time-of-Flight Mass Spectrometer
SABER	Sounding of the Atmosphere using Broadband Emission Radiometry
SDL	Space Dynamics Laboratory
SNR	Signal-to-Noise Ratio
SOFIE	Solar Occultation For Ice Experiment
TD/MCS	Time Digitizer/Multichannel Scaler
TG	Tubegetter®
TIDI	TIMED Doppler Interferometer
TIMED	Thermosphere Ionosphere Mesosphere Energetics and Dynamics
TOF-MS	Time-of-Flight Mass Spectrometry/Spectrometer
UHV	Ultrahigh Vacuum

# CHAPTER 1

## INTRODUCTION

The mesosphere/lower thermosphere (MLT) is home to a rich variety of processes and phenomena of fundamental scientific interest. Here meteors burn up, depositing metallic smoke and dust particles [Hunten *et al.*, 1980]. Meteoric smoke and dust are thought to contribute to noctilucent cloud formation [Hunten *et al.*, 1980; Turco *et al.*, 1982] and sporadic E [Whitehead, 1970; Alpers *et al.*, 1993; von Zahn and Hansen, 1988]. Noctilucent clouds, first recorded in 1884, are the highest clouds in Earth's atmosphere and form in the summer mesosphere at high latitudes [Taylor *et al.*, 2002; Gadsden and Schröder, 1989; Gadsden, 1982]. The majority of auroral emissions originate in the MLT [Störmer, 1946]. Atmospheric gravity waves break in the MLT and deposit their energy here [Espy *et al.*, 2004; Swenson and Liu, 1998].

The MLT includes the turbopause region, below which the atmosphere is well mixed and above which the atmosphere is in diffusive equilibrium. Figure 1.1 shows the relative abundance of several atmospheric species at MLT altitudes. The boundary between the mesosphere and thermosphere, called the mesopause, is home to the coldest temperatures in Earth's atmosphere. Atmospheric scientists studying this region often seek information on composition, density, temperature, electric and magnetic fields, and winds. Instruments used to probe the upper atmosphere fall into two broad classes: remote sensors and *in-situ* sensors. Remote sensors reside outside the region of interest and gather information from waves that travel through or originate from the medium. In contrast, *in-situ* sensors are placed directly in the region of interest to make measurements [Hargreaves, 1992].

### 1.1. Remote Sensing of the MLT

Remote sensing of the MLT can be conducted both from the ground and from space. Lidar and radar are two examples of active remote sensing techniques used to study this region. Lidar systems emit laser pulses and measure the resulting backscattered (resonant,

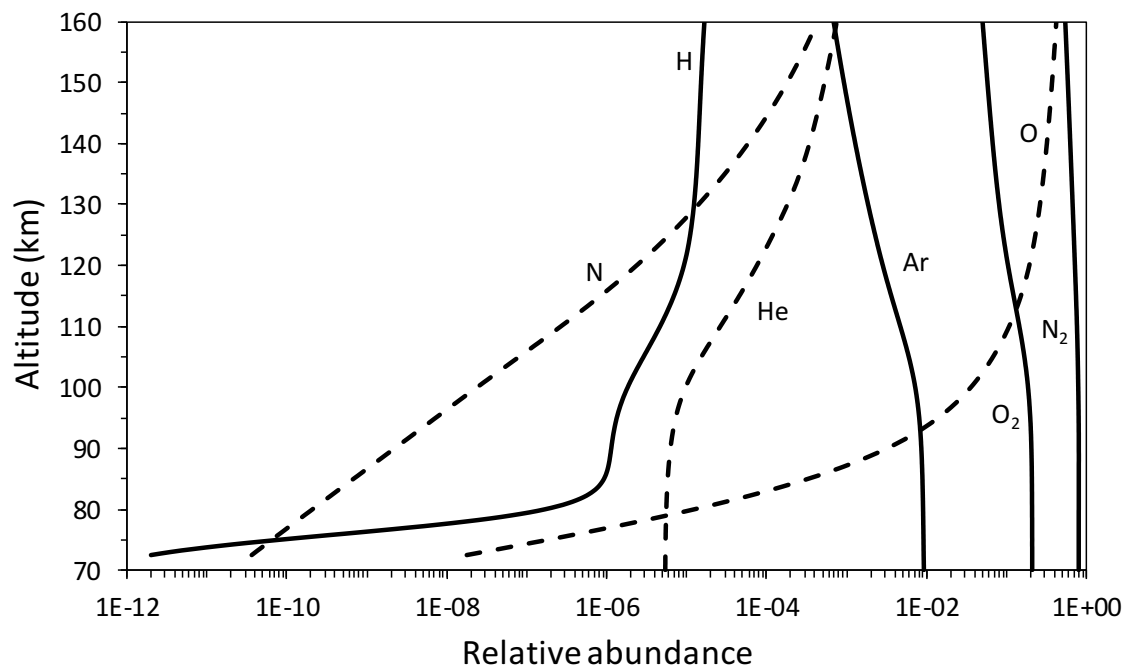


**Figure 1.1.** Relative abundance of major atmospheric species in the MLT. Data comes from an MSIS-E-90 reference atmosphere [Hedin, 1991]. The turbopause for the atmosphere represented in this figure occurs near 95 km.

Mie, Rayleigh) photons. Temperature, wind, and density information can be obtained by analyzing this signal (e.g., Doppler shift and signal intensity) [Krueger *et al.*, 2015; Höffner and Lübken, 2007; Franke *et al.*, 2005; von Zahn and Höffner, 1996]. Sodium lidars probe the MLT in the region of the sodium layer, located near the mesopause, via resonance fluorescence [Gardner *et al.*, 1986; Hu *et al.*, 2011]. Noctilucent clouds and metallic layers have also been observed with lidar [Wickwar *et al.*, 2002; Yi *et al.*, 2013; Nussbaumer *et al.*, 1996; Clemesha, 1995]. Radar is used to study polar mesospheric summer echoes [Strel'nikov *et al.*, 2006; Robertson *et al.*, 2009], noctilucent clouds [Taylor *et al.*, 1989, 2009; Stebel *et al.*, 2000], meteors and metallic layers [Rapp *et al.*, 2007; Plane *et al.*, 2015; Raizada *et al.*, 2015].

Gaseous and metallic species in the MLT emit light, called airglow, in UV, visible, and IR wavelengths [McDade, 1998; Meriwether, 1989]. Passive remote sensing techniques are used to observe these emissions, revealing information on a variety of atmospheric phe-

nomena. Temperature information, for example, can be obtained by comparing emission line ratios and profiles [Sargoytchev *et al.*, 2004; Hernandez, 1976]. Airglow emissions can also yield information on the abundance of atmospheric species [López-Puertas *et al.*, 2000]. Atmospheric temperature and density can be affected by winds and wave activity in the MLT, which can also be studied by observing airglow originating from this region [Hays *et al.*, 1993; Taylor *et al.*, 1987; Swenson and Mende, 1994].

Not all remote sensing techniques are ground-based. Satellites in low Earth orbit (LEO) provide important platforms for making optical measurements of the MLT. The Sounding of the Atmosphere using Broadband Emission Radiometry (SABER) instrument aboard the Thermosphere Ionosphere Mesosphere Energetics and Dynamics (TIMED) satellite measures airglow emissions in the upper atmosphere to determine MLT temperatures and densities at a vertical resolution of 2 km [Russell III *et al.*, 1999; Beig *et al.*, 2008; Mlynczak *et al.*, 2003; López-Puertas *et al.*, 2000]. The TIMED Doppler Interferometer (TIDI) instrument analyzes the Doppler shift of emissions from O, O<sub>2</sub>, Na, and OH in the visible and near IR range to measure winds and temperatures in the MLT [Killeen *et al.*, 1999]. The Solar Occultation For Ice Experiment (SOFIE) aboard the Aeronomy of Ice in the Mesosphere (AIM) satellite compares the intensity of different solar emission wavelengths after they pass through the Earth's limb to derive temperature, pressure, and abundance of ambient species including H<sub>2</sub>O, O<sub>3</sub>, CO<sub>2</sub>, CH<sub>4</sub>, and NO [Russell III *et al.*, 2009]. SOFIE achieves a vertical resolution of better than 2 km and makes measurements of the MLT region up to an altitude of about 110 km [Gordley *et al.*, 2009]. The Ionospheric Connection Explorer (ICON) satellite, set to be launched in 2017, will employ several optical sensors to detect UV emissions to study the coupling between the lower atmosphere and the ionosphere [Immel *et al.*, 2012; Stephan *et al.*, 2013; Immel *et al.*, 2013].

Remote sensing techniques generally offer the ability to make measurements over a wide spatial and/or temporal range. Ground-based remote sensors are easier to repair, replace, and calibrate than space-based sensors (including *in-situ* instruments). However,

data from remote sensors can be difficult to interpret due to interactions between the emitted waves and the ambient atmosphere they pass through [Hargreaves, 1992]. Measurements of species that do not emit strongly, including trace species, are difficult to make with remote sensors at high spatial resolution. Different remote sensing techniques often complement each other and are sometimes combined with *in-situ* sensors to study the upper atmosphere [Robertson *et al.*, 2009; Strelnikov *et al.*, 2006].

## 1.2. In-Situ Sensing of the MLT

Despite the processes of fundamental importance that occur in the MLT, this region constitutes a no man's land of sorts with regard to *in-situ* measurements. For example, although the minor isotopologues of carbon dioxide play a major role in the temperature and energy balance of the MLT [Brasseur and Solomon, 2005; Mlynchak, 2011], few *in-situ* measurements of carbon dioxide have been made here [Mlynchak *et al.*, 2012]. Here the atmosphere is too thin to support winged aircraft and balloons, yet too dense for satellites. Sounding rockets provide the only platform for making *in-situ* measurements at these altitudes. Sounding rocket flights are brief, allowing no more than a few minutes of sampling time, all while rapidly changing altitude. Instruments carried on high speed sounding rockets interact with the atmosphere (representative ambient densities and temperatures shown in Figure 1.2) forming a region of enhanced temperature and pressure that can disrupt particle flow and even induce chemical reactions involving atmospheric species [Gumbel, 2001a; Krankowsky *et al.*, 1979]. This region is called a bow shock. These effects can be reduced and at least partially mitigated by careful instrument design [Offermann *et al.*, 1981; Offermann and von Zahn, 1971] and modeling [Rapp *et al.*, 2001; Amyx *et al.*, 2008; Knappmiller *et al.*, 2008].

*In-situ* sensors are critical to studying the MLT and provide vertical measurement profiles of important ambient characteristics such as composition, density, wind, and electric fields. Species of interest include both neutral and charged particles, and range in mass

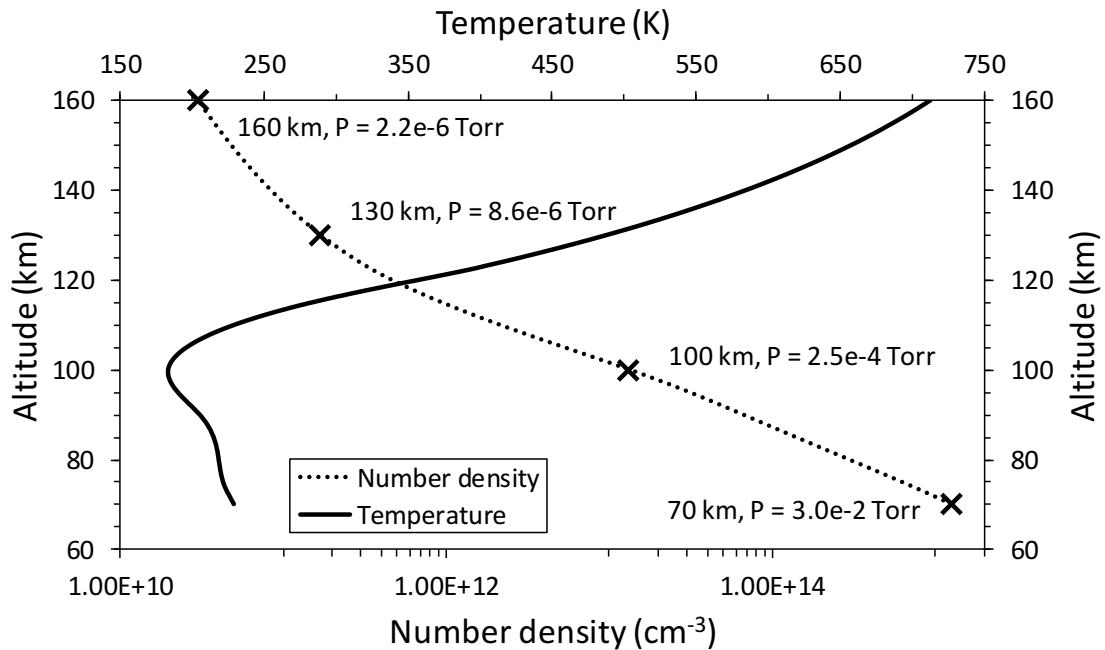


**Figure 1.2.** Representative densities and temperatures in the MLT. Data comes from an MSIS-E-90 reference atmosphere [Hedin, 1991].

from electrons to meteoric smoke and dust particles. Despite the challenges of conducting *in-situ* experiments in the MLT, many rocket-borne experiments have been performed to enhance our understanding of this region. These began in the late 1940s, with captured German V-2 rockets configured to carry scientific payloads [Stuhlinger, 2001]. In contrast with remote sensing techniques (section 1.1), *in-situ* sensors allow extremely localized measurements; in essence a snapshot in time of a specific column of the atmosphere.

Langmuir probes [Barjatya and Swenson, 2006; Young *et al.*, 1967; Gelinas *et al.*, 2005] and retarding potential analyzers (RPA) [Strelnikova *et al.*, 2009; Maier, 1969] represent two classes of sensors deployed to directly sense the plasma characteristics of the MLT. Electron density measurements in this region have also been made using rocket-borne radio propagation experiments [Johannessen and Krankowsky, 1972; Kopp *et al.*, 1985; Plane *et al.*, 2014]. Electric fields in the MLT have been measured with dedicated probes on rocket experiments [Mozer and Bruston, 1967; Goldberg *et al.*, 2001; Pfaff *et al.*, 2001].

Rocket-borne chemical release and falling sphere experiments are used to study winds in the MLT. Chemoluminescent material released in the MLT moves in response to ambient winds and turbulence; ground-based cameras are used to observe the resulting motion [Lehmacher *et al.*, 2011]. Chaff released high in the atmosphere can be tracked via radar to yield information on high-altitude winds [Alpers *et al.*, 1993]. Falling spheres, released at high altitude from sounding rockets, are also used to study winds in the MLT. Such spheres are either tracked after release with radar [Alpers *et al.*, 1993] or are instrumented with sensitive accelerometers [Philbrick *et al.*, 1985].

A variety of instruments to detect charged smoke and dust particles have been deployed to the MLT. Some of these sensors operate similar to a Faraday cup [Strelnikova *et al.*, 2009]; charged particles impacting a conducting surface deposit their charge, inducing a detectable current. Deflecting electric fields, combined with position-sensitive charge detectors, have been used to measure the mass distributions of charged smoke particles [Robertson *et al.*, 2014; Knappmiller *et al.*, 2008]. Additionally, Hedin *et al.* [2007a] report on an instrument intended to collect and return mesospheric smoke particles for laboratory analysis.

MLT composition and density are also measured with rocket-borne instruments. Photometers are used to measure airglow emissions, for example from oxygen [Offermann and Drescher, 1973; Plane *et al.*, 2014]. Oxygen densities can also be measured with a resonance fluorescence technique, utilizing the absorption of 130.4 nm photons by ambient oxygen [Hedin *et al.*, 2009; Sharp, 1980]. Ionization gauges (IG) have been widely used to measure absolute densities in the MLT [Rapp *et al.*, 2001; Lehmacher *et al.*, 2013]. Despite the success of these instruments, mass spectrometers offer the only method for making comprehensive composition measurements in this region, and are discussed in detail in the following section.

### 1.2.1. Mass Spectrometers in the MLT

Conducting mass spectrometer experiments in the MLT presents some unique challenges. Species of interest include both neutral and charged particles and range in size from electrons to molecules and even smoke and dust particles of meteoric origin. Rocket-borne mass spectrometers travel at speeds ranging from several hundred to several thousand meters per second (Figure 1.3), causing a bow shock to form on the leading edge of the rocket. The bow shock can lead to anomalous measurements by inducing reactions involving ambient particles, as well as causing mass and size-dependent flow discrimination near the ram surface of an instrument [Gumbel, 2001a; Hedin *et al.*, 2007b]. (The bow shock is not an issue for satellites, where the mean free path of ambient particles is many times the size of satellites.) Additionally, rocket-borne instruments have strict size and weight restrictions.

The velocities of particles sampled by mass spectrometers in the upper atmosphere can be described by a Maxwellian distribution drifting at the rocket (or satellite) velocity. The initial energies of sampled particles depend on the vehicle velocity (Figure 1.4). For

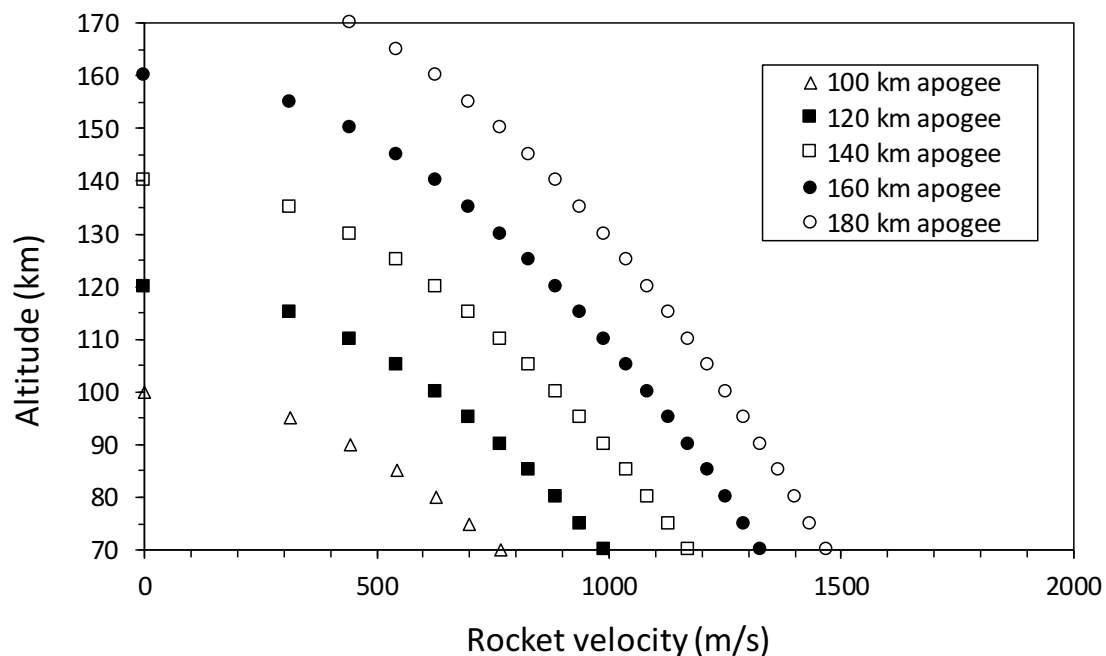


**Figure 1.3.** Rocket velocities in the MLT for ballistic apogees between 100 and 180 km.

a rocket traveling at 1000 m/s, atomic oxygen has a mean energy of 0.08 eV, while the mean value for hydrogen is 0.005 eV. For a satellite in LEO traveling at 7 km/s, the mean energy for atomic oxygen is 4.1 eV (versus 0.25 eV for hydrogen). The distribution of particle velocities in the upper atmosphere (Figure 1.5) introduces a kinetic energy spread in sampled particles. At mesospheric altitudes, the coldest part of Earth's atmosphere, this distribution is small. At higher altitudes the energy spread becomes significant, increasing as temperatures increase.

For ion mass spectrometers in the upper atmosphere, the ionosphere itself becomes the ion source. Sampling neutral species in the upper atmosphere is more complicated. Not only do ambient neutral particles need to be ionized, but ambient plasma must be blocked to prevent interference with measurements. This can be accomplished by employing a pair of appropriately biased grids in front of the instrument aperture to reject charged particles.

Another problem, which has plagued mass spectrometers, whether on rockets or satel-

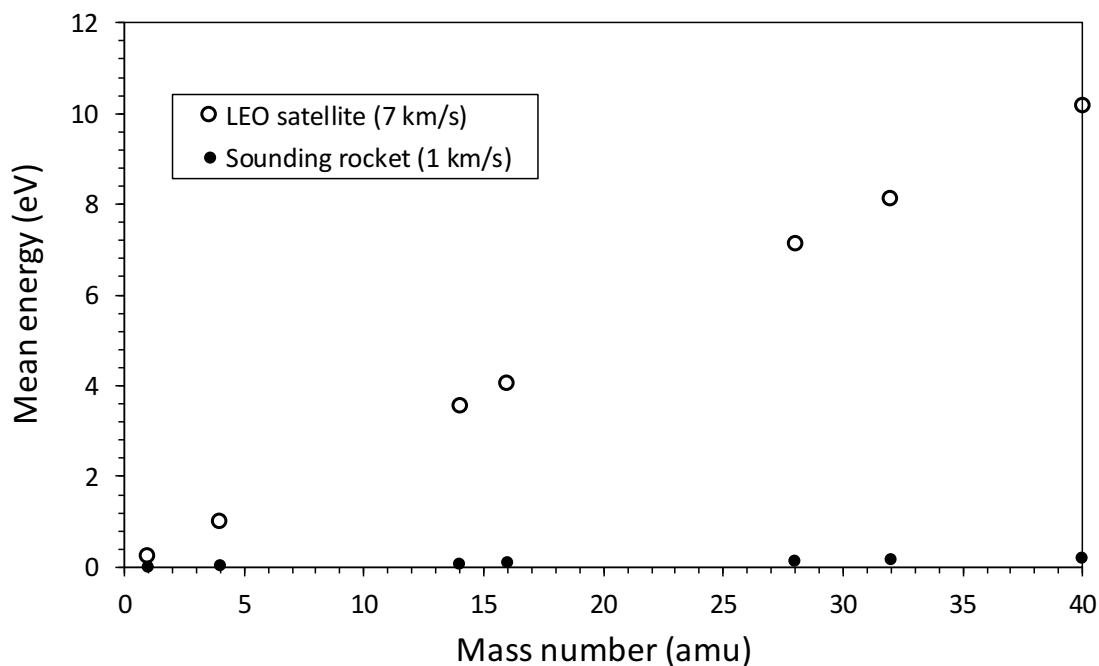


**Figure 1.4.** Mean energies of major atmospheric species at 1000 m/s (typical rocket speed) and 7000 m/s (typical satellite speed in LEO).

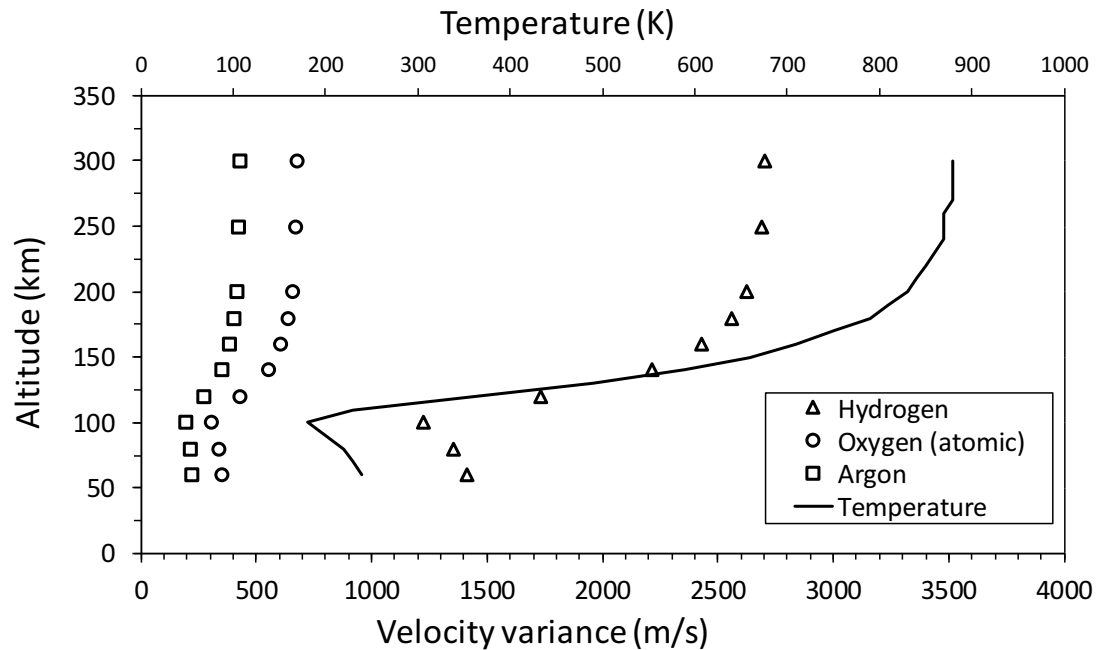


**Figure 1.5.** Velocity variance  $\left(\sqrt{k_B T/m}\right)$  for H, O, and Ar in the MLT.

lites, is atomic oxygen. In the past, suspicious  $\text{CO}_2$  and atomic oxygen measurements from rocket-borne mass spectrometers indicated that atomic oxygen was reacting with ion source surfaces and subsequently detected [von Zahn, 1967; Offermann and von Zahn, 1971; Nier et al., 1976; Lake and Nier, 1973]. One method used to reduce these issues is to cool instrument surfaces to liquid helium temperatures to condense, or freeze incident ambient particles to instrument surfaces [Offermann and von Zahn, 1971; Offermann and Scholz, 1973; Krankowsky et al., 1979; Offermann et al., 1981; Offermann and Tatarczyk, 1973; Brown et al., 1970]. For satellites, the oxygen issue can be more simply resolved by using the initial kinetic energy of ambient particles relative to the spacecraft to distinguish them from particles that have interacted with instrument surfaces. Particles that interact with instrument surfaces partially accommodate and lose some or all of their original kinetic energy. Particles that do not interact with instrument surfaces retain all of their original kinetic energy. By properly positioning and biasing a grid in the ion source, only particles with energy above a certain threshold are allowed to pass into the mass analyzer [Nier et al.,

1974; *Kayser et al.*, 1979]. Particles that have accommodated to instrument surfaces lack sufficient energy to travel past the grid and enter the analyzer.

As early as 1952 a mass spectrometer was designed specifically as a sounding rocket payload [*Townsend*, 1952]. (One source indicates that a rocket-borne mass spectrometer flew as early as 1950, but this is difficult to verify [*Smith and Pressly*, 1959].) The first well-documented, rocket-borne mass spectrometer flight in the MLT occurred in 1953, although the results were inconclusive [*Johnson*, 1961]. The frequency of mass spectrometer launches aboard sounding rockets increased throughout the 1950's, and at least by the end of the decade the Soviet Union was also involved in mass spectrometer research of the upper atmosphere [*Johnson and Heppner*, 1956; *Johnson*, 1961]. Although many of the early mass spectrometers used in upper atmospheric research measured ions, at least one neutral mass spectrometer had flown by 1956 [*Meadows and Townsend*, 1956].

The frequency of mass spectrometer measurements in the MLT continued to increase in the 1960's, as did the development of new mass spectrometers for use in this region. Among these new types of mass spectrometers were sector instruments (employing electric and magnetic fields to achieve mass separation) [*Nier et al.*, 1964; *Kasprzak et al.*, 1968], quadrupole instruments [*Narcisi and Bailey*, 1965; *Schaefer*, 1969], time-of-flight instruments [*Mamyrin*, 2001], and a monopole instrument [*von Zahn*, 1963; *Offermann et al.*, 1981]. Although rocket-borne instruments are the focus here, it is important to note that mass spectrometers have also been included on satellite payloads to make measurements of Earth's atmosphere at orbital altitudes [*Trinks and von Zahn*, 1975; *Kayser et al.*, 1979; *Nier*, 1977].

Rocket-born mass spectrometers have made important contributions to our understanding of the upper atmosphere. In 1960 a rocket-borne mass spectrometer made the first recognized detection of metal ions of meteoric origin in the MLT [*Istomin*, 1963]. Negative ion measurements in 1970 detected  $\text{Cl}^-$  [*Arnold et al.*, 1971], which led to a paper several years later suggesting ozone depletion by chlorofluorocarbons [*Molina and Row-*

land, 1974]. Rocket-borne (as well as satellite) mass spectrometer data is employed in the widely used Mass Spectrometer and Incoherent Scatter radar (MSIS) family of atmospheric models [Hedin, 1987, 1991]. Composition measurements by rocket-borne mass spectrometers have also been used to estimate the location of the turbopause and to study turbulence in the lower thermosphere [Johnson, 1961; von Zahn *et al.*, 1990].

Notwithstanding the contributions that mass spectrometers have made in furthering the understanding of the MLT, much remains to be learned about this region. For example, discrepancies exist between O<sub>2</sub> densities in models, occultation experiments, and *in-situ* measurements using mass spectrometers [Aikin *et al.*, 1993; Lumpe *et al.*, 2007]. *In-situ* measurements of CO<sub>2</sub> densities could be used to improve temperature measurements made by the SABER instrument [Mertens *et al.*, 2003]. Additionally, empirical atmospheric models (NRLMSISE-00, for example) of necessity rely on new and additional data to remain current and improve in accuracy [Picone *et al.*, 2002]. Despite the need for *in-situ* composition measurements in the MLT, the use of rocket-borne mass spectrometers has waned. From their introduction in the 1950s, the frequency of suborbital flights of mass spectrometers peaked in the few years around 1970 and have declined since [Grebowsky and Bilitza, 2000]. In the region of the mesopause, for example, the last published data from an ion mass spectrometer was for a rocket flight that occurred more than 20 years ago [Balsiger *et al.*, 1996; Dickson *et al.*, 2013].

Mass spectrometry in the upper atmosphere is challenging. Resources normally taken for granted in laboratory settings, e.g., space, mass, power, and vacuum equipment, are at a premium on sounding rockets. Species of interest in the MLT range in mass from electrons to smoke and dust particles. The high speed of sounding rockets requires an instrument with a fast response time in order to resolve thin structures [Balsiger *et al.*, 1993; SteinWeg *et al.*, 1992]. The most commonly used types of mass spectrometers in the MLT have been sector and quadrupole instruments. These instruments have made important and invaluable contributions to our knowledge of this region of Earth's atmosphere. However,

these instruments have often been limited in scan speed and mass range [von Zahn and Gross, 1969; Balsiger et al., 1971; Offermann and Trinks, 1971; Zbinden et al., 1975; SteinWeg et al., 1992]. These limitations restrict the vertical resolution attainable with mass spectrometers. Despite this, SteinWeg et al. [1992] report a vertical resolution better than 200 m, but at the expense of mass resolution. Balsiger et al. [1993] achieved a vertical resolution better than 20 m between 80-85 km at the expense of mass resolution, but also aided by an unexpectedly low apogee. The same group later achieved an unprecedented vertical resolution of 12 m at 83 km without sacrificing mass resolution [Balsiger et al., 1996].

#### 1.2.2. Increasing the Frequency of *In-Situ* MLT Measurements

Perhaps the most difficult challenge to MLT research is the infrequency of *in-situ* experiments. As noted previously, the last published rocket-borne ion mass spectrometer measurements in the MLT took place in 1993 (23 years ago) [Balsiger et al., 1996; Dickson et al., 2013]. Regular access to the MLT would improve the identification and study of short-term behavior and trends [Summers, 2011].

Sounding rockets currently offer the only method of directly sampling the MLT. Small inexpensive rockets, such as the Viper-Dart, have been proposed to make frequent flights with small payloads. However, these rockets have proven less than ideal in this role [Sounding Rocket Working Group, National Aeronautics and Space Administration, 2003]. Larger rockets are available, but are not well suited for regular, repeated probing of this region. A need exists for an inexpensive rocket capable of carrying small payloads to the MLT.

The burgeoning commercial space industry currently represents the best option for making multiple, repeated *in-situ* measurements in the MLT. Originally intended for space tourism, commercial space flight companies designing and operating suborbital vehicles have received interest from (and responded favorably to) scientists who have expressed desires to utilize these platforms for space, atmospheric, and microgravity research [Seed-

house, 2012]. Some commercial spaceflight vehicles are being designed specifically with scientific payloads in mind, scientific experiments could also be included as secondary payloads for tourist flights [Pomerantz *et al.*, 2012; Seedhouse, 2016]. Flights to altitudes as high as 110 km may become not only commonplace, but repeatable on a weekly or even daily basis [Pomerantz *et al.*, 2012; Thurairajah *et al.*, 2013; Smith, 2013]. Scientific payloads would be returned and available for reuse. As the commercial suborbital space industry grows, launch locations will increase and offer the possibility of more geographically diverse experiments [Pomerantz *et al.*, 2012].

Perhaps most important, commercial access to the MLT is expected to be significantly less expensive than using sounding rockets [Smith, 2013]. Current and past instruments deployed on sounding rockets can be adapted for integration with commercial space vehicles. Lower costs will encourage new instrument development. Ultimately, more frequent access to the MLT will result in a greater understanding of this important region of Earth's atmosphere.

### 1.3. Introduction to Time-of-Flight Mass Spectrometry

Species of interest in the MLT cover a wide mass range, from electrons to meteoric smoke and dust particles. The high speed of sounding rockets also makes the spatial resolution of thin structures in the MLT difficult. Time-of-flight mass spectrometry (TOF-MS), with its ability to make fast, accurate measurements over a theoretically unlimited mass range, appears to be an obvious choice for use in the MLT.

TOF-MS is performed by using an electric field to accelerate a packet (also called a pulse or bundle) of ions to a nominally uniform kinetic energy (KE) and then measuring the amount of time required for the ions to drift across a field-free region of known length [Cotter, 1997; Guilhaus, 1995]. The kinetic energy, KE, gained by a charged particle in an electric field is given by

$$\text{KE} = qV_{\text{acc}}, \quad (1.1)$$

where  $q$  is the ion charge and  $V_{\text{acc}}$  is the potential difference in the acceleration region (Figure 1.6). Kinetic energy in terms of particle mass,  $m$ , and velocity,  $v$ , is

$$\text{KE} = \frac{1}{2}mv^2. \quad (1.2)$$

The velocity,  $v$ , of an ion of mass,  $m$ , and charge,  $q$ , accelerated through a potential difference of  $V_{\text{acc}}$ , can be calculated by equating equations 1.1 and 1.2. Solving for  $v$  yields

$$v = \sqrt{\frac{2qV_{\text{acc}}}{m}}. \quad (1.3)$$

The time required for an ion traveling at velocity  $v$  to travel a distance  $D$  is

$$t = D\sqrt{\frac{m}{2qV_{\text{acc}}}}. \quad (1.4)$$

Here,  $D$  represents the length of the drift region in Figure 1.6. Equation 1.4 shows that the time required for an ion to travel the length of the drift region depends on  $q$ ,  $m$ , and  $V_{\text{acc}}$ . Equation 1.4 can be rearranged to give the mass-to-charge ratio, or  $m/z$ . (In mass spectrometry, the net charge,  $q$ , on an ion is expressed as  $z$ , which represents the number of elementary charges ( $e$ ) that make up  $q$ . For example, an  $\text{Ar}^{2+}$  ion has  $z = 2e$ .) In terms of  $D$ ,  $t$ , and  $V$ , the ratio  $m/z$  is

$$\frac{m}{z} = 2V_{\text{acc}} \frac{t^2}{D^2}. \quad (1.5)$$

Similarly charged ions accelerated by the same potential difference separate according to mass as they travel through the drift region, the heavier ions traveling slower than lighter ions. The time between ion pulses must be long enough to allow the highest-mass ion of interest to travel the drift length before introducing a new ion pulse to the drift region; otherwise, light ions will overtake heavy ions from a previous pulse. This time between pulses can be adjusted and leads to the theoretically unlimited mass range of TOF-MS.

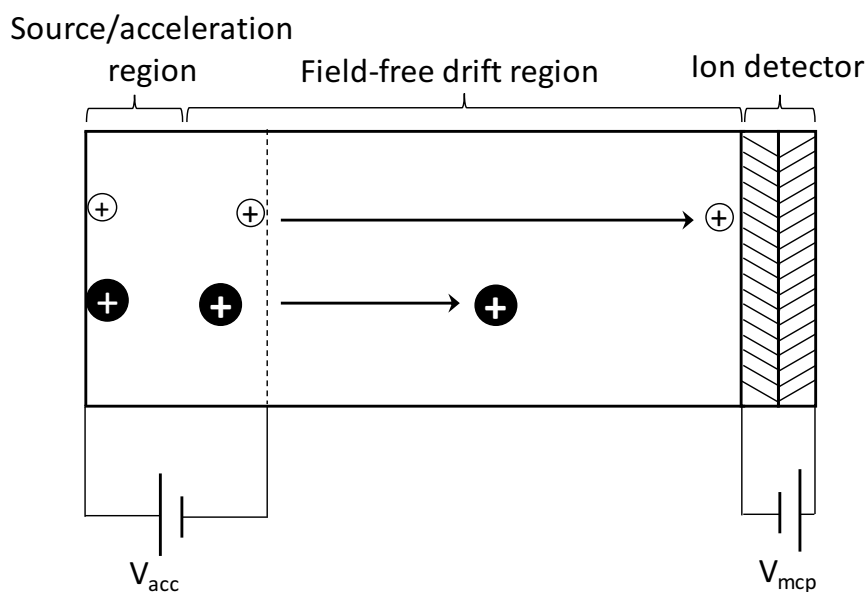


**Figure 1.6.** Principal of operation for a TOF-MS instrument. An electric field accelerates ions to a uniform kinetic energy. Ions then separate according to mass as they travel the length of a field-free drift region, where they are detected. Light ions arrive at the detector before heavier ions.

A microchannel plate (MCP) detector detects ions after they cross the drift region. The arrival time,  $t$ , of ions at the MCP detector is the quantity that is measured by a TOF-MS instrument. A TOF spectrum results from binning the arrival times of ions from multiple pulses. A TOF spectrum can be converted to an  $m/z$  spectrum by using the TOF for two known species to determine the constants  $a$  and  $b$  that satisfy [Cotter, 1997]

$$t_1 = a\sqrt{(m/z)_1} + b, \quad (1.6)$$

and

$$t_2 = a\sqrt{(m/z)_2} + b. \quad (1.7)$$

### 1.3.1. Mass Resolution

Three major factors that affect ion TOF, but do not directly appear in equation 1.4, are uncertainties in the ion initial kinetic energy distribution, temporal uncertainty, and

spatial uncertainty [Cotter, 1997; Guilhaus, 1995]. Ions generally have an initial kinetic energy in addition to the energy gained in the acceleration region. For a mass spectrometer sampling in the MLT, the initial ion kinetic energy depends on the ambient temperature. Near the mesopause, the coldest region in Earth's atmosphere, the kinetic energy spread is small. Above the mesopause the temperature increases with altitude, leading to larger kinetic energy distributions. Temporal uncertainty relates to the difference in time of ion formation, which affects the time at which ions enter the field-free drift region. Spatial uncertainty pertains to the location at which particles are ionized in the ionization region, which affects the energy ions have after being extracted from the ionization region. These three factors result in a TOF distribution for ions with the same  $m/z$  ratio [de Hoffmann and Stroobant, 2007].

The initial ion kinetic energy distribution, temporal uncertainty, and spatial uncertainty result in a spread of flight times for identical ions. As noted previously (section 1.3), the arrival times of ions from many pulses are binned to form a TOF spectrum, which can then be converted into a mass spectrum. Mass resolution is defined as [Cotter, 1997; Guilhaus, 1995]

$$\frac{m}{\Delta m} = \frac{t}{2\Delta t}, \quad (1.8)$$

where  $\Delta m$  is the width of the mass peak at some fraction of the peak height and  $\Delta t$  is the width of the peak in terms of arrival time. Common peak height fractions at which to measure  $\Delta m$  include 50% (FWHM) [Cotter, 1997; de Hoffmann and Stroobant, 2007], 10%, and 5% of peak maximum.

Assuming no contributions to peak broadening from initial kinetic energy distribution and negligible spatial uncertainty,  $t$  and  $\Delta t$  in equation 1.8 can be expressed as  $D/v$  and  $\Delta x/v$ , respectively (where  $v$  is the ion velocity and  $\Delta x$  is the ion pulse width). Mass resolution can then be expressed as

$$\frac{m}{\Delta m} = \frac{D}{2\Delta x}, \quad (1.9)$$

where the major contributors to resolution are drift length and the ion pulse width. In this case, lengthening the drift region, shortening the pulse width, or a combination of the two can be used to improve mass resolution.

### 1.3.2. Reflectron TOF-MS

Ions sampled in the MLT have an inherent kinetic energy spread directly related to the ambient temperature (see section 1.3.1). At higher altitudes this can have a substantial negative effect on mass resolution. A widely used method of correcting for kinetic energy spread is to use a reflectron [*Cotter, 1997; Mamyrin, 2001; de Hoffmann and Stroobant, 2007; Guilhaus, 1995*]. A reflectron employs a set of meshes and electrodes positioned at the end of the drift region to form an ion mirror opposite the source region. Voltages applied to reflectron electrodes create an electric field that causes ions to reverse direction and travel back through the drift region until they reach the MCP detector, which in this case is located on the source side of the drift region. A reflectron corrects for the kinetic energy spread of ions with the same  $m/z$  ratio.

The TOF equation for a reflectron time-of-flight mass spectrometer (RTOF-MS) is different than for a linear TOF-MS instrument. Equation 1.3 gives the velocity of an ion after exiting the acceleration region, assuming all kinetic energy is due to the acceleration. In the MLT the kinetic energy of a group of ions will exhibit statistical uncertainty due to thermal effects. Letting  $v_0$  represent the initial velocity of an ion relative to an RTOF-MS instrument (including contributions from ambient wind velocity, vehicle velocity, and thermal velocity), equation 1.3 can be written as

$$v = \sqrt{\frac{2qV_{\text{acc}}}{m} + v_0^2}. \quad (1.10)$$

A collection of ions will exhibit a statistical uncertainty in  $v$ , reflecting the distribution of velocities due to ambient temperature. The time required for an ion to travel the length of

the drift region,  $D_1$ , is

$$t_1 = D_1 \sqrt{\frac{m}{2qV_{\text{acc}} + mv_0^2}}. \quad (1.11)$$

After crossing the drift region, the ions enter the reflectron where they slow and eventually reverse direction.

The simplest reflectron is a single-stage design, which produces a (nominally) uniform electric field parallel to the drift region axis. A single-stage reflectron can be made with two electrodes positioned perpendicular to the drift region axis. The first electrode, a grid, is located at the end of the drift region and is at the same potential as the drift region. A planar electrode is located a distance  $L$  behind the first mesh and is biased at voltage  $V_r$  relative to the first mesh (where  $V_r > V_{\text{acc}}$ ). Ions entering the reflectron experience a force

$$F = qE = \frac{qV_r}{L}, \quad (1.12)$$

where  $E$  is the electric field in the reflectron. Conservation of energy can be used to find the penetration depth,  $d$ , of an ion in the reflectron by comparing the kinetic energy of an ion at the reflectron entrance to the ion's potential energy at the turnaround point:

$$\frac{1}{2}mv^2 = qEd = \frac{qdV_r}{L}. \quad (1.13)$$

The ion velocity given in equation 1.10 can be substituted into equation 1.13, giving a penetration depth of

$$d = \frac{L}{2qV_r} (2qV_{\text{acc}} + mv_0^2). \quad (1.14)$$

The average velocity of an ion from the time it enters the reflectron until it reverses direction is simply  $\bar{v} = v/2$ . Since the ion travels a distance  $2d$  in the reflectron, the time it spends in the reflectron is

$$t_r = \frac{4d}{v} = \frac{2L}{qV_r} \sqrt{\frac{2qV_{\text{acc}} + mv_0^2}{m}}. \quad (1.15)$$

The ion then exits the reflectron with the same kinetic energy with which it entered and again travels through the drift region until it reaches the MCP detector. This distance is  $D_2$  and can, but does not have to, be the same as  $D_1$ . In general

$$t_2 = D_2 \sqrt{\frac{m}{2qV_{\text{acc}} + mv_0^2}}. \quad (1.16)$$

Ions with a higher initial velocity,  $v_0$ , spend more time in the reflectron than ions with lower initial velocities, which provides a correction to the initial velocity spread. The total amount of time required for an ion to travel from the source to the detector in a RTOF-MS instrument is

$$t_{\text{tot}} = t_1 + t_2 + t_r. \quad (1.17)$$

The distances  $D_1$  and  $D_2$  can be adjusted to provide maximum correction to the initial kinetic energy spread. Setting the distances

$$D_1 + D_2 = 4d \quad (1.18)$$

optimizes the mass resolution for a single-stage reflectron instrument [Cotter, 1997].

Use of a reflectron incurs a duty cycle penalty compared to a linear instrument, assuming the only difference between instruments is the presence or absence of a reflectron. A single stage RTOF-MS with drift length  $D$  will have a duty cycle that is 25% that of a linear TOF-MS with drift length  $D$ . The advantages of improved mass resolution with a reflectron instrument must be weighed against the duty cycle advantage of a linear instrument during the instrument design process.

### 1.3.3. Hadamard Transform Time-of-Flight Mass Spectrometry

The duty cycle for traditional TOF-MS instruments is generally on the order of 1%. A Hadamard-transform (HT) TOF-MS technique can be employed to increase the duty cy-

cle to 50% or, in a two-detector configuration, 100% [Brock *et al.*, 1998]. Because the HT-TOF-MS technique has been described and demonstrated elsewhere, only a brief description is given here [Brock *et al.*, 1998; Trapp *et al.*, 2004; Brock *et al.*, 2000; Fernández *et al.*, 2001; Zare *et al.*, 2003; Kimmel *et al.*, 2003; Fernández *et al.*, 2002; Yoon *et al.*, 2005].

Traditional TOF-MS instruments analyze one ion pulse at a time (section 1.3). The duty cycle is limited by the requirement that the heaviest ions of interest must transit the drift region before a new ion pulse can be introduced; this prevents lighter ions from overtaking heavier ions from a previous pulse. In contrast, HT-TOF-MS is a multiplexing technique that allows multiple ion pulses to exist in the drift region at the same time and be analyzed concurrently, regardless of whether the instrument is a linear or reflectron TOF-MS.

To perform HT-TOF-MS, ion pulses are introduced into the field-free drift region according to a pseudorandom binary sequence (PRBS), with a 1 representing on and a 0 representing off. A PRBS of length  $2^n - 1$ , where  $n$  is an integer, can be generated using a maximal length shift-register technique as described in Harwit and Sloane [1979]. An example of a PRBS with  $n = 3$  is

$$1 \ 1 \ 1 \ 0 \ 1 \ 0 \ 0 \ . \quad (1.19)$$

The pulse sequence starts from the right side of the PRBS. Using equation 1.19 as an example, the ion pulse would be off for two periods, on for one period, off for one period, and then on for three periods. The sequence then repeats. As ion pulses are introduced to the drift region, lighter ions from later pulses overtake heavier ions from earlier pulses.

The PRBS corresponds to the first row of an  $S$  matrix, with subsequent rows of  $S$  created “by cyclically shifting the previous row one place to the left” [Harwit and Sloane, 1979].

An example of a  $7 \times 7$   $S$  matrix is

$$S = \begin{bmatrix} 1 & 1 & 1 & 0 & 1 & 0 & 0 \\ 1 & 1 & 0 & 1 & 0 & 0 & 1 \\ 1 & 0 & 1 & 0 & 0 & 1 & 1 \\ 0 & 1 & 0 & 0 & 1 & 1 & 1 \\ 1 & 0 & 0 & 1 & 1 & 1 & 0 \\ 0 & 0 & 1 & 1 & 1 & 0 & 1 \\ 0 & 1 & 1 & 1 & 0 & 1 & 0 \end{bmatrix}, \quad (1.20)$$

and more examples are given in [Harwit and Sloane, 1979; Zare *et al.*, 2003]. Actual PRBSs and  $S$  matrices used for HT-TOF-MS are much larger than equations 1.19 and 1.20 [Zare *et al.*, 2003; Fernández *et al.*, 2001; Brock *et al.*, 2000]. For large  $S$  matrices, the ratio of 0s to 1s is very nearly 0.5; each row contains one fewer 0s than 1s. Since a 1 represents an ion pulse, the duty cycle of a HT-TOF-MS is 50%.

The flight times for individual species in the sample can be represented by a column matrix, TOF, with the same number of rows as  $S$ . The resulting spectrum has the appearance of random noise and is the product [Brock *et al.*, 1998; Fernández *et al.*, 2001; Zare *et al.*, 2003]

$$Z = S \times \text{TOF}. \quad (1.21)$$

$Z$  is the signal recovered from the mass spectrometer, and the time-of-flight spectrum, TOF, is unknown. The time-of-flight spectrum is deconvoluted by multiplying the inverse of  $S$  by  $Z$ , or

$$\text{TOF} = S^{-1} \times Z. \quad (1.22)$$

A simple example of HT-TOF-MS is presented in Zare *et al.* [2003].

The most obvious advantage of HT-TOF-MS over traditional TOF-MS is the increased

duty cycle. The duty cycle advantage of HT-TOF-MS has the potential to enable unprecedented spatial resolution of thin structures in the MLT that might otherwise go unnoticed. Additionally, the HT method as presented in this section can also improve the signal-to-noise ratio (SNR) by a factor of up to  $\frac{\sqrt{N}}{2}$ , where  $N$  is the number of rows in  $S$ , compared to traditional TOF-MS [Harwit and Sloane, 1979; Fernández et al., 2001].

#### 1.4. A New Time-of-Flight Mass Spectrometer for the MLT

Despite the ability of TOF-MS to make fast, accurate measurements over a theoretically unlimited mass range, this method has rarely been applied in the MLT, where ambient pressures can exceed 10 mTorr (Figure 1.2) [Viggiano and Hunton, 1999; Mamyrin, 2001]. TOF-MS traditionally employs acceleration voltages in the tens of kV range, making electrical discharge a concern at MLT pressures. This technique also relies on MCP detectors, high-voltage devices that are prone to elevated background count rates and destructive discharge events at pressures above  $10^{-6}$  Torr. Furthermore, higher pressures lead to increased collisions between accelerated ions and residual gases in the drift region, contributing to degraded mass resolution [Schuerch et al., 1994; de Hoffmann and Stroobant, 2007].

The subject of this dissertation is a new axially sampling TOF-MS instrument, developed at the Space Dynamics Laboratory (SDL), suitable for making measurements in the MLT. The instrument was originally conceived by Dr. Erik Syrstad, an instrument scientist at SDL, for the purpose of measuring thin metal layers of meteoric origin in the MLT. This work was funded by NASA (grant # NNX09AH97G). During the course of this research, new applications for this versatile instrument were identified, including general atmospheric composition measurements. The instrument has been included as a vital component for several sounding rocket proposals. The goal of the research presented in this dissertation was to build a functional instrument head that could be tested in the existing ion optics facilities at SDL, using rack-mounted power supplies and commercial pulse-processing electronics, to demonstrate the instrument concept. This research culminated in

the construction and testing of an engineering demonstration unit (EDU) of a linear TOF-MS. As a matter of definition, the terms the instrument, the SDL instrument, and SDL TOF-MS will refer to the concept of the new instrument under development, EDU will refer to the laboratory prototype instrument that was constructed in conjunction with this research, and TOF-MS will be used in reference to the time-of-flight technique of mass spectrometry.

The SDL instrument incorporates several design features to enable successful operation in the MLT; these are summarized in Table 1.1. The instrument employs modest acceleration voltages (100 - 300 V) and a pressure tolerant MCP detector [Cochran *et al.*, 2005; Laprade and Cochran, 2006; Laprade *et al.*, 2006] to reduce the possibility of electrical discharge events in the instrument while operating in the MLT. A drift region of 15 cm in length is employed to reduce collisions with residual gases as ions traverse the drift region. The SDL TOF-MS is small, compact, and inherently adaptable. It may be configured to measure either ions or neutral particles and may be designed as a linear instrument or as a reflectron instrument, depending on the kinetic energy distribution of the atmosphere to be sampled. During a rocket flight the instrument pressure can be managed by an appropriately sized sampling aperture combined with one of three different pumping schemes: miniature turbo pump, barium loaded Tubegetters<sup>®</sup> (TG), or cryogenic pumping, depending on mission requirements.

**Table 1.1.** Challenges to Performing TOF-MS in the MLT, and Corresponding Solutions Incorporated in the SDL Instrument

Challenge	Solution
High acceleration potentials leading to arcing	Modest acceleration potentials (100 to 300 V)
Reliance on pressure sensitive MCP detectors	Pressure-tolerant MCP detector (Photonis)
Collisions between ions and residual gases in drift region	Employ a 15 cm drift length

The diagram in Figure 1.7 shows the major components that make up the SDL instrument. The concept for the instrument is simple: ambient particles enter the instrument axially through a pinhole sampling aperture; the particles are then ionized (neutral mode only) via electron impact (EI) and subsequently accelerated (ion and neutral modes), forming a continuous ion beam with a nominally uniform energy; a Bradbury-Nielsen gate (BNG) [Bradbury and Nielsen, 1936] modulates the resulting ion beam, ultimately creating the ion pulses that then travel across a field-free drift region to reach the MCP detector. The MCP detector converts particle impact events into electrical pulses, which are then analyzed with fast pulse processing electronics (not shown).

The SDL instrument incorporates design elements to minimize the contributions to peak broadening discussed in section 1.3.1. These are summarized in Table 1.2. The BNG acts as a space-focus plane, greatly reducing the spatial uncertainty contribution to resolution degradation [Yoon *et al.*, 2007]. Temporal uncertainty is also reduced by the BNG, to the length of the start pulse [Trapp *et al.*, 2004; Kimmel *et al.*, 2003]. The ionization region is designed to be field free or to have a very small electric field with respect to the acceleration potential (adding a fraction of an eV to sampled ions), meaning that the instrument contribution to kinetic energy spread is small. To sample regions of the atmosphere with

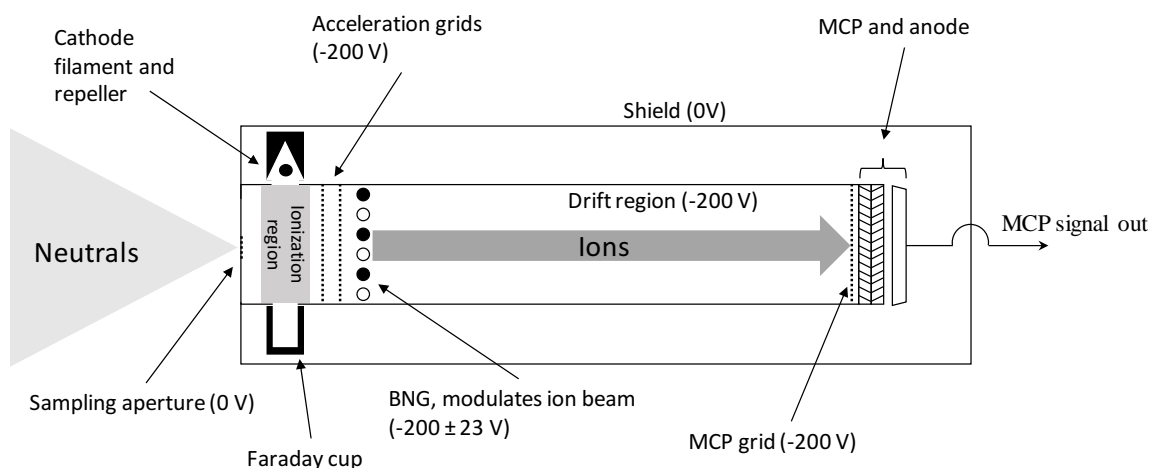


**Figure 1.7.** Instrument concept for the SDL TOF-MS.

energy spreads high enough to require correction, the instrument can employ a reflectron. The short drift length reduces the probability of collisions between ions and residual gases. These design considerations are compatible with an instrument small enough to be used on a sounding rocket, or even a CubeSat.

During testing, the EDU demonstrated the ability to collect mass spectra with FWHM resolution of 100 at  $m/z$  40 (argon), indicating that at the FWHM resolution level, the instrument is capable of resolving the major atmospheric gas species, as well as some metal atoms. The EDU has demonstrated its ability to operate at elevated pressures by successfully collecting mass spectra at pressures extending into the low  $10^{-4}$  Torr range. Additionally, the MCP detector used in the EDU has been extensively tested and has demonstrated low background count rates ( $\sim 1$  count/second) at pressures as high as 10 mTorr, validating previous high-pressure results with this particular model of MCP [Cochran *et al.*, 2005; Laprade and Cochran, 2006; Laprade *et al.*, 2006].

*In-situ* composition measurements made with the new TOF-MS will contribute to a better understanding of the MLT. This dissertation describes the design and characterization of the SDL instrument, with specific emphasis on the EDU. Chapter 2 describes the ion optics and electrical design of the EDU, while Chapter 3 describes the mechanical design and construction of the EDU. Chapter 4 describes experiments that were performed at ele-

**Table 1.2.** Factors that Contribute to Peak Broadening, and Corresponding Solutions Incorporated in the SDL TOF-MS.

Contributor to peak broadening	Solution
Spatial uncertainty	BNG
Temporal uncertainty	BNG
Initial kinetic energy distribution of sampled particles	Field-free ionizer, reflectron
Collisions between ions and residual gases	Employ short (15 cm) drift region

vated pressures with the MCP detector used in the EDU, demonstrating the ability of this particular detector to perform and survive at MLT pressures. Chapter 5 presents the pumping characteristics of a new getter-based pumping system proposed for use with the new instrument. Chapter 6 describes modeling of the bow shock and instrument pressure for a rocket-borne version of the instrument. Chapter 7 describes experiments performed in the SDL Ion Optics Test Facility (IOTF) with the EDU. Chapter 8 details instrument performance modeling, specifically the effect of critical operating parameters on instrument resolution. An instrument sensitivity analysis and predicted number density accuracy performance analysis are presented in Chapter 9. Finally, Chapter 10 discusses conclusions and directions for future work.

## CHAPTER 2

### ION OPTICS DESIGN

The ion optics of the SDL instrument are simple and consist of the following: a mesh at the entrance aperture (to improve field uniformity), an EI ionizer assembly (for ionization of neutral particles), two high-transmission acceleration grids, a BNG (to create ion pulses), a field-free drift region, and an acceleration grid (part of the MCP assembly) between the drift region and the face of the MCP detector. During instrument operation, the BNG switches between two states: beam-on and beam-off [Yoon *et al.*, 2007]. In the beam-on state, the BNG is held at the acceleration potential. In this state the BNG is transparent to the accelerated ions, allowing them to reach the MCP detector at the end of the drift region. In the beam-off state, the BNG deflects ions to prevent them from reaching the MCP detector. Results from ion optics modeling of the SDL instrument were applied in the design and construction of the EDU.

#### 2.1. Ion Optics Simulation Methods

SIMION<sup>®</sup> is an ion optics simulation program that allows the user to geometrically define electrodes and magnetic poles, called potential arrays, and to simulate ion trajectories through the resulting fields [Dahl, 2000; Manura and Dahl, 2011]. These potential arrays can be 2D or 3D and can have either planar, cylindrical, or no symmetry. An over-relaxation finite difference technique is used to solve the Laplace equation for the user-defined electrodes. Ion trajectories are calculated using a fourth order Runge-Kutta method with a self-adjustable time step. Ion definition variables include mass, charge, initial position, initial direction of motion, and initial kinetic energy. SIMION<sup>®</sup> (versions 7.0 and 8.1) was used to simulate deflection angles for ions passing through a BNG in the beam-off state, model electric fields and ion trajectories inside the instrument, and validate analytical equations for ion trajectories. Results from these simulations were used as inputs to a Monte Carlo model to predict ion behavior inside the instrument.

Ion trajectories inside the instrument can be described using kinematic equations and assuming ideal, uniform electric fields. However, individual ion behavior is difficult to predict because ions can enter the instrument at any location in the pinhole aperture and with a range of velocities in the  $x$ ,  $y$ , and  $z$  directions. A Monte Carlo model, written in MATLAB<sup>®</sup>, was used to simulate the collective ion behavior inside the instrument in beam-on and beam-off modes. These large-scale ion behavior simulations could have been performed using SIMION<sup>®</sup>; however, MATLAB<sup>®</sup> was chosen mainly for its ease of use and availability.

The Monte Carlo ion behavior model used the MATLAB<sup>®</sup> random number generator to randomize starting positions and velocities for simulated ions (typically numbering  $10^6$  -  $10^7$ ) at the instrument aperture. Simulated ion velocities at the aperture were randomized in the  $x$ ,  $y$ , and  $z$  directions according to a Maxwell velocity distribution,

$$f(v) = \sqrt{\frac{m}{2\pi k_B T}} \exp\left(\frac{-mv^2}{2k_B T}\right), \quad (2.1)$$

where  $m$  represents the ion mass,  $v$  is the velocity,  $k_B$  is Boltzmann's constant, and  $T$  is the temperature. Kinematic equations were then applied to calculate the position of each simulated ion at the MCP detector, located at the end of the drift region. For ion behavior simulations for the beam-off state, deflection of simulated ions at the BNG was randomized based on results from SIMION<sup>®</sup> simulations. Instrument operating parameters (e.g., aperture size, acceleration potential, BNG deflection potential), as well as ion characteristics (e.g., temperature and mass) were user adjustable, allowing instrument operating parameters to be easily and quickly examined. These Monte Carlo simulations and their results will be discussed in more detail in sections 2.2 and 2.3.3.

## 2.2. Ion Behavior, Beam-on State

In the beam-on state the BNG is held at the same potential as the acceleration grid. Ions enter the instrument through the sampling aperture and enter the acceleration region. The acceleration region was modeled as a uniform electric field, resulting in a constant ion acceleration. After acceleration, ions pass into the field-free drift region. The uniform field in the acceleration region and the lack of fields in the drift region allow ion trajectories to be modeled using kinematic equations. Equations to describe the ion trajectories were developed and employed in a Monte Carlo simulation to determine the ion behavior in the beam-on state for different acceleration potentials. A derivation of these equations follows. The  $z$  direction is taken to lie along the instrument axis, and the  $x$  and  $y$  directions are perpendicular to the instrument axis and parallel to the MCP detector plane.

The strength of the electric field in the acceleration region is

$$E_z = \frac{V_{\text{acc}}}{d_{\text{acc}}}, \quad (2.2)$$

where  $V_{\text{acc}}$  is the potential difference between the entrance aperture and the acceleration grid, and  $d_{\text{acc}}$  is the distance from the entrance aperture to the acceleration grid.  $E_z$  is parallel to the instrument axis. The force on a charged particle in the acceleration region is

$$F_z = qE_z, \quad (2.3)$$

where  $q$  represents the ion charge. Applying Newton's second law gives

$$qE_z = ma_z, \quad (2.4)$$

where  $m$  is the ion mass. The acceleration of the ion in the  $z$  direction is

$$a_z = \frac{qV_{\text{acc}}}{md_{\text{acc}}}. \quad (2.5)$$

There is assumed to be no acceleration in either the  $x$  or  $y$  direction.

If an ion's initial velocity in the  $z$  direction is  $v_{iz}$ , and  $t_{\text{acc}}$  is the amount of time the ion spends in the acceleration region, then

$$d_{\text{acc}} = v_{iz}t_{\text{acc}} + \frac{1}{2}a_z t_{\text{acc}}^2. \quad (2.6)$$

Solving equation 2.6 for  $t_{\text{acc}}$  yields

$$t_{\text{acc}} = \frac{-v_{iz} + \sqrt{v_{iz}^2 + 2a_z d_{\text{acc}}}}{a_z}. \quad (2.7)$$

The velocity of an ion in the  $z$  direction at the end of the acceleration region can be expressed in terms of  $v_{iz}$ ,  $a_z$ , and  $d_{\text{acc}}$ , as

$$v_{fz} = \sqrt{v_{iz}^2 + 2a_z d_{\text{acc}}}. \quad (2.8)$$

Assuming no forces act in the  $x$  and  $y$  directions, the  $x$  and  $y$  positions of an ion at the plane of the acceleration grid are given by

$$x_{\text{acc}} = x_i + v_x t_{\text{acc}} \quad (2.9)$$

$$y_{\text{acc}} = y_i + v_y t_{\text{acc}}, \quad (2.10)$$

where  $x_i$  and  $y_i$  are the initial positions of the ion at the entrance aperture.

The drift region is field free; therefore, no forces act on ions here. The ion velocity in the drift region is equal to the ion velocity at the end of the acceleration region. Using

equation 2.8 for the ion velocity in the drift region, the time for an ion to travel the length of the drift region,  $d_{\text{drift}}$ , is

$$t_{\text{drift}} = \frac{d_{\text{drift}}}{v_{fz}} = \frac{d_{\text{drift}}}{\sqrt{v_{iz}^2 + 2a_z d_{\text{acc}}}}. \quad (2.11)$$

The  $x$  and  $y$  positions of the ion at the end of the drift region (the MCP detector plane) are

$$\begin{aligned} x_f &= v_x t_{\text{drift}} + x_{\text{acc}} \\ y_f &= v_y t_{\text{drift}} + y_{\text{acc}}. \end{aligned} \quad (2.12)$$

Using equations 2.9, 2.7, and 2.11,  $x_f$  and  $y_f$  are expressed as

$$x_f = v_x \left( \frac{d_{\text{drift}}}{\sqrt{v_{iz}^2 + 2\frac{qV_{\text{acc}}}{m}}} \right) + \frac{v_x m}{qV_{\text{acc}}} \left( \sqrt{v_{iz}^2 + 2\frac{qV_{\text{acc}}}{m}} - v_{iz} \right) + x_i \quad (2.13)$$

$$y_f = v_y \left( \frac{d_{\text{drift}}}{\sqrt{v_{iz}^2 + 2\frac{qV_{\text{acc}}}{m}}} \right) + \frac{v_y m}{qV_{\text{acc}}} \left( \sqrt{v_{iz}^2 + 2\frac{qV_{\text{acc}}}{m}} - v_{iz} \right) + y_i. \quad (2.14)$$

This analysis has assumed that no forces act on the ions in the  $x$  or  $y$  directions. In reality, there could be forces acting in the  $x$  and  $y$  directions, including magnetic fields (gyroradius) and gravity. The worst case scenario for magnetic field effects is a hydrogen ion traveling exactly perpendicular to a magnetic field. The gyroradius is given by

$$r = \frac{mv_{\perp}}{qB}, \quad (2.15)$$

where  $m$  is the particle mass,  $B$  is the magnitude of the magnetic field, and  $q$  is the charge of a particle traveling at a velocity,  $v_{\perp}$ , perpendicular to the magnetic field. The maximum magnetic flux due to Earth's magnetic field occurs at the geomagnetic poles and is about 60,000 nT [Pisacane, 2008]. The gyroradius for a 200 eV (typical energy for the instru-

ment) hydrogen ion traveling perpendicular to this magnetic field is 34 m. This translates to a deviation of about 0.3 mm in the position at which a hydrogen ion would impact the detector in the instrument. Heavier ions would be affected even less. The gravitational effect on a 200 eV argon ion would cause a deviation in trajectory of less than a nanometer over the length of the drift region; gravitational forces are also negligible. Nonideal meshes, misaligned instrument components (mechanical defects), and nonuniform surfaces could lead to nonuniform electric fields inside the instrument, but were ignored in this analysis.

A SIMION<sup>®</sup> model of the SDL instrument (Figure 2.1) was used to validate equations 2.13 and 2.14. These equations were subsequently used in a MATLAB<sup>®</sup> Monte Carlo model of ion behavior for the beam-on state. As described in section 2.1, the model assigned random starting positions to ions distributed uniformly across the instrument aperture. Ion velocities were assumed to behave according to a nondrifting Maxwellian distribution [Hargreaves, 1979], and the initial velocities of the simulated ions,  $v_x$ ,  $v_y$ , and  $v_{iz}$  were randomized accordingly. Simulated instrument dimensions of  $d_{\text{drift}} = 15$  cm and  $d_{\text{acc}} = 0.44$  cm were used to represent an appropriately sized instrument for use on a sounding rocket. The simulated detector diameter was 18 mm, identical to the MCP intended for use in the SDL TOF-MS. The center of the MCP detector lay on the instrument axis. Equations 2.13 and 2.14 were applied to determine the arrival location of each simulated ion at the MCP detector plane. The physical dimensions of the instrument were not varied during simulations. The percentage of ions with a final radial position within one MCP detector radius of the instrument axis was measured for each simulation, and the simulation was repeated for different acceleration potentials from 100 to 250 V.

Figure 2.2 shows results from a simulation performed with initial ion velocities corresponding to a temperature of 600 K, chosen as a representative temperature in the MLT (see Figure 1.2). At the very modest acceleration potential of  $V_{\text{acc}} = 100$  V, 99.6% of simulated ions reach the MCP detector, increasing to 99.998% at  $V_{\text{acc}} = 200$ . To consider the effect of rocket speed on the ion collection efficiency, a drifting Maxwellian velocity distribution

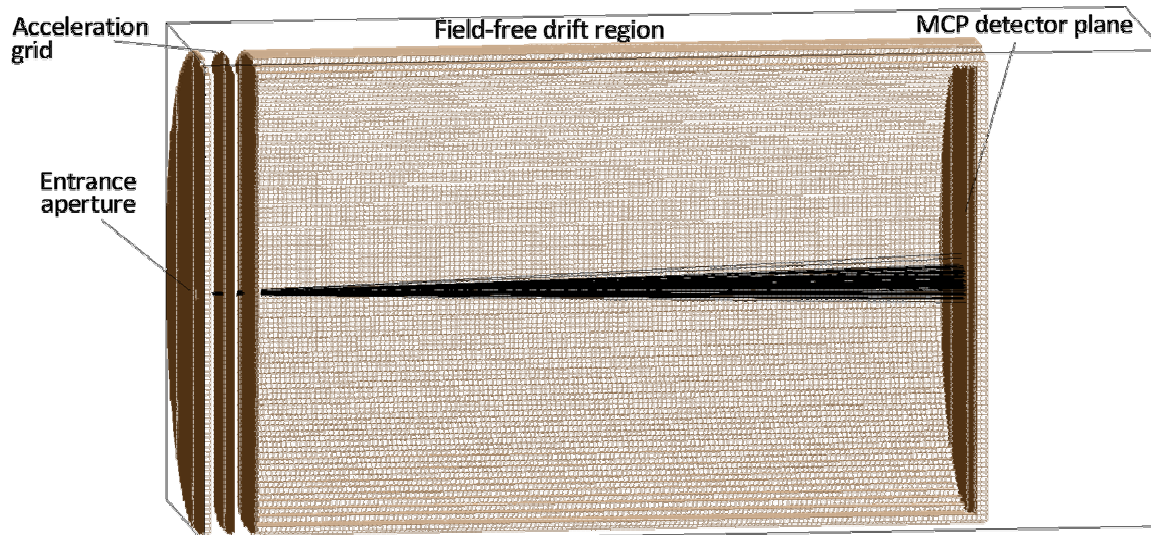


**Figure 2.1.** SIMION<sup>®</sup> model of the SDL instrument. Ion trajectories are shown as black lines. This model was used to validate equations 2.13 and 2.14, which were used in a MATLAB<sup>®</sup> Monte Carlo simulation of ion trajectories in the instrument in the beam-on state.

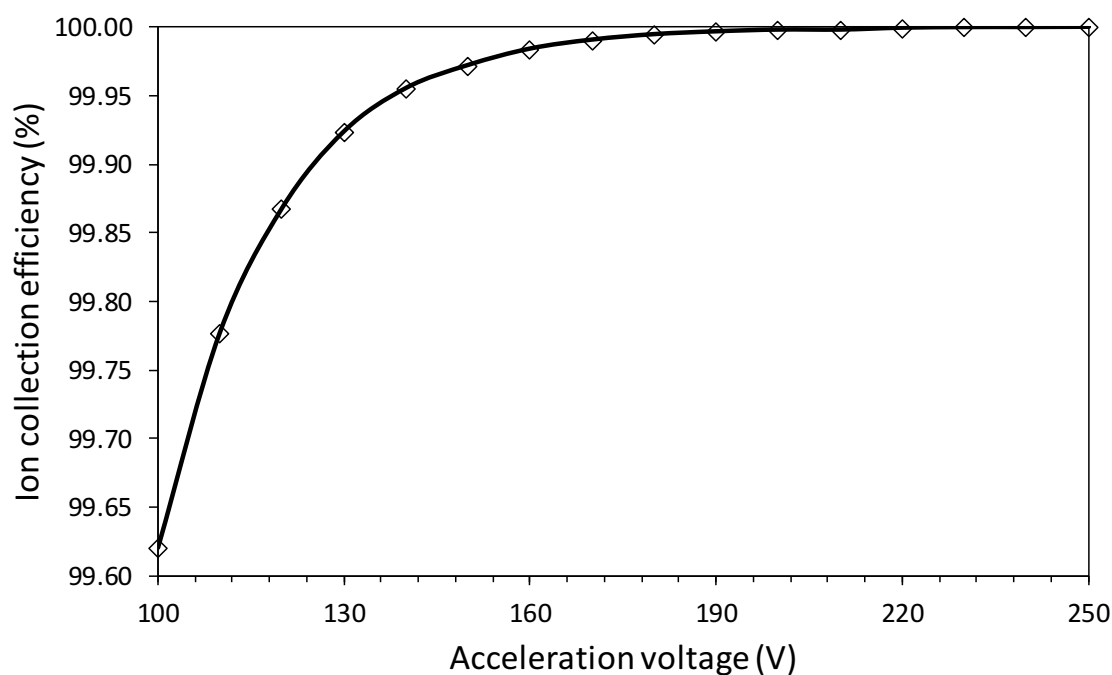


**Figure 2.2.** Ion collection efficiency, beam-on state. Monte Carlo simulation results for ion collection efficiency (defined as the fraction of simulated ions arriving at the MCP detector plane that land within the MCP active area) in the beam-on state. Initial ion velocities correspond to a 600 K Maxwellian velocity distribution.

in the  $z$  direction could be used in the simulation. This would have the effect of slightly improving the collection efficiency (due to higher  $v_z$ ), but was not considered for this simulation. The results from these simulations indicated that an MCP detector with an active diameter of 18 mm would be appropriate to use in the SDL instrument.

### 2.3. Ion Behavior, Beam-off State

The BNG is perhaps the single most important piece of enabling technology for the SDL instrument, as it permits the axial sampling and precise modulation of ion beams [Zare *et al.*, 2003; Yoon *et al.*, 2005]. The BNG is positioned behind the acceleration grid such that the instrument axis is normal to the BNG plane. Ions enter the instrument with a velocity vector nominally parallel to the instrument axis. The BNG chops the incoming ion beam, creating the ion pulses necessary to perform TOF-MS. SIMION<sup>®</sup> was used to model individual ion trajectories with the BNG in the beam-off state. Results from these simulations were used in a MATLAB<sup>®</sup> Monte Carlo model to simulate ion behavior in the beam-off state. The simulation results were used to determine the deflection voltages to apply to the BNG in the beam-off state.

#### 2.3.1. Bradbury-Nielsen Gate: An introduction

The basic principle behind the TOF-MS technique involves imparting a known energy to a packet of ions and measuring the amount of time required by the ions to travel a known distance, as described in section 1.3. The SDL instrument employs a BNG to create ion packets from the incoming ion beam. The BNG acts as an ion gate by allowing ions to travel unimpeded to the MCP detector (beam-on state) or deflecting ions to prevent them from reaching the detector (beam-off state) [Bradbury and Nielsen, 1936; Yoon *et al.*, 2007, 2008]. A BNG consists of two interleaved sets of wires, each set electrically isolated from the other. Figure 2.3 describes BNG operation for both the beam-on and beam-off states, with illustrations representing both an axial and side view of a BNG. In the beam-on state, both wire sets that comprise the BNG are held at the acceleration potential,  $V_{acc}$ .

Since the drift region is also at  $V_{\text{acc}}$ , ions pass through the BNG without being deflected. In the beam-off state a deflection potential ( $V_{\text{def}}$ ) is applied to offset each set of wires from the acceleration potential. The deflection potential for one set of wires is positive ( $V_{\text{acc}} + V_{\text{def}}$ ) while the deflection potential for the other set of wires is negative ( $V_{\text{acc}} - V_{\text{def}}$ ). Ions passing through the gate pass between two wires, each with a different potential. In the case of positive ions, ions are attracted to the wire with potential  $V_{\text{acc}} - V_{\text{def}}$  and repelled from the wire with potential  $V_{\text{acc}} + V_{\text{def}}$ . The resulting deflection causes the incoming ion beam to split in two, each traveling away from the instrument axis and thus missing the MCP detector.

In the beam-off state the deflection field generated by the BNG is only visible to ions when they are within a distance of a few wire spacings of the BNG [Yoon *et al.*, 2007]. Outside of this distance the deflection field from the BNG is indistinguishable from the acceleration potential. Ions that are traveling toward the BNG, but are still some distance

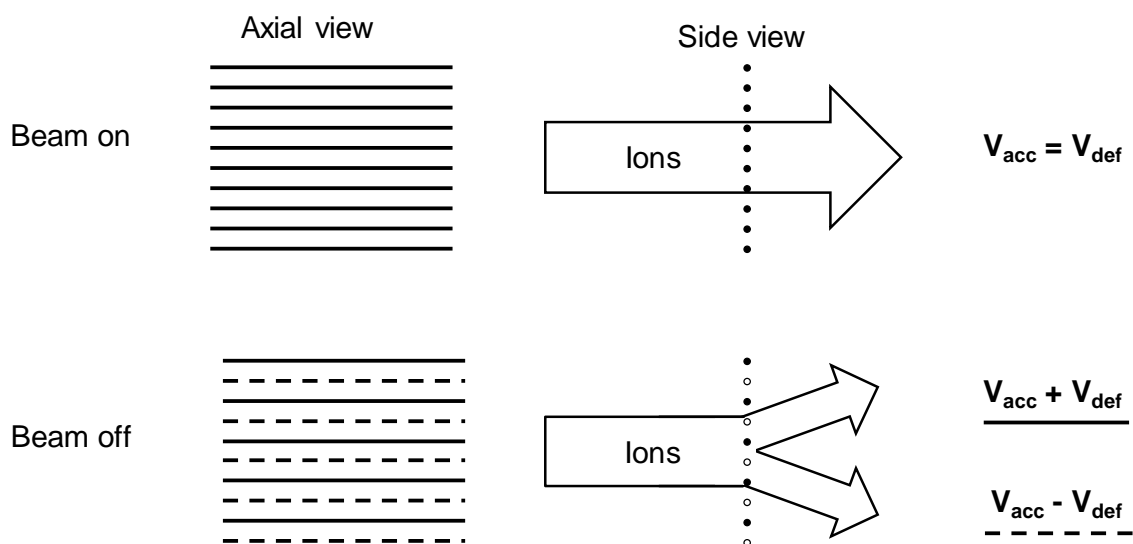


**Figure 2.3.** Illustration representing axial and side views of a BNG for both beam-on and beam-off states. In the beam-on state, both sets of wires that comprise the BNG are held at the acceleration potential. A charged particle traveling toward the BNG experiences no deflection. In the beam-off state (lower figure, solid and dotted wires) each set of wires is offset from the acceleration potential by  $+V_{\text{def}}$  or  $-V_{\text{def}}$  and ions are deflected away from the TOF-MS instrument axis.

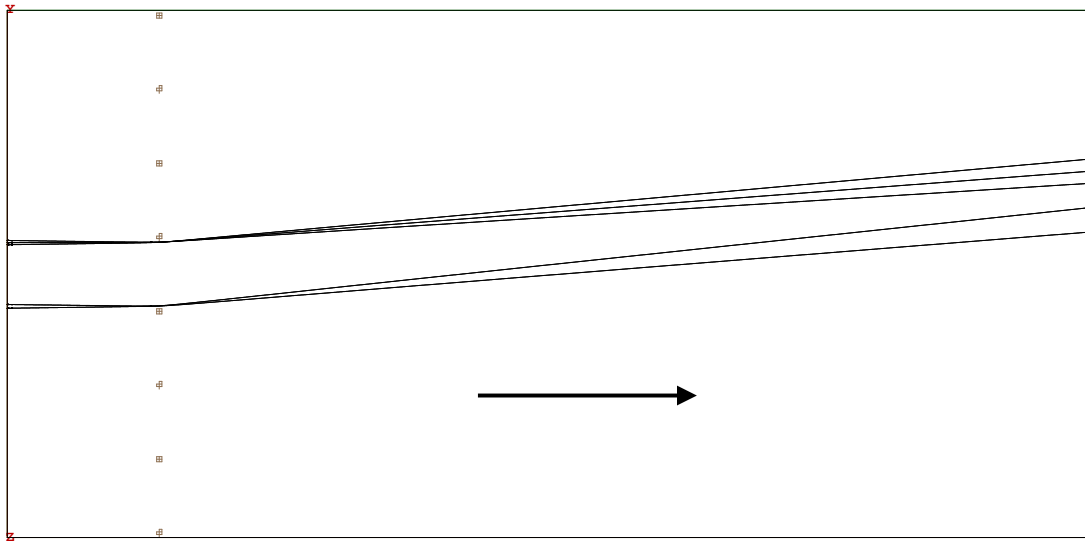
away, are affected negligibly by the BNG in the beam-off state. If switching between beam-on and beam-off states is fast enough, most ions experience the full effect of either the beam-off state or the beam-on state, yielding very-well-defined ion packets [Zare *et al.*, 2003; Yoon *et al.*, 2005, 2007].

### 2.3.2. SIMION<sup>®</sup> Modeling of the BNG

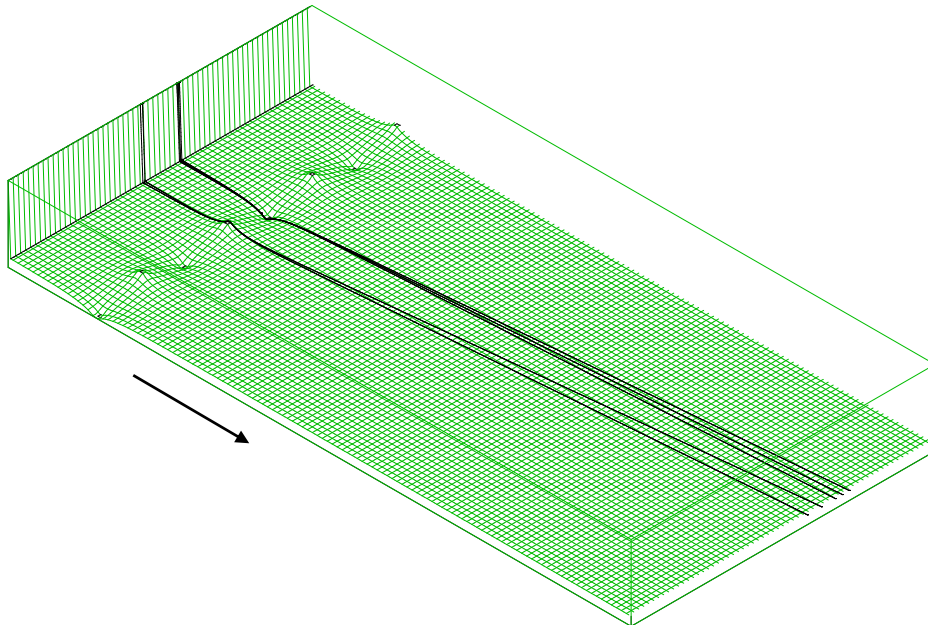
A 2D model of the BNG was created using SIMION<sup>®</sup> to simulate ions passing through the BNG and to find the resulting deflection angles of the ions. The model included an acceleration region and a 32-electrode BNG. Each electrode represented a 10  $\mu\text{m}$  diameter wire. The wire spacing was 75  $\mu\text{m}$ , center to center, resulting in 87% ion transmission in the beam-on state. Simulated ions were given initial positions such that after acceleration, they passed between the middle two electrodes in the simulation. The ions experienced a deflection as they passed through the BNG, and the deflection angle was measured as a function of the initial ion position. Simulations were conducted for acceleration potentials between 100 V and 200 V and for a range of deflection potentials.

A SIMION<sup>®</sup> simulation of positive ions being deflected by a BNG is shown in Figure 2.4. After being accelerated, the ions approach and pass through the middle two electrodes of the BNG, which is visible in the left half of Figure 2.4a as a vertical row of dots. The upper electrode is biased negative relative to the lower electrode, causing ions to deflect upward. Figure 2.4b shows a potential energy view of the simulation, with the dark dots at the tops and bottoms of the alternating peaks and depressions representing the BNG wires. The acceleration region is the steep drop on the upper left side of Figure 2.4b, after which the ions pass through the BNG and are deflected in the direction of the more negative electrode.

Simulation results indicated a relationship between the deflection angle and the ratio  $V_{\text{acc}}/V_{\text{def}}$ . Figure 2.5 shows the deflection angle from SIMION<sup>®</sup> simulations for  $V_{\text{acc}}/V_{\text{def}}$  ratios ranging from 4 to 10, which yield deflection angles appropriate for our geometry. For



(a)



(b)

**Figure 2.4.** BNG simulation using SIMION<sup>®</sup>. In each view ions travel in the direction of the black arrow. (a) An xy-plane view is shown, with electrodes visible in the left half of the figure as a vertical row of dots. (b) Potential energy view of the same BNG simulation. The green mesh represents the potential energy surface generated by the BNG electrodes, located at the centers of the alternating hills and pits, with deflection potentials applied. The deflecting effect of the BNG is particularly evident in the potential energy view.

example, a 100 eV ion that passes through a BNG with  $V_{\text{def}} = \pm 20$  V will be deflected the same amount as a 200 eV ion that passes through a BNG with  $V_{\text{def}} = \pm 40$  V. The starting position referred to in Figure 2.5 denotes the initial ion position with respect to the two central electrodes of the simulation. The center of the positive electrode is taken to be at  $0 \mu\text{m}$  and the center of the negative electrode is at  $75 \mu\text{m}$ . Ions with starting positions less than  $6 \mu\text{m}$  and greater than  $70 \mu\text{m}$  impacted the BNG electrodes and yielded no deflection data.

Figure 2.5 shows that decreasing the  $V_{\text{acc}}/V_{\text{def}}$  ratio increases the deflection angle. Based on this conclusion,  $V_{\text{acc}}$  could be made arbitrarily small to achieve the desired deflection angle, requiring only a small deflection potential. However, sampled particles exhibit an initial energy spread, related to their ambient temperature. At too low a value of  $V_{\text{acc}}$ , the resulting spread of ion pulses would degrade resolution. To prevent this,  $V_{\text{acc}}$  must be

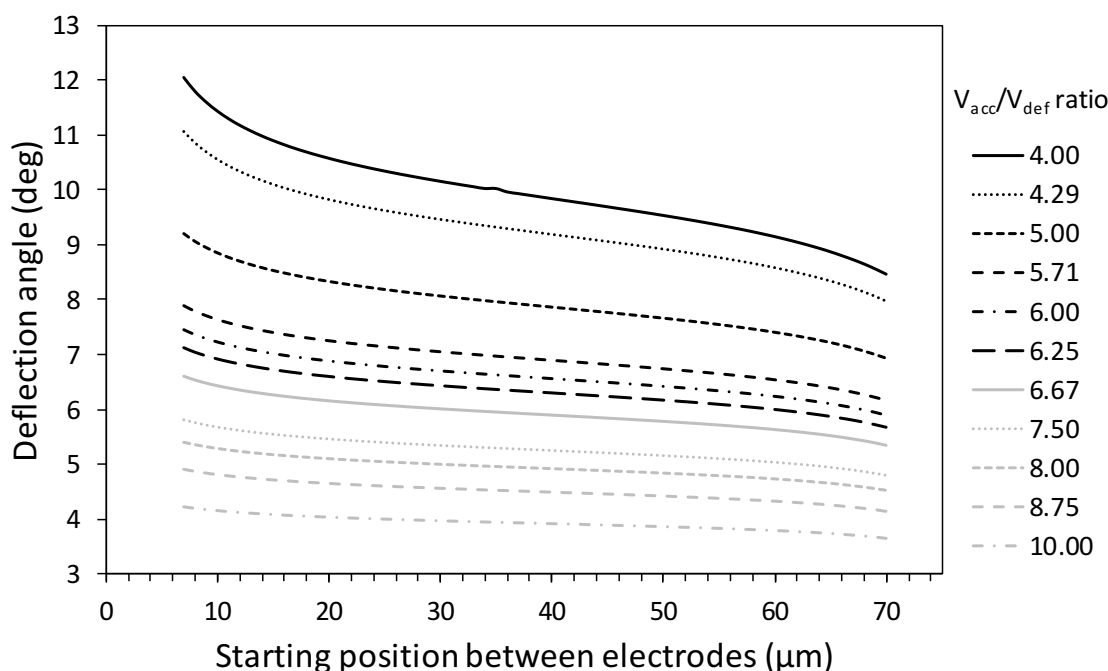


**Figure 2.5.** Deflection angles resulting from SIMION<sup>®</sup> simulations of ions passing through a BNG for  $V_{\text{acc}}/V_{\text{def}}$  ratios ranging from 4 to 10. The center of a positive electrode is located at  $0 \mu\text{m}$  and the center of a negative electrode is at  $75 \mu\text{m}$ . The simulated electrodes have a diameter of  $10 \mu\text{m}$ .

large compared to the thermal energy. Thermalized ions at 620 K, for example, have an average thermal energy of 0.08 eV. An acceleration potential of 200 V then yields a  $V_{\text{acc}}$  to thermal energy ratio of 2500. Ultimately,  $V_{\text{acc}}$  is chosen to strike a balance between the competing interests of achieving sufficient ion deflection at the BNG and minimizing the impact of the initial ion energy spread.

The deflection angle for each  $V_{\text{acc}}/V_{\text{def}}$  ratio shown in Figure 2.5 was fit to a third order polynomial,

$$\theta(x) = a_1x^3 + a_2x^2 + a_3x + a_4, \quad (2.16)$$

with the constants  $a_1$ ,  $a_2$ ,  $a_3$ , and  $a_4$  unique to each  $V_{\text{acc}}/V_{\text{def}}$  ratio. The normalized position between adjacent BNG wires is represented by  $x$  and ranges from  $0 \leq x \leq 1$ . A starting position of 75  $\mu\text{m}$  corresponds to  $x = 1$ . The fitting coefficients for equation 2.16 are shown in Figure 2.6 for several values of  $V_{\text{acc}}/V_{\text{def}}$ . Although the fitting constants were unique to each  $V_{\text{acc}}/V_{\text{def}}$  ratio, each  $a_i$  followed a trend that could be described by an equation of the form

$$a_i = c_1e^{c_2y} + c_3, \quad (2.17)$$

where  $y \equiv V_{\text{acc}}/V_{\text{def}}$ . The resulting equations for each fitting coefficient  $a_i$  were

$$a_1 = -56.199e^{-0.556y} - 0.937, \quad (2.18)$$

$$a_2 = -100.748e^{-0.574y} - 1.461, \quad (2.19)$$

$$a_3 = -66.959e^{-0.567y} - 0.986, \quad (2.20)$$

and

$$a_4 = -36.279e^{-0.367y} - 3.391. \quad (2.21)$$

Applying equations 2.18 through 2.21 to equation 2.16 allows the deflection angle of an ion by a BNG to be calculated solely in terms of the initial ion position and the  $V_{\text{acc}}/V_{\text{def}}$

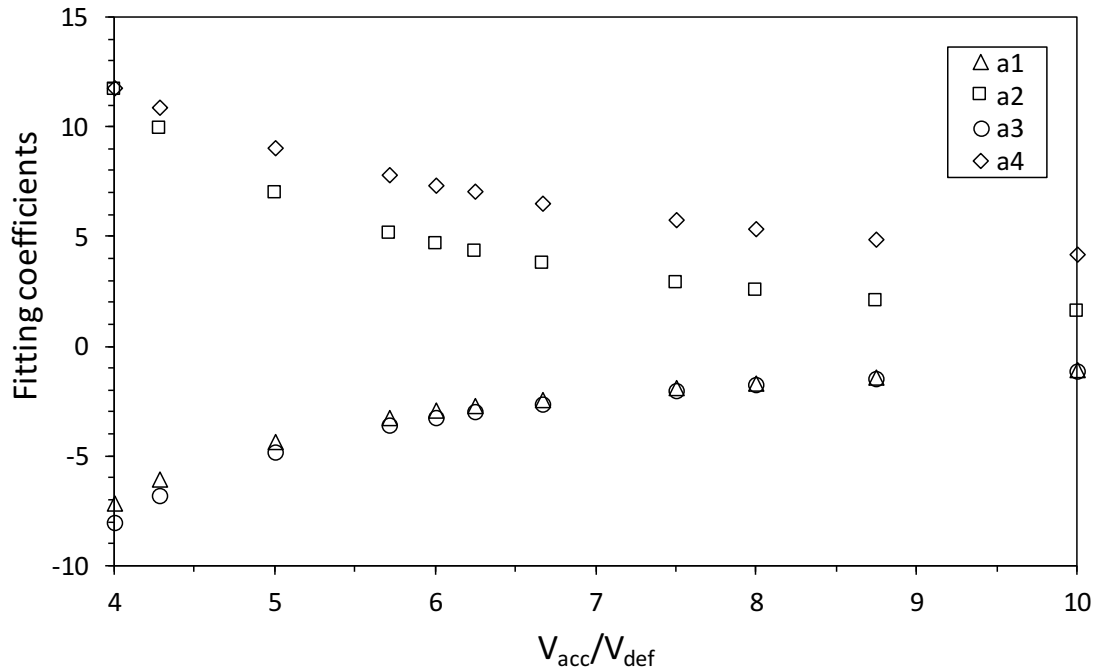


**Figure 2.6.** Fitting coefficients  $a_1$ ,  $a_2$ ,  $a_3$ , and  $a_4$  for equation 2.16, plotted against the ratio  $V_{acc}/V_{def}$ .

ratio. For values of  $V_{acc}/V_{def}$  from 4 to 10, this method of calculating the deflection angle is in very close agreement with SIMION<sup>®</sup> simulations. In fact, most discrepancies between the two methods are on the order of  $0.001^\circ$ . The largest discrepancy observed was  $0.025^\circ$ . For comparison, from the location of the BNG the MCP detector subtends an angle of  $6.9^\circ$ . Equation 2.16, using randomized starting positions, was used in a Monte Carlo model (section 2.3.3) to simulate the collective behavior of ions passing through a BNG in the beam off state.

### 2.3.3. BNG Deflection Efficiency

A MATLAB<sup>®</sup> Monte Carlo model, similar to the model described in section 2.2, was used to estimate the fraction of ions that would reach the MCP detector for different deflection potentials. Simulated ions, typically numbering  $10^6$ , were assigned random starting positions at the instrument aperture. Each ion was then assigned a random velocity in the  $x$ ,  $y$ , and  $z$  directions, corresponding to a Maxwell velocity distribution (equation 2.1). The

simulated ions were then accelerated from the aperture to the acceleration grid as described in section 2.2, equations 2.2 - 2.10. The ion trajectory was then continued to a location on the BNG, where a deflection angle was assigned to each ion using equations 2.16 and 2.18 - 2.21, with  $y = V_{\text{acc}}/V_{\text{def}}$ . A random value between 0 and 1, representing the position between the BNG electrodes, was assigned to the variable  $x$  in equation 2.16 for each ion. Using the deflection angle and  $d_{\text{drift}}$ , the distance from the BNG to the detector plane, the  $x$  and  $y$  locations of the ion at the detector plane were calculated. As with the simulation of ions in the beam-on state described in section 2.2, the values  $d_{\text{acc}} = 0.44$  cm,  $d_{\text{drift}} = 15$  cm, and a detector diameter of 18 mm were used.

*Yoon et al.* [2005] derive an expression for the BNG deflection angle, which is expressed as

$$\tan \alpha(x_0, x_1; y_0) = k \frac{V_{\text{def}}}{V_{\text{acc}}} [\Theta(x_1, y_0) - \Theta(x_0, y_0)], \quad (2.22)$$

where  $k$  is a constant that depends on the BNG wire radius,  $R$ , and wire spacing,  $d$ , and is given by

$$k \equiv \frac{\pi}{2 \ln \left[ \cot \left( \frac{\pi R}{2d} \right) \right]}. \quad (2.23)$$

$\Theta(x, y)$  is defined as

$$\Theta(x, y) \equiv \frac{1}{\pi} \left[ \arctan \left( \frac{e^{\pi x/d} + \sin(\pi y/d)}{\cos(\pi y/d)} \right) + \arctan \left( \frac{e^{\pi x/d} - \sin(\pi y/d)}{\cos(\pi y/d)} \right) \right], \quad (2.24)$$

where  $x$  is the distance of an ion from the BNG plane and  $y$  represents the spacing of an ion between adjacent BNG wires. Equation 2.22 is valid for  $V_{\text{acc}} \gg V_{\text{def}}$ . Typical values of  $V_{\text{acc}}/V_{\text{def}}$  used in *Yoon et al.* [2005] range from 10 - 100, which is higher than the values used in this study (section 2.3.2).

A Monte Carlo simulation, similar to that described earlier in this section, was performed to compare equations 2.22 and 2.16, and results are shown in Figure 2.7 for  $V_{\text{acc}} = 200$  V. For values of  $V_{\text{def}} > 20$  V (corresponding to  $V_{\text{acc}}/V_{\text{def}} = 10$ ), the deflection efficiency

for both methods is in close agreement. At  $V_{\text{def}} = 22.5$  V, where the BNG was actually operated, equation 2.16 gives a deflection efficiency of 92.0%, while equation 2.22 gives a deflection efficiency of 90.3%.

#### 2.4. Conclusions

The major design considerations resulting from ion optics modeling presented in this chapter were the acceleration and BNG deflection potentials to apply to the SDL instrument. These simulations showed that an acceleration potential of 200 V should be sufficient to collect over 99.99% of ions entering the instrument aperture (Figure 2.2). At this value of  $V_{\text{acc}}$ , the simulated BNG deflection efficiency is between 90.3% and 92.0% for  $V_{\text{def}} = 22.5$  V, increasing to 99.9% at  $V_{\text{def}} = 30$  V (Figure 2.7).

After the EDU was constructed and placed in the ion optics test chamber, actual BNG

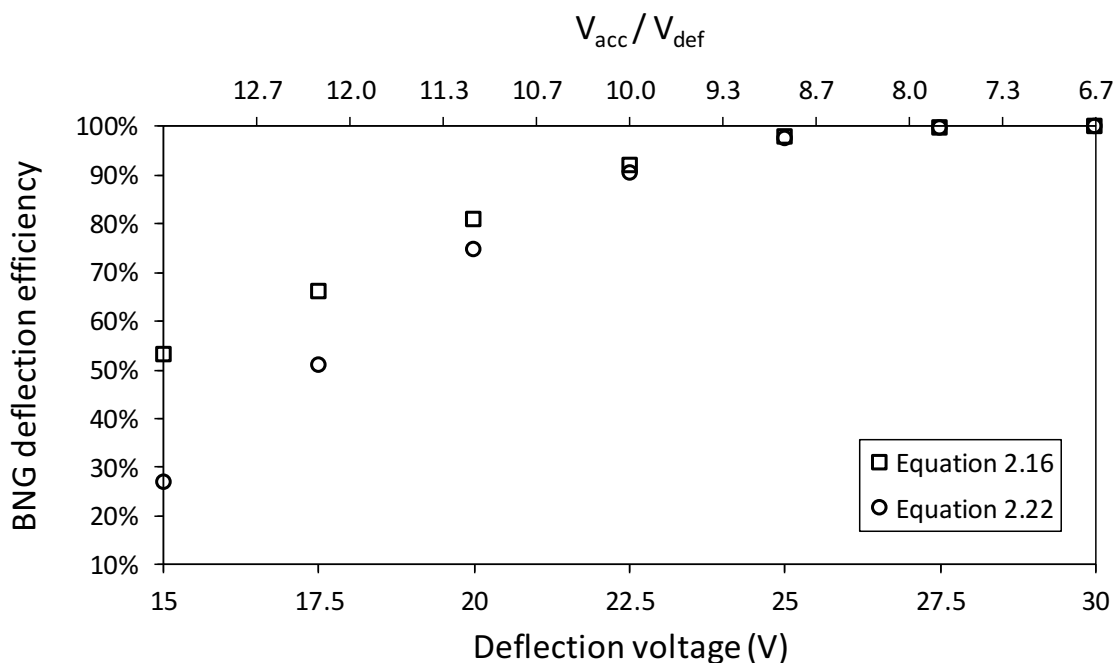


**Figure 2.7.** Comparison of BNG deflection efficiency simulations, based on simulated and theoretically calculated BNG deflection angles. Both simulations used  $V_{\text{acc}} = 200$  V,  $d_{\text{drift}} = 15$  cm, with a detector diameter of 18 mm. Particles were assumed to be thermalized at 600 K.

deflection performance was compared to simulation results. In making this comparison, it is important to remember that ions may have significant kinetic energy before entering the instrument. For example, ions that enter the instrument with an initial energy of 20 eV (generated by an ion gun) that are subsequently accelerated by a potential of  $V_{\text{acc}} = 180$  V will encounter the BNG with an energy of 200 eV. Figure 2.8 shows the experimental BNG deflection efficiency for 200 eV ions compared to simulation results using the same energy for both equation 2.16 and equation 2.22 [Yoon *et al.*, 2005]. The actual BNG deflection efficiency is not as high as either of the simulated deflection efficiencies for  $V_{\text{def}} > 20$  V. At  $V_{\text{def}} = 20$  V, the experimental BNG deflection efficiency is 50.5%, compared to simulated deflection efficiencies of 80.8% (equation 2.16) and 74.5% (equation 2.22). The reason for this discrepancy is unclear, but may be due to nonuniformities in the BNG or even stray or nonuniform fields inside the EDU. Regardless, the deflection simulations provided an initial estimate of the deflection voltages that would need to be supplied to the BNG. The actual performance of the BNG is discussed further in section 7.2.1.

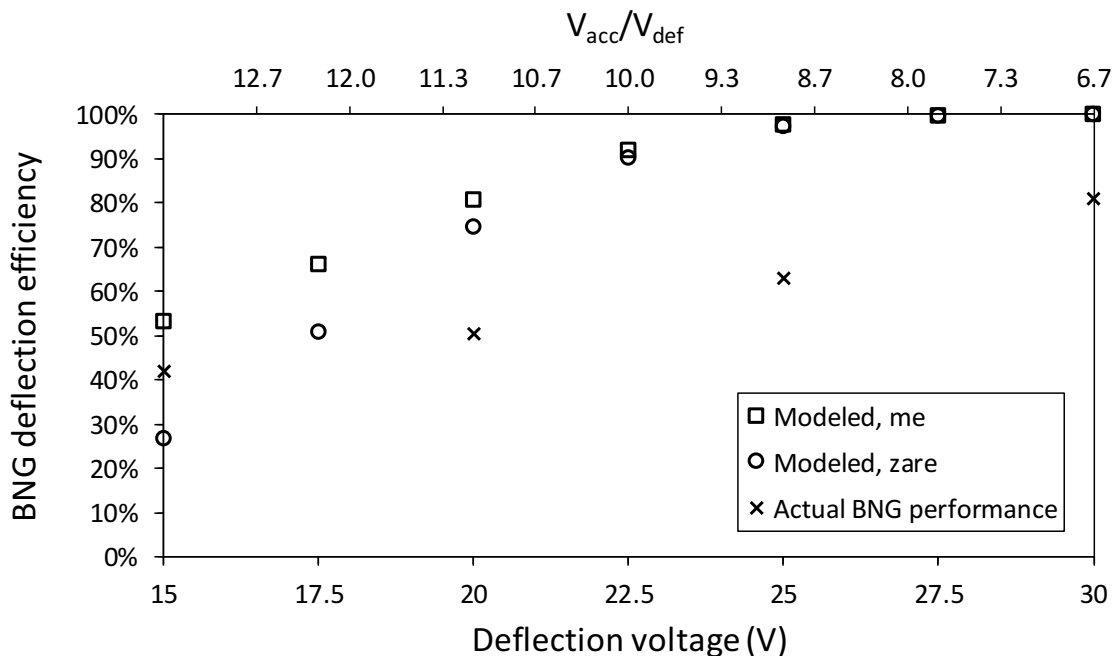


**Figure 2.8.** Comparison of simulated BNG performance with experimental results.

## CHAPTER 3

## ELECTRICAL AND MECHANICAL DESIGN

The goal of this project was to design and fabricate a functional prototype time-of-flight mass spectrometer and characterize it in the SDL IOTF. An overview of the instrument concept is given in section 1.4. This chapter describes the electrical and mechanical design of the instrument.

### 3.1. Electrical Design

Because the main objective of this project was to validate the SDL instrument concept, commercial electronics are used wherever possible. The electrical system, schematic shown in Figure 3.1, consists of three functional subassemblies: DC power, BNG modulation driver board (MDB), and data acquisition. Commercial laboratory DC power supplies provide voltages to instrument components including the MCP detector, acceleration grids, and the ionizer. HT TOF-MS requires the BNG to be modulated according to pseudorandom sequences. A driver board to provide deflection potentials ( $\pm V_{\text{def}}$ ), with an accompanying pseudorandom sequence generator, was designed and constructed in-house at SDL. The EDU uses commercially available data acquisition electronics (with accompanying analysis software) to detect, amplify, and process pulses resulting from ions impacting the MCP detector. An overview of each electrical subassembly follows.

#### 3.1.1. DC Power

DC power requirements for the instrument range from a fraction of a volt to -2400 V, as shown in Figure 3.1. During normal operation the second acceleration grid, drift tube, and MCP grid require a modest potential,  $V_{\text{acc}}$ , usually -200 V. One set of BNG wires floats at  $V_{\text{acc}} + V_{\text{def}}$  (-180 V) while the other set floats at  $V_{\text{acc}} - V_{\text{def}}$  (-220 V). The BNG modulation potential is discussed further in section 3.1.2.

The ionizer consists of a barium-oxide coated tungsten filament, a repeller, and a Fara-

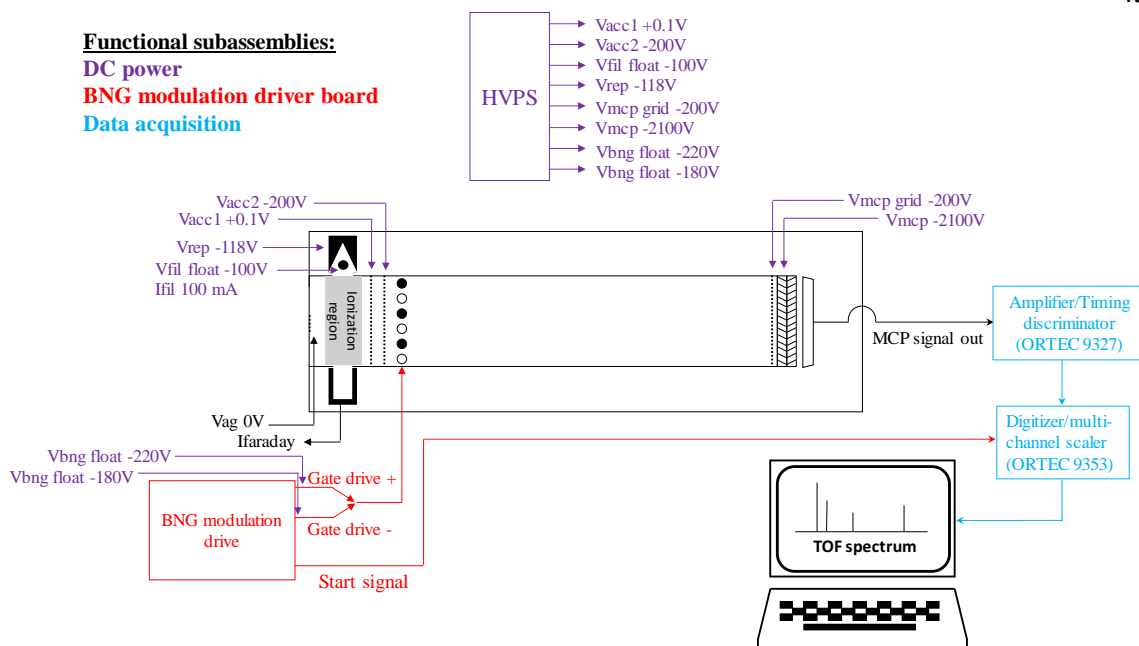


**Figure 3.1.** Electronics schematic for the EDU, showing the three functional subassemblies of the electrical system.

day cup (Figure 3.2a). The filament floats at  $-100\text{ V}$  while being heated by a current of  $100\text{ mA}$ , with a potential difference of  $1.35\text{ V}$  across the filament (wiring diagram shown in Figure 3.2b). The repeller is biased at  $-118\text{ V}$ , which maximizes the electron current flowing through the ionization region to reach the Faraday cup (Figure 3.3). Neutral particles are ionized via EI in the ionization region. The first high-transmission grid (also referred to as the first acceleration grid) is biased slightly positive ( $+0.1\text{ V}$ ) to reject background ions thermalized by interactions with instrument surfaces.

Lack of a supersonic neutral beam during laboratory testing of the EDU required some adjustments to the acceleration grid operating potentials. SIMION<sup>®</sup> simulations of the ionization region were conducted to determine the proper potentials to place on the acceleration grids in neutral mode (Figure 3.4). But, with the cathode and repeller biased as described in the preceding paragraph, neutral spectra were only obtained with both acceleration grids biased at  $+100\text{ V}$ . In this case the BNG provided the acceleration potential. Analysis of ion flight times yielded an energy of  $238\text{ eV}$  with the BNG centered on

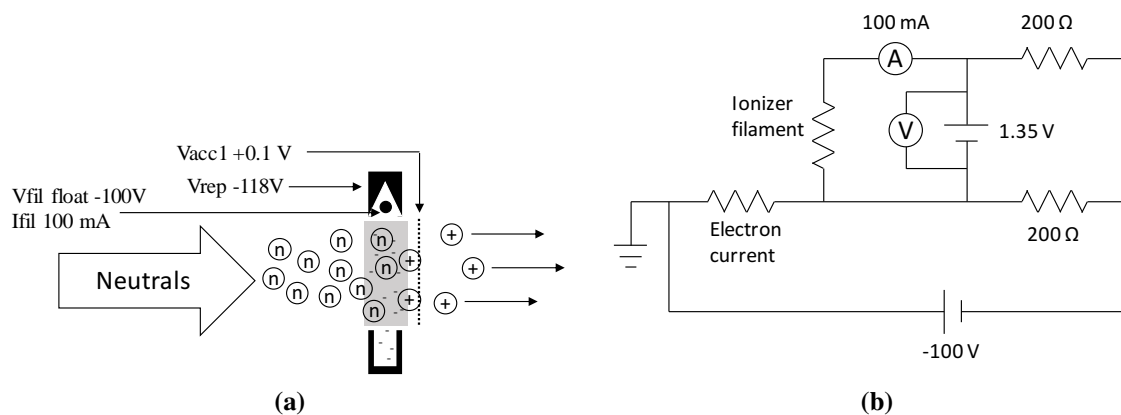


**Figure 3.2.** Ionizer drawing and wiring diagram. (a) Neutral particles are ionized via EI. The ionizer assembly consists of a cathode filament, repeller, and Faraday cup. (b) Wiring diagram for the filament.

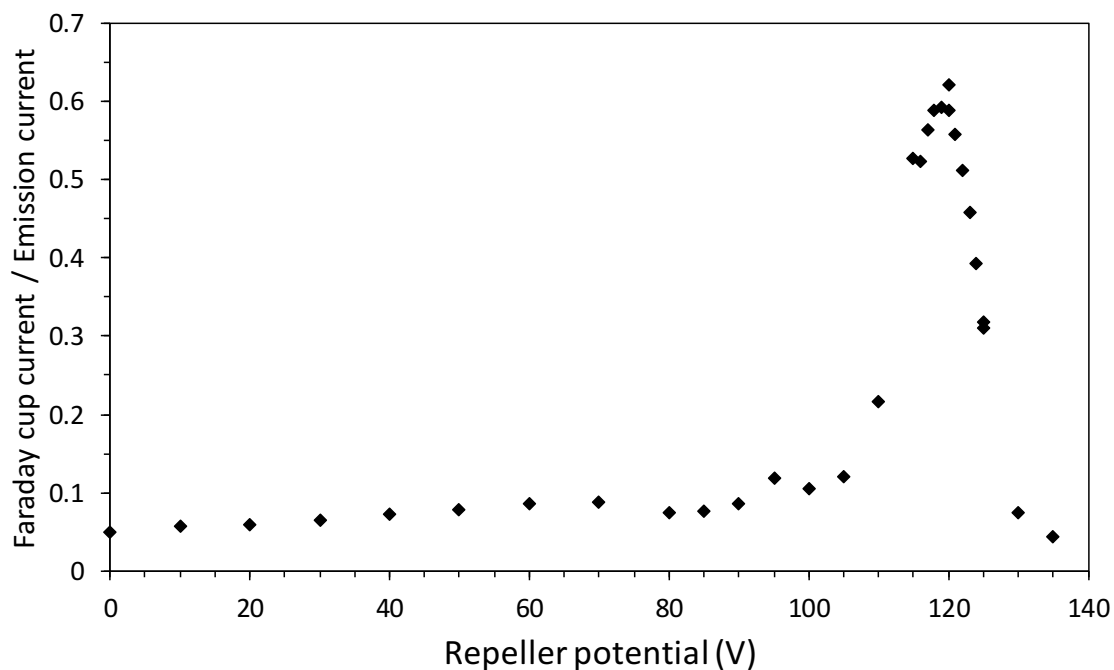
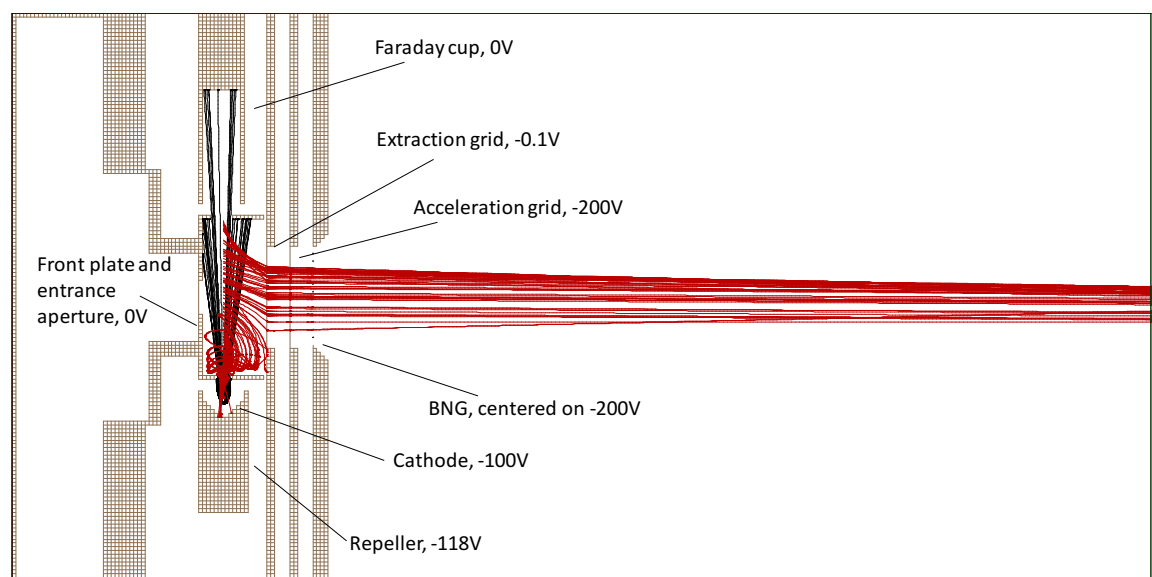


**Figure 3.3.** Ratio of Faraday cup current to the ionizer cathode emission current with the cathode floating at -100 V.

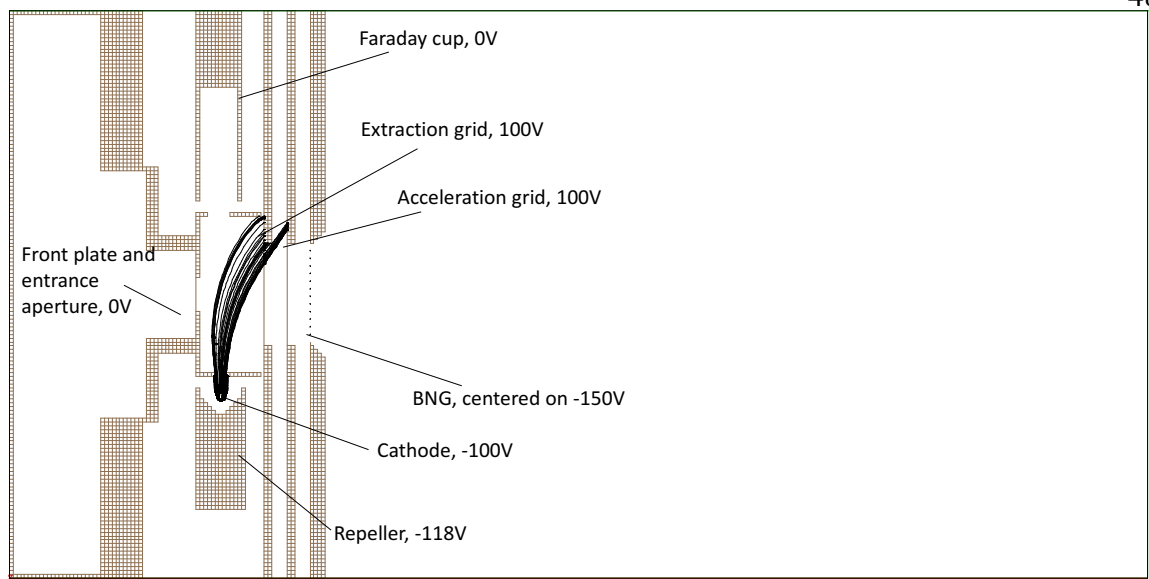
$V_{\text{acc}} = -200$  V, indicating that under these conditions ionization was taking place between the second acceleration grid and the BNG.

Figure 3.5 shows a SIMION<sup>®</sup> simulation of the ionizing electrons with the potentials that were actually applied to the high-transmission grids and the BNG in neutral mode. The difference between the expected and actual operation of the ionizer are likely caused by using ambient neutrals (with randomly distributed initial velocities) instead of a supersonic neutral beam. Ions produced from a supersonic beam would have an initial velocity sufficient to carry them beyond the ionization region and into the acceleration region. Additionally, a space-charge potential caused by the electron beam may impede ions from leaving the ionization region. It is expected that, during operation of the SDL instrument in the MLT or in LEO, ionized particles will retain a significant portion of their initial velocity relative to the instrument and pass through to the acceleration region.

The MCP detector is housed in a cartridge with a high-transmission grid at the input (Figure 3.6). The MCP itself is connected to the cartridge by a 10 M $\Omega$  resistor, and the



**Figure 3.4.** SIMION<sup>®</sup> simulation of ionizing electron and ion trajectories in neutral mode, for acceleration potentials that were expected to be used. Simulated electron trajectories are represented by black lines, while ions are shown as red lines.



**Figure 3.5.** SIMION<sup>®</sup> simulation of ionizing electron trajectories in neutral mode, for acceleration potentials that were actually used.

cartridge is in electrical contact with the drift tube. The MCP-HV is typically -2100 V and floats on the acceleration potential. The MCP is protected by setting a current limit on the MCP-HV power supply equal to 110% of the strip current. If the current through the MCP-HV power supply exceeds the current limit, the power supply immediately shuts down to protect the MCP from potentially damaging discharge events.

### 3.1.2. BNG Modulation Driver Board

Since the EDU built for this project was intended to be capable of operating in either traditional or HT mode, a custom-built MDB was constructed to provide BNG modulation deflection potentials ( $V_{\text{def}}$ ) and synchronized start pulses. The MDB stores Hadamard sequences with lengths for values of  $n$  from 4 to 15. Additionally, the MDB allows the pulse widths and repetition rate to be varied. The MDB was designed and programmed at SDL by senior electrical engineer, Wayne Sanderson, and electrical engineering students, Cameron Weston and Dan Allen. Board layout and fabrication were performed in-house at the SDL Electronics Assembly Laboratory.

A previous pseudorandom binary sequence generator for use in HT TOF-MS has been

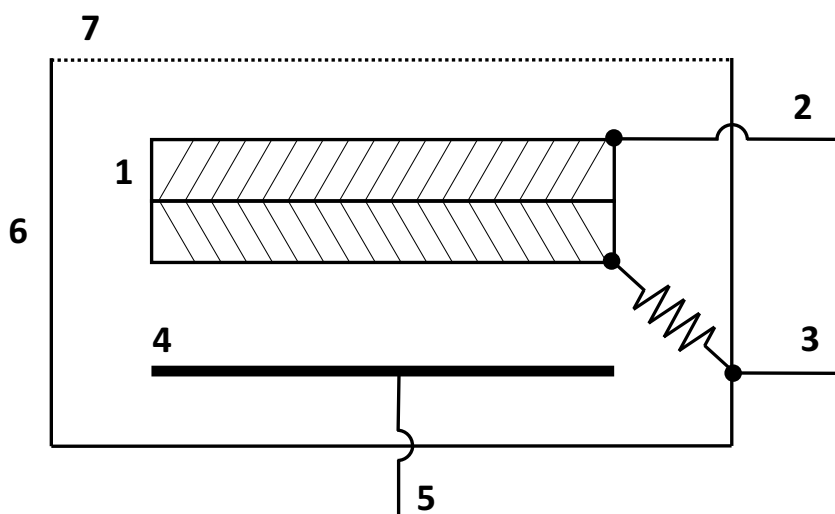
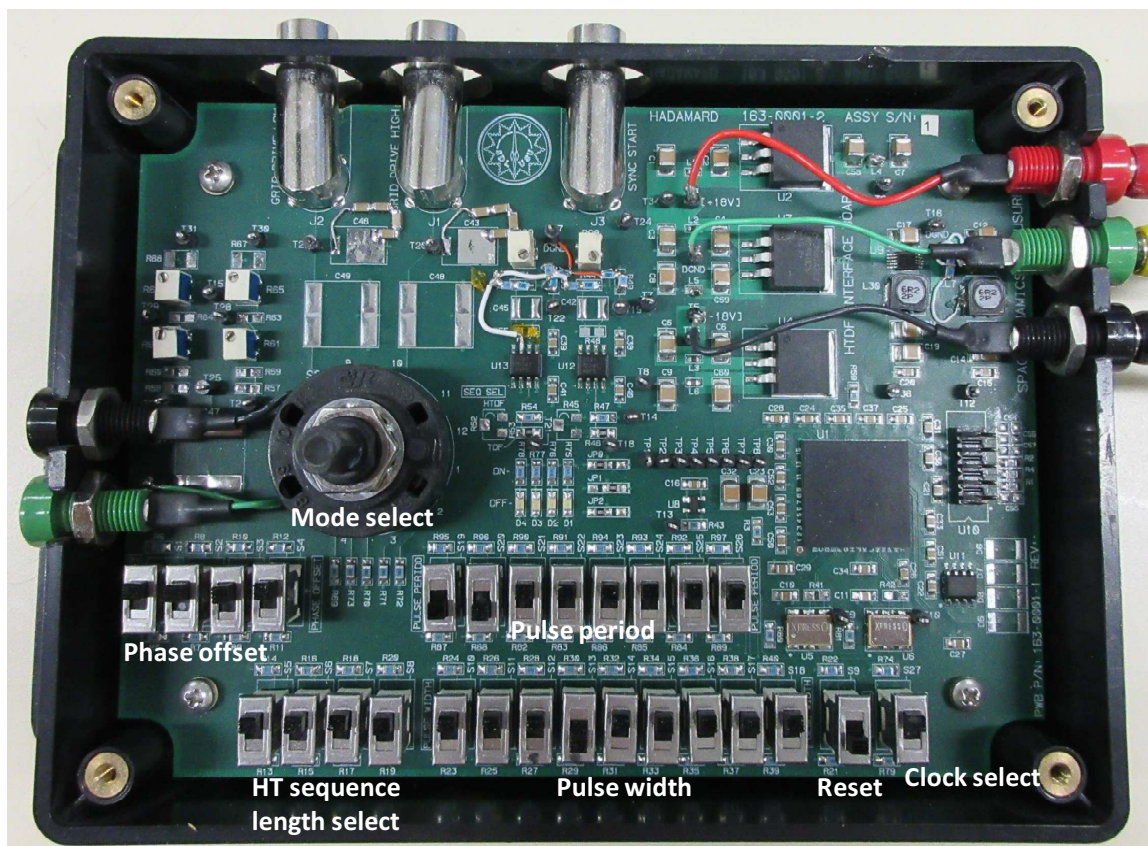


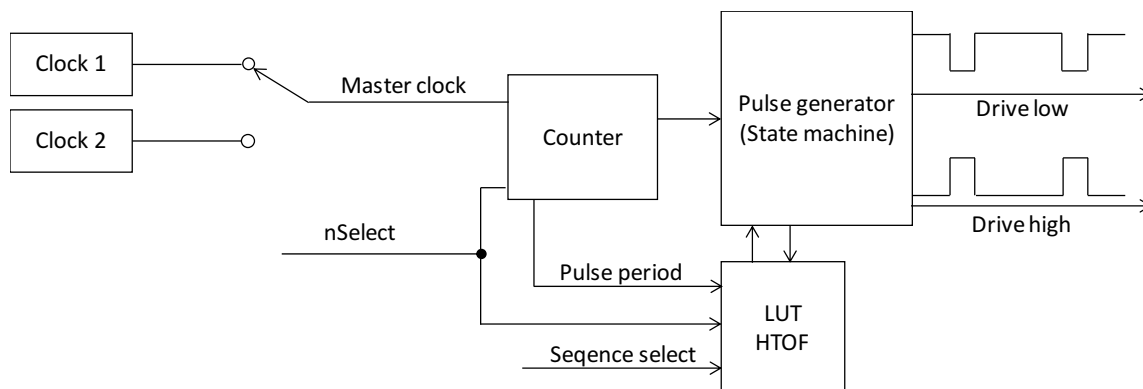
**Figure 3.6.** MCP detector wiring diagram. (1) MCP detector, (2) MCP high voltage in, (3) MCP housing/grid bias, (4) anode, (5) signal out, (6) MCP housing cartridge, and (7) high-transmission grid.

described by *Brock et al.* [2000] and *Yoon et al.* [2005]. In these instances, a feedback shift register technique was used to generate Hadamard sequences. The sequences were then passed to a modulation driver that supplied the BNG deflection potentials. In contrast, the MDB described here simply stores Hadamard sequences in a lookup table (LUT).

The driver board is centered around an Altera Cyclone III FPGA (EP3C5F256C6N), chosen for “its fast switching speed,” as well as its capacity to “store several Hadamard sequences of different lengths” [*Sanderson*, 2010–2016]. A photograph of the completed board is shown in Figure 3.7a, and a schematic of the board is shown in Figure 3.7b. Two different clocks (user selectable, 100 MHz and 200 MHz) were used in the driver board to allow for a greater range of modulation pulse widths and periods. The counter runs off of the selected clock and is used to keep track of the pulse period. Its signal is sent to the FPGA, which in turn sends a voltage to a pair of operational amplifiers that produce the deflection potential ( $\pm V_{\text{def}}$ ) corresponding to the beam on or off state. During operation in traditional TOF mode, the modulation pulse occurs once per period. In HT mode, the FPGA sends a series of on/off signals corresponding to Hadamard sequences, which are



(a)



(b)

**Figure 3.7.** BNG modulation drive board. (a) Photo of completed board, and (b) schematic, courtesy of Sanderson [2010–2016].

stored in a LUT. A start pulse, synchronized with the beginning of the pulse period, is also generated by the driver board and sent to the pulse processing electronics (section 3.1.3) for use in calculating the TOF of ions arriving at the MCP.

In addition to the clock, user selectable settings on the MDB include mode, pulse width, pulse period, pulse offset, and Hadamard sequence length. Available mode settings are HT TOF-MS, traditional TOF-MS, beam-on, and beam-off. The pulse width can be adjusted from 10 to 2550 ns in increments of 5 ns. The pulse period, or time between successive start pulses, is adjustable from 7.685 to 652.8  $\mu$ s in 2.56  $\mu$ s increments. The pulse offset is used to compensate for timing delays between the grid high ( $V_{\text{acc}} + V_{\text{def}}$ ) and low ( $V_{\text{acc}} - V_{\text{def}}$ ) drives, and is adjustable from 0 to 60 ns in 5 ns increments. Hadamard sequences of length  $2^{n+1} - 1$  can be selected, where n is a positive integer from 4 to 15. The MDB also included a spare switch to be used when switching between modes or Hadamard sequences, or to reset the board if necessary [Sanderson, 2010–2016]. The MDB has two BNC outputs for the modulation drive (grid high and grid low), and one BNC output for the start pulse. Unfortunately, noise originating in the MDB interfered with the pulse processing electronics to the extent that the EDU was unable to operate in HT TOF-MS mode.

As originally designed, the acceleration voltage was fed into the driver board and the BNG modulation voltages were floated on the acceleration voltage. However, problems with this setup led to modifications; currently each set of BNG wires is held separately at the beam-off potential, with the modulation voltage from the driver board floating on the beam-off potential for each wire set. Resistors (10 k $\Omega$ ) are placed in series between each BNG drive output and its respective wire set to prevent interference between the BNG power supply and the MDB.

The driver board provides a deflection potential of about  $\pm 23$  V to each set of BNG wires. With no load attached to the driver board, the deflection potential rise time is 5 ns, measured at the board output (Figure 3.8a). Initially, attaching the BNG to the driver board resulted in a significantly distorted waveform (Figure 3.8b). The BNG, which had a mea-

sured capacitance of 57 pF, introduced instabilities in the operational amplifiers and led to the ringing seen in Figure 3.8b [Sanderson, 2010–2016]. This ringing impacted instrument performance by effectively creating multiple ion packets of nonuniform intensities for each start pulse. This presented in spectra as multiple peaks from identical masses (example shown later in section 7.2.3).

Different combinations of resistors and capacitors were placed between the driver board and the BNG in an effort to improve the modulation waveform. The best solution found was to place a 150  $\Omega$  resistor in series between the driver board and each set of BNG wires. The resistors greatly reduced the overshoot and ringing after each pulse by damping the modulation signal. Figure 3.9a shows the improved modulation waveform, as measured at the BNG leads (Figure 3.9b). The reduction in ringing came at a cost: the pulse rise time increased from 5 ns to 30 ns. Ideally, the BNG is completely on or off. In reality, the gate takes time to transition from beam on to beam off, and vice versa. This period of transition is directly related to the rise time of the modulation pulse and blurs the edges of the ion packets produced with each start pulse. The improved waveform eliminated

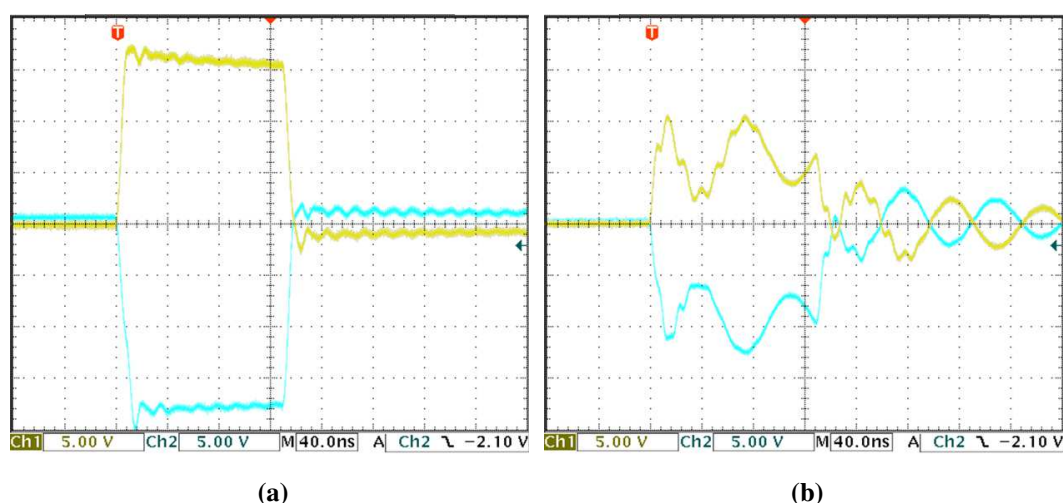


**Figure 3.8.** Initial waveforms from the BNG modulation driver board. (a) No load attached and (b) the BNG attached to the driver board. Vertical divisions are 5 V and horizontal divisions are 40 ns. Full-scale voltage range is -20 to 20 V and full-scale time range is -200 to 200 ns.

the multiple peaks due to ringing. The  $150\ \Omega$  resistors were employed throughout the remainder of the experiments with the EDU. In subsequent generations of this instrument, ringing and rise time issues can be at least partially mitigated with an improved BNG design, discussed further in section 3.2.1. A previous driver board reported by *Brock et al.* [2000] and *Kimmel et al.* [2003], capable of generating a  $V_{\text{def}}$  of  $\pm 15\ \text{V}$ , also exhibited significant ringing problems. In this case a capacitor/resistor snubber was used to reduce ringing in the modulation signal while maintaining a 10 ns rise time.

### 3.1.3. Pulse Processing Electronics

Figure 3.10 illustrates how signals from the MCP are collected and processed to generate spectra. The driver board (section 3.1.2) provides the modulation voltage to switch the BNG to the beam-on state, creating an ion pulse. The driver board also sends a synchronized start pulse to a Time Digitizer/Multichannel Scaler (TD/MCS, ORTEC model 9353). The ions in the pulse then travel across the drift region to the MCP detector. Ions that impact inside one of the channels in the MCP create an electron cascade, which in

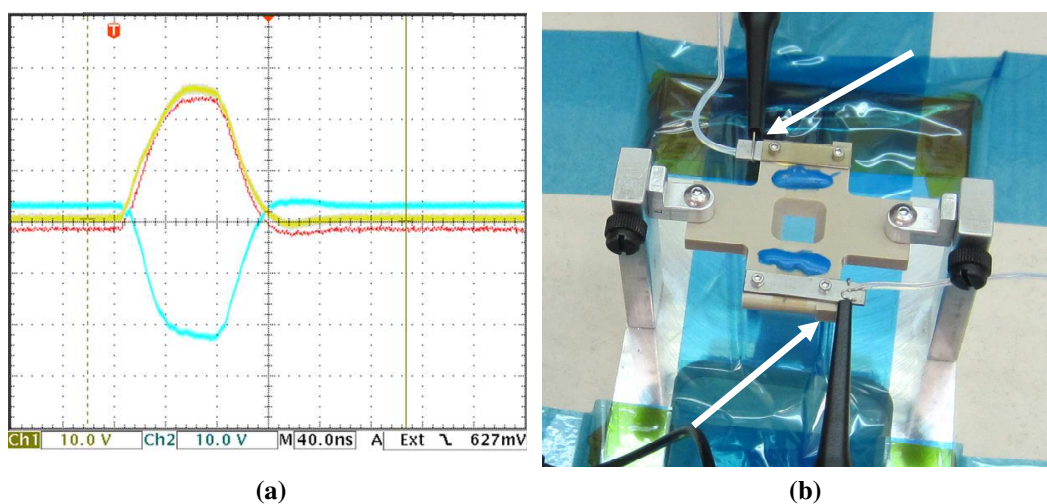


**Figure 3.9.** MDB waveforms after placing a  $150\ \Omega$  resistor in series with each BNG channel. (a) Waveform, measured at the BNG leads. Vertical divisions are 10 V and horizontal divisions are 40 ns. Full-scale voltage range is -40 to 40 V and full-scale time range is -200 to 200 ns. (b) Probe placement (white arrows) for measuring the MDB waveform shown in (a).

turn creates an electronic pulse in the anode (see Figure 3.6) [Wiza, 1979]. Pulses from the MCP detector used in the EDU have a typical pulse width of 750 ps [Photonis, 2015a]. The pulses then pass to a 1 GHz amplifier/timing discriminator (A/TD, ORTEC model 9327). The A/TD has a pulse-pair resolution of <10 ns. The pulses are then sent to the TD/MCS, which resides on a half-length PCI card mounted in a desktop computer. The TD/MCS has a 1 ns pulse-pair resolving time and a built-in dead time correction capability. The arrival times of stop pulses from the MCP are compared at the TD/MCS to the start pulse from the driver board. The corresponding time difference between start and subsequent stop pulses is the time-of-flight for which TOF-MS is named. These times are recorded by the TD/MCS and accompanying software (Time Digitizer 9353-B32 version 2.0, from ORTEC) and binned to create a TOF spectrum. The resulting TOF spectrum can be calibrated using peaks from known species and converted to a mass-to-charge ratio ( $m/z$ ) spectrum.

### 3.2. Mechanical Design

Mechanical design of the instrument was performed in-house at SDL under the supervision and direction of senior mechanical engineer, Mike Watson. USU engineering

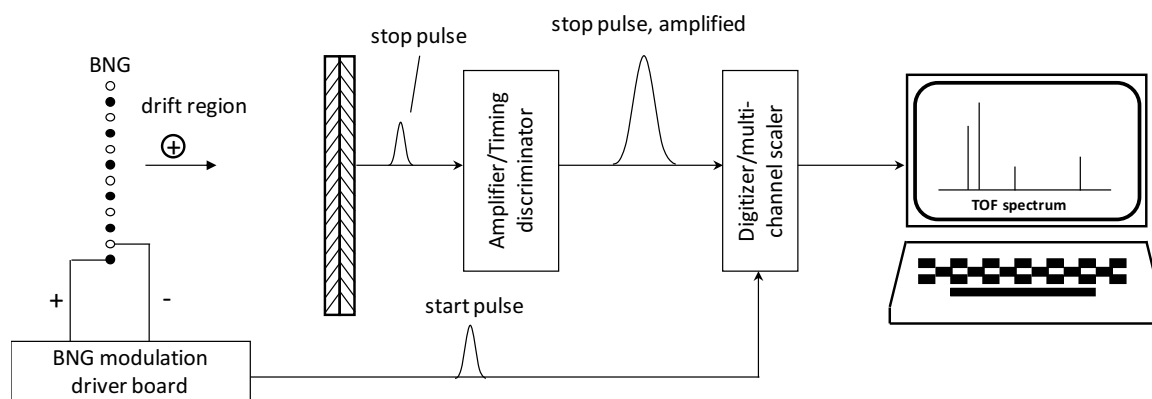


**Figure 3.10.** SDL TOF-MS electronics overview. Ions passing through the BNG in the beam-on state impact the MCP detector, generating a charge pulse that is then amplified. A TD/MCS is used to compare the arrival times of the amplified pulses to a start pulse from the driver board. Multiple stop pulses are binned according to arrival time, from which a TOF spectrum is created.

students, Ben Sampson and Dalon Work, also contributed to the mechanical design. Figure 3.11 shows a cut-away solid model of the EDU including the front plate, front assembly, drift tube, Faraday cage, MCP detector cartridge and MCP mount. During laboratory experiments with the EDU, the front plate, Faraday cage, and MCP mount were electrically connected to the experimental chamber to minimize stray electric fields inside the chamber. Figure 3.12 shows the front assembly of the EDU, which consists of a sampling aperture, EI ionizer, acceleration grids, and BNG. The ionizer consists of a cathode and repeller assembly on one side of the ionization region and a Faraday cup on the opposite side to monitor the ionization current.

The EDU was constructed mainly with stainless steel and aluminum, using standard machining techniques. Additional vacuum compatible insulating materials such as polytetrafluoroethylene (PTFE, or Teflon™), polyether ether ketone (PEEK), and Nylon were employed where electric isolation of instrument components was necessary (Figure 3.13). These insulating materials included screws, washers, spacers, tubing, and custom-cut sheets. The BNG assembly and much of the framework in the front assembly were constructed from PEEK to electrically insulate instrument components. Additionally, wire leads were

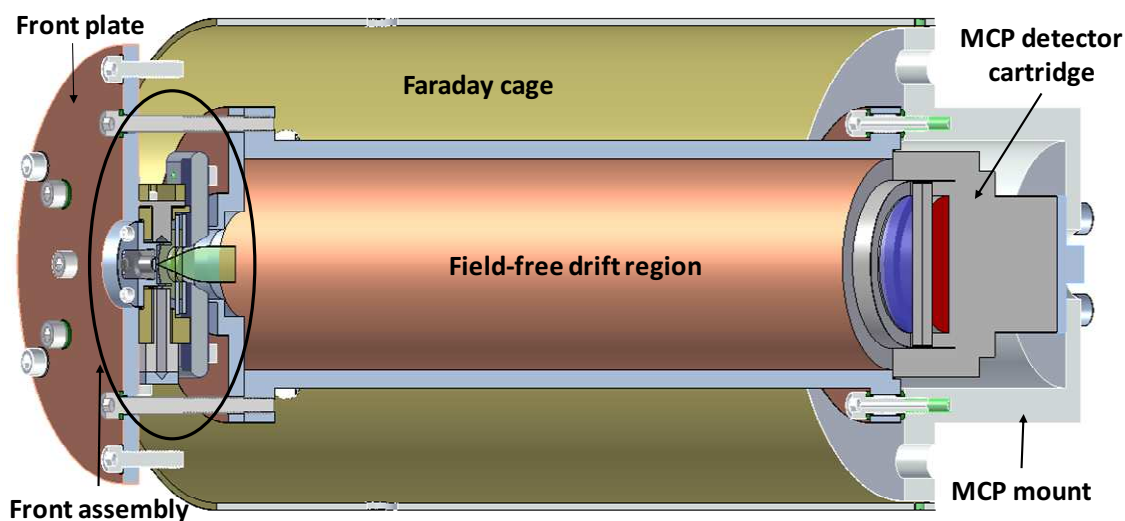


**Figure 3.11.** Solid model of the EDU, showing the arrangement of major instrument components.

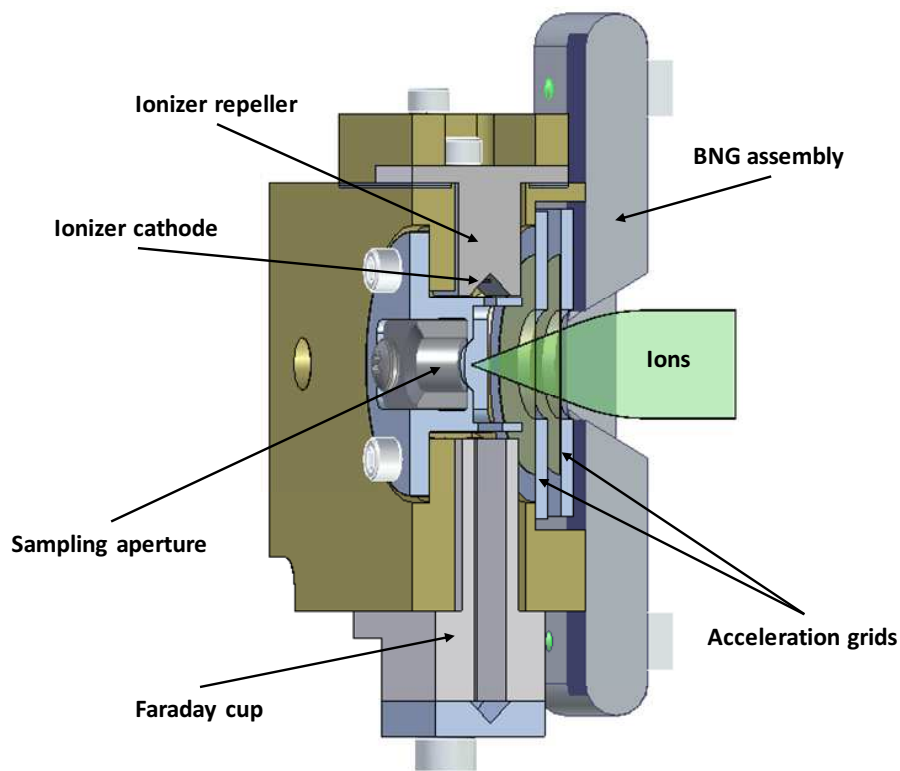


**Figure 3.12.** Solid model of the EDU front assembly.

insulated with Teflon™ sleeving. Electrical isolation of instrument components was tested at various stages during and after instrument assembly, including a final checkout after the assembled instrument had been mounted in the ion optics test chamber.

The acceleration grids were constructed by SDL technician, Scott Schicker, with the author's assistance. Electrical leads were tack-welded to the acceleration grid plates. A fine mesh (330 lines per inch) was then bonded to the acceleration grid plates with a conductive epoxy (Figure 3.14a). After the epoxy cured, the mesh was trimmed and the acceleration grids were ready for installation in the EDU (Figure 3.14b). Insulating washers separated the acceleration grids by less than a millimeter.

The machining process in some cases left unwanted residue on individual parts. Before final assembly of the EDU, individual parts were cleaned by ultrasonication with water and detergent, followed by ultrasonication in an isopropyl alcohol (IPA) bath, and a final rinse with IPA. The sonication/rinse process was repeated until parts left no visible residue when

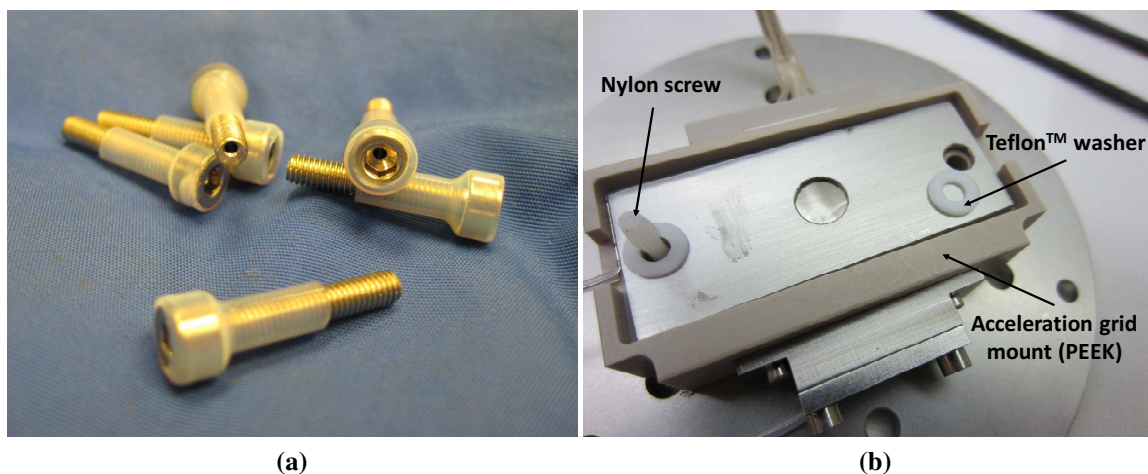


**Figure 3.13.** Examples of electrical isolation in the EDU. (a) Vented screws with Teflon™ heat-shrink tubing applied in order to connect the drift tube flange to the drift tube while still allowing the drift tube to float at the acceleration potential. (b) The front assembly includes Nylon screws, Teflon™ washers, and an acceleration grid mount (machined PEEK).

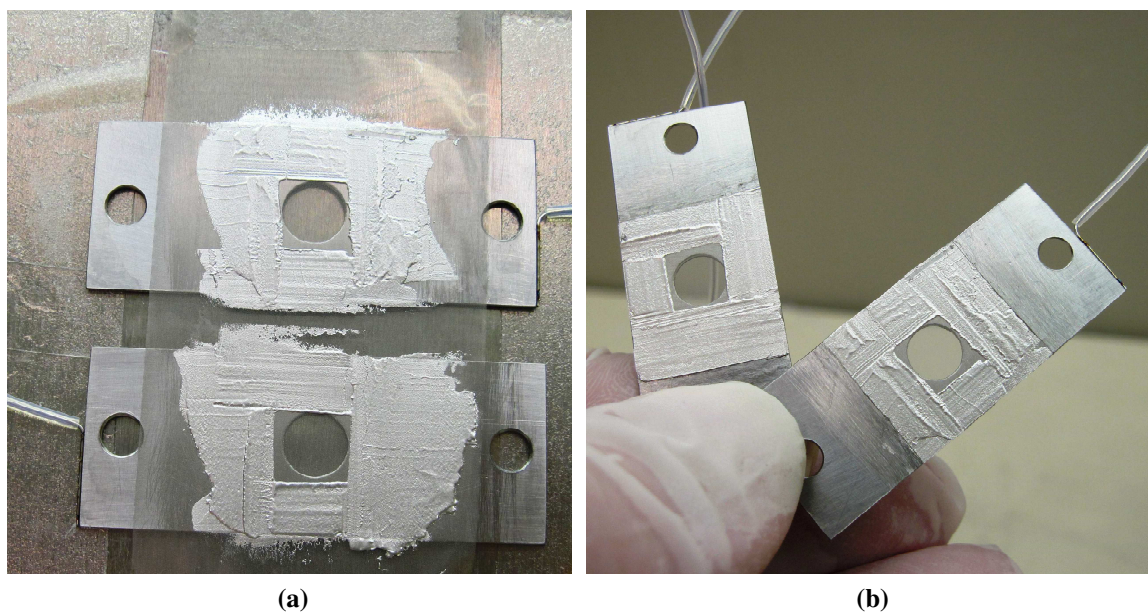


**Figure 3.14.** Acceleration grid fabrication. (a) Grid mesh attached to acceleration grid plates with conductive epoxy, and (b) finished acceleration grids before installation in the EDU.

wiped with a clean, white, lint-free wipe saturated with IPA. Individual parts were then bagged to maintain cleanliness until instrument assembly. The EDU was assembled on a vertical laminar flow clean bench to avoid particulate contamination.

During laboratory experiments with the EDU, a rapid change in voltage between the two acceleration grid plates welded them together. The EDU was subsequently disassembled to examine and repair the grids. The arc was discovered to have occurred between the plates in an area where the surface of the epoxy was rough, and not in the transmission area of the grids. To reduce the chance of a similar arcing incident, the epoxy surface was gently sanded with an emery board to remove any sharp peaks left over from the grid construction. The acceleration grids were then cleaned and the EDU was reassembled. From then on, strict current limits were set on the acceleration grid power supplies in subsequent experiments. To date there have been no more arcing incidents between the two grids.

### 3.2.1. BNG Fabrication

The BNG was designed and fabricated by a USU mechanical engineering student, Ben Sampson, under the supervision of senior mechanical engineer, Mike Watson, and Dr. Erik Syrstad at SDL. The author also assisted with the fabrication of two BNGs (see section 2.3 for a discussion on BNG operation). A template machined from PEEK holds the two sets of wires in place for the BNG. Parallel grooves were machined on both sides of the PEEK template, running the length of the template. The bottoms of the grooves were 75 microns apart.

Gold plated tungsten wire with a diameter of 10  $\mu\text{m}$  (Goodfellow part # W 005210) was used to construct the BNG. The wire was wound to the PEEK template using a loom similar to that described by *Yoon et al.* [2007]. The first set of wires was wound by laying wire in every other groove of the template. Because the wire was so fine that it was mostly invisible to the naked eye, winding was performed under a microscope. A rectangular electrode was attached to the wires on one side of the template with a conductive silver

epoxy (Epoxy Technology, part # EJ2189) to electrically connect all of the wires in the first set. On the opposite side of the template, insulating epoxy (Tra-bond 2151, blue colored epoxy in Figure 3.15) was applied to hold the wires and to provide electrical isolation from the next wire set. The first set of wires was then cut to remove them from the back of the template (Figure 3.15b). An insulating strip was placed on each side of the template over the first set of wires, and the second set of wires was wound by laying wire in each empty groove. Conductive silver epoxy was then used to connect the second set of wires to a rectangular electrode on the side of the template opposite the first electrode. Insulating epoxy (Tra-bond 2151) was again applied to hold the opposite side of the second set of wires in place while maintaining electrical isolation from the first wire set. The second set of wires was also cut to remove them from the back side of the template. The BNG was then tested to ensure that the two wire sets were electrically isolated. Figure 3.15 shows front and back views of a completed BNG.

Ideally, the BNG wires should all lie in the same plane with equidistant spacing between adjacent wires. A coordinate measuring machine (CMM) was used to measure the planarity and spacing of the BNG wires (Figure 3.16). Planarity was determined by mea-

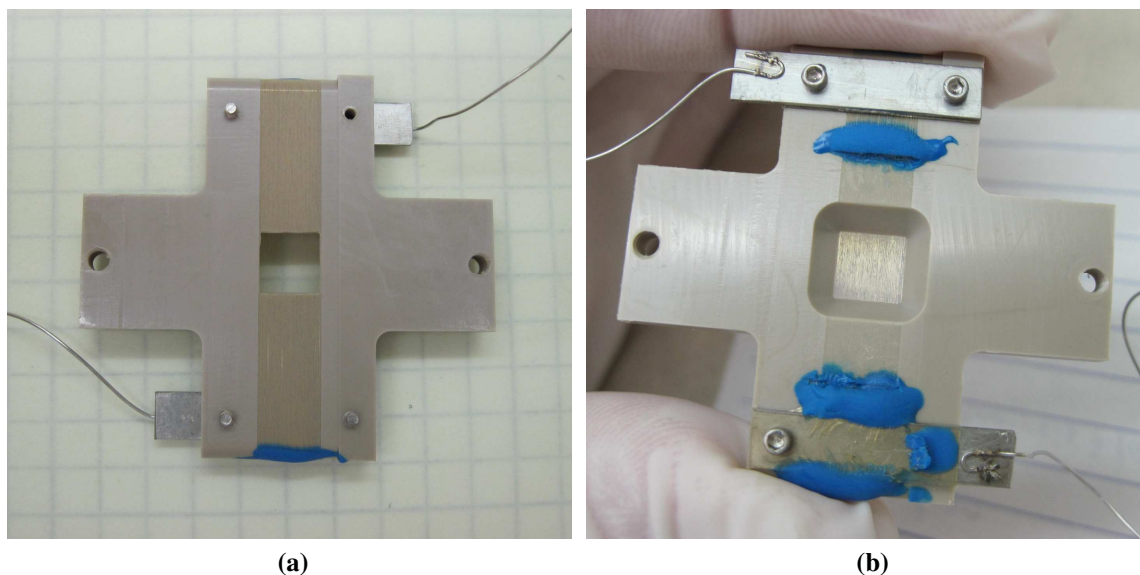


**Figure 3.15.** Front (a) and back (b) views of the BNG, as built.

asuring the distance,  $z$ , from a fixed reference point on the CMM to the BNG wires. This was accomplished by adjusting the focus of the CMM microscope on each individual wire with respect to the fixed reference distance and then recording the focus distance. Wire spacing measurements were made on each side of the BNG, designated left and right. The average wire spacing on the left side of the BNG was  $75.0 \pm 1.0 \mu\text{m}$ , and the average wire spacing on the right side was  $75.7 \pm 0.5 \mu\text{m}$ , where the quoted uncertainty is the standard deviation of the mean wire spacing. The planarity of the wires is given as a standard deviation and measured to be  $\pm 1.2 \mu\text{m}$  on the left side and  $\pm 1.4 \mu\text{m}$  on the right side.

The capacitance of the BNG is believed to be a major contributor to the modulation waveform distortions discussed in section 3.1.2. The capacitance,  $C$ , of a parallel-plate capacitor is

$$C = \frac{\epsilon A}{d}, \quad (3.1)$$

where  $A$  is the area of the plates,  $d$  is the spacing between the plates, and  $\epsilon$  is the permittivity of the material between the plates. Since the BNG is operated under vacuum conditions,  $\epsilon \approx \epsilon_0$ , the permittivity of free space in the transmission portion of the gate. Elsewhere,  $\epsilon$

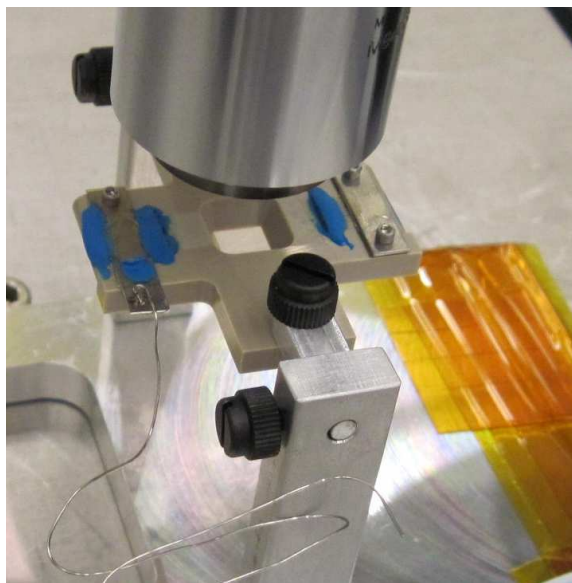


**Figure 3.16.** BNG mounted on CMM for measuring wire spacing and planarity.

depends on the specific type of PEEK used in the template; one value given for PEEK is  $\epsilon = 3.3\epsilon_0$  [Boedeker Plastics, 2016]. Increasing the open area of the template would reduce the amount of PEEK between wires, in turn reducing the gate capacitance. Reducing the width of the gate, using smaller-diameter wire, or a combination of the two would reduce the effective area of the gate, reducing capacitance. The distance between wires could be increased; however, increasing the distance between wires requires a higher  $V_{\text{def}}$  to achieve the same deflection angle, making this option undesirable.

### 3.2.2. Completion of the Engineering Demonstration Unit

SDL technician, Scott Schicker, with assistance from the author, assembled the EDU, which is shown in Figure 3.17. The fully assembled instrument measures 8 cm in diameter and 20 cm in length. Electrical leads provide connections to instrument components including: the BNG, acceleration grids, the ionizer cathode and repeller, Faraday cup, MCP high voltage, MCP signal output, and Faraday cage. For installation in the ion optics test chamber, the EDU is mounted in a custom-designed frame.

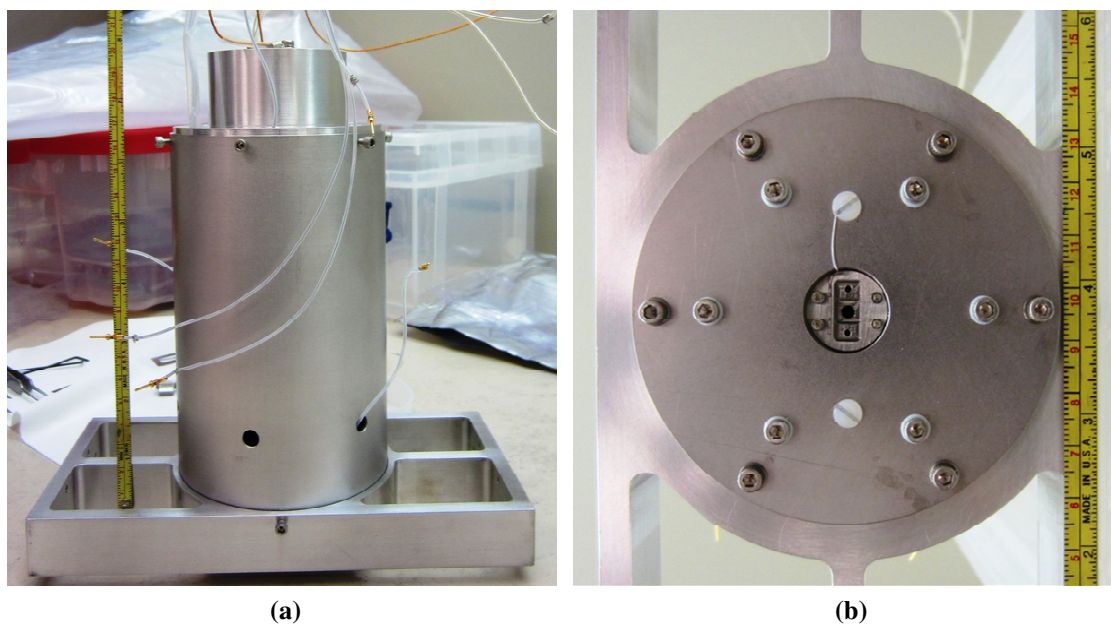


**Figure 3.17.** Fully assembled prototype time-of-flight mass spectrometer, with mounting frame attached. (a) Side, and (b) front views.

### 3.3. Vacuum Design

The EDU did not require a dedicated vacuum system, since it was tested in an ultrahigh vacuum (UHV) chamber. However, in order for the SDL instrument to operate successfully in the MLT, sufficient vacuum pumping must be provided. The SDL instrument is adaptable, and three different vacuum pumping methods have been considered: barium-loaded TGs, a miniature turbomolecular pump, and cryogenic pumping. In some situations, active pumping may be either unfeasible or unnecessary, in which case, the vacuum conditions inside the instrument would be determined entirely by the net flux of particles into the instrument through the aperture.

The original proposal for the SDL instrument proposed TGs, each loaded with nanostructured barium, to provide vacuum pumping. In this configuration the TGs would be mounted parallel to the instrument axis in an annular arrangement (Figure 3.18). TGs are activated by breaching an indium seal to expose the barium. Noninert gases are sorbed by the barium, effectively removing them from the instrument volume.

Recently, a small turbo pump, similar in size to a D battery, with a pumping speed of 4

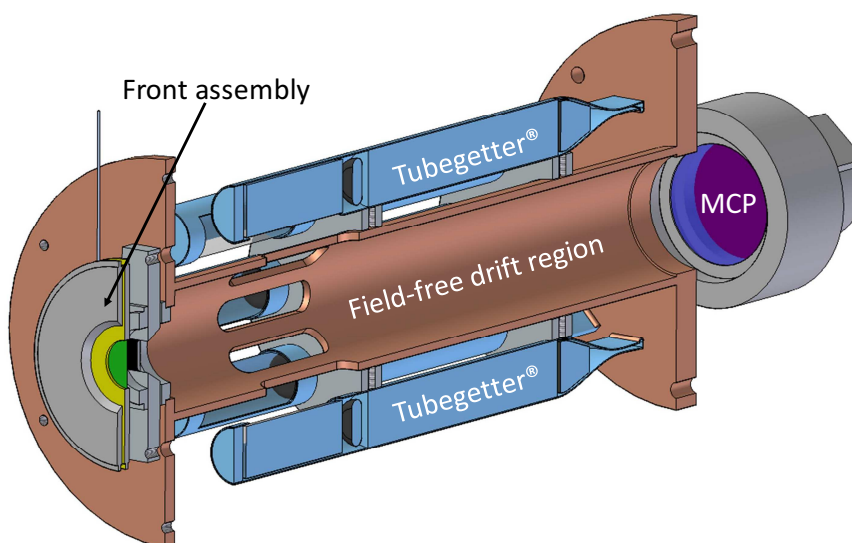


**Figure 3.18.** Solid model showing potential TG arrangement for pumping the SDL instrument.

L/s has been developed for use in space applications [Mahaffy *et al.*, 2012; Kline-Schoder, 2011; Creare, 2014]. A turbo pump could easily be incorporated in the instrument by providing a suitable pumping port and attachment point. One advantage of a turbo pump is its ability to pump both inert and noninert gases.

The instrument could also be pumped using cryogenics. The most likely scenario involves the use of a cryogenic fluid (liquid helium) to cool the ram surface of the instrument, to remove the bow shock, while also cooling the interior instrument walls (see Chapter 6). Figure 3.19 shows a solid model of a reflectron version of the SDL instrument mounted inside a dewar of liquid helium. The outsides of the instrument walls are in contact with the helium. The liquid helium dewar is itself surrounded by liquid nitrogen to insulate the liquid helium dewar from the rest of the rocket body. In this case the interior walls of the instrument effectively become a large-area cryopump.

Cryogenic pumping can be very effective, but cryogenics are difficult to handle and have a limited lifetime on the launch pad. Although a turbo pump acts on both inert and non-

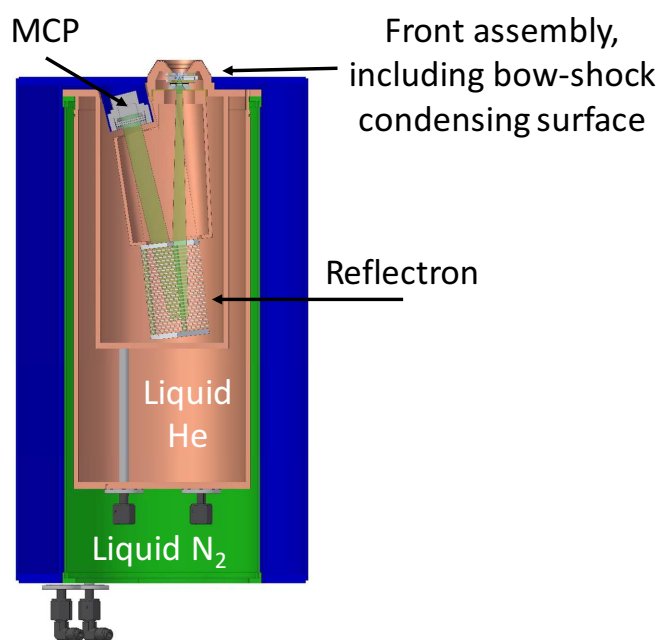


**Figure 3.19.** Solid model of a reflectron version of the SDL TOF-MS mounted inside a dewar of liquid helium. In this case the instrument walls effectively become a cryopump.

inert gases, these pumps can be very expensive and moving parts increase the risk of failure. TGs have no moving parts and can operate at room temperature, although their pumping speed is lower than the other methods discussed here. Ultimately, the pumping method will have to be specifically tailored to mission requirements. These different vacuum pumping methods are discussed in greater detail in Chapter 6.

## CHAPTER 4

## HIGH PRESSURE MICROCHANNEL PLATE TESTING

The ion detector of choice for TOF-MS instruments is the MCP [Koppelaar *et al.*, 2005; de Hoffmann and Stroobant, 2007]. However, background events in MCPs can result in a degraded signal for TOF-MS instruments. These events have been attributed to various sources, including cosmic rays, ion feedback, and radioactive decay in the MCP material [Siegmond *et al.*, 1988]. To prevent potentially damaging discharge events, as well as the problematic issue of degraded signal due to increased background count rates at elevated pressures, MCP detectors have traditionally been limited to operating pressures below  $10^{-5}$  Torr [Wiza, 1979; Rager and Renaud, 1974; Photonis, 2015b]. Because TOF-MS systems tend to reside in laboratories with ample space and resources for the necessary vacuum pumps and associated equipment, pressure is not usually an issue for MCP detectors in these instruments. However, the ambient pressure in the MLT presents a major obstacle to performing TOF-MS *in-situ*.

In contrast to laboratory-bound TOF-MS systems, rocket-borne instruments, such as the SDL TOF-MS, have strict limitations on the resources normally associated with vacuum pumping including mass, power, and space. Ambient pressures in the MLT can extend into the mTorr range (Figure 1.2), well above conventional MCP operating pressures. Successful operation of MCP detectors under such conditions requires either a vacuum system, a pressure tolerant detector, or a combination of the two.

Recently, researchers at PHOTONIS USA, Inc. demonstrated the operation of an MCP detector with 5  $\mu\text{m}$  diameter pores at pressures as high as 15 mTorr under argon and laboratory air backfill [Cochran *et al.*, 2005; Laprade and Cochran, 2006; Laprade *et al.*, 2006]. These experiments demonstrated a low background count rate (<10 counts per second) at pressures up to 10 mTorr, four orders of magnitude above the normally recommended operation pressure for MCP detectors. Although this detector has been operated at such high

pressures, the manufacturer lists a maximum operating pressure of  $10^{-6}$  Torr [Photonis, 2015a]. Results from these experiments with laboratory air are shown in Figure 4.1. We obtained a similar MCP detector and performed experiments to determine whether this detector would be appropriate for the SDL instrument. Experiments performed on the detector included tracking the background count rate and discharge events at elevated pressures, monitoring detector performance under exposure to varying humidity levels, and actually operating the EDU at elevated pressures. These experiments demonstrated the ability of the SDL instrument to not only survive, but make measurements under the harsh environment of the MLT.

#### 4.1. Experiment Description

The experiments described in this chapter were conducted using an AP-TOF MCP detector from PHOTONIS USA, Inc. This detector incorporates a chevron stack design with a detection diameter of 18 mm, intended for pulse-counting applications, in particular TOF-

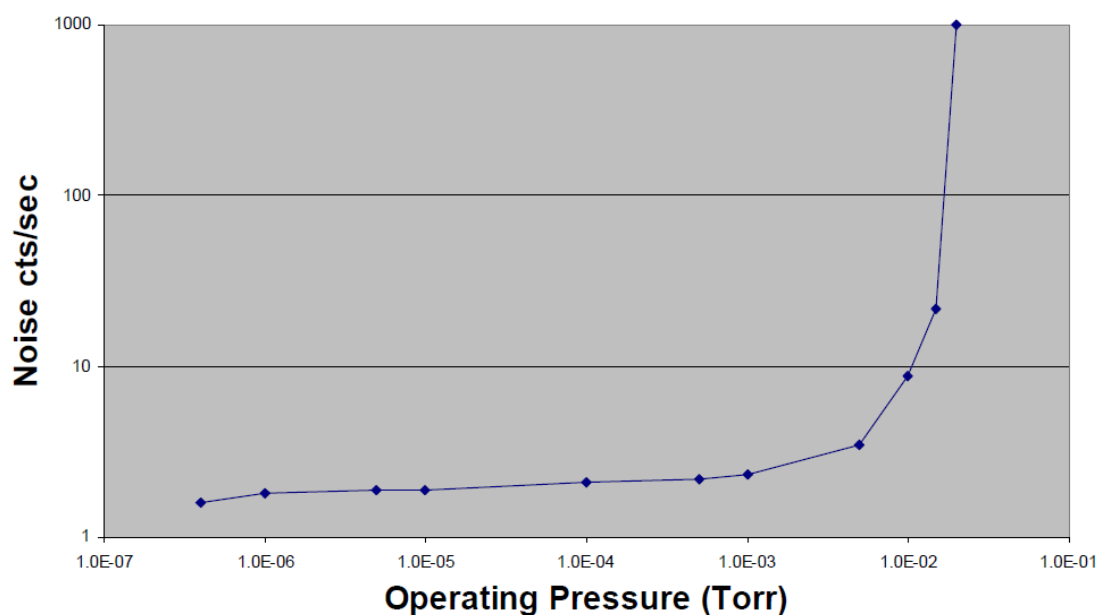


**Figure 4.1.** Background count rate as a function of laboratory air backfill pressure for a  $5 \mu\text{m}$  pore MCP detector from PHOTONIS USA, Inc. Figure reproduced from [Cochran *et al.*, 2005], with permission (Appendix C).

MS. The average width of pulses from the AP-TOF MCP is 750 ps with an average rise time of 450 ps [Photonis, 2015a]. Detector details are given in Table 4.1. This particular detector was chosen based on instrument size constraints and ion trajectory simulations described in Chapter 2. A similar detector, but with a larger active area, has previously been demonstrated to operate at pressures into the mTorr range under argon and laboratory air backfill [Cochran *et al.*, 2005; Laprade and Cochran, 2006; Laprade *et al.*, 2006].

#### 4.1.1. MCP Scrub

MCP detectors benefit from a scrub, or burn-in, process to improve detector stability [Sandel *et al.*, 1977; Timothy, 1981; Siegmund, 1989; Siegmund and Stock, 1991; Thomas and Behnke, 1993; Siegmund *et al.*, 1994; Martin *et al.*, 2003; Griffiths, 2012]. Scrubbing involves stimulating the MCP with electrons or UV photons to remove gas molecules that have adsorbed to the MCP surfaces. During the initial part of the scrub MCPs experience a sharp drop in gain, with the gain stabilizing as the scrub progresses [Siegmund and Stock, 1991; Kore Technology Limited, 2015]. Major benefits of scrubbing include more uniform detector gain and a reduction of background events [Siegmund *et al.*, 1988]. MCP scrubbing is detector and mission specific. For example, an MCP detector intended for a long term satellite mission may be scrubbed more than a detector intended for a short-term mission. This would result in a greater overall drop in, but much more stable, detector gain. For

**Table 4.1.** Characteristics of the AP-TOF MCP Detector Used in the EDU

MCP characteristic	Value
Detection diameter	18 mm
Pore diameter	5 $\mu\text{m}$
Pitch (center-to-center distance)	6 $\mu\text{m}$
Bias angle	12°
Aspect ratio	60:1
Plate spacing	50 $\mu\text{m}$ between plates

a short-term mission, such as a sounding rocket flight, the change in detector gain would be negligible. In this case a minimal scrub may suffice or scrubbing may not even be necessary.

Experiments to evaluate MCP performance at elevated pressures were performed on the AP-TOF MCP detector, both before and after scrubbing, and are described in section 4.1.2. MCP pulses were recorded using an oscilloscope (Tektronix, DPO-7254) and analyzed to obtain pulse-height distributions. Additionally, gain measurements were made with a time-to-digital converter and a channel timing and charge amplifier (Sensor Sciences, models DSTDC-F and DDLA-101).

The MCP was first scrubbed using UV photons from a mercury pen lamp, which was positioned outside the vacuum chamber housing the detector. Photons from the pen lamp passed through a UV window and diffuser to the MCP. The diffuser was used to generate a spatially uniform source of photons and prevent preferential scrubbing of the detector. With the MCP under UV exposure, the detector high voltage was increased until the output current reached several  $\mu\text{A}$ . Output current and time were tracked to calculate the amount of charge removed from the detector. The first scrub removed 0.5 C of charge from the detector. After conducting performance experiments at elevated pressures with the MCP (section 4.1.2), it was stored under vacuum for several months. The detector was removed from vacuum in November of 2011 and spent about a week exposed to lab air on a clean bench while it was incorporated into the EDU. The EDU was then mounted in the ion optics test chamber and placed under vacuum.

During the first half of 2012, the MCP was again exposed to lab air on a clean bench while repairs and adjustments were performed on the EDU and the ion optics test chamber. These periods of exposure to lab air ranged from less than 24 hours to six weeks. Additionally, much of the experimental data taken after the initial scrub was found to be unusable, due to incorrect oscilloscope trigger settings. It was decided to repeat the postscrub pressure experiments, but due to the amount of time the MCP had spent exposed to air at

atmospheric pressure, it was rescrubbed. Rather than disassemble the EDU, the MCP was scrubbed in its installed position in the instrument while inside the ion optics test chamber. In this configuration the entrance aperture of the EDU was too small to fully illuminate the MCP with the mercury pen lamp, so UV photons generated in the ionizer (Figure 3.2) were used instead. The acceleration grids and the BNG (see Figures 1.7 and 3.12) were biased to prevent electrons and ions from reaching the detector. The scrubbing current, which was typically held under 5  $\mu\text{A}$ , was recorded periodically to determine the amount of charge extracted from the MCP. The scrubbing process was interrupted periodically to make gain measurements. The results of the rescrub are described in section 4.2.1.

#### 4.1.2. MCP Pressure Experiments

Ambient pressures in the MLT can exceed the recommended operational pressure range of MCP detectors by several orders of magnitude (Figure 1.2). Previous experiments demonstrated MCP operation at pressures above 1 mTorr under laboratory air and argon backfill [Cochran *et al.*, 2005; Laprade and Cochran, 2006; Laprade *et al.*, 2006]. The author performed experiments to confirm these previous reports of high pressure MCP operation, which involved recording the background count rate of the detector under chamber backfills of air and argon. The experiments were taken further by using, helium, nitrogen, and oxygen as additional backfill gases. The pressures at which detector discharge events occurred were also recorded. These experiments were conducted both before and after scrubbing to study the effect of scrubbing on detector survival and operability. In addition, the EDU was also operated at elevated pressures. These experiments were performed to determine the suitability of the AP-TOF MCP detector to operate as part of a rocket-borne instrument in the MLT.

##### 4.1.2.1. Materials

The pressure experiments described here were conducted in the SDL IOTF. Prescrub and postscrub experiments were conducted in different vacuum chambers, but the basic ex-

perimental setup, shown in Figure 4.2, was similar in both cases. Backfill gas was directed through a particulate filter and introduced to the chamber through nylon and Teflon™ tubing. Gas flow into the chamber was controlled with a variable leak valve. The vacuum chamber was pumped by a turbo pump backed by a roughing pump and separated from the vacuum volume by a pneumatic gate valve. The combination of the variable leak valve and the turbo pump made precise pressure control possible during the backfill experiments.

The MCP backfill experiments took place at pressures ranging from  $10^{-8}$  Torr to above  $10^{-2}$  Torr. An IG was used to measure pressures below about  $10^{-4}$  Torr, and a Baratron® capacitance manometer (MKS model 6288) was used to measure pressures above  $10^{-4}$  Torr. The pressure gauges were calibrated regularly during the experiments. This was accomplished by first zeroing the Baratron® at a pressure below  $10^{-6}$  Torr, as measured by the ion gauge. Next, the vacuum chamber was backfilled with the test gas to between  $9.0 \times 10^{-4}$

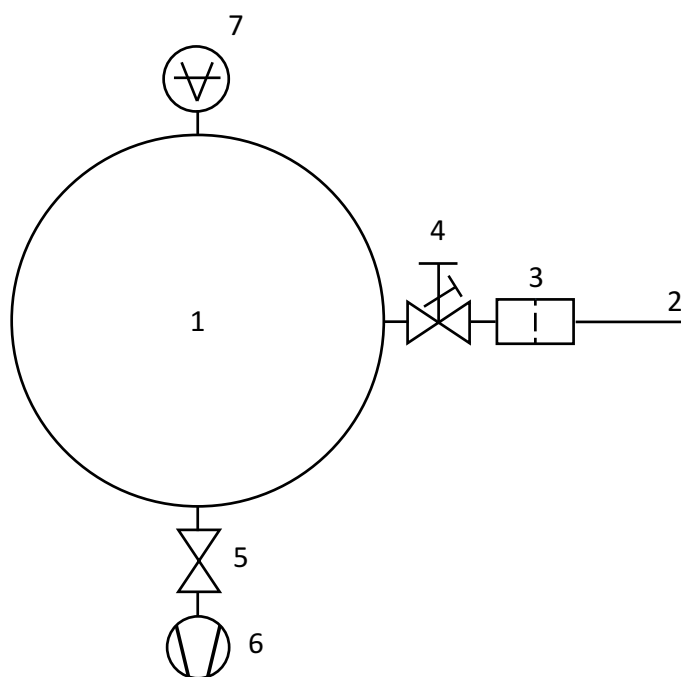


**Figure 4.2.** Experimental setup for the MCP pressure experiments. The different components are 1) vacuum chamber, 2) line in for backfill gas, 3) particulate filter, 4) variable leak valve, 5) gate valve, 6) turbo pump, and 7) vacuum measurement (Baratron® capacitance manometer and IG).

and  $9.9 \times 10^{-4}$  Torr as read by the Baratron<sup>®</sup>. The ion gauge sensitivity was then adjusted until the ion gauge pressure matched the Baratron<sup>®</sup> pressure. A 0.1 Torr Baratron<sup>®</sup> was used during the prescrub experiments but failed during the postscrub experiments. It was replaced with a 1 Torr Baratron<sup>®</sup>.

The backfill gases argon, oxygen and helium were supplied from gas cylinders. Nitrogen was obtained from facility supplies utilizing N<sub>2</sub> boil off from a large dewar located outside the building. The facility is plumbed such that the boil off is available for laboratory use. For lab air, a small diaphragm pump was used to pressurize the backfill gas line to deliver air to the vacuum chamber. Oxygen and helium were only used during prescrub experiments with the MCP detector.

Experiments with water vapor, added to nitrogen and laboratory air backfills, were performed on the MCP after it had been scrubbed. The humidity experimental setup was similar to the pressure experiment setup, but with a few additional components (Figure 4.3). Water vapor was added to the backfill gas by splitting the backfill line into two branches, the flow through each regulated by a flowmeter. One branch passed through a water bubbler to increase the moisture content of the gas in that line. The two gas lines were then brought back together and the resulting gas mixture passed through a particulate filter. The water content of the backfill gas was measured with hygrometer (Alpha Moisture Systems Intrinsically Safe Portable Dewpoint Hygrometer, model DSP-Ex), after which it entered the vacuum chamber through the variable leak valve.

During the backfill experiments, MCP background counts were recorded using the pulse counting electronics described in section 3.1.3. Gain settings on the A/TD were identical for both the prescrub and the postscrub experiments. The threshold setting was adjusted for each individual backfill experiment using the procedure outlined by the manufacturer and briefly explained here. With the MCP detector at operating voltage (between -1600 V and -2400 V, depending on the experiment), all apparent sources of detector stimulation were removed. The threshold potentiometer was adjusted until the indicator, an LED on the

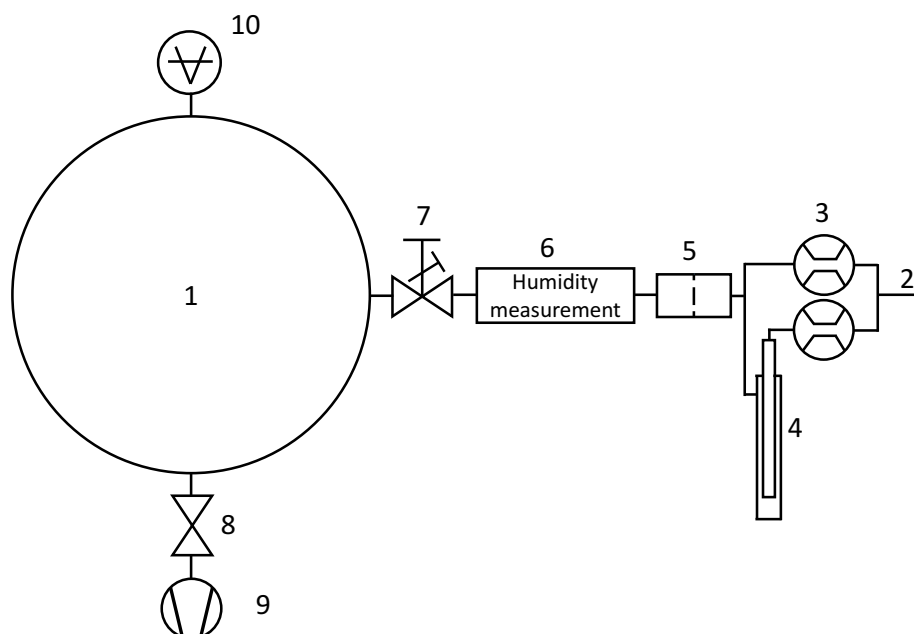


**Figure 4.3.** Experimental setup for MCP humidity experiments. The different components are 1) vacuum chamber, 2) line in for backfill gas, 3) flowmeters, 4) bubbler, 5) particulate filter, 6) portable hygrometer, 7) variable leak valve, 8) gate valve, 9) turbo pump, and 10) vacuum measurement (Baratron<sup>®</sup> capacitance manometer and ion gauge).

discriminator that blinks each time a threshold-crossing pulse is detected, glowed steadily. Noise was triggering the A/TD at this point. The threshold was then increased until the LED stopped glowing steady, and then increased further until the LED blinked at a rate of approximately one time per second.

A Bertan power supply (model 225) supplied high voltage to the MCP detector during all of the backfill pressure experiments, and a strict current limit of 10% above the MCP strip current was set to protect the detector. An arcing event was defined as any instance when the strip current exceeded the current limit, causing the power supply to shut off. (As a note, the current limit procedure was performed EVERY time high voltage was applied to the MCP, and not just for the MCP experiments at elevated pressures.) The postscrub backfill experiments were performed for two distinct MCP detector conditions: voltage matched and gain matched. Voltage matched experiments were performed at potentials identical to prescrub experiments (-1900 V). Because the scrubbing process results in lower

detector gain, the postscrub experiments were also performed with the MCP voltage set at -2350 V, to match the gain of certain prescrub experiments.

#### 4.1.2.2. Procedures

The background count rate at elevated pressures experiments were performed by the following steps. First, the chamber was backfilled by opening the variable leak valve while the turbo pump actively pumped the vacuum chamber. After the pressure stabilized, background counts were recorded for an amount of time (usually 10, 30, or 60 seconds) using the ORTEC<sup>®</sup> pulse counting electronics and accompanying software (see sections 3.1.3 and 4.1.2.1). The process was then repeated at higher pressures by further opening the leak valve. The MCP HV power supply eventually tripped indicating an arcing event. The pressure of each arcing event that occurred during the background count rate experiments was recorded. A few additional arcing experiments were performed without taking time to stop and record background count rates. In these experiments the backfill pressure was simply increased until the MCP HV power supply tripped. The duration of the arcing only experiments varied from rapid (< one minute) to slow (> 20 minutes). In between background count rate and detector arcing experiments the chamber was allowed to pump down to the  $10^{-7}$  Torr range or better.

#### 4.1.2.3. TOF-MS at Elevated Pressures

The EDU was operated at elevated pressures under argon backfill to observe both instrument and detector behavior. These experiments were performed in the IOTF with the instrument operating in neutral mode. The IOTF consists of a 24" diameter UHV chamber with an attached ion gun (Colutron Research Corporation<sup>®</sup> model G-2-D ion gun system), each with its own pumping system. The EDU was mounted to a manipulator in the UHV chamber, which was then isolated from its pump. The ion gun pump was used to pump both volumes. The system was backfilled with argon from the ion gun system, but the ion gun itself was off during this experiment. The chamber pressure was allowed to stabilize before

collecting each spectrum. Argon was used as the backfill gas during these experiments to limit damage to the ionizer filament.

## 4.2. Results

The results from each set of experiments are now presented, beginning with the MCP scrubbing process. Next, results from the detector background count rate experiments are given. The detector discharge events are then presented, followed by actual operation of the EDU at elevated pressures.

### 4.2.1. MCP Scrubbing

Due to exposure to atmosphere for prolonged periods of time, the MCP detector used in the EDU was scrubbed in several stages, as explained in section 4.1.1. The second scrub was the most extensive, removing 2.0 C of charge from the detector. (Subsequent scrubbing served only to ensure that the detector had not experienced a scrub reversal from exposure to atmosphere.) At different points during this process the detector gain was measured at three different voltages, shown in Figure 4.4. The scrubbing target was a rate of change of less than 50% per Coulomb per  $\text{cm}^2$ . Figure 4.4 shows the change in detector gain versus charge removed. After the initial rapid decrease in detector gain, the change in gain leveled out as the scrub progressed. The data shown in Figure 4.4 is similar to that observed in other MCP detectors [Netolicky, 2012].

The target detector gain rate of change was nearly reached after scrubbing 0.4  $\text{C}/\text{cm}^2$  from the MCP. At this point, however, electrical interference from laboratory equipment caused the gain measurement hardware (section 4.1.1) to malfunction, leading to erroneous gain measurements. The discontinuity appearing between 0.4 and 0.5  $\text{C}/\text{cm}^2$  of charge removed in Figure 4.4 was the result of this interference. Once the source of the problem (an ion gauge) was identified and eliminated, the gain measurement hardware settings were returned as close to their original state as possible and gain measurements were continued. The scrub was then further extended to assure that the target rate of change in detector gain

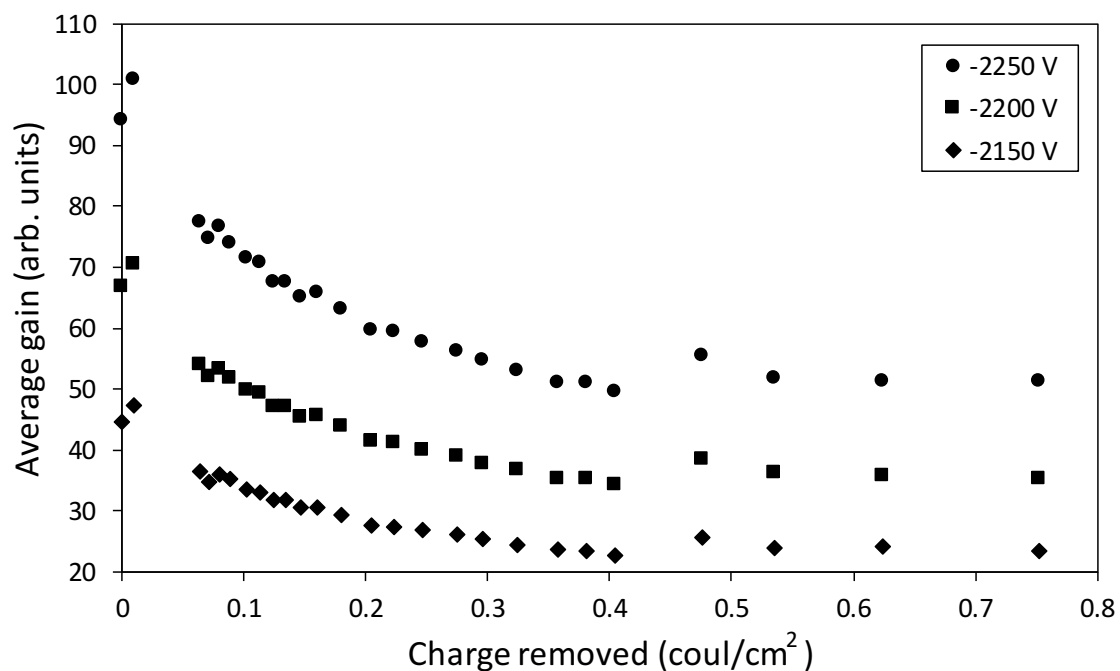


**Figure 4.4.** Detector gain during the second scrub of the MCP used in the EDU.

was reached, and ultimately a total of  $0.75 \text{ C/cm}^2$  was removed from the MCP. Due to the decrease in detector gain, a postscrub operation potential of  $-2320 \text{ V}$  was required to match the prescrub gain at  $-1900 \text{ V}$ .

#### 4.2.2. Background Count Rate Versus Pressure

Prescrub and postscrub detector background count rates are shown in Figures 4.5, 4.6, and 4.7 for backfill gases of nitrogen, argon, and laboratory air. The data shown in these figures are representative of the many backfill experiments performed with these gases. In all three cases the prescrub ( $-1900 \text{ V}$ ) count rate increased rapidly at pressures above  $10^{-2}$  Torr. The detector exhibited improved background characteristics after being scrubbed and being operated in the voltage matched ( $-1900 \text{ V}$ ) state; in each case the onset of higher background rates began at pressures above  $5 \times 10^{-2}$  Torr. For nitrogen, argon, and laboratory air the postscrub voltage matched count rate is similar to prescrub count rates for lower pressures.

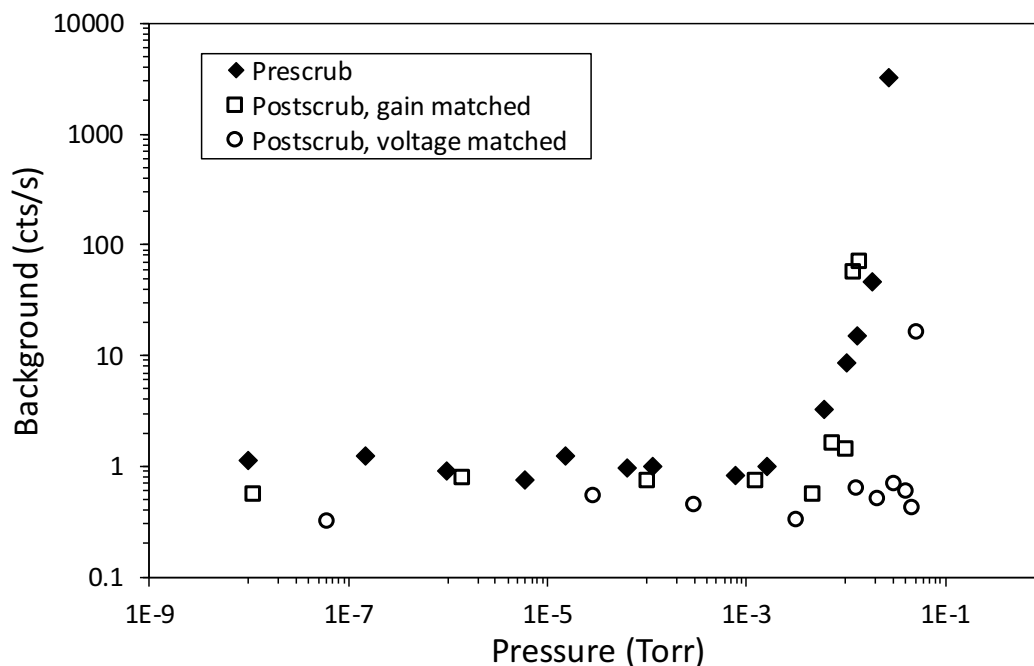


**Figure 4.5.** MCP background count rates under  $N_2$  backfill. Prescrub count rates obtained with the detector operating at -1900 V are compared to gain matched (-2320 V) and voltage matched (-1900 V) postscrub count rates.

For nitrogen (Figure 4.5), the prescrub MCP background count rate is very similar to the postscrub gain matched (-2320 V) background count rate. For argon (Figure 4.6) backfill, the gain matched postscrub MCP background count rate is noticeably lower than the prescrub count rate over most of the pressure range. In the case of laboratory air backfill (Figure 4.7), the postscrub gain matched MCP background count rate has a later onset (higher pressure) of increased counts. At higher pressures for laboratory air though ( $>10^{-2}$  Torr), the postscrub gain matched count rates behave similar to the prescrub count rates. The postscrub count rates for laboratory air show good qualitative agreement with results obtained by researchers at PHOTONIS USA, Inc., shown in Figure 4.1.

Figure 4.8 shows the prescrub MCP background count rate for helium. Under helium backfill, the onset of higher count rates occurred at higher pressures than for argon and laboratory air (Figures 4.6 - 4.7). Also, count rates were obtained at higher backfill pressures for helium than for any of the other gases tested. The maximum pressure at which the MCP

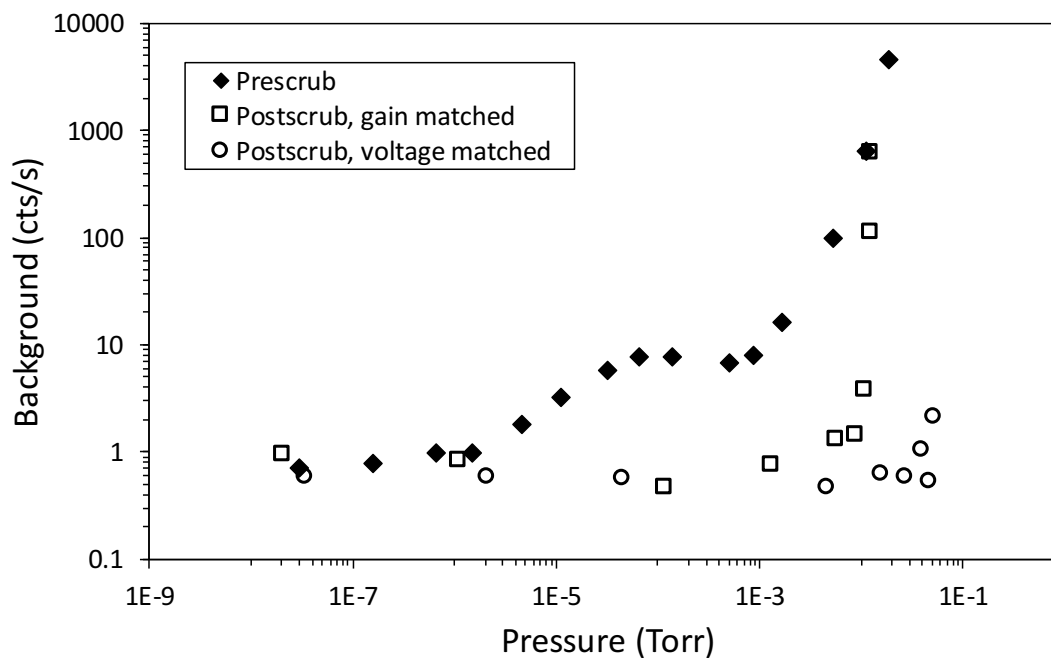


**Figure 4.6.** MCP background count rates under Ar backfill. Prescrub count rates obtained with the detector operating at -1900 V are compared to gain matched (-2320 V) and voltage matched (-1900 V) postscrub count rates.

was tested with other gases was determined by detector arcing. However, the detector did not arc under helium backfill. In fact, the count rate experiments with helium were limited by the turbo pump used in the backfill experiments, which actually shut down due to the elevated helium backfill pressure. No helium backfill experiments were conducted with the MCP detector after it was scrubbed.

Prescrub MCP background count rates are compared in Figure 4.9 for all gases tested, with the detector operating at -1900 V. At low pressures (below about  $1 \times 10^{-5}$  Torr) the background count rate was similar for all gases tested. At higher pressures (above about  $1 \times 10^{-2}$  Torr) nitrogen, argon, and laboratory air again exhibited similar background count rates. Above  $1 \times 10^{-2}$  Torr the background count rates for helium and nitrogen were noticeably lower than for argon and laboratory air. The step in background count rate at midrange pressures for both argon and laboratory air does not appear to be anomalous, since it was present in repeated experiments with these two gases. The reason for the step

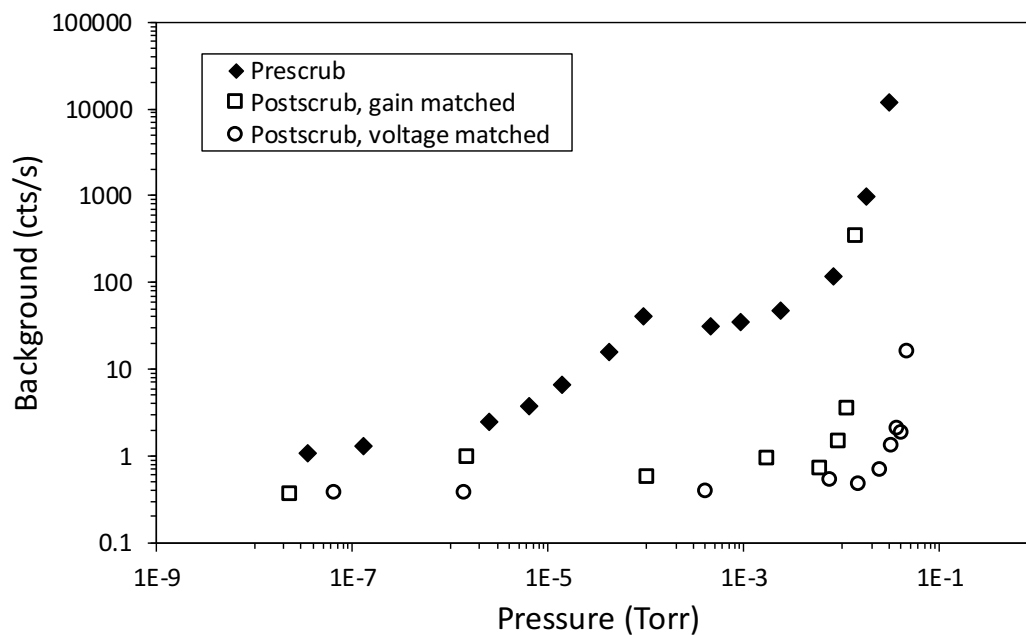


**Figure 4.7.** MCP background count rates under laboratory air backfill. Prescrub count rates obtained with the detector operating at -1900 V are compared to gain matched (-2320 V) and voltage matched (-1900 V) postscrib count rates. Compare postscrib count rates to Figure 4.1.

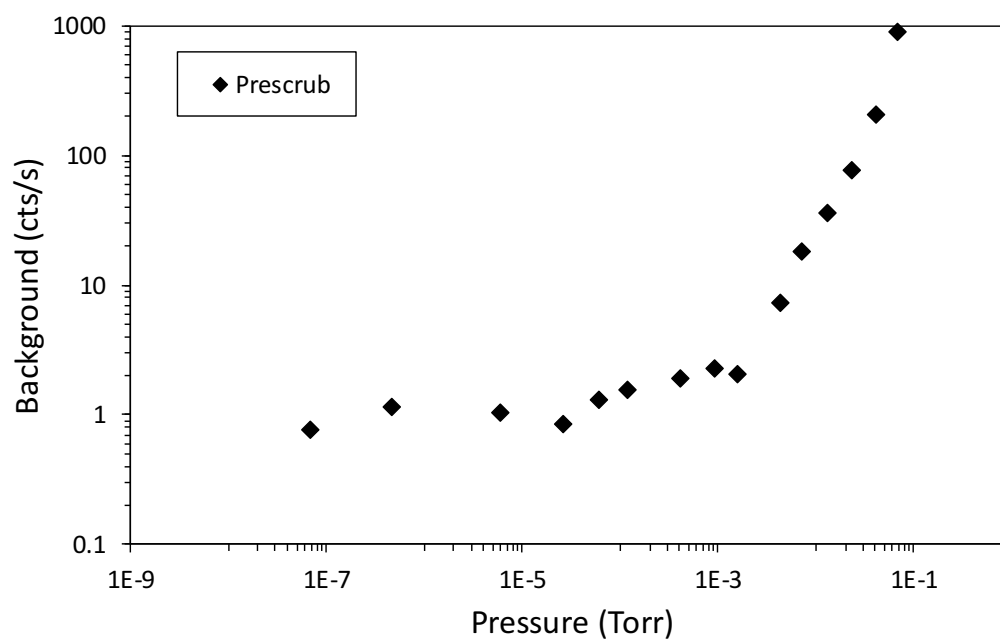


**Figure 4.8.** MCP background count rates under He backfill. The data shown here was collected prescrub at -1900 V. No postscrib experiments were conducted with He.

is unclear. The step was not observed for helium backfill at any MCP voltage and was only occasionally observed in the background count rates for nitrogen backfill.

Gain matched (-2320 V) postscrub MCP background count rates are shown in Figure 4.10, and voltage matched (-1900 V) count rates are shown in Figure 4.11. In contrast with Figure 4.9, the postscrub count rates exhibit little variation between gas species. The step that appears between  $10^{-5}$  and  $10^{-3}$  Torr in Figure 4.9 was not observed in the postscrub experiments. Gain matched background count rates were at or below  $1 \text{ s}^{-1}$  well into the  $10^{-3}$  Torr range (Figure 4.10). Voltage matched background count rates were even lower and did not rise above  $1 \text{ s}^{-1}$  until the backfill pressure entered the  $10^{-2}$  Torr range (Figure 4.11).

Humidity effects on MCP detector background count rates were also studied, and results are shown in Figure 4.12 (nitrogen backfill) and Figure 4.13 (laboratory air backfill). Data for both figures was collected with the MCP operating at -2320 V. The laboratory

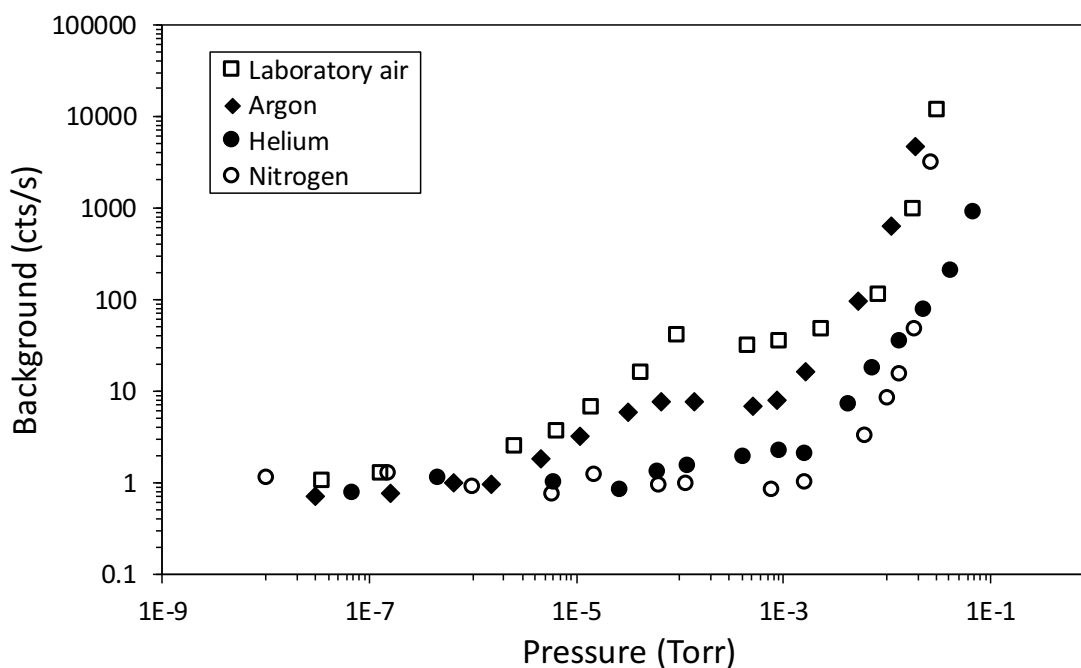


**Figure 4.9.** Prescrub background count rates for laboratory air, argon, helium, and nitrogen, with the MCP operating at -1900 V.

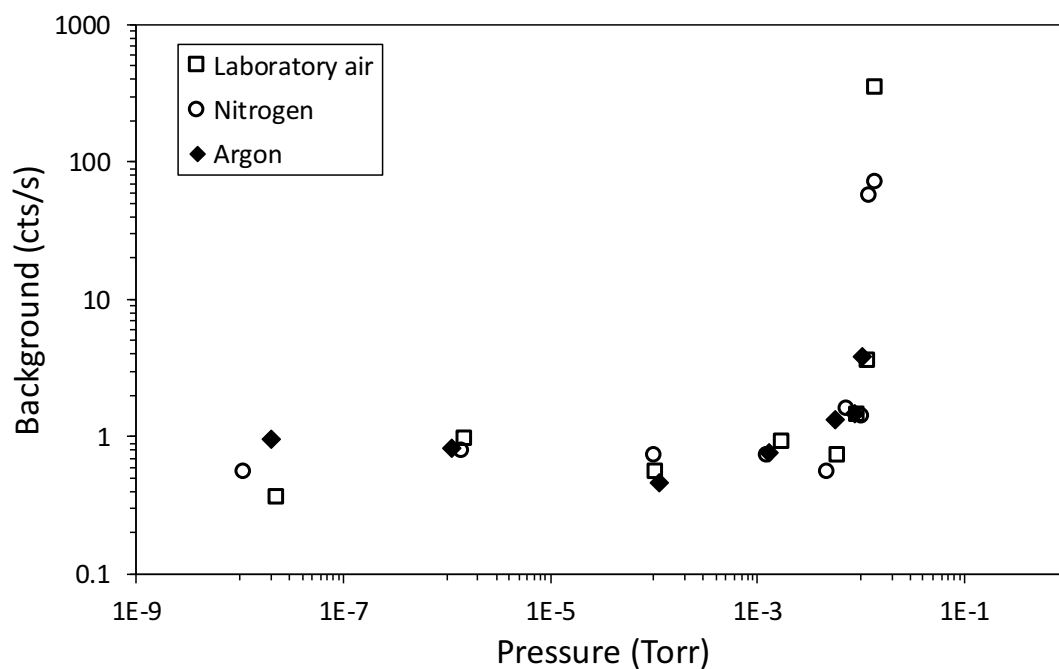


**Figure 4.10.** Gain-matched postscrub MCP background count rates for laboratory air, nitrogen, and argon. The MCP operating potential was -2320 V for the data in this figure.

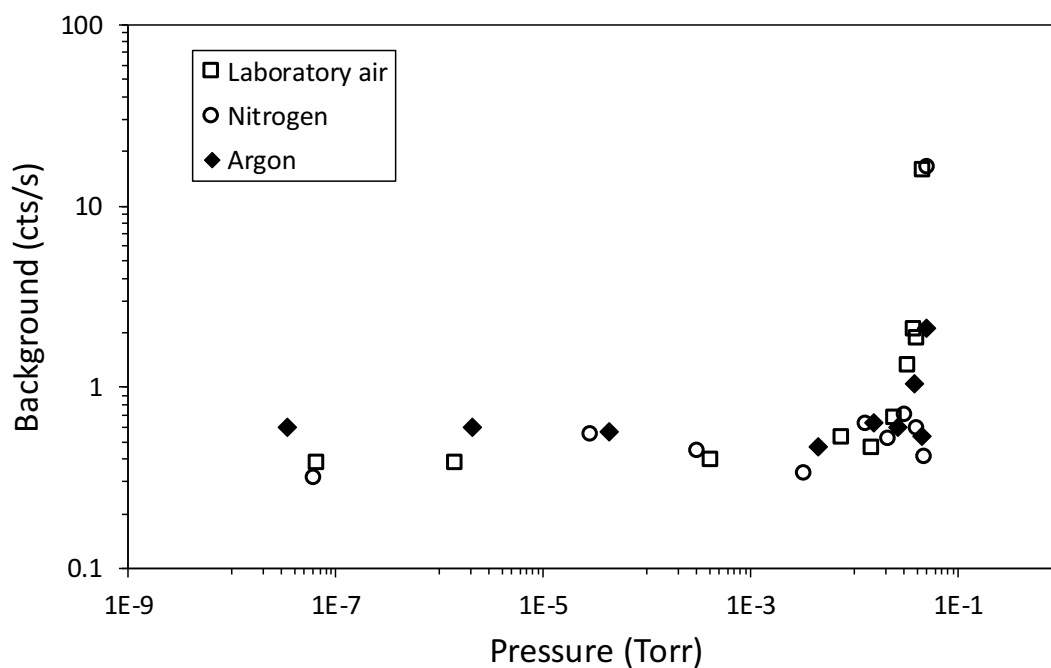


**Figure 4.11.** Voltage-matched postscrub MCP background count rates for laboratory air, nitrogen, and argon. The MCP operating potential was -1900 V for the data in this figure.

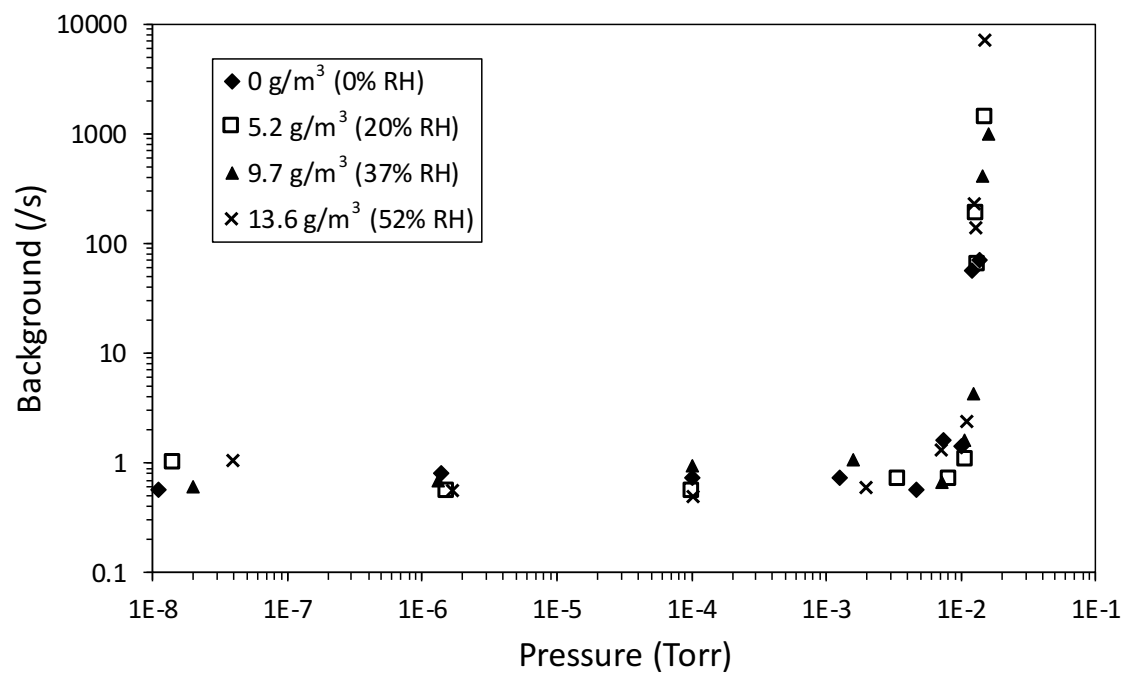


**Figure 4.12.** Effect of humidity on MCP background count rates for nitrogen backfill. The MCP was operated at -2320 V to collect the data in this figure

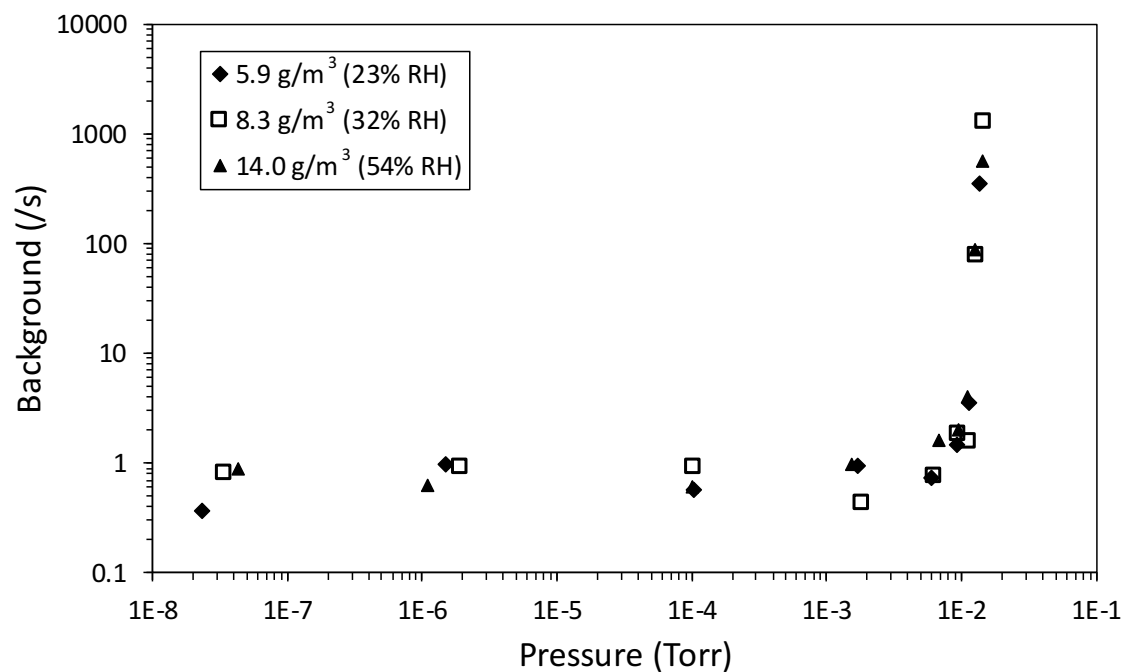


**Figure 4.13.** Effect of humidity on MCP background count rates for laboratory air backfill. The MCP was operated at -2320 V to collect the data in this figure.

facility nitrogen contained only trace amounts of water, as measured by a portable hygrometer, and the moisture content of the gas was increased as described in section 4.1.2.1. Background count rates were obtained for nitrogen with water contents ranging from 0 g/m<sup>3</sup> (0% RH) to 13.65 g/m<sup>3</sup> (52% RH). For laboratory air, the lowest water content attainable was 5.9 g/m<sup>3</sup>, corresponding to a relative humidity (RH) of 23%. Background count rates were measured for laboratory air at water content levels of 5.9 g/m<sup>3</sup> (23% RH), 8.3 g/m<sup>3</sup> (32% RH), and 14.0 g/m<sup>3</sup> (54% RH). For both nitrogen and laboratory air, the MCP background count rate appears to be unaffected by the humidity level. The onset of higher count rates for both nitrogen and laboratory air occurred at about  $1 \times 10^{-2}$  Torr, regardless of the water content in the test gas.

#### 4.2.3. Pressure Induced MCP Arcing

Whereas high background count rates due to elevated pressures (section 4.2.2) can result in a poor signal-to-noise ratio, runaway arcing or discharge events in an MCP can actually terminate an experiment and destroy the detector. An arc, or discharge event was defined as an occurrence in which the MCP high-voltage power supply tripped due to exceeding a preset current limit (section 4.1.2). This section presents results from experiments exploring the discharge behavior of the MCP detector at elevated pressures under argon, nitrogen, oxygen, and laboratory air backfill. Data for helium is noticeably absent from the plots in this section because no discharge events occurred under helium backfill.

Prescrub discharge pressures as a function of the applied MCP voltage are shown for backfill with nitrogen, argon, and laboratory air in Figure 4.14. After removing 0.2 C/cm<sup>2</sup> of charge from the MCP, discharge pressures were noted for backfill with nitrogen, laboratory air, and oxygen, and are shown in Figure 4.15. Discharge pressures for backfill with argon were not measured at this point. Figure 4.16 shows discharge pressures for nitrogen, argon, and laboratory air after all scrubbing was completed, which removed a total of 0.75 C/cm<sup>2</sup> of charge from the detector (section 4.2.1). The postscrub discharge pressures were

noticeably higher than the prescrub discharge pressures. Comparing Figure 4.14 to Figures 4.15 and 4.16 shows that the scrubbing process had a stabilizing effect on the MCP. This effect is even more apparent in Figure 4.17, which shows the pressures of arcing events for an MCP bias of -2000 V at different points during the scrubbing process. This indicates that the stabilizing effect of scrubbing occurs very early in the scrubbing process.

The prescrub discharge data in Figure 4.14 shows a consistently lower discharge pressure for argon than for nitrogen and laboratory air at all MCP voltages tested except -2000 V. In Figure 4.15, the detector discharge pressures under oxygen backfill are consistently lower than for nitrogen and laboratory air. Figure 4.16 though, which presents discharge data after all scrubbing was completed, shows no apparent discharge dependence on backfill gas. MCP discharge pressures for each test gas can be explained, at least qualitatively, by considering the ionization energies of each (Table 4.2). Since the ionization energy for  $O_2$  is more than 3 eV lower than for  $N_2$  and Ar, the lower discharge pressure for oxygen in

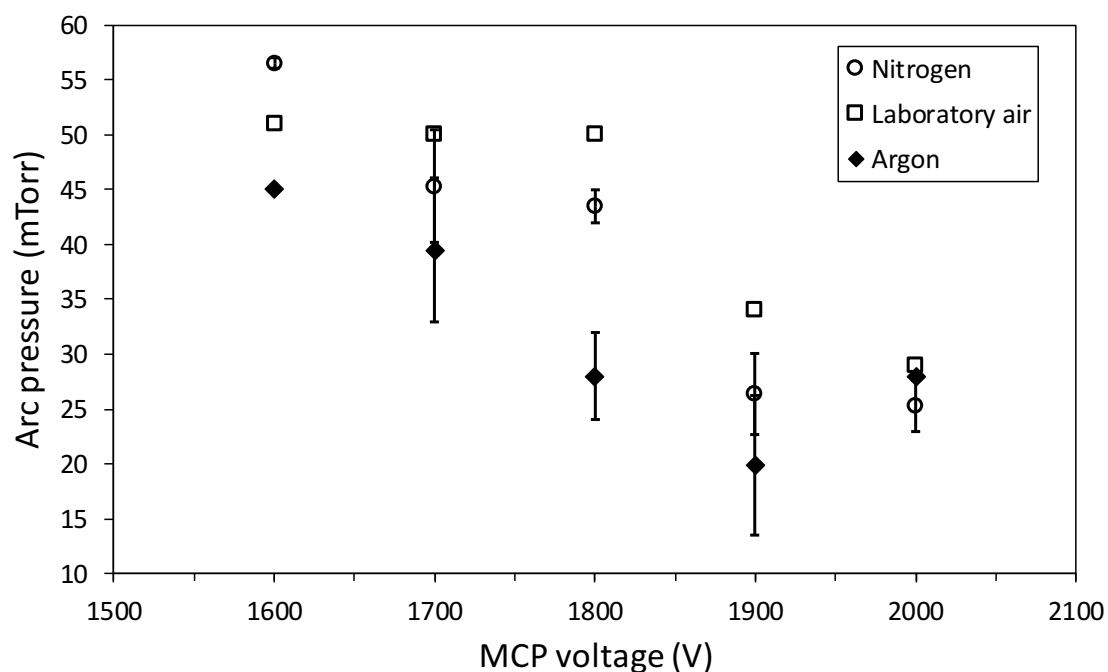


**Figure 4.14.** Prescrub MCP discharge events under nitrogen, argon, and laboratory air backfills. Data points without error bars indicate single measurements.

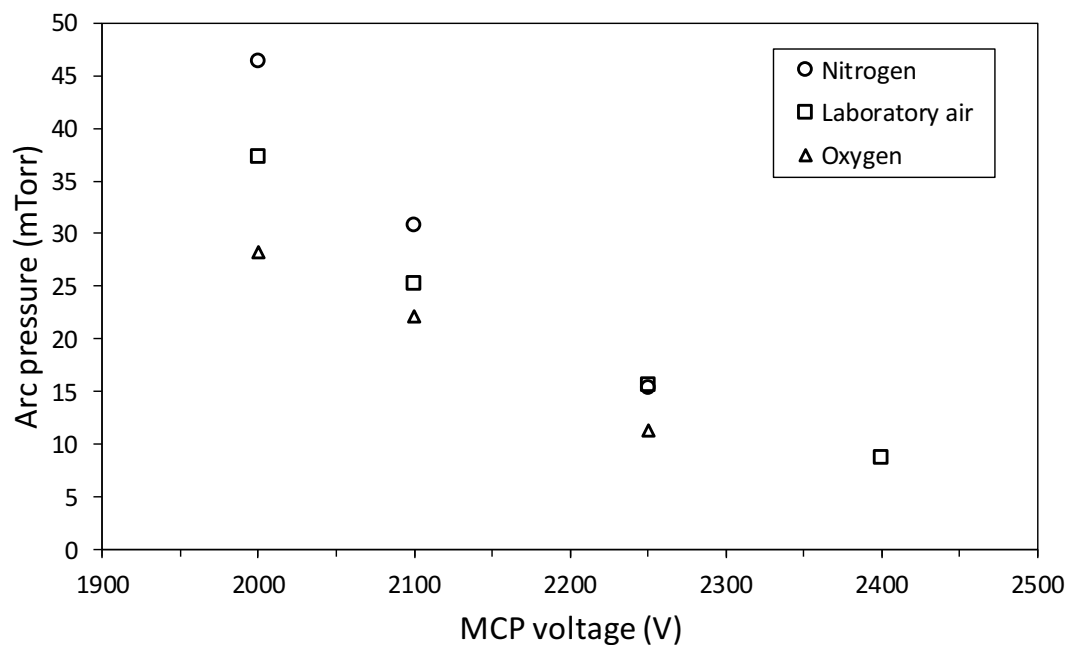


**Figure 4.15.** MCP discharge events measured after the first scrub, under nitrogen, laboratory air, and oxygen backfills. With the exception of the data points for nitrogen and lab air at 2000 V, which both have errors of  $\pm 1.2$  mTorr, errors are the same size or smaller than the symbols used in the plot.

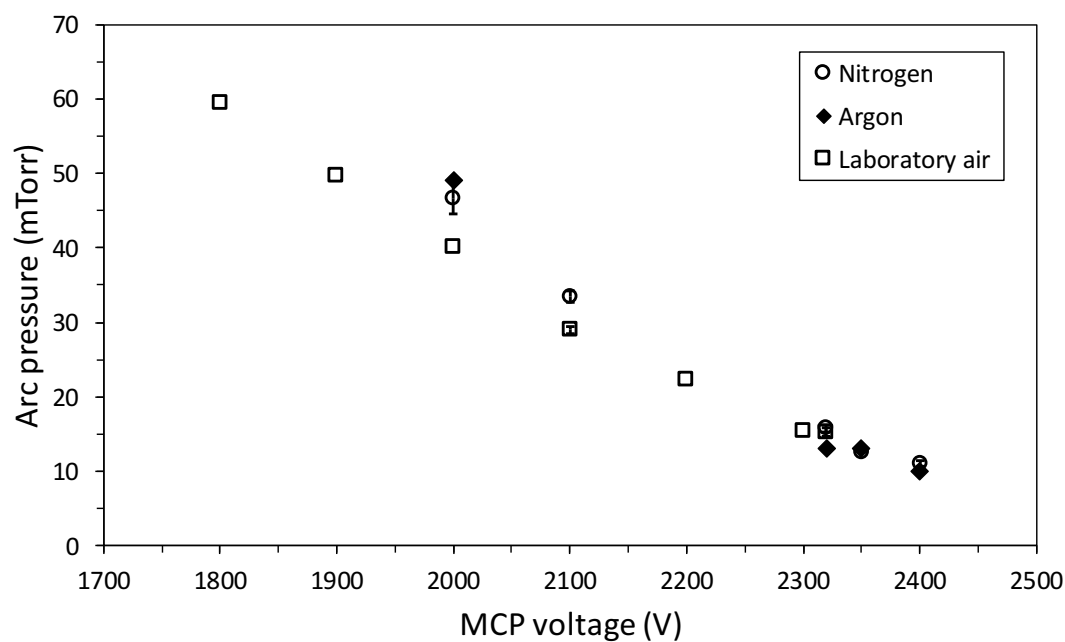


**Figure 4.16.** Postscrub discharge events for the MCP detector under nitrogen, argon, and laboratory air backfills. Data points without error bars indicate single measurements.

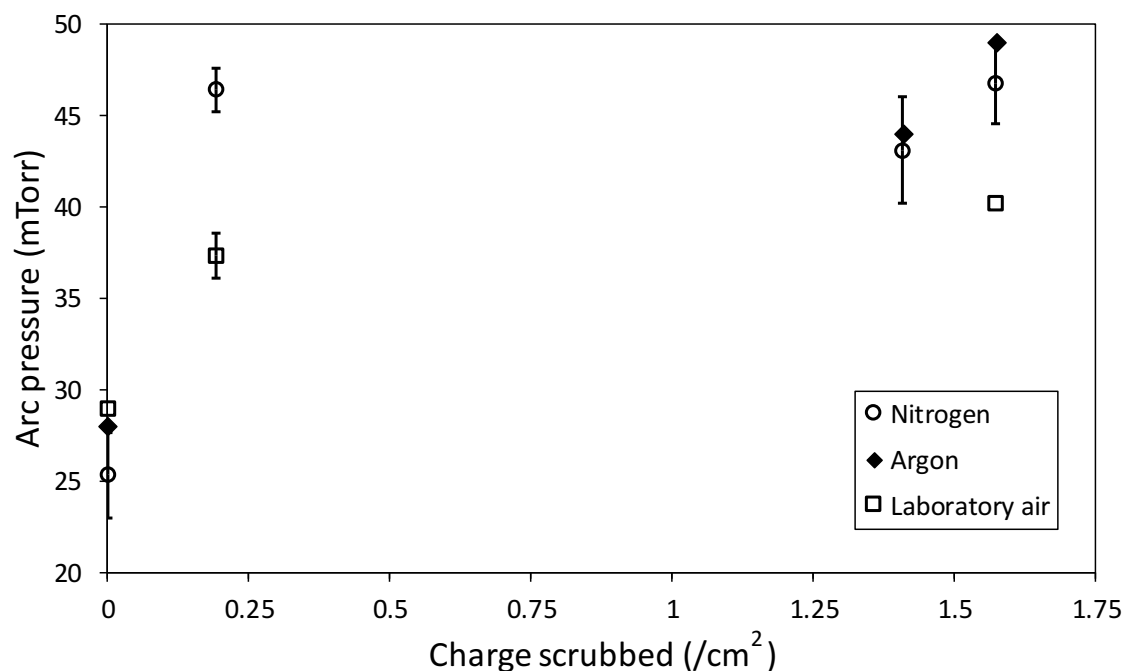


**Figure 4.17.** Pressures of detector discharge events at different points during the progression of the MCP scrub. Data was taken with the MCP biased at -2000 V.

**Table 4.2.** Ionization Energies for Molecular Nitrogen, Molecular Oxygen, and Argon [Linstrom and Mallard, 2001]

Species	Ionization energy (eV)
N <sub>2</sub>	15.6
O <sub>2</sub>	12.1
Ar	15.8

Figure 4.15 is expected. However, the reason for lower discharge pressure of the MCP under argon backfill in Figure 4.14 is unclear. Laboratory air, which is composed mainly of nitrogen and oxygen, shows discharge pressures similar to these two gases in Figures 4.15 and 4.16.

The effect of humidity on detector discharge was also studied after the MCP had been scrubbed. For these experiments water was added with the backfill gas as described in section 4.1.2.1. Detector discharge events are shown at different humidity levels for nitrogen

in Figure 4.18 and for laboratory air in Figure 4.19. Water content levels used during these experiments ranged from 0 g/m<sup>3</sup> (0% RH) to 13.7 g/m<sup>3</sup> (52% RH) for nitrogen and from 5.9 g/m<sup>3</sup> (23% RH) to 14.0 g/m<sup>3</sup> (54% RH) for laboratory air. The facility nitrogen had only a trace amount of water, 0.02 g/m<sup>3</sup> as measured with the portable hygrometer; this allowed experiments to be performed with a nearly water-free backfill gas. Conversely, laboratory air contained moisture simply by virtue of being ambient air. Although water has a lower ionization potential (12.6 eV [Linstrom and Mallard, 2001]) than molecular nitrogen, the introduction of water into the nitrogen backfill did not noticeably affect arcing pressures (Figure 4.18). Similarly, laboratory air was likewise unaffected even though the moisture content was more than doubled when compared to ambient laboratory air (Figure 4.19). Because introduction of moisture to the backfill gases had no noticeable effect on discharge pressure, these discharge events were included in the data for Figures 4.16 and 4.17 without making a distinction based on the amount of water in the backfill gas.

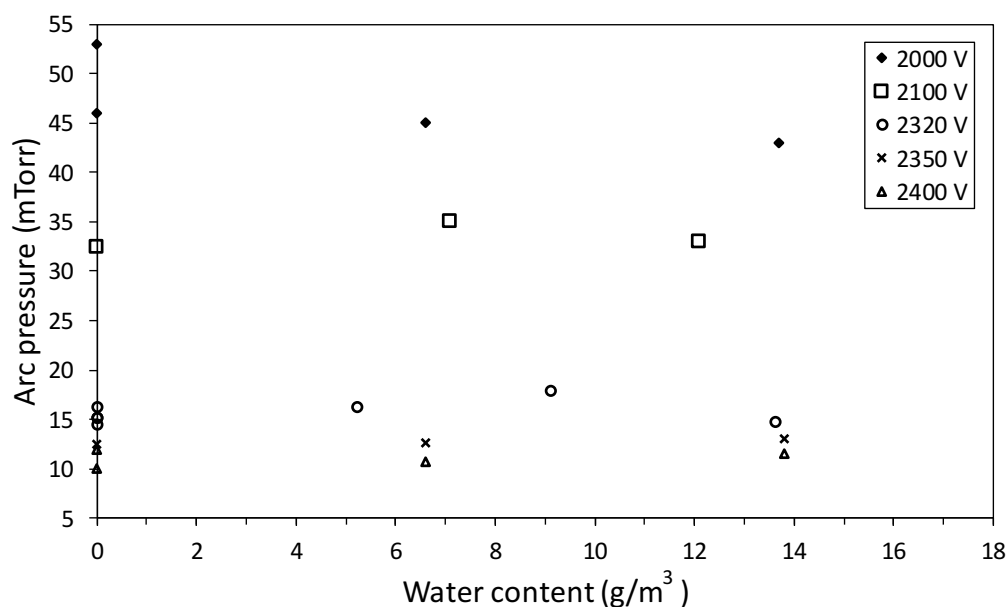


**Figure 4.18.** Detector discharge events for nitrogen backfill, for different amounts of water added to the backfill gas. The water content (horizontal axis) is the amount of water present in the backfill gas, measured at atmospheric pressure, before introducing the gas to the test chamber.

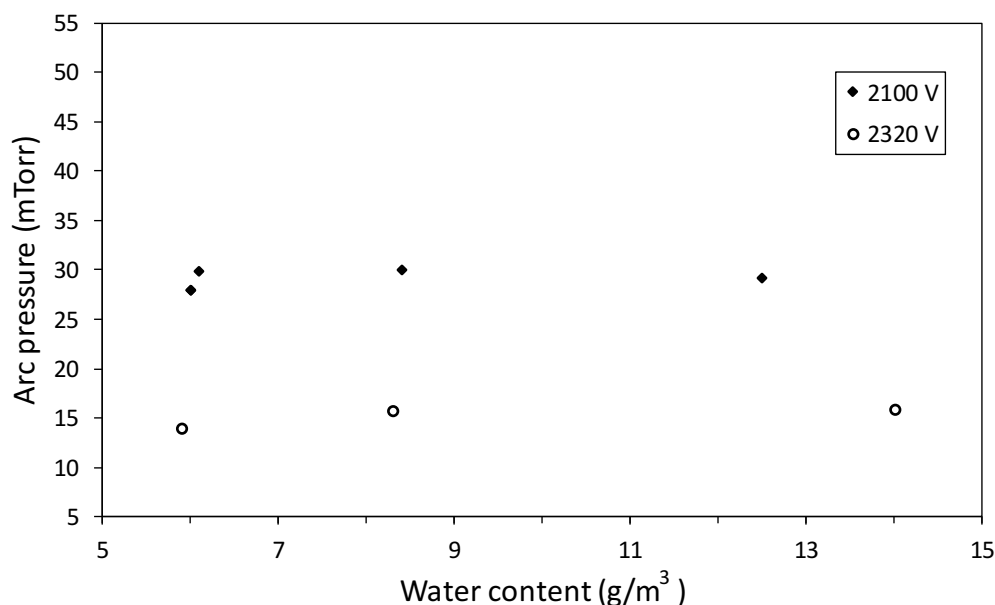


**Figure 4.19.** Detector discharge events for laboratory air backfill, for different amounts of water added to the backfill gas. The water content (horizontal axis) is the amount of water present in the backfill gas, measured at atmospheric pressure, before introducing the gas to the test chamber.

#### 4.2.4. TOF-MS at Elevated Pressures

The MCP background count rate versus pressure experiments and the detector arcing experiments were performed without actively stimulating the MCP with ions or UV photons. Additional experiments were performed to find if the instrument could collect spectra at elevated pressures. Figure 4.20 shows a mass spectrum that was collected with the EDU operating in neutral mode under argon backfill at a pressure of  $2 \times 10^{-4}$  Torr, and represents the highest pressure at which the instrument has been successfully operated. The spectrum contains peaks due to singly and doubly ionized argon. The EDU operated at a duty cycle of 0.5% and the integration time for the spectrum was 75 s to obtain this spectrum. The MCP high voltage was -1946 V. The average count rate, including noise, was  $2.5 \times 10^7$  Hz; the majority of the noise was due to the elevated pressure and was not observed in spectra taken at lower pressures. This noise may be due to UV photons originating in the ionization volume of the instrument. The maximum count rate occurred at the  $\text{Ar}^+$  peak and

was  $4.2 \times 10^7$  Hz. The mean free path (mfp) at  $2 \times 10^{-4}$  Torr is about 30 cm, or roughly twice the drift length of the EDU. The resolution at FWHM and SNR of the  $m/z$  40 peak ( $\text{Ar}^+$ ) peak in Figure 4.20 are 50 and 144, respectively. This demonstrates the ability of the TOF-MS to operate at pressures extending into the  $10^{-4}$  Torr range.

### 4.3. Discussion

The first primary objective of the experiments in this chapter was to replicate earlier reports of MCP detector performance at elevated pressures. The results from MCP background count rate experiments presented in section 4.2.2 are very similar to those reported in [Cochran *et al.*, 2005; Laprade and Cochran, 2006; Laprade *et al.*, 2006]. The other primary objective was to study the arcing characteristics of the MCP. Arcing experiments were performed to determine the range of pressures the MCP detector could be safely exposed to with operational voltages applied. These results are encouraging, demonstrating the ability of the MCP detector used in the SDL instrument to not only survive, but to also

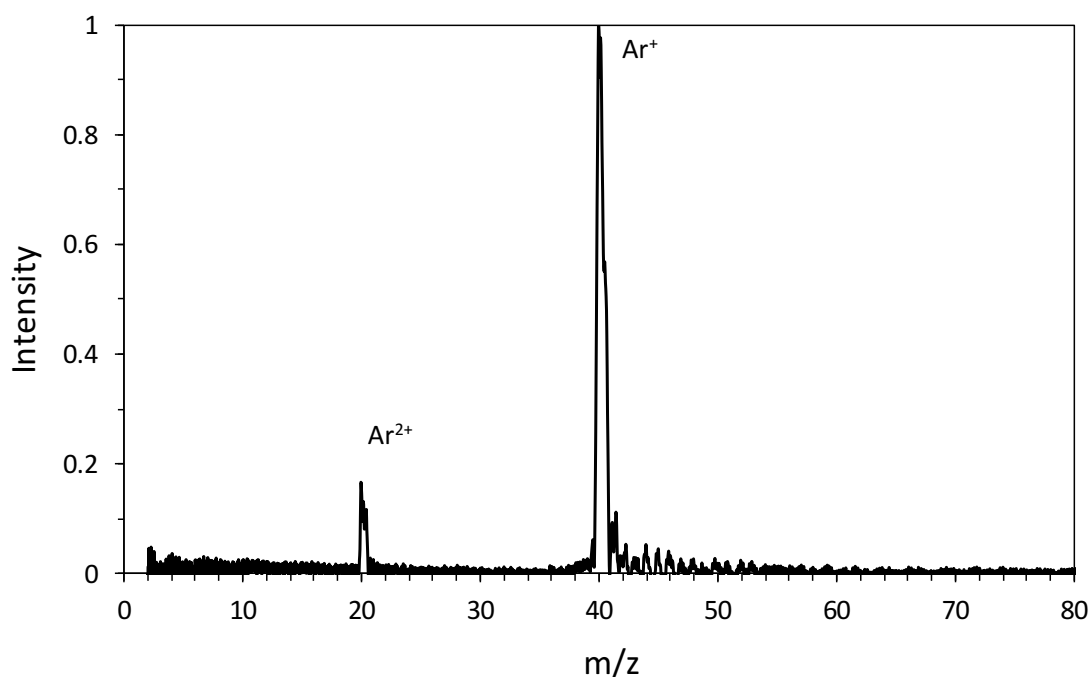


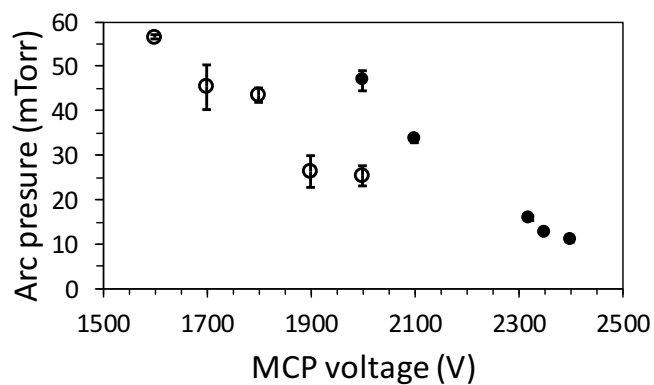
**Figure 4.20.** Mass spectrum taken with the EDU operating under argon backfill at  $2 \times 10^{-4}$  Torr.

maintain low background count rates at elevated pressures.

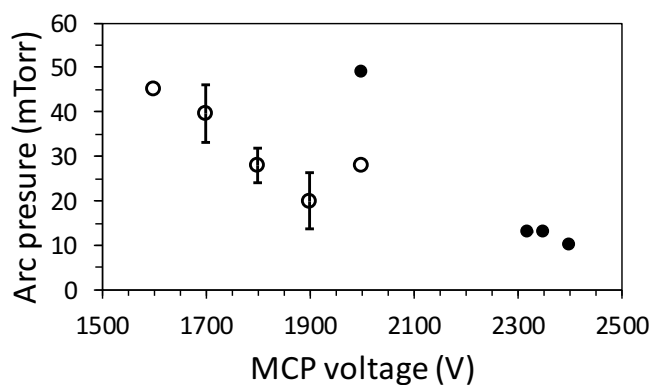
Although MCP background count rate experiments were performed with a variety of gases, the most relevant results for the SDL instrument are contained in Figure 4.7, which shows background count rates versus pressure for the MCP under laboratory air backfill. As a rocket-borne instrument in the MLT, the instrument will be sampling air of similar composition to that found in the laboratory, at least below the turbopause. When operating the EDU to collect spectra in the laboratory, the MCP is typically biased between -1950 and -2050 V. This is well below the gain matched voltage of -2320 V, but somewhat higher than the voltage matched -1900 V. However, the background count rate in laboratory air was small ( $\sim 1$  ct/s) for the postscrub MCP at pressures up to  $1 \times 10^{-3}$  Torr and below 10 ct/s at pressures up to  $1 \times 10^{-2}$  Torr. Figures 4.5 and 4.6 show similar results for nitrogen (the main component of air) and argon.

Like the background count rate experiments, results from the detector discharge experiments with laboratory air backfill (section 4.2.3) are most relevant to the SDL instrument. Comparison of prescrub detector arcing behavior (Figure 4.14) to postscrub detector arcing behavior (Figure 4.16) shows that scrubbing has a stabilizing effect on MCP performance. Figure 4.21 presents the discharge data in Figures 4.14 - 4.16 for each gas individually, and clearly shows the improvement in detector performance due to scrubbing. In each case, the discharge pressures are higher after scrubbing than before. Figure 4.17 shows that this stabilizing effect occurs early in the scrubbing process. The greatest change in discharge pressure occurred after removing about  $0.2$  C/cm<sup>2</sup> of charge from the detector. This suggests that MCP discharge behavior can be greatly improved by scrubbing even a small amount of charge. Removal of this much charge could be carried out fairly quickly, a few days at most, and would greatly reduce the risk of catastrophic damage to the detector in elevated pressure environments.

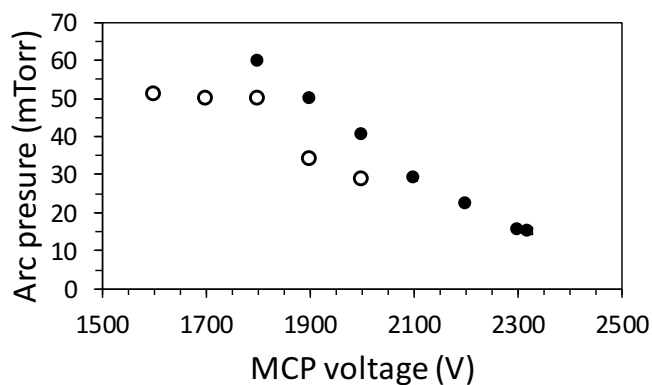
A scrubbed MCP can safely be exposed to significantly higher pressures with less risk of potentially damaging discharge events. Considering that the EDU is typically operated



(a)



(b)



(c)

**Figure 4.21.** Comparison of prescrub and postscrub MCP arcing events. Prescrub (hollow circles) and postscrub (solid circles) discharge pressures are shown for (a) nitrogen, (b) argon, and (c) laboratory air backfills over a range of applied voltages.

with the MCP biased between -1950 and -2050 V, these results are particularly encouraging. At these operating potentials an unstimulated, scrubbed AP-TOF detector can be safely exposed to pressures up to 20 mTorr and perhaps even as high as 30 mTorr. An unscrubbed detector will not have quite the operational pressure range, but should still withstand exposure to pressures in the low mTorr range (Figure 4.14).

Ion feedback is the likely cause of detector discharge. Ion feedback occurs when gas particles are ionized on the anode side of the detector and accelerated back through the MCP channels. If the ions gain sufficient energy and collide with a channel wall, they liberate more electrons and the process continues. There are two main sources of ions that contribute to ion feedback: ions liberated from channel walls due to electron bombardment, and EI of ambient gas particles that are either inside the MCP channels or near the anode side of the detector [Wiza, 1979]. The first, ions liberated from channel walls due to electron bombardment, depends a great deal on the state of the MCP. The scrubbing process reduces this effect by removing gas particles from the walls of the MCP channels [Timothy, 1981; Siegmund, 1989; Thomas and Behnke, 1993]. The effect of this is seen in Figure 4.21, as the postscrub discharge pressures are lower than before scrubbing the detector. The second, EI of ambient gas particles, is entirely due to the ambient gas surrounding the MCP. Though ion feedback originating inside the MCP channels decreases due to scrubbing, feedback due to ambient gas particles in the vicinity of the detector is still present.

Factors that contribute to the breakdown of a gas in a vacuum include: voltage, gas species, electrode material, and distance between electrodes. Lieberman and Lichtenberg derive the following equation for breakdown voltage,  $V_b$ , between two planar electrodes [Lieberman and Lichtenberg, 2005]:

$$V_b = \frac{Bpd}{\ln Apd - \ln [\ln (1 + 1/\gamma_{se})]}, \quad (4.1)$$

where  $p$  is the pressure of the gas,  $d$  is the distance between the electrodes, and  $\gamma_{se}$  is the

secondary electron yield at the cathode.  $A$  and  $B$  are constants, specific to the gas participating in the discharge, and are determined experimentally. Below a certain value of  $pd$ , ionizing collisions between electrons and the background gas are too infrequent to sustain a breakdown. At larger  $pd$ , the numerator in equation 4.1 dominates and  $V_b$  increases linearly. Between these two extremes  $V_b$  has a minimum value [Lieberman and Lichtenberg, 2005]. It is at this value of  $pd$ , also called the Paschen minimum, where breakdown is most likely to occur. A process similar (though more complicated) to that described in equation 4.1 is likely responsible for discharge in an MCP. With the MCP at operating voltage, backfilling increases the pressure of the background gas until the  $pd$  value for minimum  $V_b$  is reached. Discharges do not always occur at the exact same pressure for a given MCP potential, although they do tend to occur at similar pressures. Reasons for this may include: discharge originating at different depths in MCP channels; residual gas from previous backfills lingering in or adsorbing to channel surfaces and being subsequently involved in a discharge event, especially after a rapid backfill experiment; involvement (or noninvolvement) of MCP hot spots in the developing discharge; the number of channels involved in the discharge.

The decision of whether or not to scrub an MCP detector ultimately depends on its intended use. Sections 4.1.1 and 4.2 describe some of the benefits of scrubbing, which include lower background count rates, more favorable discharge characteristics, and gain stabilization. MCPs exposed to elevated pressures during short duration missions (sounding rocket at lower altitudes, for example) would certainly benefit from a preconditioning scrub. MCPs used in instruments for longer duration missions (satellites, for example) would not be exposed to pressures high enough to cause discharge, but would benefit from the gain stabilization that results from scrubbing. However, scrubbing may not be necessary in all cases. For example, an unscrubbed MCP could be safely used in a sounding rocket experiment at high altitudes, where pressures would be below  $10^{-6}$  Torr. Regardless, scrubbing even a small amount of charge from an MCP (see Figure 4.17) results in

improved performance. Ultimately, mission requirements must be taken into consideration in deciding whether or not, and to what extent, to perform an MCP scrub.

Results from background count rate and detector discharge experiments at elevated humidity levels are encouraging. Figures 4.12 and 4.13 show no noticeable change in background count rate, regardless of the amount of water in the backfill gas. Likewise, Figures 4.18 and 4.19 show no trend in discharge pressures at increasing humidity levels. Water vapor mixing ratios in the MLT reach a maximum value near 82 km altitude and can be as great as 15 ppmv [Summers *et al.*, 2001]. This corresponds to a value of  $0.012 \text{ g/m}^3$  in Figures 4.13 and 4.19. Since backfill count rate and detector arcing experiments were performed at water vapor levels much higher than occur in the MLT, water vapor is not expected to pose a problem for the SDL instrument.

The background count rate and detector discharge experiments presented in this chapter were conducted without any active stimulation of the MCP detector. During operation of the SDL instrument to collect mass spectra, the MCP will be actively stimulated. To test this, the EDU was operated in neutral mode under argon backfill at pressures up to and including  $2 \times 10^{-4}$  Torr. Figure 4.20 shows a mass spectrum obtained at a pressure of  $2 \times 10^{-4}$  Torr, which represents the highest pressure at which the EDU has been successfully operated. The MCP high-voltage power supply tripped (signifying a detector discharge event) at a pressure of  $2.3 \times 10^{-4}$  Torr shortly after the spectrum in Figure 4.20 was taken.

The background count rate during collection of the data for Figure 4.20 was quite high ( $\sim 2.5 \times 10^7 \text{ s}^{-1}$ ). This background is attributed to the elevated pressure; it was observed to increase as the pressure increased. However, the count rate data shown in Figure 4.6 for argon backfill suggests that the background observed in Figure 4.20 was not due to pressure effects on the MCP detector. At  $2 \times 10^{-4}$  Torr, a background count rate of at most a few counts per second would be expected. Another source must be responsible for the background in the spectrum at elevated pressure.

UV emissions originating in the ionizer region of the EDU are most likely responsible

for the high background in Figure 4.20. Increasing the number of argon atoms in the ionization volume leads to increased UV emissions from argon in excited states. The linear design of the EDU means that the active area of the MCP is in the direct line of sight of the ionization volume, allowing UV photons produced in the ionizer to arrive at and stimulate the detector. This suggests that in neutral mode a linear version of the SDL instrument has a maximum operating pressure of about  $2 \times 10^{-4}$  Torr, but should probably be operated at pressures a little lower to maintain an operational safety buffer. At least in the lower MLT, a linear SDL instrument would require active pumping to maintain an operable pressure in neutral mode. Alternatively, a reflectron version of the SDL instrument would not have a direct line of sight from the ionizer to the MCP. Thus, it is postulated that a reflectron instrument would have a lower background count rate, allowing operation at higher pressures than a linear instrument. However, this was not able to be confirmed with the EDU.

Due to concerns with the ion gun at elevated pressures, the EDU has not been tested at high pressures in ion mode. When operating the SDL instrument in ion mode, the absence of UV emissions from the ionizer would result in a much lower background compared to neutral mode. The maximum operating pressure would depend on the count rate of the peak in the mass spectrum due to the most abundant ion species. This suggests that the SDL instrument can operate at higher pressures in ion mode than neutral mode.

#### 4.4. Conclusions

Experiments were performed to evaluate the behavior of the MCP detector used in the SDL instrument at elevated pressures. Scrubbing the detector resulted in lower background count rates and higher discharge pressures; these improvements occurred early in the scrubbing process. Scrubbing the MCP is recommended in most cases to help stabilize detector gain, decrease the number of background counts, and improve detector resistance to discharge events. Background count rate and detector discharge experiments were performed

at elevated pressures under nitrogen, argon, helium, oxygen, and laboratory air backfill. The effect of humidity on detector performance was also tested by adding water to nitrogen and laboratory air backfills. The humidity levels used in these experiments were found to have little, if any, effect on background count rates or detector discharge events.

The experiments presented in this chapter demonstrate that the MCP detector used in the SDL instrument is capable of operating at pressures extending into the  $10^{-4}$  Torr range. The unstimulated detector maintained low background count rates at pressures well into the milliTorr range. Although the MCP used in these experiments performed well under backfills with various gases at elevated pressures, the detector should not be unnecessarily exposed to elevated pressures. These experiments also show that an appropriate vacuum system will be required for the SDL instrument to successfully make measurements in the lower MLT, which will be explored further in Chapter 6.

## CHAPTER 5

## EXPERIMENTAL TESTS OF A GETTER-BASED PUMPING SYSTEM

A vacuum system is an integral part of a TOF-MS. MCP detectors require low pressures to operate (see Chapter 4). Additionally, low instrument pressures minimize the number of resolution-degrading collisions between sampled ions and residual gases. Rocket-borne mass analyzers have employed cryogenic pumping [Balsiger *et al.*, 1996; Offermann *et al.*, 1981; Schulte and Arnold, 1992; Zbinden *et al.*, 1975]; ion pumping [von Zahn and Gross, 1969; Balsiger *et al.*, 1971]; and in at least one case, a passive vacuum system employing venting ports [Knappmiller *et al.*, 2008], to provide suitable pressures for making measurements. No mention of a nonevaporable getter (NEG) used to pump a rocket-borne mass analyzer was found in a literature search.

The SDL TOF-MS is a versatile instrument with a simple design and can easily be adapted to incorporate any of the different pumping methods mentioned above. Provided that sufficient pumping speeds could be realized, an NEG could provide a simple, inexpensive method to evacuate the interior of rocket-borne instruments in the MLT. The Tubegetter<sup>®</sup>, formerly manufactured by Alvatec Alkali Vacuum Technologies GmbH (now available from AlfaVakuo e.U.), is a recent development in NEG technology and was considered in the original instrument proposal to provide vacuum pumping for the SDL instrument [Londer *et al.*, 2007; AlfaVakuo, 2016]. Barium has been widely used as an evaporable getter [Wagener, 1951; Turnbull, 1977; Ferrario, 1996]. The TGs proposed for use in the SDL TOF-MS are small, less than 2 cm diameter and 20 cm length, and loaded with 3 g of nanostructured barium as the active NEG material [Alvatec, 2014]. The barium is protected from the atmosphere by an indium seal. Activating the TGs is accomplished by breaching the seal, either mechanically or by applying heat, to expose the barium getter.

An important aspect of this research for this dissertation involved performing experiments with several TGs to determine their pumping speeds at different pressures and

amounts of gas sorbed. This chapter discusses the experimental determination of the TG pumping characteristics. Results from these experiments were later used as inputs to a vacuum performance model to simulate their effectiveness in providing vacuum in the SDL TOF-MS during a sounding rocket flight in the MLT (see Chapter 6).

### 5.1. Experimental Setup and Procedures

Pumping speed data for the TGs acting on air is sparse and only available for a barium load of 1 g at a pressure of  $7.5 \times 10^{-7}$  Torr [Alvatec, 2014]. The TGs intended for use on the TOF-MS, model ATG-12-110-008-01, have a 3 g barium load. Moreover, during a rocket flight to the MLT, instrument pressures in the SDL TOF-MS are expected to range over several orders of magnitude. Experiments were designed and carried out on several TGs (model ATG-12-110-008-01) in order to determine their pumping characteristics over a range of pressures. These experiments were performed by activating TGs inside a vacuum chamber, backfilling the chamber with air, and recording the chamber pressure over time. The goal of these experiments was to determine the TG pumping speed at different pressures and amounts of gas sorbed and to utilize these data in a computer model to simulate the pressure inside the SDL instrument during sounding rocket flights (see Chapter 6).

#### 5.1.1. Experimental Setup

The publicly available TG pumping data (from Alvatec) was obtained using ASTM standard F798-97, which describes a method for measuring the pumping characteristics of getters in the molecular flow regime [ASTM Standard F798-97, Reapproved 2002]. The technique described in ASTM standard F798-97 was not employed in the TG experiments described in this chapter for the following reasons: TG pumping information at pressures extending from the molecular flow regime well into the transition flow regime was desired, and there were concerns that at higher pressures this technique would saturate the TGs too quickly to yield much useful information. Detector survivability at elevated pressures

(discussed in Chapter 4) and instrument mfp requirements were primary considerations, so the experiment was designed to measure the TG pumping speeds at pressures ranging from  $10^{-5}$  to  $10^{-2}$  Torr. This range of pressures could potentially result in complications for the SDL TOF-MS on a sounding rocket.

The experimental setup comprised two volumes separated by a pneumatic gate valve (Figure 5.1). The test volume was constructed with ConFlat™-style (CF) vacuum components. TGs were tested individually. During each experiment a TG was held in place on a custom built mount that attached to a feedthrough on the volume 1 side of the experimental apparatus (Figure 5.2a). The feedthrough provided access for both a TG activation heating current and a type K thermocouple to monitor TG temperature. The pressure in each volume was measured with a 0.1 Torr Baratron® capacitance manometer with a resolution of  $1 \times 10^{-6}$  Torr. Additionally, an IG was attached to volume 2 to measure pressures below  $10^{-3}$  Torr. The IG was primarily used to zero the Baratron® gauges and also to measure chamber pressure during TG cool down. The IG was usually off during backfill experiments, which often involved pressures above  $10^{-3}$  Torr. A pneumatic right-angle valve separated volume 1 from a turbo pump. Chamber backfill was accomplished via a variable leak valve attached to volume 2. A data logger (Agilent model 34970A) recorded pressure data at one-second intervals from the two Baratron® gauges, the ion gauge, and the thermocouple sensor.

The TG mounting process is shown in Figure 5.2. TGs were prepared by first cleaning them with a clean, white, lint-free wipe and IPA until no visible residue was observed on the wipe. A type K thermocouple was then attached to the TG, near the location of the indium seal, using a small piece of Kapton® tape (Figure 5.2b). Ceramic sleeving was placed around the TG at the location of the indium seal, and a nichrome heating coil was then placed around the ceramic sleeving. The sleeving was used to electrically isolate the heating coil from the TG. Prior to its use in these experiments, the sleeving was baked at 1050 degrees Celsius for 30 minutes to remove any residual volatiles. The TG was then

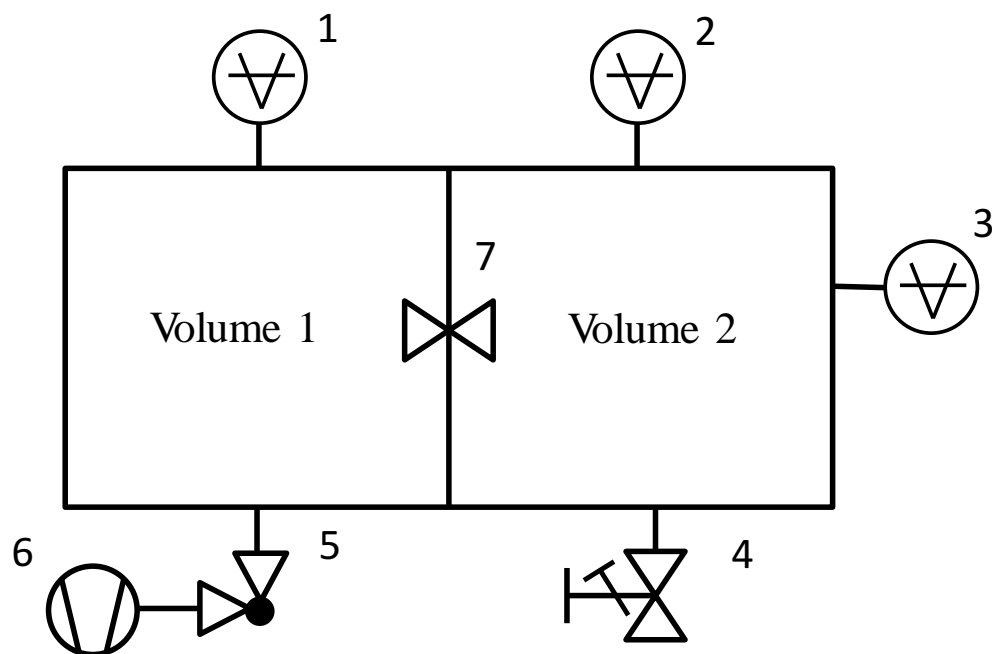
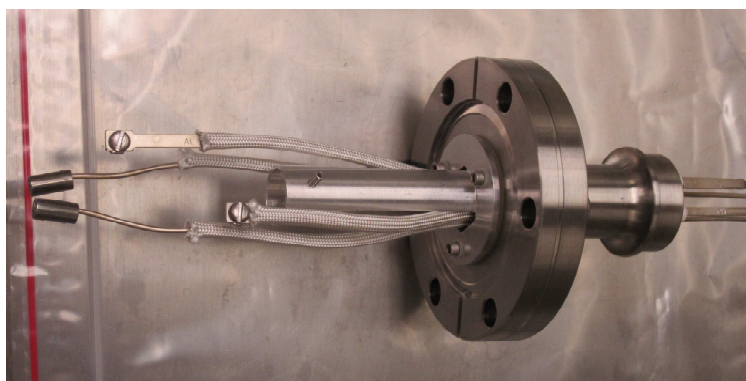


**Figure 5.1.** Schematic of the TG experimental apparatus. The different components are: 1) and 2) Baratron<sup>®</sup> capacitance manometers, 3) ion gauge, 4) variable leak valve, 5) right-angle valve, 6) vacuum pump, and 7) gate valve. The TG is mounted in volume 1.

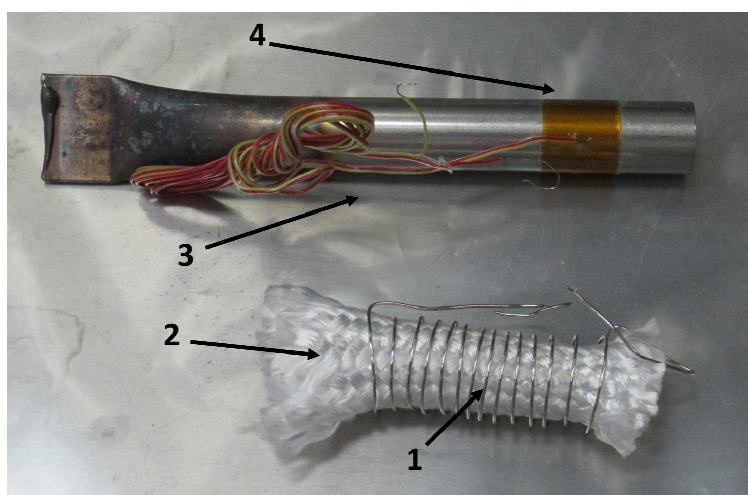
mounted in the tube mount (Figure 5.2c), and the thermocouple wires and the nichrome heating coil were attached to the feedthrough. A thin disk made of PEEK electrically isolated the feedthrough from the TG mount. The feedthrough, with mounted TG, was then affixed to volume 1 of the experimental apparatus. Nitrile gloves were worn while handling the TG, tube mount, and feedthrough during TG preparation. TG activation and cool down were performed under vacuum in order to minimize the amount of gas sorbed by the TG during the activation and cool down period.

### 5.1.2. Experimental Procedure

The Baratron<sup>®</sup> capacitance manometers and the IG were zeroed prior to TG activation. This was accomplished by lowering the pressure in the experimental volume below the Baratron<sup>®</sup> resolution ( $1 \times 10^{-6}$ ) and adjusting the Baratron<sup>®</sup> gauges to read zero. Next, the experimental volume was backfilled with lab air to between  $9.0 \times 10^{-4}$  and  $9.9 \times 10^{-4}$  Torr as read by the Baratron<sup>®</sup> gauges. The IG sensitivity was then adjusted until the IG and



(a)



(b)



(c)

**Figure 5.2.** TG preparation for pumping experiments. (a) Custom built TG mount attached to the electrical/thermocouple feedthrough. (b) Tubegetter preparation: heating coil (A) and ceramic sleeving (B) before placement on TG; thermocouple (C) is attached to TG with Kapton<sup>®</sup> tape (D). (c) TG secured in mount with thermocouple and heating coil in place prior to installation in volume 1 of the experimental apparatus.

Baratron<sup>®</sup> pressure readings were identical. After zeroing the pressure gauges, the variable leak valve was closed, and the experimental volume was evacuated by the turbo pump. The experimental chamber was pumped continually throughout the TG activation process.

TG activation was accomplished by applying a DC current to the nichrome heating coil to melt the indium seal, exposing the barium getter. Chamber pressure and TG temperature were monitored and logged during the activation process. Figure 5.3 shows typical TG activation temperature and pressure curves. Generally, a pressure spike one to two orders of magnitude, due to argon trapped in the TG during the manufacturing process, indicated melting of the indium seal and TG activation [Dengg, 2011]. However, some TGs activated without exhibiting the expected pressure spike. After TG activation, the heating current was turned off. The TG was allowed to cool to within a few degrees of the laboratory temperature (~27 °C) before beginning pumping experiments. This cool down period typically lasted 1-2 hours. Occasionally, pressure spikes seen during activation heating of the TG were mistaken for activation; when this occurred the activation process was repeated.

The TG pumping experiments consisted of backfilling the experimental volume (Figure 5.1) and recording the pressure as the TG sorbed the backfilled gas, effectively pumping and removing it from the chamber. This experiment was performed multiple times on each TG. The process is illustrated in Figure 5.4, which shows the pressures of each side of the experimental setup for two individual backfill experiments. The following steps were followed to perform backfill experiments (refer to Figure 5.4). First, the gate valve separating volumes 1 and 2 was closed. The variable leak valve was opened to backfill volume 2 with laboratory air, labeled a in the figure. The variable leak valve was closed after volume 2 reached the desired pressure, labeled b. The right-angle valve separating volume 1 from the turbo pump was then closed. At c, the gate valve between volumes 1 and 2 of the experimental apparatus was opened to allow the air originally in volume 2 to fill the entire experimental volume; and d shows the pressure in the experimental volume decreasing due to the gettering action of the TG. The right-angle valve was then opened

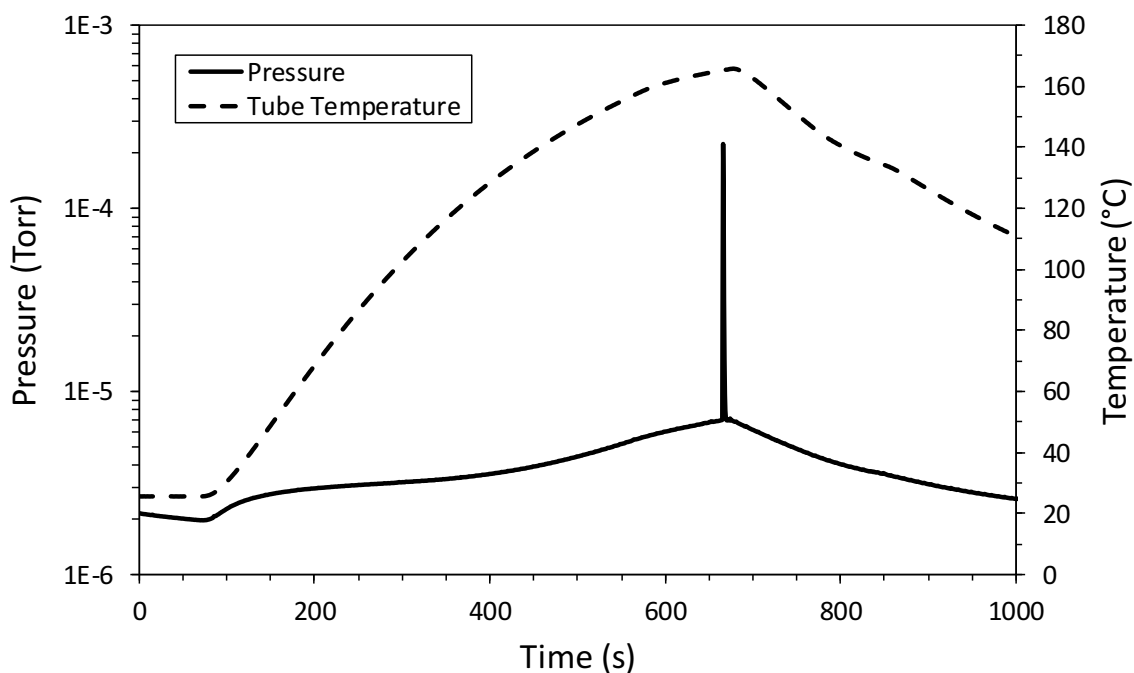


**Figure 5.3.** Pressure and temperature during the activation process for TG 10383-1. The pressure spike at 666 seconds indicates TG activation and is due to argon escaping from the TG when the indium seal melted.

to allow the entire experimental volume to be evacuated by the turbo pump, labeled e. These steps were repeated for a range of backfill pressures until the desired amount of data was collected or until the TG pumping speed had slowed considerably. Pressure and temperature data were logged at one-second intervals during these experiments.

Inert gases are unaffected by the TGs. Because laboratory air contains 1% argon, during each TG backfill experiment the pressure in the experimental apparatus can only decrease by a maximum of 99%. As the TG sorbs more gas, its pumping speed slows considerably. In practice, changes in pressure below  $1 \times 10^{-5}$  Torr were difficult to measure even though the Baratron<sup>®</sup> resolution was  $1 \times 10^{-6}$  Torr, due to fluctuations in the Baratron<sup>®</sup> readout.

## 5.2. Data Analysis

Raw data from the TG experiments consisted of total pressure vs. time and was analyzed to determine the effects of the noninert gas partial pressure and quantity of gas sorbed

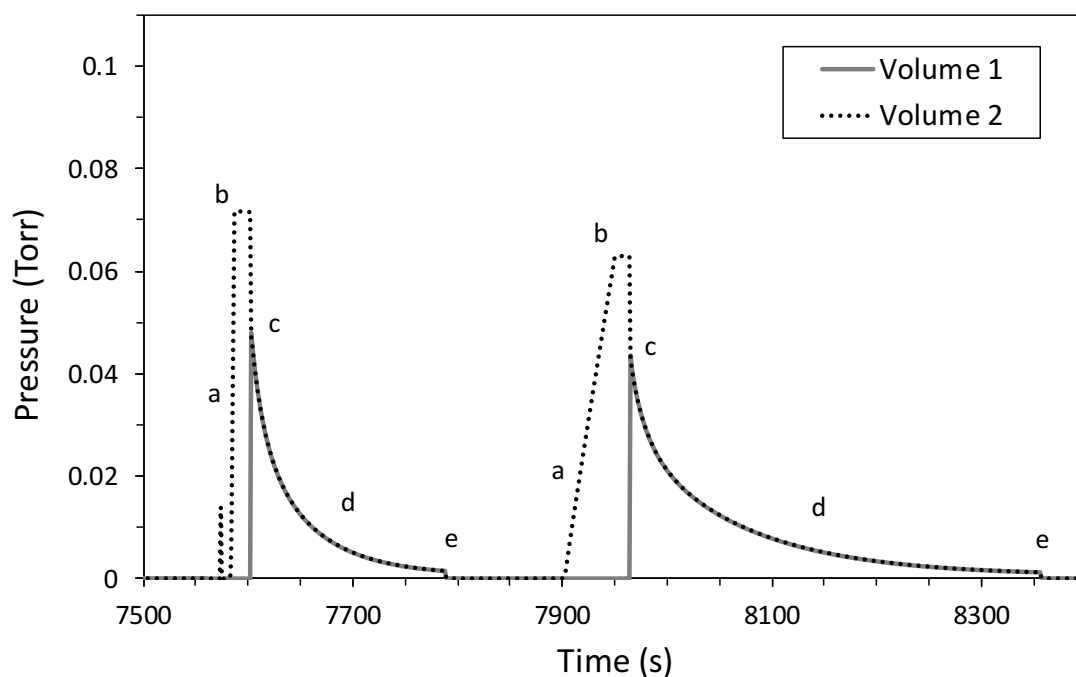


**Figure 5.4.** Example data from backfill experiments with TG 10383-1, showing the Baratron<sup>®</sup> pressure readings for both volumes of the experimental setup.

on TG pumping speed. Data from experiments with five TGs was ultimately analyzed. Figure 5.5 shows the range of noninert gas partial pressure and quantity of gas sorbed covered in the backfill experiments for one of the TGs tested (TG 10383-1). Data for the additional TGs tested is shown in Figures B.1 through B.4. Both the noninert gas partial pressure and quantity of gas sorbed covered several orders of magnitude for each TG tested.

Prior to analyzing the TG pumping data, background calculations were performed to determine the volume of the experimental chamber and to estimate the effective pumping speed of the turbo pump. This information was used to calculate the amount of gas sorbed by each TG during the cool down period following activation, as well as between individual backfill experiments. The raw data from each individual backfill experiment were then analyzed to determine the TG pumping speed at each time step, along with the corresponding noninert gas partial pressure and quantity of gas sorbed.

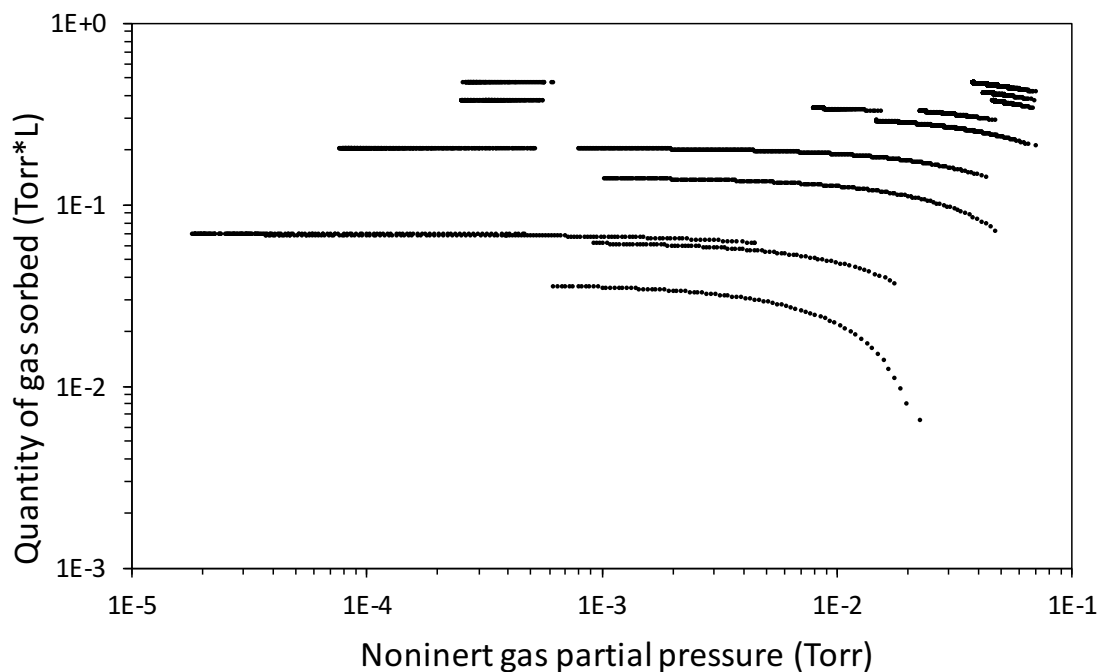


**Figure 5.5.** Range of noninert gas partial pressure and quantity of gas sorbed during back-fill experiments with TG 10383-1.

### 5.2.1. Background Calculations

Accurate measurement of the volume of the experimental apparatus was essential for correct analysis of the TG experiment data. The contribution of each piece of the experimental apparatus to the total experimental volume was carefully measured where possible and estimated where direct measurement was impossible. Details of these measurements and the calculation of the volume of the TG experimental apparatus are found in Appendix A. Two very similar experimental setups, referred to as setup (a) and setup (b), were employed for the TG experiments. The only difference between the two setups was an additional 2.75" CF nipple in setup (a). The volumes for the experimental setups were calculated to be 1.55 L for (a)<sup>1</sup> and 1.42 L for (b), both with an uncertainty of  $\pm 3\%$ .

<sup>1</sup>A miscalculation resulted in a value of 1.53 L being used to analyze the data from the TG backfill experiments. Due to the final uncertainty in experimentally determined TG pumping speeds (see Figure 5.14), which was not a result of the volume miscalculation mentioned here, but rather the variation in individual TG performance, the use of 1.53 L instead of 1.55 L was determined to be inconsequential.

To minimize the amount of gas sorbed by the TG outside of the pressure experiments, the experimental volume was actively pumped during tube activation, cool down, and between individual backfill experiments. To estimate the amount of gas sorbed by the TG during these times, the base pressure of the experimental volume before TG activation was compared to the pressure of the experimental volume after TG activation. This required finding the effective pumping speed of the turbo pump used in these experiments, which has a nearly constant pumping speed for pressures below about  $10^{-3}$  Torr. Pressures during TG activation and cool down, and in between individual pressure experiments, were usually  $10^{-5}$  Torr or lower.

The base pressure,  $P_{\text{base}}$ , of a vacuum chamber depends on the amount of gas entering and leaving the chamber. The amount of gas entering a chamber can be described as a throughput,  $Q_{\text{in}}$ , with units of Torr·L·s<sup>-1</sup>. During TG activation, cooldown, and between experiments,  $Q_{\text{in}}$  was assumed to result mainly from outgassing. The speed at which gas is removed from the system is the effective pumping speed  $S_{\text{effective}}$ , with units of L·s<sup>-1</sup>, and can be expressed as

$$S_{\text{effective}} = \frac{Q_{\text{in}}}{P_{\text{base}}}. \quad (5.1)$$

$Q_{\text{in}}$  was found by making pressure rate-of-rise (ROR) measurements with the chamber isolated from any pumping. In this case,  $Q_{\text{in}}$  is expressed as

$$Q_{\text{in}} = \frac{\Delta P}{\Delta t} V, \quad (5.2)$$

where  $\Delta P/\Delta t$  is the chamber pressure ROR and  $V$  is the chamber volume.  $S_{\text{effective}}$  was measured several times and then averaged, yielding a value of  $0.47 \pm 0.02$  L·s<sup>-1</sup>. This value was used to estimate the amount of gas sorbed by the TGs during the cool down period following activation and also between individual backfill experiments.

### 5.2.2. Gas Sorbed During Cool Down and Between Backfill Experiments

A TG begins to adsorb gas upon activation; this means that during the cool down period and between individual backfill experiments, the TG is sorbing gas. The chamber was actively pumped during these times to minimize the amount of gas taken up by the TG. To calculate the amount of gas sorbed by the TG during these periods,  $Q_{in}$  (with contributions from the chamber and TG itself) during activation is assumed to be similar to  $Q_{in}$  during the cool down period. Also,  $Q_{in}$  between individual TG backfill experiments is assumed to be comparable to  $Q_{in}$  at similar temperatures before TG activation.

Estimating the amount of gas sorbed by a TG during cool down and between individual backfill experiments begins with the pumping equation [*Chambers, 2005*],

$$Vdp = Qdt - Spdt. \quad (5.3)$$

$V$  is the experimental chamber volume,  $dp$  is the change in pressure,  $Q$  is a throughput (the gas load, due mainly to outgassing in this case),  $dt$  is the change in time,  $S$  is the effective pumping speed calculated in section 5.2.1, and  $p$  is the chamber pressure. Leaks in the experimental chamber are assumed to have a negligible contribution to  $Q$ . Indeed, throughout the course of the TG experiments there were no indications of leaks that would need to be taken into consideration for the calculations presented here. Equation 5.3 can be solved for  $Q$ , the gas load, to give

$$Q = V \frac{dp}{dt} + Sp. \quad (5.4)$$

(Note, as  $\frac{dp}{dt} \rightarrow 0$  equation 5.4 reduces to equation 5.1, which was used to find the effective pumping speed of the turbo pump.) Pressure data recorded before and during TG activation can be used to estimate  $Q$  at each time step.  $Q$  can then be plotted against the TG temperature during activation heating, as shown in Figure 5.6.

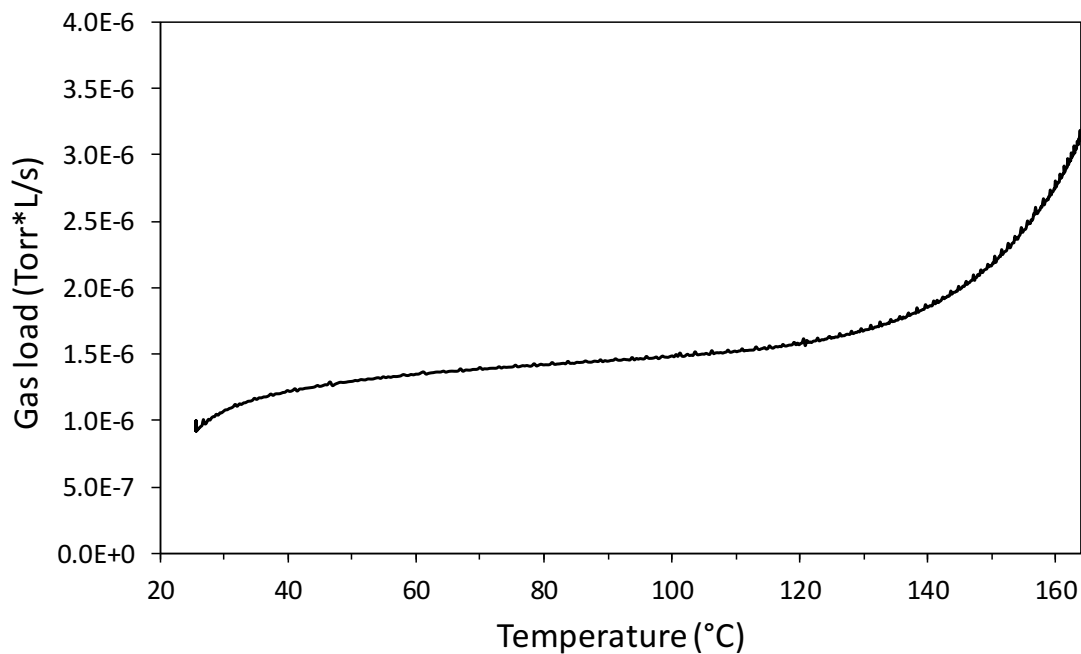


**Figure 5.6.** Gas load due to outgassing during the activation heating of TG 10383-1.

Applying equation 5.4 at each time step gives

$$Q_n = V \left( \frac{p_{n+1} - p_n}{\Delta t} \right) + (S_{\text{turbo}} + S_{\text{TG}}) p_n, \quad (5.5)$$

which can be applied to the cool down period after TG activation.  $S_{\text{turbo}}$  is the effective pumping speed of the turbo pump (equivalent to  $S_{\text{effective}}$  in equation 5.1), and  $S_{\text{TG}}$  is the pumping speed of the activated TG. The pressure at each time step is denoted by  $p_n$ . Solving for  $S_{\text{TG}} p_n \Delta t$  gives the amount of gas sorbed by the TG during time step  $n$  (in units of Torr·L),

$$S_{\text{TG}} p_n \Delta t = Q_n \Delta t - V (p_{n+1} - p_n) - S_{\text{turbo}} p_n \Delta t. \quad (5.6)$$

$Q_n$  is the gas load due to outgassing and is a function of temperature, determined from plotting  $Q_n$  versus temperature as shown in Figure 5.6. The time step,  $\Delta t$ , was 1 s for the TG experiments.

### 5.2.3. TG Pumping Speed Calculations

Section 5.1.2 describes the TG experiment procedure. As stated earlier, TGs do not pump inert gases (Ar and He, for example). The inert gas partial pressure for each TG backfill experiment was estimated to be 1% of the total pressure at the first time step of each individual experiment and was assumed to remain constant for the duration of each individual experiment. The TG pumping speed was calculated based on the noninert gas partial pressure in the experimental chamber. Equation 5.3 can be rearranged to give the TG pumping speed,

$$S_{\text{TG}} = \frac{Q}{p} - \frac{V}{p} \left( \frac{dp}{dt} \right). \quad (5.7)$$

In equation 5.7  $p$  represents the noninert gas partial pressure in the experimental chamber.  $Q$  is the gas load due to outgassing, discussed in section 5.2.2. Setting  $dp/dt = \Delta p/\Delta t$ , equation 5.7 becomes

$$S_{\text{TG}} = \frac{Q}{p} - \frac{V}{p} \left( \frac{\Delta p}{\Delta t} \right). \quad (5.8)$$

Writing  $\Delta p = p_{n+1} - p_n$  and  $\Delta t = t_{n+1} - t_n$  in equation 5.8 allows the TG pumping speed at time step  $n$  to be expressed as

$$S_{\text{TG}n} = \frac{Q_n}{p_n} - \frac{V}{p_n} \left( \frac{p_{n+1} - p_n}{t_{n+1} - t_n} \right). \quad (5.9)$$

Equation 5.6, using  $S_{\text{turbo}} = 0$  and  $p_n$  for the noninert gas partial pressure, is used to calculate the amount of gas sorbed by the TG at each time step. Altogether, this allows the TG pumping speed, amount of gas sorbed, and noninert gas partial pressure to be calculated at each time step.

## 5.3. Results

The experimental data from backfill experiments with five TGs was analyzed according to the methods described in section 5.2 to obtain the pumping speed over a range of

pressures and amounts of gas sorbed. The data from these TGs were averaged and used to create a database of pumping speeds over a range of pressures and amounts of gas sorbed. The database was then used in a vacuum performance model to estimate the pressure inside the SDL TOF-MS on a typical sounding rocket flight to the MLT for an instrument pumped by TGs (Chapter 6).

### 5.3.1. Results: Individual TG Pumping Speeds

Multiple backfill experiments were performed on each TG. Time and pressure data from these experiments were analyzed as outlined in section 5.2 to obtain the pumping speed versus noninert gas partial pressure and versus quantity of gas sorbed. Figure 5.7 shows the pumping speed versus noninert gas partial pressure for one of the TGs tested. Figure 5.8 shows the pumping speed versus quantity of gas sorbed for the same TG. Figures B.5 through B.8, and B.9 through B.12 show similar plots for the additional TGs tested in these experiments.

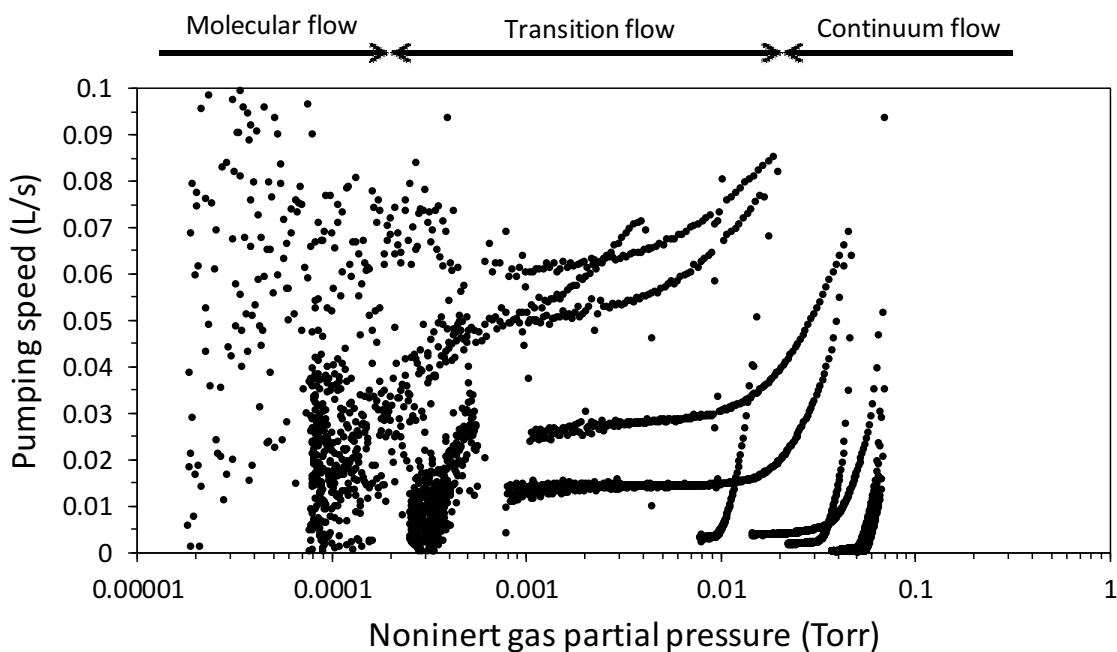


**Figure 5.7.** Pumping speed versus noninert gas partial pressure during experiments with TG 10383-1. Approximate flow regime boundaries are noted.

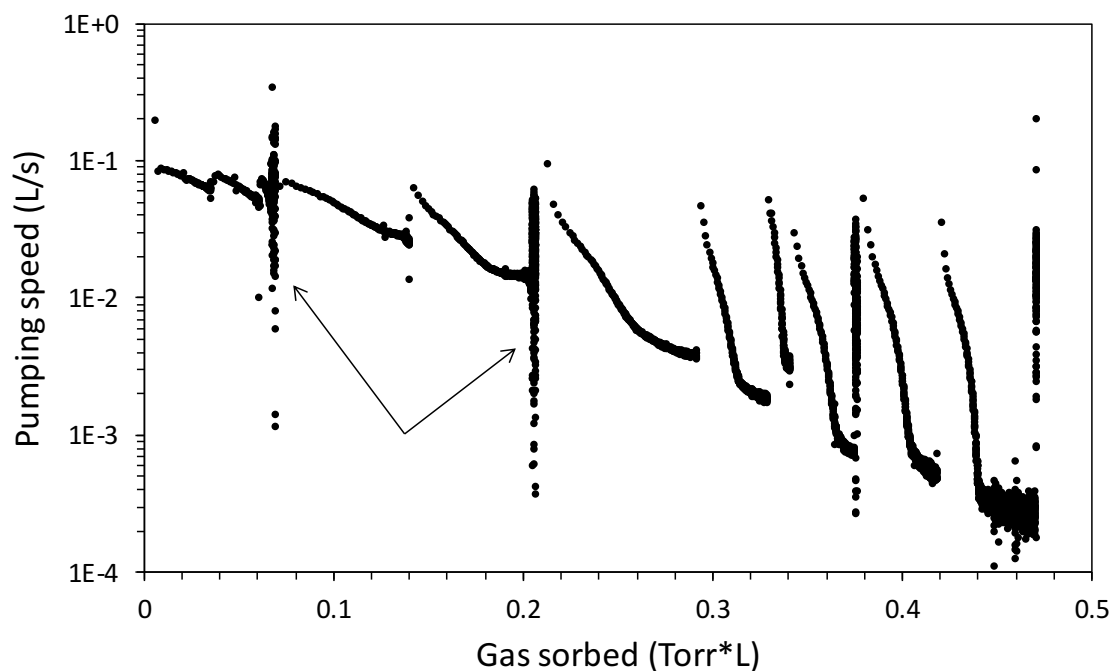


**Figure 5.8.** Pumping speed versus quantity of gas sorbed for TG 10383-1. Arrows denote two backfill experiments performed at pressures below  $10^{-3}$  Torr, for which the amount of gas sorbed did not change substantially.

Individual backfill experiment results presented in Figures 5.7 and B.5 through B.8 show a decreasing pumping speed as the noninert gas partial pressure decreases. However, no clear trend emerges when considering results from individual experiments for any particular TG. Figures 5.8 and B.9 through B.12 show TG pumping speed as a function of the cumulative amount of gas sorbed. In this case, the pumping speed appears to follow an exponential relationship with respect to the amount of gas sorbed. The pumping speed decreases as the amount of gas sorbed by the TG increases. This is expected, since less getter material is available to sorb gas as the amount of gas sorbed increases.

There is significant scatter in the calculated TG pumping speed at the lower end of the range of pressures tested (see Figure 5.7). These scattered points are not as apparent when the TG pumping speed is plotted against gas sorbed. The amount of gas being taken up at these points is small, and there is little separation between points on the gas sorbed axis in Figure 5.8. The vertical stack of data points near 0.07 Torr·L gas sorbed in Figure 5.8

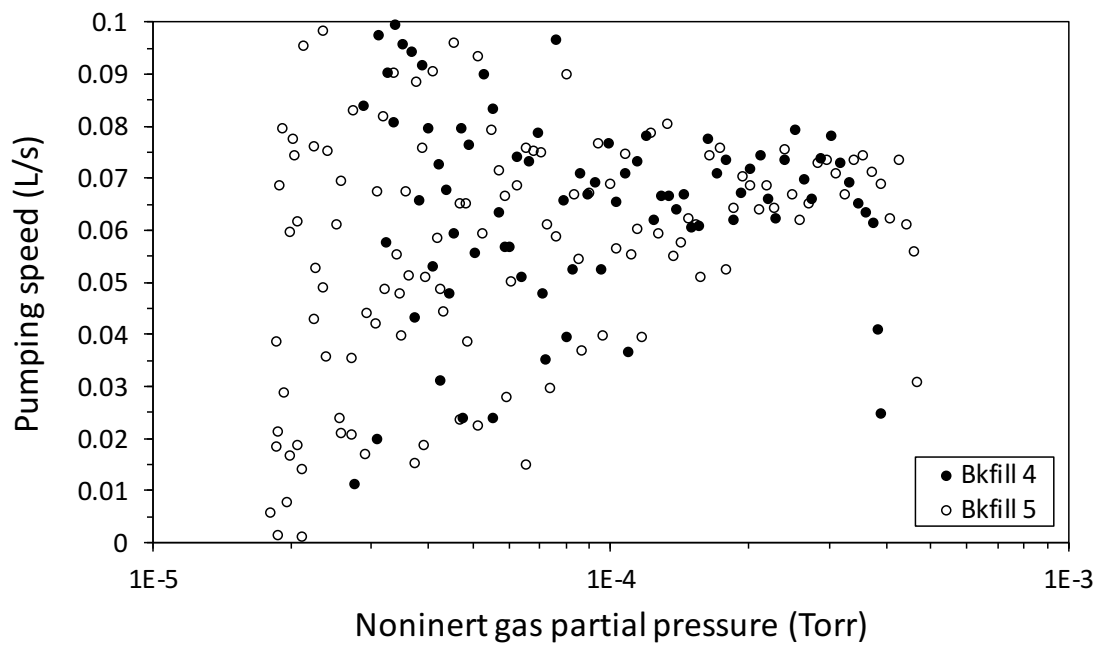
is a good example of this and corresponds to the pressure curve that flattens out at a tube speed of approximately 0.6 L/s in Figure 5.7. These data points are actually due to two separate backfill experiments, labeled backfill experiments 4 and 5, and are shown in detail in Figure 5.9. The average pumping speeds for backfill experiments 4 and 5 are 0.61 L/s and 0.59 L/s respectively, which is very similar to the speeds observed in adjacent backfill experiments.

### 5.3.2. Combined Data of Pumping Speed From Five TGs

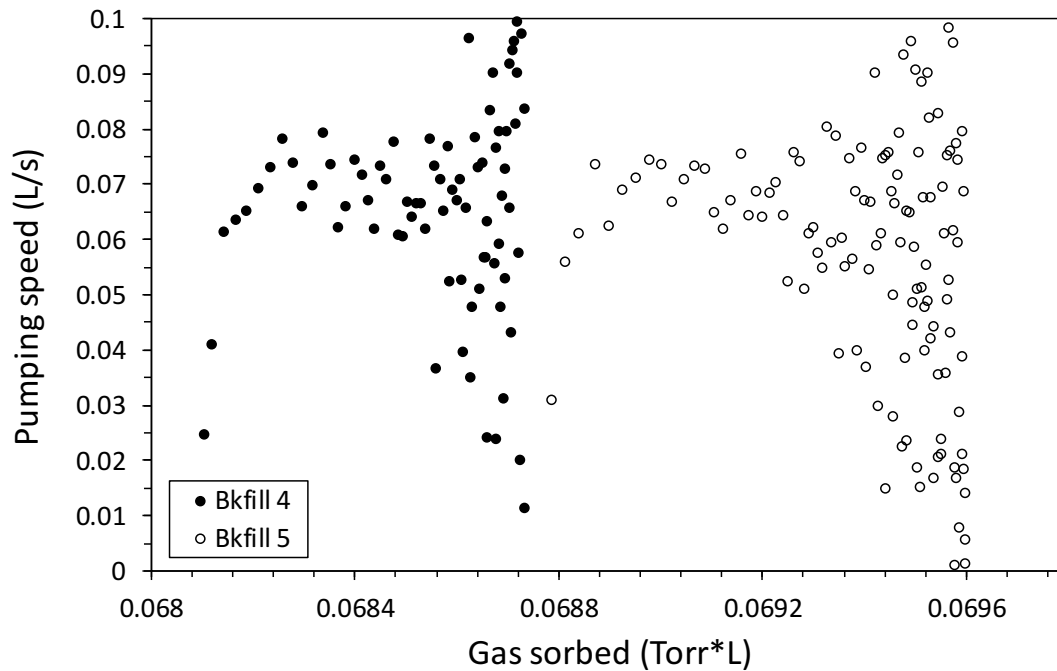
The goal of the TG pumping experiments was to determine the average pumping speed for a range of pressures and amounts of gas sorbed, and use this information in a computer model to simulate the pressure inside the SDL instrument for a typical MLT flight profile (see Chapter 6). This section discusses how experimental data from five TGs was combined to obtain average TG behavior.

Figures 5.5 and B.1 - B.4 show the range of pressures and amounts of gas sorbed during backfill experiments with each TG. Each data point in these figures has an associated pumping speed. The MATLAB<sup>®</sup> surface fit tool was used to fit the pumping speed data from each individual TG against both pressure and amount of gas sorbed. This was accomplished by taking the  $\log_{10}$  of both the pressure and amount of gas sorbed data to linearize the raw TG pumping speed data. The surface fit tool was then applied to the experimental data with:  $x = \log_{10}(P)$ , where  $P$  is the noninert gas partial pressure,  $y = \log_{10}(QS)$ , where  $QS$  represents the amount of gas sorbed, and  $z = TS$ , the pumping speed. A cubic interpolant was then used to perform a surface fit on data from each of five different TGs. The surface fit for TG 10384-3 is shown in Figure 5.10.

The region of the surface fit below the first individual backfill pressure experiment for each TG was influenced strongly by the first and last data points of the experiment. This led to sharp peaks and valleys in the interpolated pumping speeds that were inconsistent with the rest of the surface fit. These points were removed from the surface fits. In some



(a)



(b)

**Figure 5.9.** Pressure runs four and five for TG 10383-1, showing the scatter (at low pressures) in the experimentally calculated pumping speed.

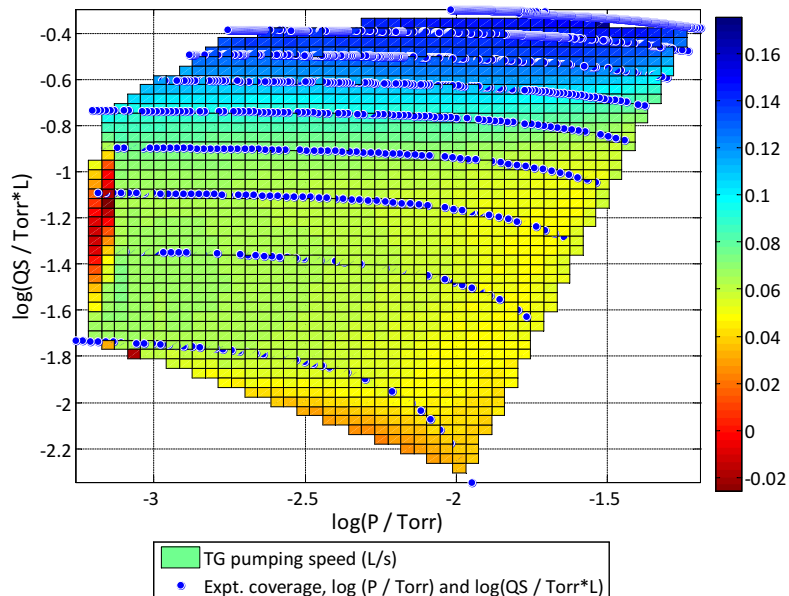


**Figure 5.10.** Surface fit of TG pumping speed versus noninert gas partial pressure and amount of gas sorbed for TG 10384-3. Note, the TG pumping speed (colormap shown) is plotted against  $\log(P)$  and  $\log(QS)$ . Therefore, the value  $-2$  on the  $\log(P)$  axis corresponds to a noninert gas partial pressure of  $10^{-2}$  Torr.

cases, the surface fit near the end points of individual backfill experiments exhibited peaks and valleys with extreme values compared to neighboring points, due to fluctuations in the calculated pumping speeds at low pressures. These regions were also removed. Figure 5.11 shows the surface fit for TG 10384-3 after removal of the fitted points discussed in this paragraph (compare to Figure 5.10). Similar steps were performed on data from all five TGs.

Data from five TGs were combined and averaged. First, a grid was set up, ranging from  $-5$  to  $-1$  for the  $\log(P)$  data, and from  $-2.5$  to  $0$  for the  $\log(QS)$  data. Next, the pumping speed at each point on the grid was interpolated for each TG based on its surface fit. The resulting average pumping speed was then calculated at each grid point. Pumping speeds were interpolated only, not extrapolated. Individual TGs contributed nothing to the average pumping speed for grid points outside their experimentally tested range. The resulting average TG pumping speed is shown in Figure 5.12; it covers a range of pressures from

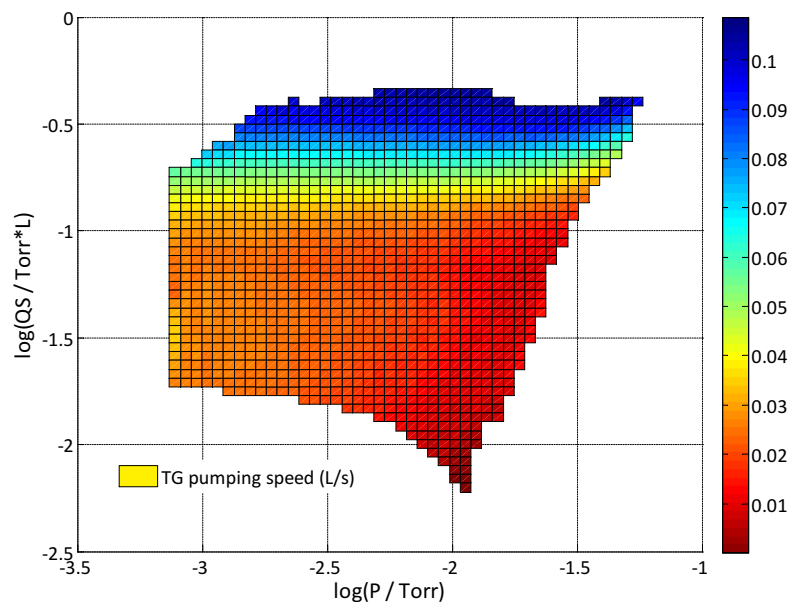


**Figure 5.11.** Surface fit of pumping speed for TG 10384-3, with inconsistent data points removed. Data point removal is discussed in section 5.3.2. This is otherwise the same surface as shown in Figure 5.10. Note that the colormap scale has changed significantly compared to Figure 5.10.

about  $4 \times 10^{-5}$  Torr to  $5 \times 10^{-2}$  Torr and amounts of gas sorbed from about  $6 \times 10^{-3}$  Torr·L to  $4 \times 10^{-1}$  Torr·L. This represents the data used later to model the instrument pressure (Chapter 6).

The number of data points used to calculate the average TG pumping speed at each grid point is shown in Figure 5.13. The random uncertainty in pumping speed at each grid point is shown in Figure 5.14. This uncertainty increases at larger values of amount of gas sorbed, rising to 70% at a few points. Generally, though, the pumping speed uncertainty is better than 30%. At points on the grid where data from only one TG is available, the uncertainty is undefined.

#### 5.4. Discussion and Conclusions

Prior to conducting the experiments described in this chapter, it was expected that both the noninert gas partial pressure and the amount of gas sorbed would significantly affect

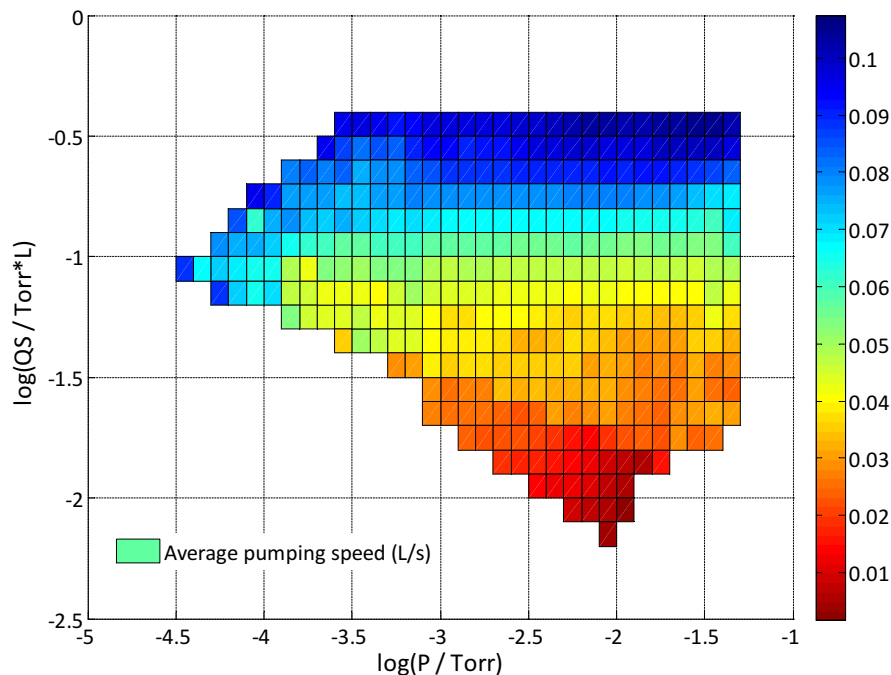


**Figure 5.12.** Average TG pumping speed, based on data from experiments with five TGs. The average TG pumping speed is plotted against  $\log(P)$  and  $\log(QS)$ .

TG pumping speed. These experiments, however, do not reveal any significant effect on pumping speed from the noninert gas partial pressure. The TG pumping speed for three constant values of quantity of gas sorbed is shown in Figure 5.15. At low pressures ( $<10^{-4}$  Torr) the pumping speed appears to decrease. However, it is difficult to support this conclusion due to the scarcity of data at these pressures combined with the large uncertainties in the rest of the data set.

Pumping speed versus quantity of gas sorbed, shown in Figure 5.16, exhibits an exponential trend at some constant pressures. The relationship between quantity of gas sorbed and TG pumping speed seems obvious, at least qualitatively; as gas molecules stick to the surface of the barium getter material, fewer sites are available to sorb gas molecules. Although diffusion of gas molecules into the bulk material may occur, making new sorption sites available on the barium surface, this process is slow at room temperature [Bloomer, 1957a, b; Hoffman et al., 1997; Verhoeven and van Doveren, 1982]. Thus diffusion of

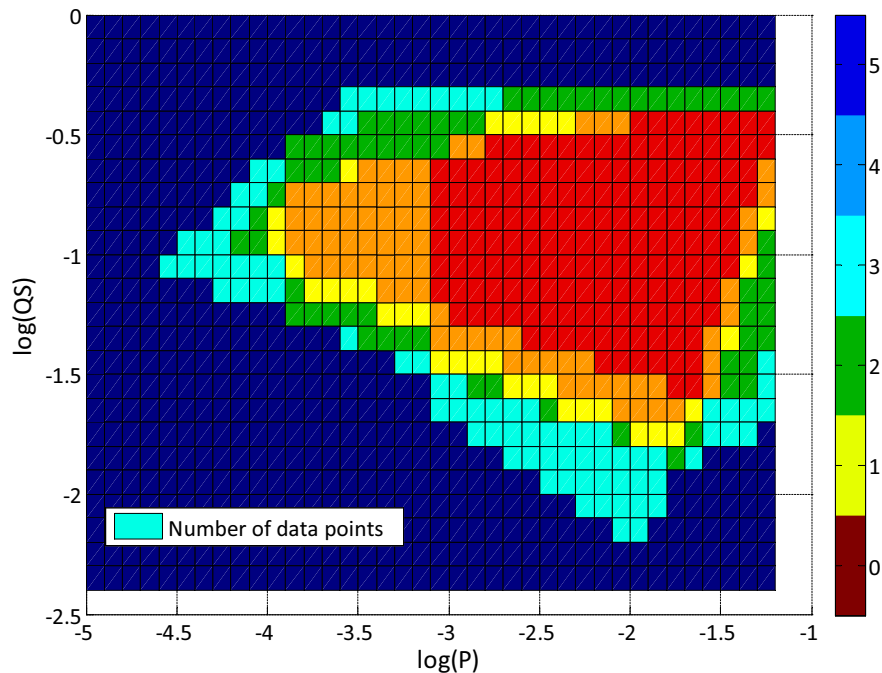


**Figure 5.13.** Number of data points used to calculate the average TG pumping speeds shown in Figure 5.12.

gettered gas into the bulk barium had a negligible effect on the TG backfill experiments and would also be of little consequence on the time scale (and temperature) of a sounding rocket flight.

It is appropriate at this point to compare results from the TG backfill experiments described here with pumping speeds quoted by the manufacturer. Data from plots in a product brochure were used to estimate TG pumping speeds for air,  $N_2$ , and  $O_2$ , and are shown in Figure 5.17 [Alvatec, 2014]. For comparison, the curve at  $1E-2$  Torr in Figure 5.16 is included in Figure 5.17. The manufacturer's experiments for air and  $O_2$  were conducted at  $7.5 \times 10^{-7}$  Torr, with a 1 g barium load. A 0.5 g barium load was used to test  $N_2$ , at a pressure between  $7.5 \times 10^{-7}$  and  $7.5 \times 10^{-5}$  Torr (the test pressure for  $N_2$  is not explicitly noted). Manufacturer pumping speeds were multiplied by 3 (6) for air and  $O_2$  ( $N_2$ ) to compare with the experiments described in this chapter, which used TGs with a 3 g barium load.

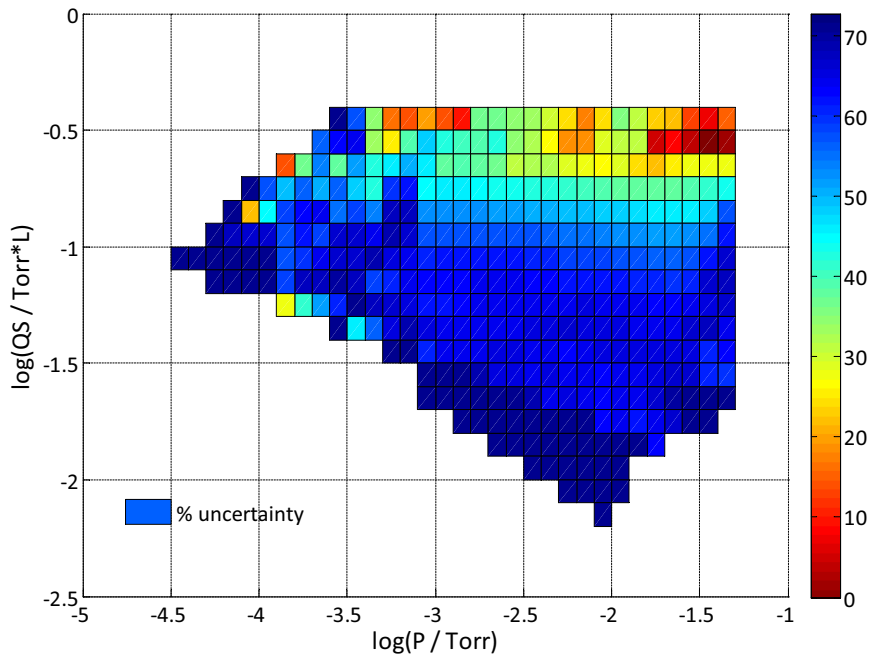


**Figure 5.14.** Random uncertainty, shown as a percentage, in the average TG pumping speeds shown in Figure 5.12. The dark blue represents points where experimental data from only one TG was available, resulting in an undefined uncertainty.

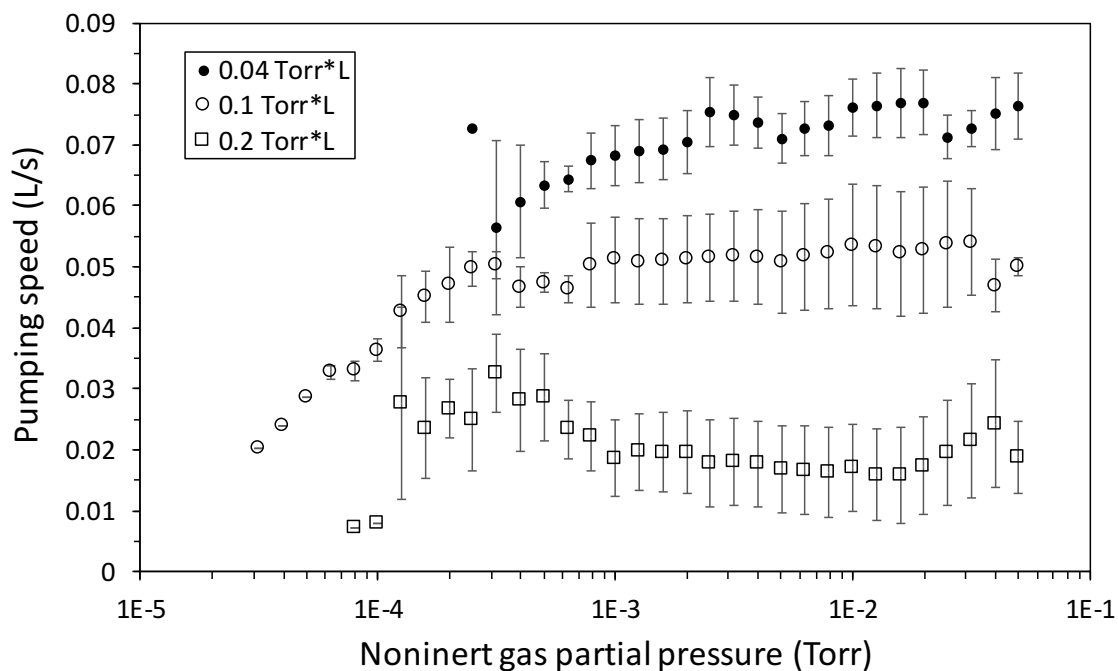


**Figure 5.15.** Average TG pumping speed versus noninert gas partial pressure for several constant amounts of gas sorbed.

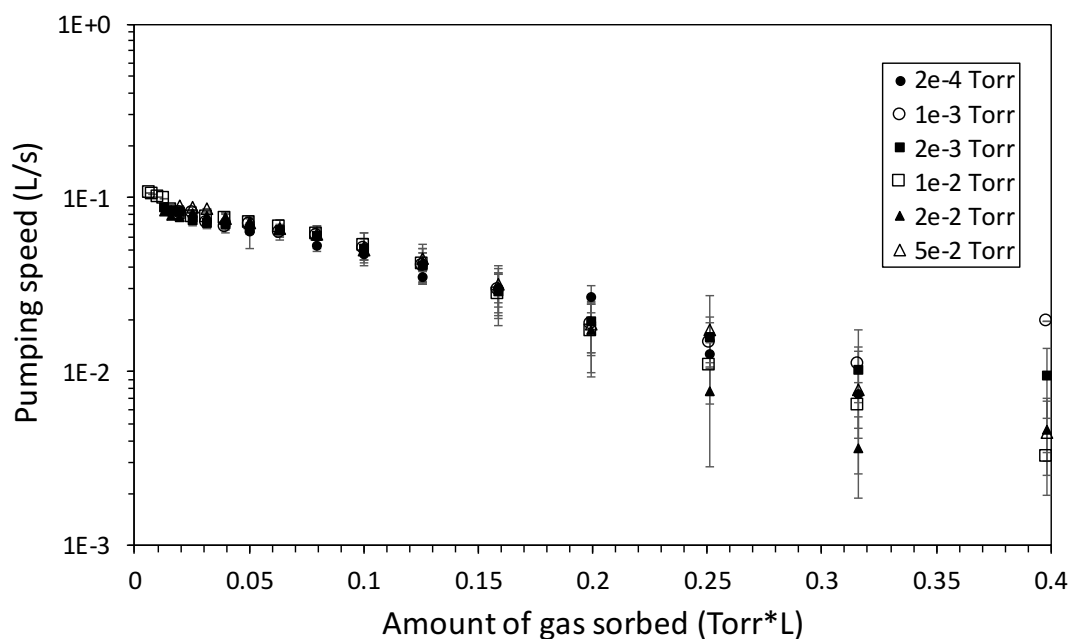


**Figure 5.16.** Average TG pumping speed versus amount of gas sorbed for several constant noninert gas partial pressures. The data exhibit an exponential trend.

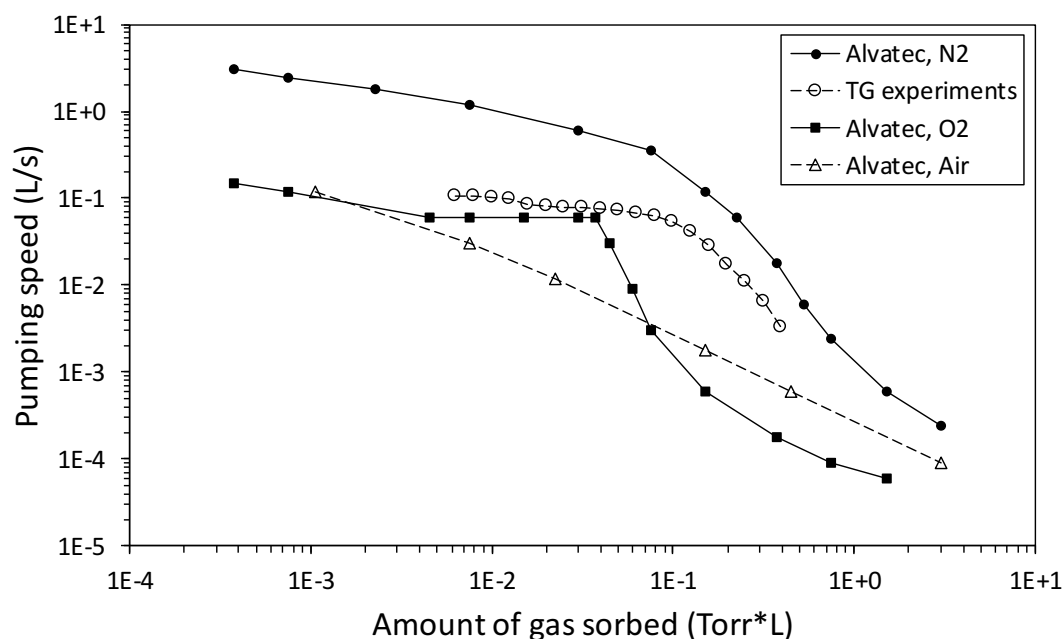


**Figure 5.17.** Comparison of experimentally derived TG pumping speeds with speeds quoted by the manufacturer. Pumping speeds quoted by the manufacturer [Alvatec, 2014] were taken at a pressure of  $7.5 \times 10^{-7}$  Torr, and have been adjusted to reflect the difference in barium loads between the TGs in the experiments described in this chapter and those quoted by the manufacturer.

The Alvatec curves in Figure 5.17 range over several orders of magnitude for any constant amount of gas sorbed shown in the plot. Interestingly, even though air is composed mainly of nitrogen and oxygen, the Alvatec curve for air differs from the curves for N<sub>2</sub> and O<sub>2</sub>. Results from the TG experiments described in this chapter, which were conducted with air, have good qualitative agreement with the manufacturer's curves in Figure 5.17. Additionally, pumping speeds from the TG experiments lie within the range of values from the Alvatec data. It is interesting to note that the TG experiment curve in Figure 5.17 was conducted at a pressure several orders of magnitude higher than the other curves, but still shows a similar pumping speed. This suggests that pressure does not have a large effect on pumping speed.

A database consisting of the TG pumping speed data shown in Figure 5.12 was used to simulate the SDL instrument pressure on sounding rocket missions (Chapter 6). These simulations showed that TGs have the potential to extend the range of the SDL instrument to lower altitudes by up to several kilometers. The simulations also showed that extending the range of pressures used in the TG backfill experiments to include the low 10<sup>-7</sup> Torr range would have been beneficial. However, resources were unavailable to repeat the experiments when this was realized.

Up to this point, the main focus on TGs has been as an active pumping method for the SDL TOF-MS on a sounding rocket mission. However, TGs are well suited for maintaining vacuum conditions in sealed volumes for long periods of time, and this was the original purpose for which they were intended [Londer *et al.*, 2007]. Whether or not TGs are used as an active vacuum system for rocket-borne instruments, they may well find a role maintaining vacuum during transport and storage of pressure sensitive instruments. They may also be used to maintain vacuum conditions in the SDL TOF-MS (or other instruments) while mounted on a rocket awaiting launch. In this vacuum maintenance role, TGs could reduce or eliminate the need for more sophisticated ground support equipment that would otherwise be required.

## CHAPTER 6

## BOW SHOCK AND INSTRUMENT PRESSURE MODELING

A bow shock – consisting of a region of enhanced density and temperature – forms in front of a sounding rocket traveling at supersonic speeds in the lower MLT [*Gumbel*, 2001a; *Bird*, 1988]. Interactions between reactive species in the bow shock and with instrument surfaces can result in anomalous measurements [*von Zahn*, 1967; *Offermann*, 1972; *Gumbel et al.*, 1999]. Additionally, mass and size-dependent flow discrimination have been shown to inhibit accurate sampling of ambient particles [*Hedin et al.*, 2007b]. Cryogenically cooled surfaces can be used to capture incident gas particles; *Brown et al.* [1970] demonstrated capture coefficients greater than 0.9 for gas particles incident on a 15 K surface. Cryogenics have been employed in rocket-borne mass spectrometer designs to eliminate the bow shock [*Offermann et al.*, 1981; *Offermann and Scholz*, 1973; *Krankowsky et al.*, 1979] and to reduce or eliminate reactions with instrument surfaces [*Offermann and von Zahn*, 1971; *Offermann and Tatarczyk*, 1973]. Cryopumps have also been used to provide suitable vacuum conditions for mass spectrometers in the MLT [*Zbinden et al.*, 1975; *Johannessen and Krankowsky*, 1972; *Narcisi et al.*, 1983; *Björn et al.*, 1985]. However, cryogenics add to the complexity of instrument design and operation.

Although cryopumps have been successfully used in rocket-borne mass spectrometers, additional methods are available to maintain suitable instrument operating pressures in the MLT. These include miniature turbomolecular pumps [*Ouyang and Cooks*, 2009; *Gao et al.*, 2008; *Creare*, 2016] and barium loaded TGs [*Londer et al.*, 2007]. In some cases, measurements of inert species can be conducted with no active pumping, using an instrument aerodynamically designed to minimize bow shock effects [*von Zahn et al.*, 1990]. Any of these methods would reduce the complexity of instruments and flight operations, allowing mass spectrometers and other instruments with stringent pressure requirements to successfully operate in the MLT without the need for cryogenic systems.

TOF instruments (described in Chapter 1) achieve mass separation by accelerating ions to a nominally uniform kinetic energy and then measuring the time required for them to transit a field-free drift region. Because collisions between ions and background gases in the drift region result in degraded resolution, it is desirable to minimize the number of these collisions [Schuerch *et al.*, 1994; de Hoffmann and Stroobant, 2007]. For an mfp of ten times the length of the drift region of a TOF-MS, at least 90% of ions will pass through without experiencing collisions. In this study, the term mfp requirement is used to denote the pressure at which the mfp is 1.5 m, which is ten times the drift length of the SDL instrument.

The study presented in this chapter was performed with an MCP based TOF-MS in mind. A search of the literature failed to find any reference to the use of an MCP detector in a mass spectrometer deployed to the MLT. Mass spectrometers used in rocket experiments in the MLT have typically used channel electron multiplier (CEM) detectors, which have less stringent pressure requirements than MCP detectors [Dickson *et al.*, 2013]. The advantages of an MCP based TOF-MS, which include the ability to measure multiple species simultaneously and make fast accurate measurements, make TOF-MS an attractive option for making *in-situ* measurements in the MLT. At lower altitudes (<95 km), where CEMs have obvious pressure operating advantages over MCP detectors, cryogenic removal of the bow shock is almost essential to accurately measure ambient species. In this case cryogenics can also be employed to pump the instrument volume without adding much complexity to the instrument design.

The SDL TOF-MS is designed to be adaptable and easily tailored to meet specific mission requirements. By taking into account mission requirements, pumping method, aperture size, and aperture opening altitude, the SDL instrument should be able to make measurements (in some cases) in the MLT without using cryogenics. The effects of pressure on the MCP detector used in the SDL instrument have been rigorously tested (Chapter 4). Additionally, the EDU has been successfully operated at pressures extending into the

$10^{-4}$  Torr range (section 4.2.4). These experiments have demonstrated the ability of SDL TOF-MS to successfully perform under some of the harsh pressure conditions likely to be encountered in the MLT. This chapter presents a study on the bow shock and instrument pressure for the SDL instrument.

## 6.1. Methods

The bow shock was modeled using the Direct Simulation Monte Carlo (DSMC) technique. An instrument pressure model (IPM) was developed to simulate the effects of different pumping methods on instrument pressure during a sounding rocket flight in the MLT. The model employs standard gas flow equations and incorporates results from bow shock modeling and the TG experiments from Chapter 5. Simulated pumping methods include a miniature turbo pump and barium loaded TGs. Additionally, instrument pressure for an un-pumped instrument was also simulated. Results from bow shock and instrument pressure simulations are presented in the context of making mass spectrometer measurements in the MLT without the use of cryogenics.

### 6.1.1. DSMC Simulations

The DSMC technique models gas flows by using simulated gas molecules instead of fluid flow equations. Each simulated molecule in DSMC represents a large number of real gas molecules. The positions and velocities of the simulated molecules are tracked; simulated particles also undergo collisions [Boyd, 2009a, b]. Flow characteristics are determined by sampling and averaging particle information over a large number of iterations [Boyd, 2009b]. DSMC is a well-established method for modeling the effects of high-speed sounding rockets in the MLT and also atmospheric entry [Gumbel, 2001a; Hedin *et al.*, 2007b; Bird, 1988; Gumbel, 2001b].

In this study DSMC simulations were performed to model the bow shock of the SDL TOF-MS for a typical rocket flight to the MLT. The DSMC method was invented by Professor Graeme Bird, and his DS2V program was used to obtain the results found here [Bird,

2005]. The standard MSIS-E-90 reference atmosphere was used to supply ambient atmosphere input parameters to the DS2V program [Hedin, 1991]. A nighttime autumn launch, from Poker Flat, AK, was assumed. Rocket flights were modeled for five apogees: 100, 120, 140, 160, and 180 km. In each case, the model was run at 5 km altitude intervals, beginning at 70 km. Rocket speeds at each interval were estimated assuming a vertical ballistic trajectory. The simulated instrument geometry was a cylinder, 5 cm in diameter, which represented the SDL TOF-MS sensor head. Diffuse reflection of particles from all surfaces, with full accommodation to the payload temperature (assumed to be 300 K), was applied in these simulations [Gumbel *et al.*, 1999; Horányi *et al.*, 1999].

The DSMC simulations were run to steady state, as indicated by a leveling off of the number of simulated molecules, and then allowed to continue in order to reduce noise in the simulation results [Boyd, 2009a]. Quantities of interest included number density, temperature, and mfp and were retrieved from the bow shock region of the simulations. Data from these simulations were sampled beginning at a point 0.1 mm in front of the instrument surface and continuing in a line normal to the instrument surface, extending beyond the bow shock. These data were used as input for the IPM and also to estimate ambient particle transmission through the bow shock. The Beer-Lambert law,

$$I = I_0 \exp\left(\frac{-x}{\lambda}\right), \quad (6.1)$$

can be used to calculate the fraction of particles that experience a collision after traveling a distance  $x$ .  $I$  is the intensity of a particle beam (with original intensity  $I_0$ ) after passing a distance,  $x$ , through a region with an mfp of  $\lambda$ . The transmission fraction of ambient particles through the bow shock was estimated by calculating the ratio  $I/I_0$  in equation 6.1, using the DS2V derived mfp at each sampled data point in the simulated bow shock.

### 6.1.2. Instrument Pressure Model

The IPM was developed using standard gas flow equations. The pumping equation can be expressed as

$$V \left( \frac{dP}{dt} \right) = Q_{in} - Q_{out}, \quad (6.2)$$

where  $V$  is the volume being pumped,  $P$  is the total pressure,  $t$  is time, and  $Q_{in}$  and  $Q_{out}$  are throughput values representing the amounts of gas entering and exiting the volume [Chambers, 2005; Lafferty, 1998]. The volume used in these simulations is 0.3 L, which is approximately the interior volume of the EDU. For this study,  $Q_{in}$  represents only the amount of gas entering the instrument through the sampling aperture; vacuum leaks and outgassing are assumed to be negligible.  $Q_{out}$  however, has two terms: one for gas removed from the instrument by a pump, the other for gas exiting the instrument volume through the aperture. Thus  $Q_{out}$  can be expressed as

$$Q_{out} = q_{out} + S \cdot P, \quad (6.3)$$

where  $q_{out}$  represents gas leaving the instrument through the aperture,  $S$  is the pumping speed, and  $P$  is the pressure inside the instrument. By using equation 6.3 and setting  $\frac{dP}{dt} = \frac{\Delta P}{\Delta t}$  in equation 6.2, the pumping equation becomes

$$\Delta P = \frac{\Delta t}{V} (Q_{in} - q_{out} - S \cdot P). \quad (6.4)$$

If  $\Delta t = t_n - t_{n-1}$  and  $\Delta P = P_n - P_{n-1}$ , and assuming that  $\Delta P$  is small, equation 6.4 can be expressed as

$$P_n = P_{n-1} + \frac{t_n - t_{n-1}}{V} (Q_{in} - q_{out} - S \cdot P_{n-1}) \quad (6.5)$$

to give the pressure  $P_n$  at time  $t_n$ .

The pumping equation can be solved analytically and used to check equation 6.5. In this case, the pumping speed is assumed to be constant [Lafferty, 1998]. Setting  $Q_{\text{out}} = S \cdot P$  allows equation 6.2 to be rearranged, giving

$$-\frac{dP}{P - \frac{Q_{\text{in}}}{S}} = \frac{S}{V} dt. \quad (6.6)$$

The left side of equation 6.6 is integrated from  $P_0$ , the initial pressure, to  $P$  at some later time. The right side of equation 6.6 is integrated from  $t_0 = 0$  to some later time,  $t$ . The result can be expressed as

$$P(t) = \frac{Q_{\text{in}}}{S} - \left( \frac{Q_{\text{in}}}{S} - P_0 \right) \exp\left(-\frac{S}{V}t\right). \quad (6.7)$$

Equation 6.7 was compared to equation 6.5 (with  $q_{\text{out}} = 0$ ), for  $P_0 = 0.01$  Torr,  $S = 4$  L/s,  $V = 0.5$  L,  $Q_{\text{in}} = 0.01$  Torr·L/s, and a time step of 0.01 s. Figure 6.1 shows the results of this comparison, including the percent difference between the numerical approximation and the analytic solution. For these conditions agreement between equations 6.5 and 6.7 was very close, with a maximum discrepancy of 2.5%.

The IPM solves equation 6.5 at each step  $n$  by considering the amount of gas entering the aperture, exiting the aperture, and actively pumped from the instrument interior if applicable. To model the effect of a turbo pump on the instrument pressure, a constant pumping speed of 4 L/s is used in equation 6.5. This value is based on a new pump intended specifically for space applications [Kline-Schoder, 2011; Creare, 2014]. To model the effect of TGs, results from laboratory experiments are used for  $S$  in equation 6.5 (see Chapter 5). For modeling the case of no active pumping,  $S = 0$  L/s in equation 6.5.

For most of the simulated rocket flight, gas flow through the aperture is in the molecular flow regime (Knudsen number,  $\text{Kn} > 1$ ) and traditional gas flow equations are used (see, for example [Chambers, 2005]). For the aperture diameters (0.1–2 mm) and altitudes (mini-

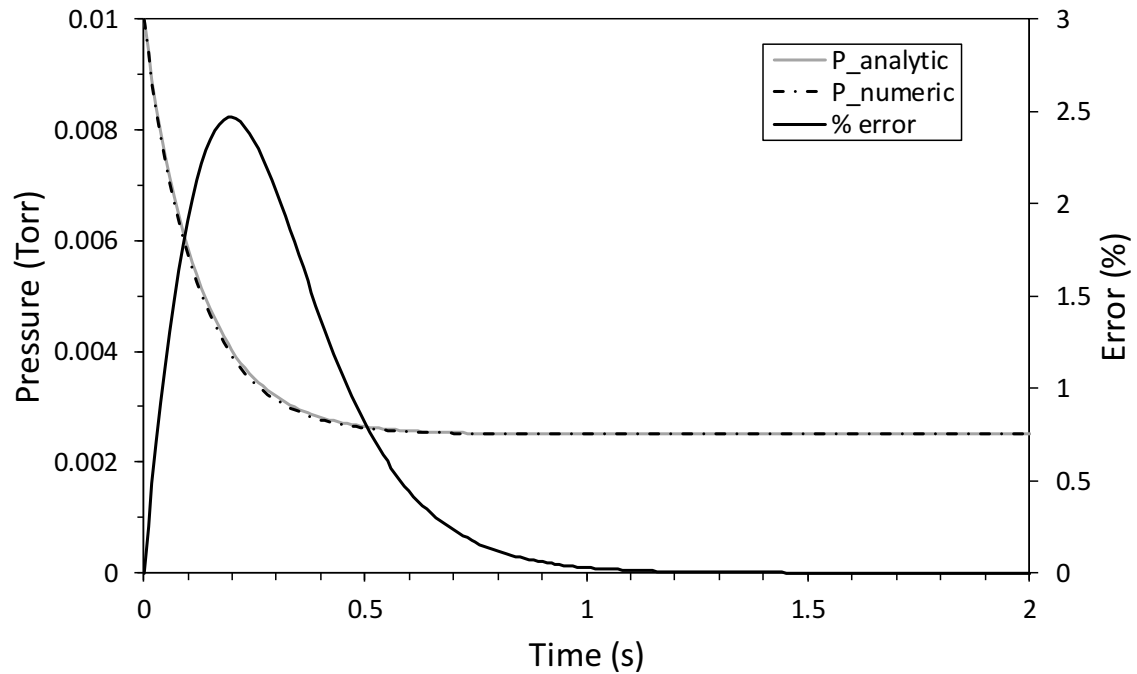


**Figure 6.1.** Comparison of the analytic solution (equation 6.7) of the pumping equation to the numerical approximation (equation 6.5) used in the IPM. See text for initial conditions.

imum 70km) modeled, flow through the aperture is never in the continuum flow regime ( $\text{Kn} < 0.01$ ). At lower altitudes however, the modeled bow shock (see section 6.2.1) is dense enough that the gas flow through the aperture is in the transition regime ( $0.01 < \text{Kn} < 1$ ).

Gas flow calculations in the transition regime present a unique difficulty in that neither the traditional continuum nor molecular flow equations accurately describe the situation. The method set forth by Livesey is employed in the IPM to calculate gas flow through the aperture in the transition flow regime [Livesey, 2001]. Livesey combines the continuum and molecular throughput equations, along with a factor based on  $\text{Kn}$ , to calculate the throughput in the transition regime according to the equation

$$Q = Q_c + \frac{Q_m}{1 + \phi(\text{Kn})}. \quad (6.8)$$

$Q_c$  and  $Q_m$  in equation 6.8 are the traditional throughput equations for the continuum and

molecular flow regimes [*Chambers, 2005*]. The factor,  $\varphi(\text{Kn})$ , is given by

$$\varphi(\text{Kn}) = \frac{k}{\text{Kn}}, \quad (6.9)$$

where  $k = 3\pi/128$  and Kn is “calculated at the mean pressure across the duct” [*Livesey, 2001*]. The IPM evaluates flow conditions at the aperture for each time step to determine whether the flow is in the transition or molecular flow regime and applies the appropriate flow equations.

At altitudes below 110 km, bow shock effects are not negligible. At these altitudes the bow shock is assumed to be stationary with respect to the instrument, and  $Q_{in}$  in equation 6.5 is calculated using bow shock number densities and temperatures retrieved from DSMC simulations (see section 6.1.1). In cases where the bow shock number density is low enough that the flow through the aperture is molecular, flow through the aperture is calculated using the particle flux on the instrument surface from DSMC simulations. At higher altitudes, above about 110 km, bow shock effects are negligible with respect to the incoming particle flux. Here the DSMC derived flux agrees very closely with flux calculations assuming a Maxwellian gas drifting at the rocket velocity (see Figure 6.7), which is used to determine  $Q_{in}$  in equation 6.5.

For the IPM, all gas particles entering the instrument are assumed to accommodate to an instrument temperature of 300 K [*Gumbel et al., 1999; Horányi et al., 1999*]. Number densities and partial pressures for the major gas species are tracked individually for two main reasons: first, and most importantly, inert gases are unaffected by the TGs; second, the flux of particles on a surface (e.g., entering or exiting the aperture) is dependent on particle mass. When modeling the pumping action of TGs on instrument pressure, it is assumed that all noninert gases are pumped at the same speed (i.e., the TGs are assumed to act on all noninert gases equally). In this case the simulated pumping speed is derived by interpolating experimentally determined pumping speeds at each time step and depends

on the instrument pressure and the total amount of gas sorbed by the TGs. A speed limit of 0.1 L/s per TG is imposed in the IPM to avoid overestimating TG pumping capabilities. The speed limit is reasonable, considering the data shown in Figure 5.12. For instrument pressures and quantities of gas sorbed that lie outside the experimental data range (see Figure 5.12) the IPM simply applies the last pumping speed used.

The initial pressure spike that occurs at aperture open represents the largest potential error in the IPM. Here the difference between the instrument and ambient pressures is greatest. The IPM was run with decreasingly smaller time steps and for different aperture sizes to observe the modeled initial pressure spike. The largest variation in initial pressure spike occurred for a simulated 2.00 mm diameter aperture with a 4 L/s pumping speed (simulating a turbo pump). The magnitude of the initial pressure spike quickly converged to 0.192 Torr as the time step decreased (Figure 6.2). Figure 6.2 also shows, as a percentage, the difference between the simulated initial pressure spike for a 1  $\mu$ s time step and the larger time steps simulated. Figure 6.3 shows the computation time required to run the simulation for several different time steps. Ultimately, a step size of 0.01 s was used in the IPM to produce the results given later in this chapter. This step size yielded a maximum pressure spike that was within 1% of the maximum pressure spike for a time step of 1  $\mu$ s, and it also allowed the IPM to run in a reasonable amount of time (1 - 2 minutes per run). Throughout the rest of the model (i.e., after the initial pressure spike) the discrepancy between pressures for different time steps is much less. This level of error is negligible compared to model input uncertainties (e.g., DSMC results and natural atmospheric variations) and the pressure during the simulated rocket flight, which ranged over several orders of magnitude.

### 6.1.3. Instrument Operational Pressure Limits

Two operational pressure limits for the SDL TOF-MS are referred to in this chapter. The mfp limit relates to the mfp of particles inside the instrument. The mfp limit used here is 10 times the field-free drift length, for which 90% of sampled ions should experience no

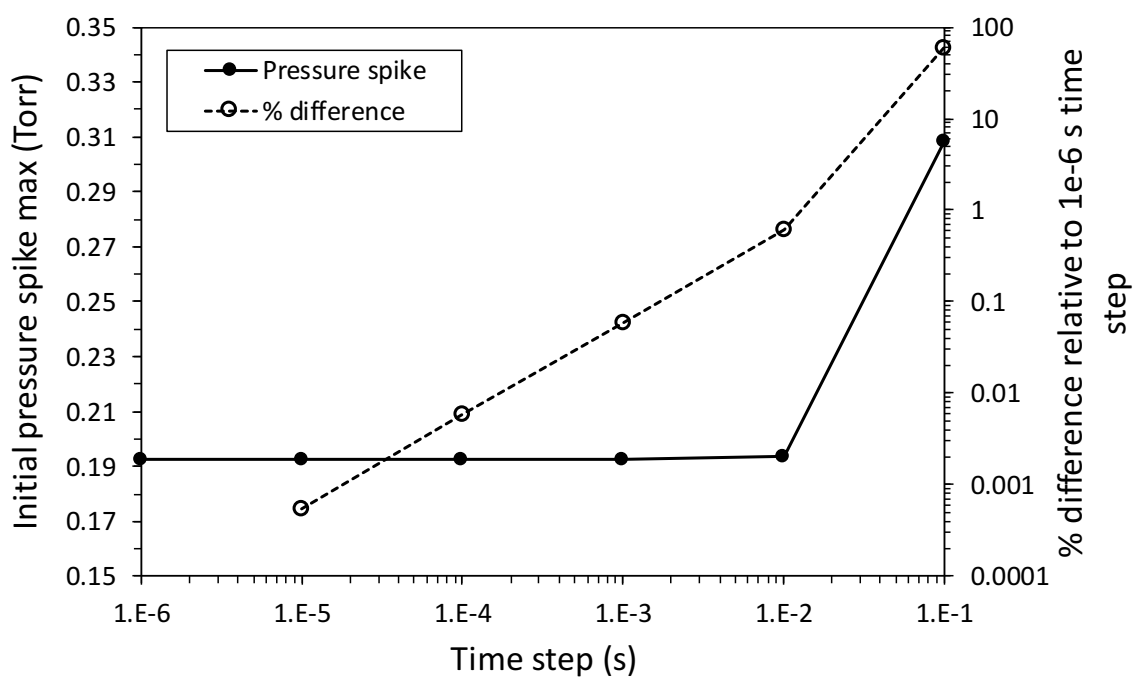


**Figure 6.2.** Convergence of the IPM, based on the initial pressure spike for time steps ranging from 1  $\mu$ s to 0.1 s. Also shown is the percent difference in the pressure spike at each time step size, compared to the pressure spike with a 1  $\mu$ s time step.

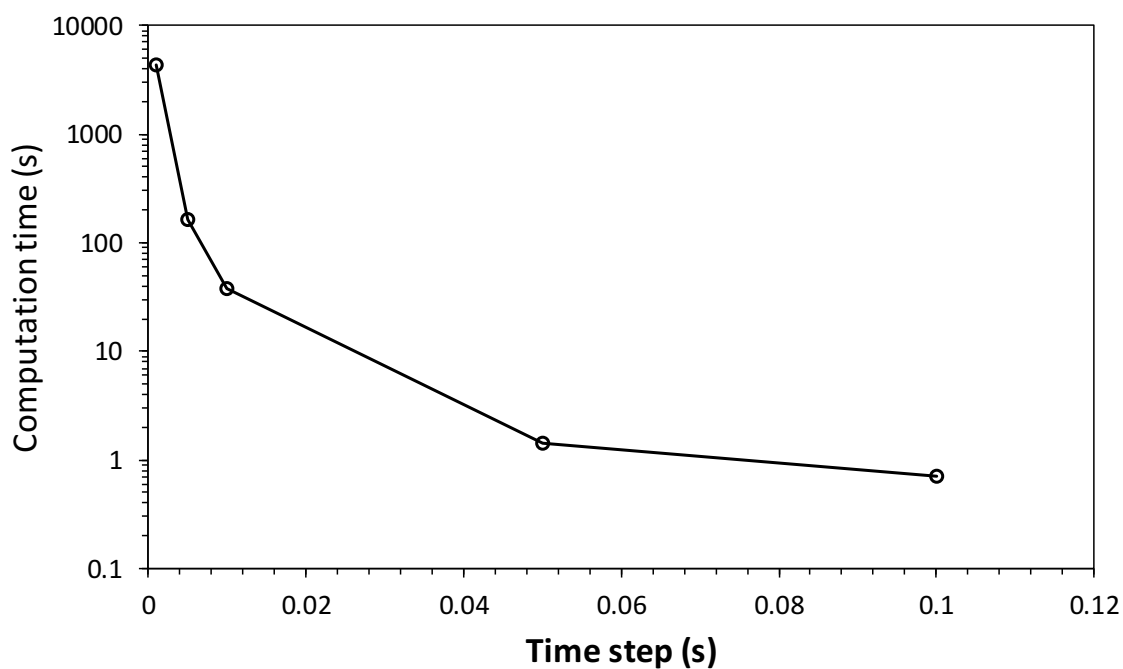


**Figure 6.3.** Computation time required to run the IPM at different time step sizes, assuming aperture open at 70 km.

collisions as they transit the drift region (see equation 6.1). For the SDL instrument, which has a field-free drift length of 15 cm, the mfp limit is met for instrument pressures below  $3.5 \times 10^{-5}$  Torr at a temperature of 300 K. The mfp limit was also calculated assuming gas composition similar to air at sea level; although mfp is species dependent, deviations are assumed to be small for the IPM. Certainly, a variation of the SDL TOF-MS with a longer drift length (reflectron design, for example) would require a lower operating pressure to meet the mfp requirement. The pressure limit relates to the pressure at which the SDL TOF-MS detector can operate. Experiments with the MCP detector used in the EDU are described in Chapter 4. During these experiments, the EDU was successfully operated at a pressure of  $2 \times 10^{-4}$  Torr, at count rates of  $\sim 100$  kcounts/s. This is the pressure limit used in this chapter. The pressure limit does not depend on the dimensions of the instrument and is an order of magnitude higher than the mfp limit.

## 6.2. Results

Bow shock simulations are presented first. These simulations were conducted to estimate the number density and temperature enhancements in the bow shock, as well as the particle flux on the ram surface of the instrument. The results of these simulations were used as inputs for the IPM at altitudes where bow shock effects are non-negligible. At higher altitudes, where bow shock effects can be ignored, particle flux is directly calculated assuming a Maxwellian gas drifting at the rocket velocity. Results based on instrument pressure profiles obtained from the IPM are then presented. These results show the instrument pressure effects of critical parameters, such as the opening altitude of the sampling aperture, aperture size, and pumping method.

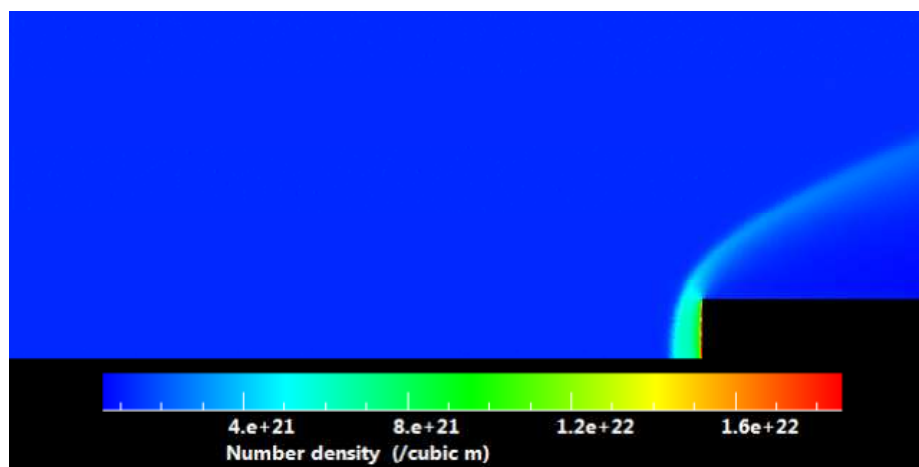
### 6.2.1. DSMC modeling of the bow shock

The DS2V program, from *Bird* [2005], was used to model the bow shock of the SDL TOF-MS on a sounding rocket at altitudes from 70 km to 155 km at 5 km intervals. The simulated apogee was 160 km. Figure 6.4 shows the modeled bow shock number den-

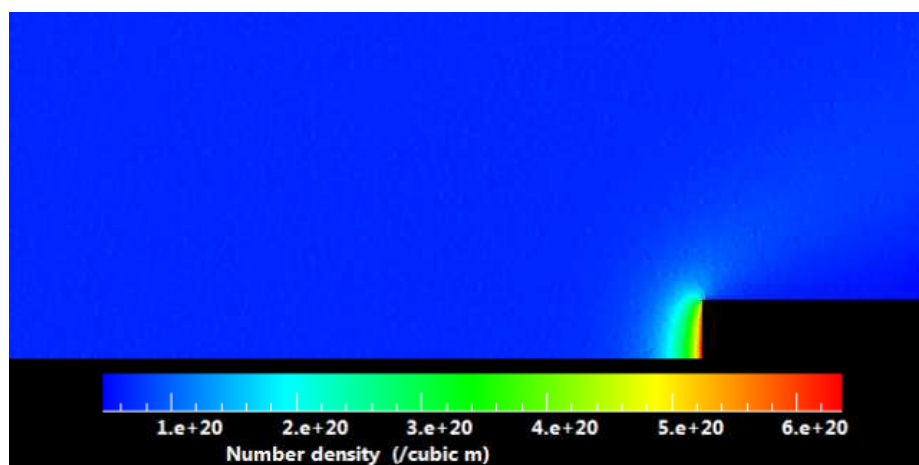
sity at 70 km, 90 km, and 130 km. Figure 6.5 shows the modeled bow shock temperature at these same altitudes. At 70 km the bow shock is well defined and spatially thin but dense. Higher altitudes correspond to lower ambient number densities and rocket speeds, but higher temperatures (above the mesopause). At increasing altitudes, the bow shock becomes less defined for all simulated apogees; it extends out further beyond the ram surface of the instrument and decreases in density. Bow shock densities and temperatures in this chapter are described in terms of enhancement factors, which are here defined as  $x/x_0$ , where  $x$  represents a parameter value in the bow shock, while  $x_0$  represents the ambient value of the same parameter. Number density and temperature enhancement factors from these simulations were retrieved at locations near the instrument sampling aperture on the DSMC models. These factors are shown in Figure 6.6, from 70 - 155 km.

The bow shock also affects the particle flux on the ram surface of a rocket-borne instrument. At lower altitudes, intermolecular collisions in the bow shock are frequent, and the particle flux is retrieved from DSMC simulations for use in the IPM. At higher altitudes bow shock effects become small, and collisions between particles in the bow shock are less frequent. Here the particle flux can be calculated using kinetic theory, assuming a gas with a Maxwellian velocity distribution drifting at the rocket velocity. Figure 6.7 compares the particle flux on the front instrument surface from DSMC simulations with the particle flux calculated using kinetic theory and assuming no bow shock effects. For altitudes of 105 km and above, the DSMC flux and the flux calculated using kinetic theory differ by 1% or less. Above 105 km, the bow shock mfp is large enough that very few incoming particles experience collisions before reaching the instrument surface. Below 110 km, the IPM uses data from DSMC simulations to calculate the amount of gas entering the instrument. Above 110 km, the IPM calculates the amount of gas entering the instrument using kinetic theory.

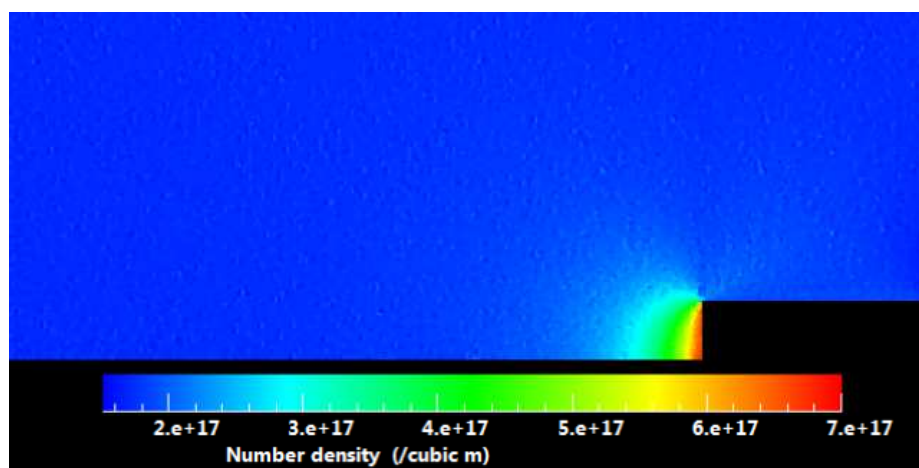
Collisions and interactions between particles in the bow shock can result in measurements that do not accurately represent actual ambient conditions. Particle transmission,



(a)

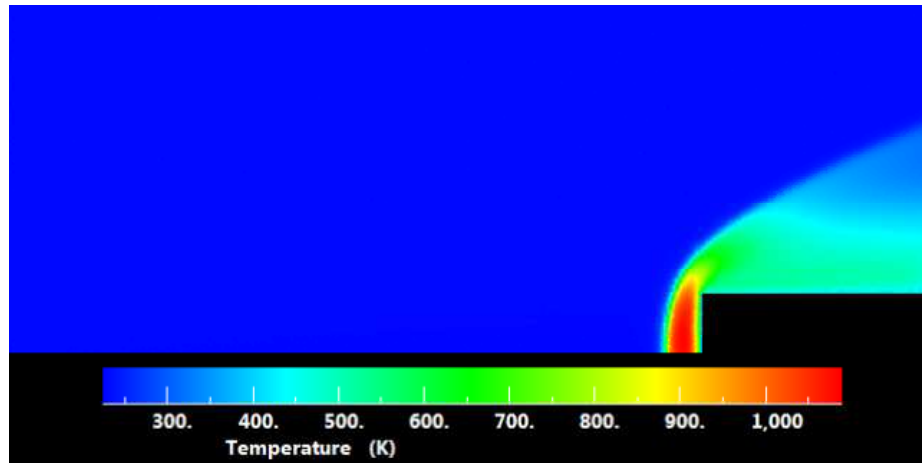


(b)

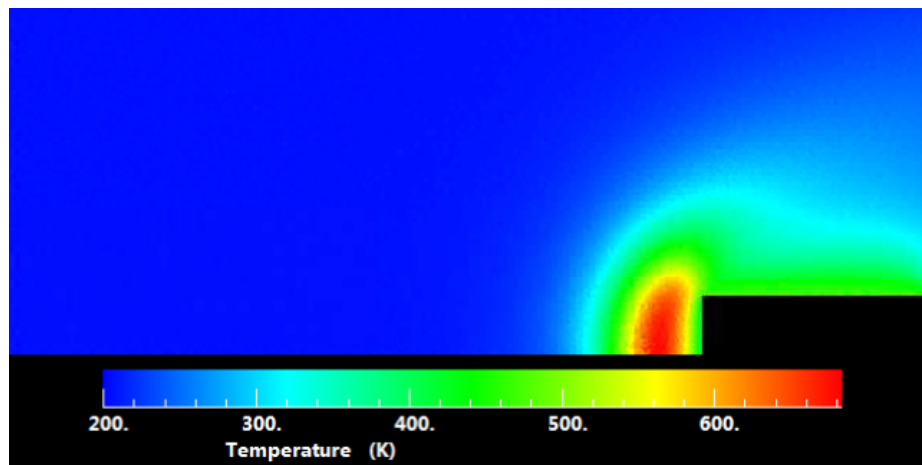


(c)

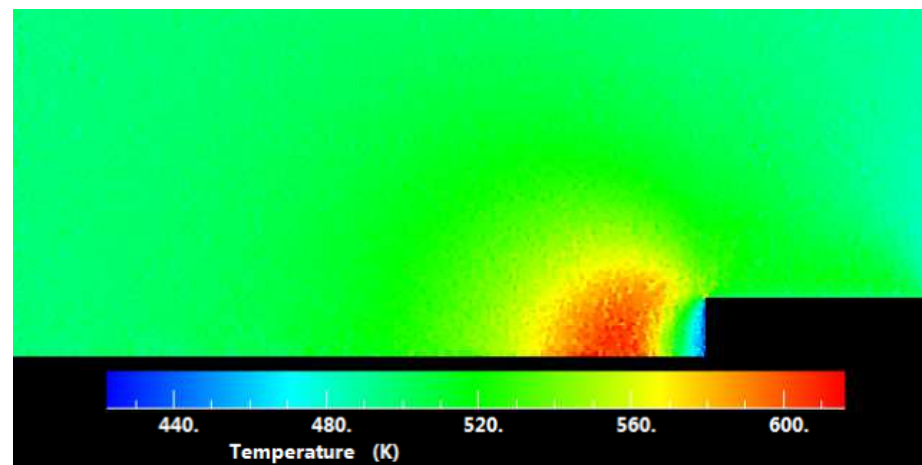
**Figure 6.4.** Bow shock number density, from DSMC simulations of the SDL TOF-MS for an apogee of 160 km. Altitudes represented are (a) 70 km, (b) 90 km, and (c) 130 km.



(a)



(b)



(c)

**Figure 6.5.** Bow shock temperatures, from DSMC simulations of the SDL TOF-MS for an apogee of 160 km. Altitudes represented are (a) 70 km, (b) 90 km, and (c) 130 km.

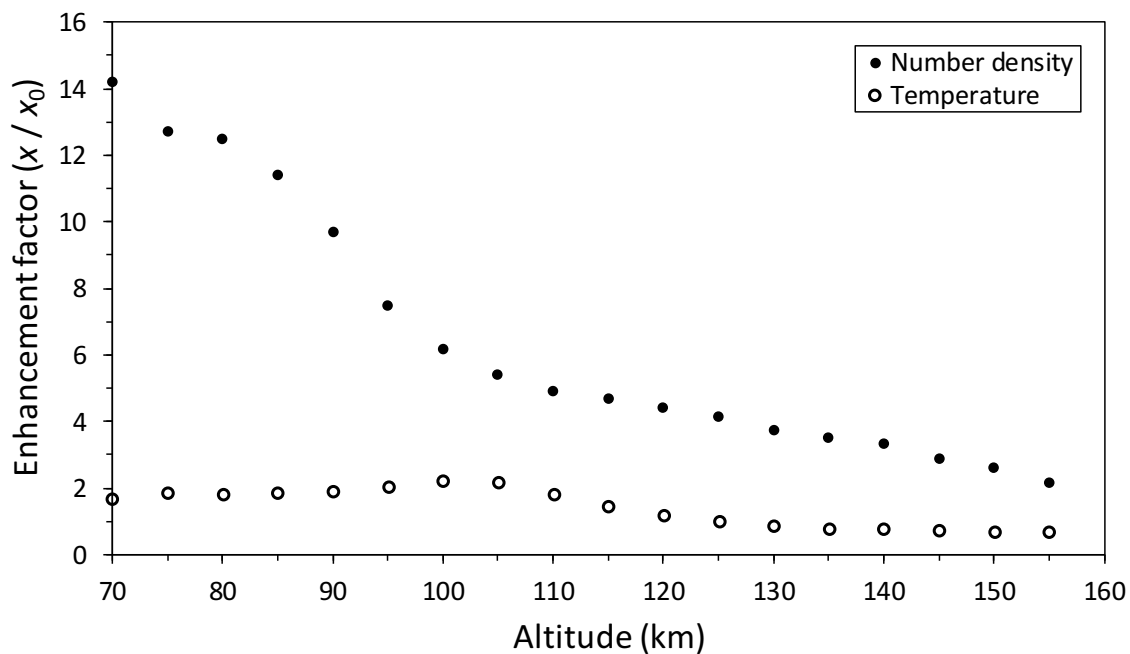


**Figure 6.6.** Bow shock enhancement factors for number density and temperature due to high speed rocket flight through the MLT. From DSMC simulations of the SDL TOF-MS, assuming a 160 km apogee.

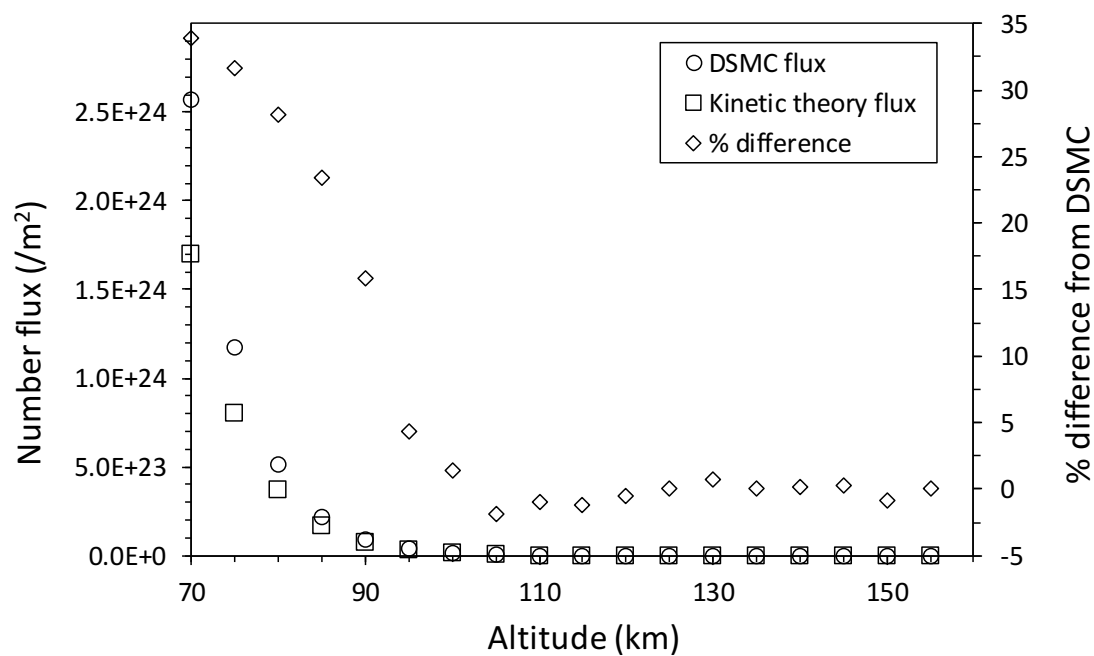


**Figure 6.7.** Particle flux for a 160 km apogee. Comparison of particle flux retrieved from DSMC simulations with particle flux calculated using kinetic theory.

defined here as the fraction of ambient particles that travel through the bow shock and reach the instrument aperture without experiencing collisions, can be calculated using the Beer Lambert law (equation 6.1) as described in section 6.1.1. The particle transmission for rocket apogees of 100 km, 120 km, 140 km, 160 km, and 180 km, based on results from DSMC simulations, is shown in Figure 6.8. At low altitudes (70 km), the transmission fraction is zero. No particles reach the instrument aperture without experiencing bow shock collisions. At higher altitudes, the bow shock mfp becomes larger and some ambient particles reach the instrument aperture without experiencing any collisions in the bow shock. The transmission fraction reaches 90% at an altitude of about 112 km.

### 6.2.2. Instrument pressure

Factors that affect instrument pressure during a rocket flight include the sampling aperture size, altitude at which the aperture is opened, and speed at which the instrument volume

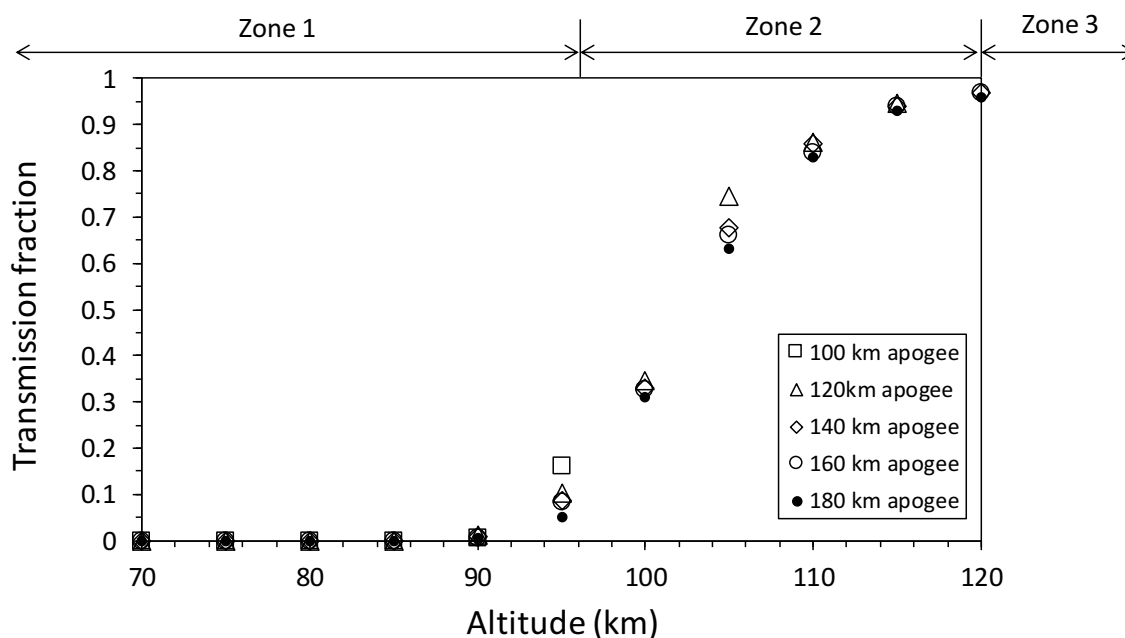


**Figure 6.8.** Particle transmission through the bow shock (i.e., fraction of ambient particles that pass through the bow shock without experiencing collisions). Zones 1, 2, and 3 are discussed in section 6.3.

is pumped. The IPM was used to simulate instrument pressure for aperture sizes of 0.1, 0.5, 1.0, and 2.0 mm, and aperture open altitudes between 70 and 160 km. The model uses an initial instrument pressure of  $10^{-6}$  Torr for an instrument pumped with a miniature turbo pump. An initial pressure of  $10^{-5}$  Torr is used for both an instrument pumped with TGs and an instrument with no active pumping. In reality, an active getter would probably be used in an instrument with no active pumping to maintain vacuum before launch, but the IPM makes no further assumptions for prelaunch pumping or pressure. All plots, figures, and data in this section were produced using the IPM, assuming a ballistic trajectory with a 160 km apogee and no horizontal motion. For reference, altitude vs. time for this trajectory is shown in Figure 6.9.

The pressure curves shown in Figure 6.10 are the result of IPM simulations of an SDL instrument with no pumping and an aperture open altitude of 90 km. This set of curves displays several notable features. When the aperture opens, there is a sharp pressure increase, which occurs regardless of the simulated aperture size. In this example the pressure

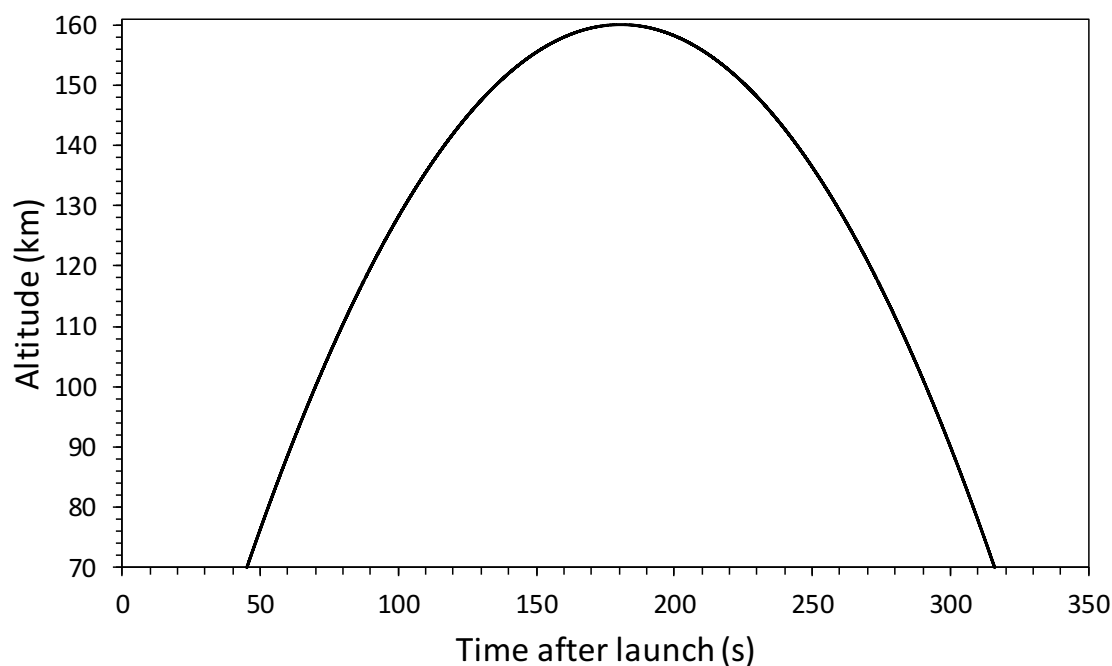


**Figure 6.9.** Altitude vs. time for a 160 km ballistic trajectory.

curve for a 0.1 mm aperture exhibits a much smaller pressure spike than the other simulated aperture sizes. However, a small aperture limits both the gas entering and exiting the instrument, and the pressure for an instrument 0.1 mm diameter aperture does not meet the pressure limit. Ultimately, the larger aperture sizes result in lower pressures. The initially puzzling result that the pressure curves for the 1.0 and 2.0 mm apertures in Figure 6.10 dip below ambient pressure has a simple explanation. The lower density gas at high altitudes has a higher temperature, and hence, a higher pressure, than the gas inside the instrument, which is assumed to accommodate to 300 K (section 6.1.2).

Instrument pressure is also strongly affected by pumping method. Figure 6.11 shows IPM simulation results for two pumped (miniature turbo pump, and eight TGs) and one unpumped instrument, all with a 0.1 mm diameter sampling aperture opening at 90 km. In this case, the curve for the instrument without any pumping (same curve as for the 0.1 mm aperture in Figure 6.10) does not reach an operable pressure for any significant portion of

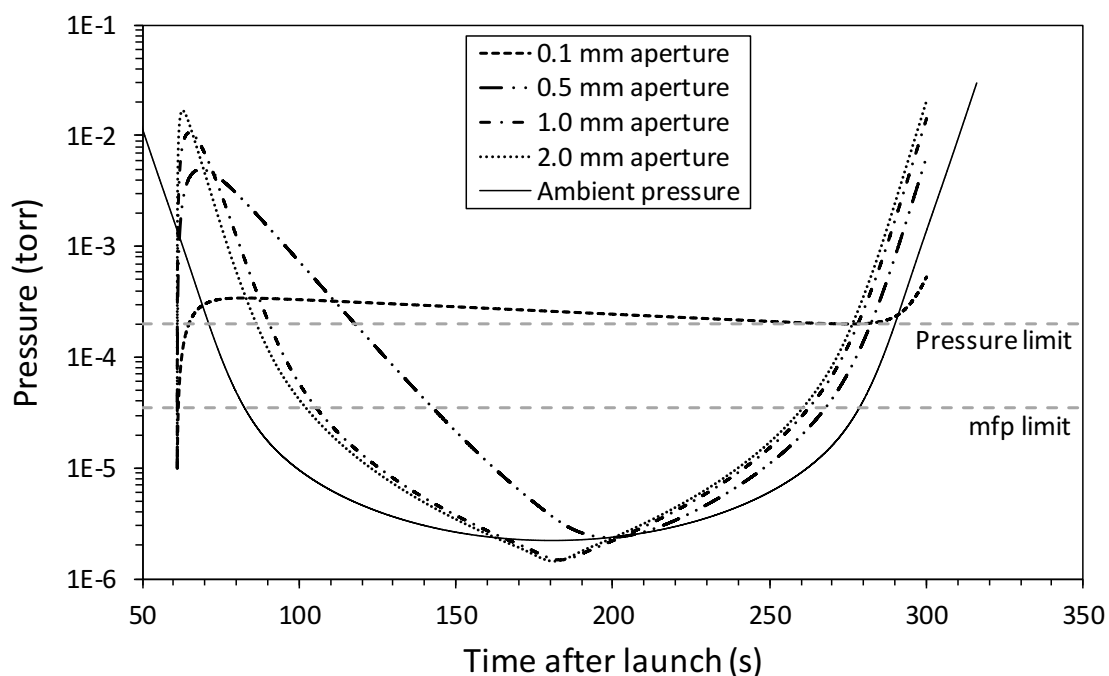
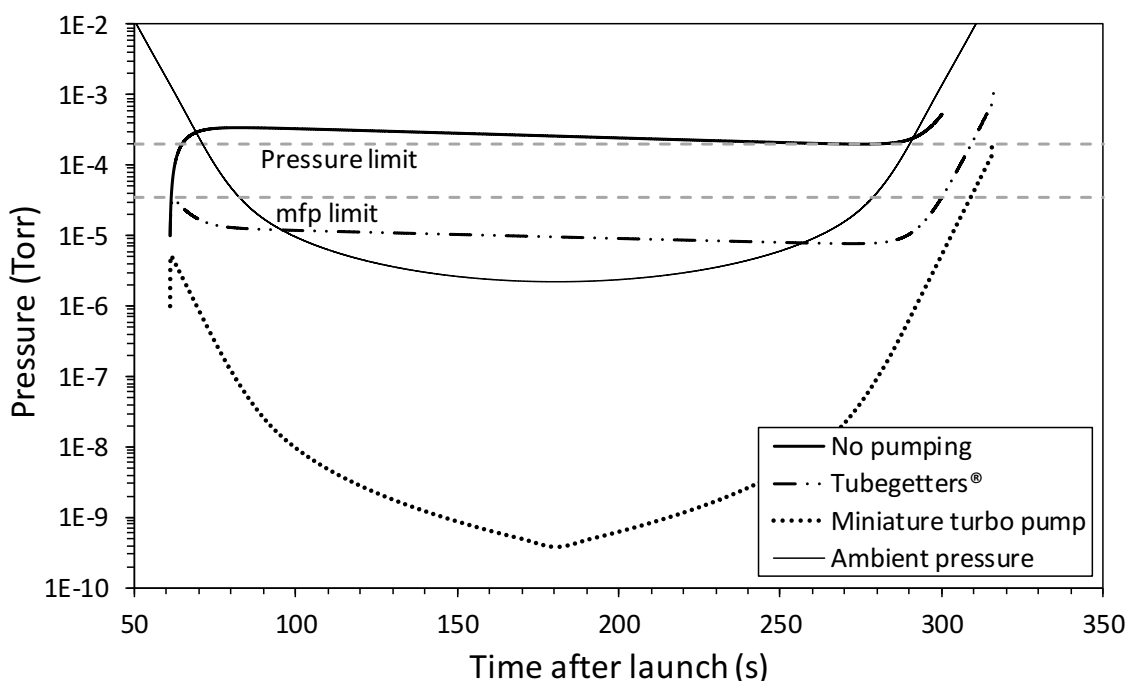


**Figure 6.10.** IPM simulation pressure curves for an SDL TOF-MS with no active pumping, opening the sampling aperture at 90 km, assuming an apogee of 160 km.

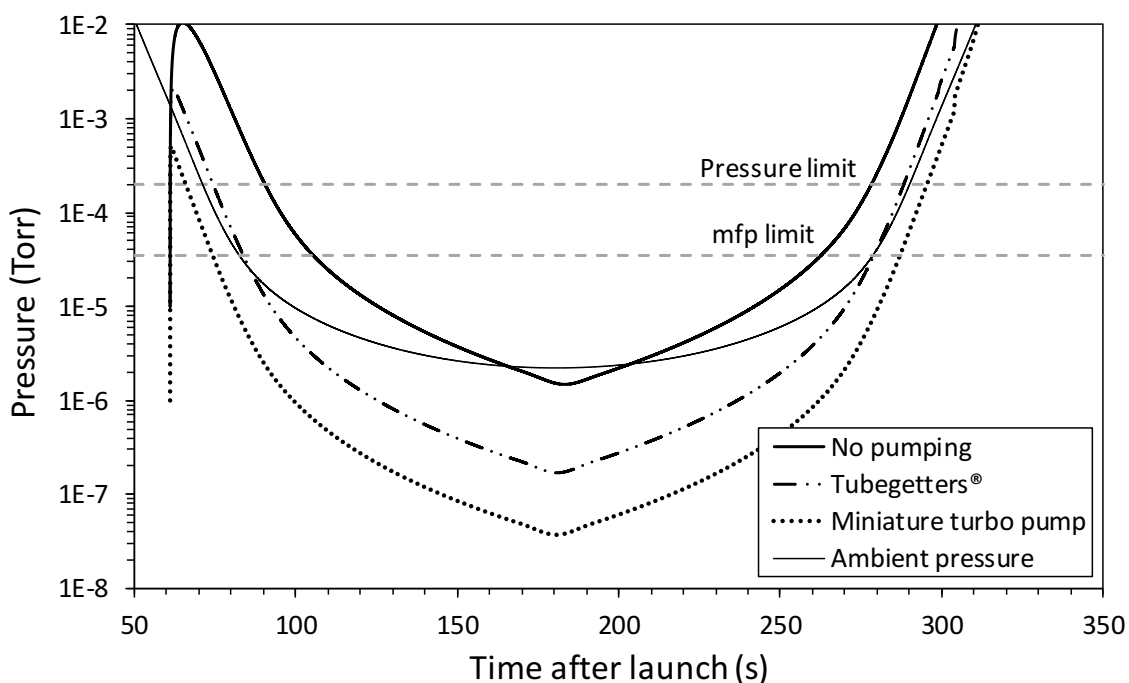
the flight. Both simulated instruments with pumping, however, meet and exceed the mfp requirement immediately upon opening the aperture. In both of these cases the effect of the initial pressure spike, although present, is sufficiently mitigated by either pumping option.

Figure 6.12 also shows IPM pressure curves for two pumped (miniature turbo pump, and eight TGs) and one unpumped instrument, but for an aperture diameter of 1.0 mm. The aperture opening altitude is again 90 km. The larger aperture size results in a significantly larger initial pressure increase, compared to that shown in Figure 6.11. In fact, for the 0.1 mm diameter aperture, the pressure spike for all three curves fails to meet either the mfp or pressure limit. These pressures are too high for the SDL TOF-MS to operate and must decrease to suitable levels for the instrument to make measurements.

The spike in pressure when the aperture is opened is perhaps the most important factor to consider when making measurements below 120 km on the up-leg portion of a rocket



**Figure 6.11.** IPM simulation pressure curves for an SDL TOF-MS with no pumping, pumping via eight TGs, and pumping provided by a miniature turbo pump (constant speed of 4 L/s), for an aperture diameter of 0.1 mm and an opening altitude of 90 km.



**Figure 6.12.** IPM simulation pressure curves for an SDL TOF-MS with no pumping, pumping via eight TGs, and pumping provided by a miniature turbo pump (constant speed of 4 L/s), for an aperture diameter of 1.0 mm and an opening altitude of 90 km.

flight. If the pressure spike is too high, the detector will fail and no data will be collected for the duration of the flight. IPM results for the maximum value of the pressure spike at aperture open altitudes from 70 to 140 km, assuming an unpumped SDL instrument, are shown in Figure 6.13. The pressure spike is too high to operate the instrument lower than 100 km for all simulated aperture diameters. The pressure limit is met for a 0.1 mm aperture instrument opening at 100 km, but the IPM indicates (not shown) that the mfp limit is not met at any point in this case. For opening altitudes of 110 km and above, however, both the pressure and mfp limits are met for a 0.1 mm aperture. For the other aperture diameters simulated, the IPM indicates that 120 km is a safe opening altitude, and the mfp limit is met by 130 km.

The simulated initial pressure spikes for an instrument with a miniature turbo pump (constant of 4 L/s) are shown in Figure 6.14. As expected, the active pumping of the instrument volume results in more favorable operating pressures than for the instrument

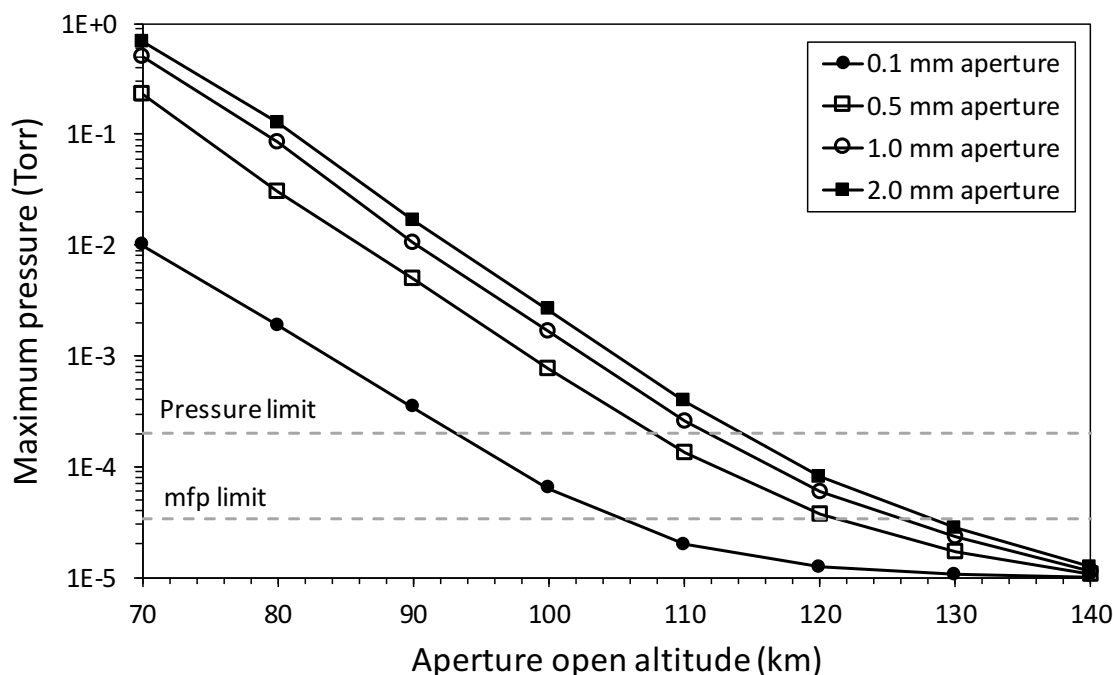


**Figure 6.13.** Maximum value of the pressure spike at aperture open for the SDL instrument, with no active pumping, as simulated with the IPM.

with no pumping. The IPM simulations indicate that a 0.1 mm diameter aperture, combined with a miniature turbo pump, would result in a pressure spike low enough to satisfy both the pressure and mfp requirements immediately upon opening at 80 km. The mfp requirement would be met at 100 km for a 0.5 mm aperture and at 110 km for a 1.0 mm aperture. For a 2.0 mm aperture, the mfp limit would be met at about 112 km.

TGs provide pumping that is intermediate to the no pumping and miniature turbo scenarios. Figure 6.15 shows pressure spike maximums for the SDL TOF-MS, with simulated pumping by eight TGs. The pressure and mfp limits in this case are satisfied at lower altitudes, by about 10 km, than for an unpumped instrument. However, given the large uncertainty in TG performance (section 5.3.2), it is best to err on the side of caution in determining minimum opening altitudes for an instrument pumped with these devices. For example, even though IPM results indicate an instrument with a 0.1 mm diameter aperture can operate upon opening at 80 km, caution would suggest an opening altitude of 85 km or

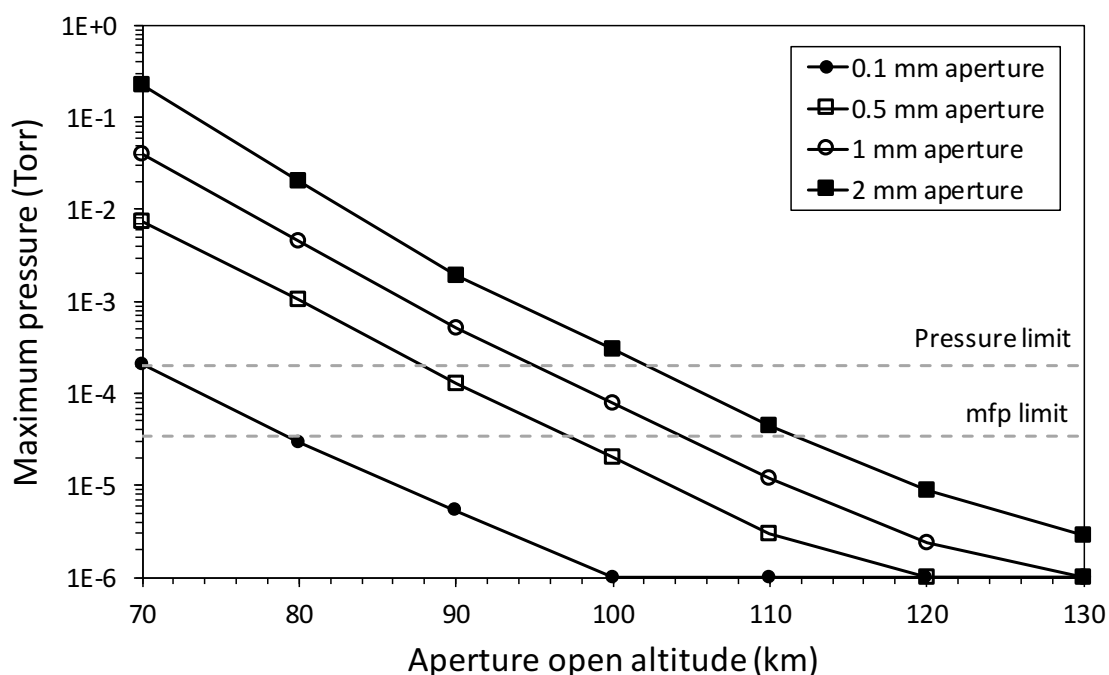


**Figure 6.14.** Maximum value of the pressure spike at aperture open for the SDL instrument, with a miniature turbo pump (constant 4 L/s), as simulated with the IPM.

higher. Even so, this still represents an improvement over an unpumped instrument.

The challenge of determining a safe opening altitude can be entirely avoided by opening the SDL instrument at an altitude sufficiently high that the initial pressure spike is negligible. In this case, both the mfp and pressure limits would immediately be met; measurements would be made along the remaining flight trajectory, including as the instrument fell back to Earth. The SDL instrument would simply continue to operate until the pressure became too great, making measurements at the lowest altitude possible with the employed pumping method. The IPM was also used to simulate this scenario for an unpumped instrument and a pumped instrument (miniature turbo pump and eight TGs).

Figure 6.16 shows the altitudes above which the pressure requirement is met with the instrument aperture opening high in the flight trajectory, based on IPM simulations. Altitudes above which the mfp requirement is met are shown in Figure 6.17. Simulations of an unpumped instrument used an opening altitude of 120 km for 0.1 and 0.5 mm diameter

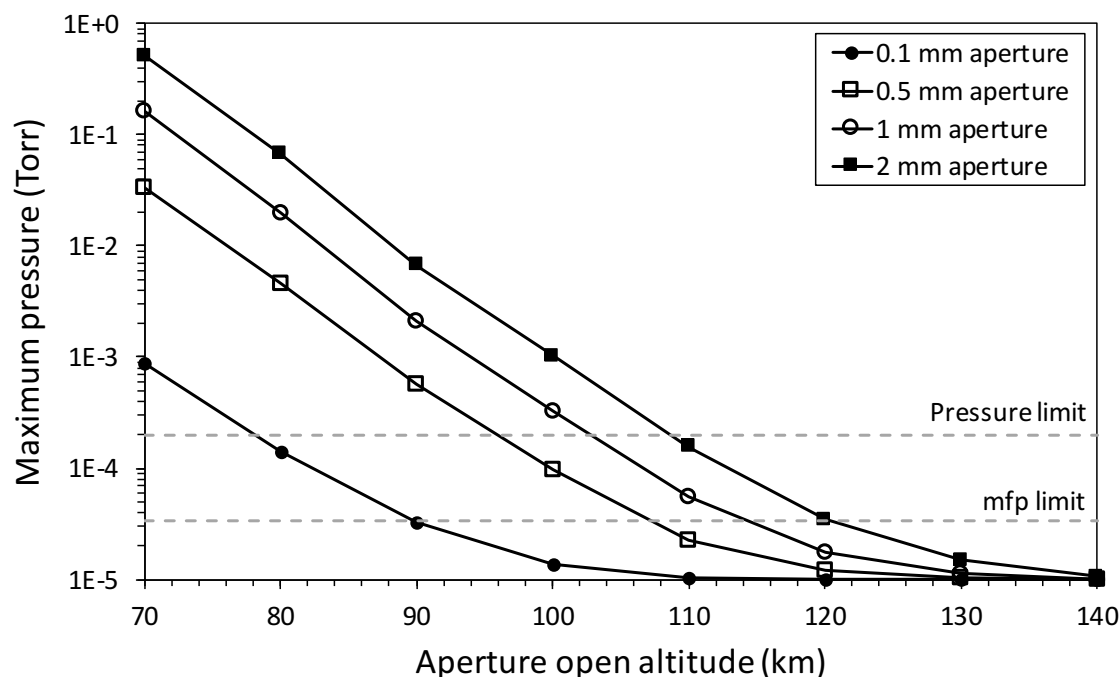


**Figure 6.15.** Maximum value of the pressure spike at aperture open for the SDL instrument, pumped with eight TGs, as simulated with the IPM.

apertures, and 130 km for 1.0 and 2.0 mm diameter apertures. The curves representing an instrument pumped by eight TGs were produced assuming a 110 km opening altitude for 0.1 and 0.5 mm diameter apertures, and 120 km for 1.0 and 2.0 mm diameter apertures. For a constant pumping speed of 4 L/s (miniature turbo pump), the IPM yields virtually identical pressures at a given altitude, regardless of whether the instrument is on the up-leg or down-leg portion of the rocket flight. Thus, the curves for a miniature turbo pump in Figures 6.16 and 6.17 represent the minimum altitudes at which the pressure and mfp requirements are met, regardless of whether the rocket is increasing or decreasing in altitude.

### 6.3. Discussion

The bow shock that forms in front of a high speed vehicle in the lower MLT can lead to measurements that do not accurately represent ambient conditions [Gumbel *et al.*, 1999]. Figure 6.7 compares the particle flux on the front surface of the SDL instrument from DSMC simulations with results calculated using kinetic theory (assuming no bow shock

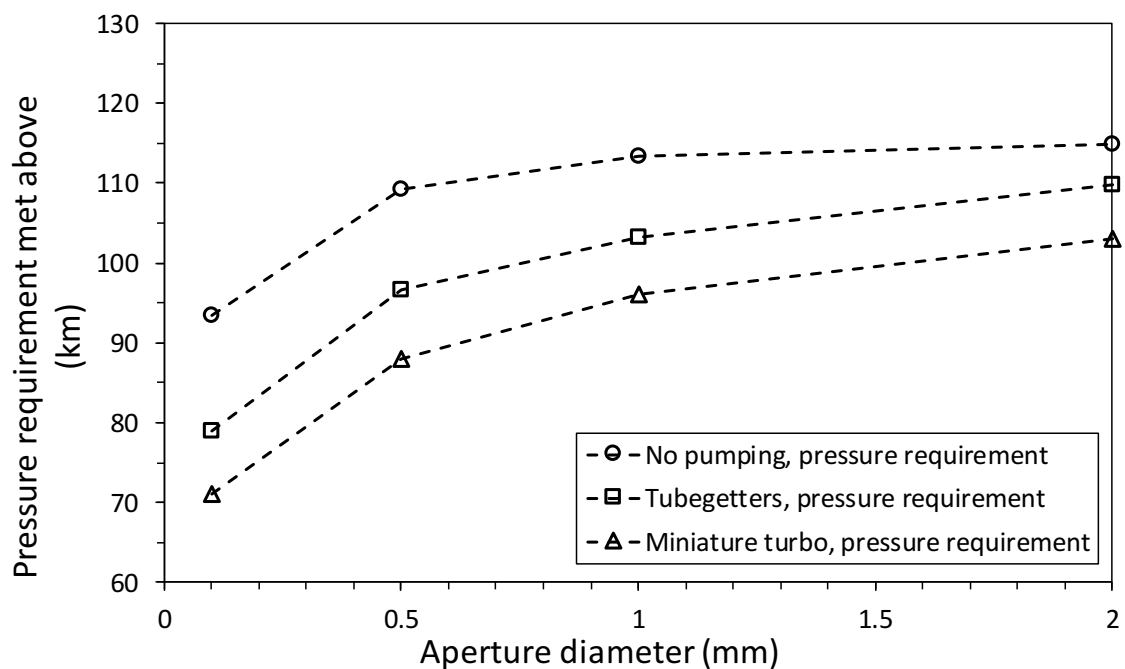


**Figure 6.16.** Altitudes above which the pressure requirement is met, based on IPM results assuming an aperture open altitude high in the rocket trajectory.

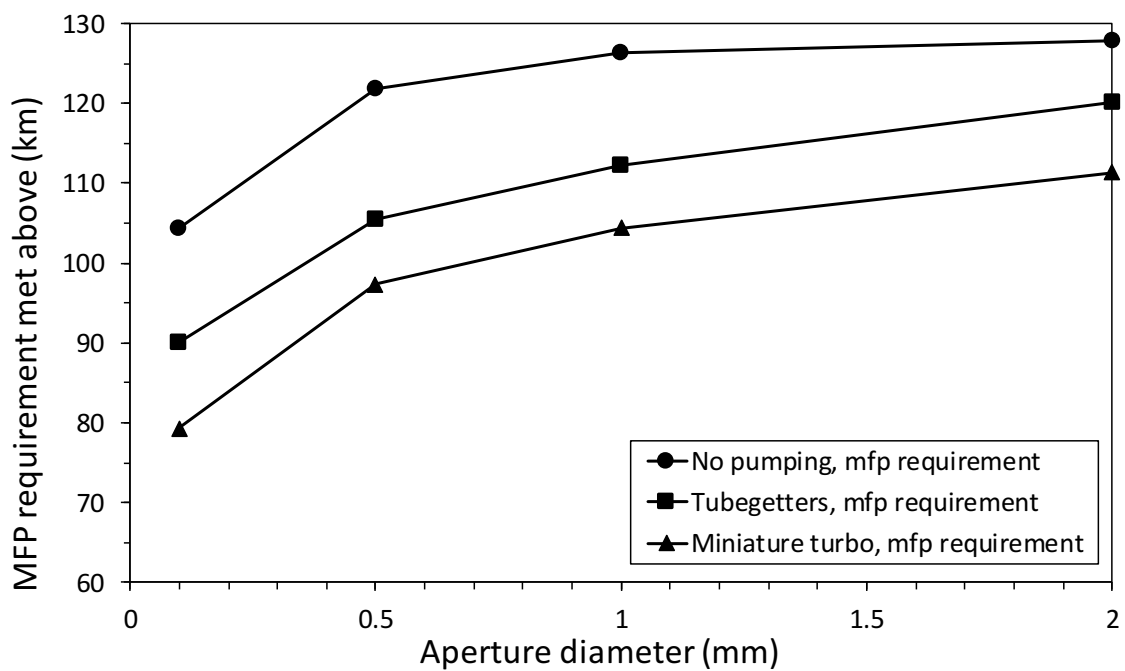


**Figure 6.17.** Altitudes above which the mfp requirement is met, based on IPM results assuming an aperture open altitude high in the rocket trajectory.

effects), for an apogee of 160 km. Ambient particle transmission through the bow shock, based on the Beer-Lambert law (equation 6.1) and DSMC simulations, is shown in Figure 6.8. The data shown in these two figures suggests that the MLT can be divided into three measurement zones: below 95 km (zone 1), between 95 and 120 km (zone 2), and above 120 km (zone 3). These zones are represented in Figure 6.8.

The primary feature of zone 1 is a bow shock so dense that virtually no ambient particles reach the sampling aperture without experiencing many collisions. The bow shock makes the calculation of particle flux on the front surface of the instrument very difficult. Kinetic theory, assuming ambient densities and particles with randomly distributed velocities centered around a Maxwellian distribution drifting at the rocket velocity, does not suffice. Additionally, the bow shock temperature can contribute to reactions with ambient species that may not otherwise occur [Gumbel *et al.*, 1999]. In zone 1 accurate composition measurements are not possible without eliminating the bow shock by cooling instrument ram surfaces to cryogenic temperatures. However, rigorous modeling (DSMC) and instrument calibration may allow absolute density measurements to be made in zone 1.

Collisions between ambient and bow shock particles, although present, are greatly reduced in zone 2. Here, density measurements may be possible without cryogenically eliminating the bow shock. Rigorous modeling (DSMC) and instrument calibration should permit accurate composition measurements, at least for species with low reactivity (e.g., argon and nitrogen). In zone 3 most ambient particles pass through the bow shock without experiencing any collisions, and both composition and density measurements can be performed without the use of cryogenics. However, accurate composition measurements of oxygen at any altitude by a rocket-borne mass spectrometer will likely require cryogenics to both eliminate the bow shock and minimize reactions of oxygen with instrument surfaces [von Zahn, 1967].

Previous mass spectrometers deployed to the MLT have employed cryogenically cooled surfaces to eliminate the bow shock, improve the accuracy of reactive species measure-

ments, and to provide instrument pumping [Offermann and von Zahn, 1971; Offermann and Tatarczyk, 1973; Offermann et al., 1981; Nier et al., 1976; Lake and Nier, 1973; Balsiger et al., 1996]. This is accomplished in both cases when incident gas particles condense on the cooled surfaces, preventing particle reflection either into the bow shock or the measurement volume. However, cryogenic systems require complicated instrument design, consume precious resources, and can be difficult to manage in the field.

Even in situations where cryogenics are not required, instrument pressure may still be a concern for the SDL TOF-MS. The main objective of any instrument vacuum system is to create and maintain an environment conducive to successfully making measurements or performing experiments. Results from pressure simulations of the SDL instrument in the MLT are presented in section 6.2.2. The significance of these results is now discussed.

The MCP used in the SDL instrument (Chapter 4) requires up to several minutes to ramp to operating high voltage. This means the MCP must be held at its operating potential during the entirety of the rocket flight, including when the instrument aperture opens. Thus the initial pressure spike that occurs when the aperture is opened (see Figures 6.13 - 6.15) presents a challenge. The pressure spike can be partially mitigated by choosing a smaller aperture and actively pumping the instrument. For example, Figure 6.14 shows that the SDL instrument should be able to operate at any altitude above 80 km if it has a 0.1 mm aperture diameter and is actively pumped at 4 L/s. However, larger sampling apertures may be necessary to achieve the instrument sensitivity required for a given mission. Larger apertures result in higher pressure spikes at aperture open, which may prevent successful instrument operation.

Laboratory experiments have shown that the MCP detector used in the SDL instrument can survive at pressures in excess of  $10^{-2}$  Torr with high voltage applied, as long as it is not actively stimulated (section 6.1.3). Although the initial pressure spike may exceed the maximum instrument operational pressure of  $2 \times 10^{-4}$  Torr, proper application of rejection grids could be employed to prevent detector stimulation until the instrument pressure is

sufficiently low for safe operation. There is, however, little reason to expose the detector to pressures that are too high for instrument operation; the aperture should only be opened at altitudes where the instrument can safely operate.

One method that has been employed with mass spectrometers in the MLT is to keep the instrument aperture closed until high in the trajectory and make measurements on the downleg portion of the rocket flight [*Trinks et al.*, 1978]. This method entirely avoids the risks of the initial pressure spike discussed previously and would provide a pressure advantage for both unpumped and TG-pumped instruments. At altitudes high enough that the ambient pressure is lower than the instrument pressure, more gas escapes than enters the instrument; the aperture itself acts as a pump. This pumping through the aperture is significant and highly dependent on aperture size, as seen in Figure 6.10. The IPM was used to model this case, and Figures 6.16 and 6.17 show the altitudes above which the pressure and mfp requirements are met for opening the aperture high in the rocket trajectory. Except for an instrument with no pumping and a 0.1 or 0.5 mm diameter aperture, this method does not appreciably extend the measurement range to lower altitudes. The major advantage of this practice lies in avoiding the pressure spike at aperture open, greatly reducing what is probably the most significant risk to successful instrument operation.

Turbo pumps are precision pieces of machinery that operate under extremely tight tolerances. Normal turbo pumps would be unlikely to survive the vibrations and movement associated with a rocket launch and flight. However, a miniature turbo pump with a reported pumping speed of 4 L/s has recently been developed for use on rocket-borne instruments and other spacecraft, including planetary probes [*Kline-Schoder*, 2011; *Creare*, 2014]. In fact, two of these pumps are currently on Mars as part of the Sample Analysis at Mars instrument suite [*Mahaffy et al.*, 2012]. These pumps consume a maximum of about 12 W, but may require less depending on the pressure. A miniature turbo pump has the obvious advantage of a relatively high constant pumping speed throughout the duration of the rocket flight. But, as a mechanical device, turbo pumps are more prone to failure than non-

mechanical pumps. These pumps are also expensive (\$30k in 2011) [Kline-Schoder, 2011]. However, if the cost and risk can be tolerated, miniature turbo pumps offer improved operating pressures over the no pumping option and TGs.

In contrast to miniature turbo pumps, TGs have no moving parts and are relatively inexpensive (~\$100/each in 2010). Although they provide less pumping than a turbo pump, several TGs can be used at the same time. The pressure simulations presented here assumed the use of eight TGs, but more could be incorporated in the instrument design to increase pumping speed. One drawback of TGs is they are ineffective at pumping inert gases such as argon and helium. The activation process, which involves melting or otherwise breaking an indium seal to expose the getter material, could also present a challenge. However, assuming activation occurs prior to launch, TGs require no in-flight power. To preserve the getter material after TG activation, the instrument could be vacuum sealed until reaching the aperture open altitude. IPM simulations indicate that by employing eight TGs to provide pumping, the SDL instrument measurement range could extend lower by 10 to 20 km than an unpumped instrument, depending on aperture size (see Figures 6.16 and 6.17).

A version of the SDL instrument with no active pumping has the obvious advantage of simplified instrument design. However, the minimum altitudes at which measurements can be made are much higher for an unpumped instrument. Aperture size and opening altitude must be carefully considered to avoid problems stemming from the initial pressure spike. Other innovative approaches may also be utilized. A novel concept for providing vacuum for a rocket-borne instrument, which utilizes vents between the instrument interior and the wake region aft of the rocket payload, has recently been reported by *Dickson et al.* [2013]. This method was used to successfully operate a CEM on a sounding rocket down to an altitude of 80 km.

TGs were initially considered for use with the SDL TOF-MS as a low cost and mechanically simple alternative to cryogenic and mechanical pumping systems. IPM simulations suggest that TGs have the potential to provide an altitude measurement advantage of 10 to

20 km over an unpumped instrument. This is a significant distance, and TGs offer a way to reduce the cost and complexity of making *in-situ* MLT measurements. TGs have other potential uses related to rocket-borne instruments. For example, TGs may be employed in pressure-sensitive instrument assemblies to maintain vacuum for extended periods of time [Londer *et al.*, 2007]. TGs could also be used as a low-cost vacuum method during storage and shipping of such instruments. TGs could also be employed, in lieu of more complex and expensive ground support vacuum pumping equipment, to maintain low instrument pressures on the launch pad.

Although this chapter focuses on the SDL TOF-MS instrument pressure in the MLT, the different pumping options described may be applicable to rocket-borne instruments in general. In any case, pressure requirements will be unique to each instrument and mission, and may be more or less stringent than those considered here. The methods described in this chapter may be applied to other experiments to meet specific pressure requirements, and enable measurements and experiments that will further our understanding of the upper atmosphere.

#### 6.4. Conclusions

Ambient MLT pressures, which can exceed 10 mTorr, present a major obstacle to making accurate *in-situ* measurements in this region. A high speed sounding rocket creates a bow shock that disturbs the ambient atmosphere, making accurate measurements difficult. Above 120 km the transmission fraction of ambient particles through the bow shock approaches unity, and bow shock effects can be ignored. Accurate measurements for all ambient species will still be difficult at lower altitudes because of bow shock effects and interactions between reactive species and instrument surfaces. The methods presented in this chapter can be employed to make mass spectrometer measurements in the MLT in situations where: the presence of a bow shock can be tolerated; inaccurate measurement of oxygen is acceptable; or where power, space, weight and/or budget constraints do not

allow for the use of cryogenics. However, the only proven method of making accurate mass spectrometer measurements of ambient oxygen in the MLT requires the use of cryogenics. Simulations of a new pumping method involving the use of barium loaded TGs were also presented. This method has the potential to provide sufficient vacuum pumping to extend measurements to as much as 20 km lower than an un-pumped instrument. A new miniature turbo pump, developed specifically for space instruments, will allow successful instrument operation at even lower altitudes, depending on aperture size. The different instrument pressure management solutions discussed in this chapter provide several alternatives to using cryogenics in rocket-borne mass spectrometers.

## CHAPTER 7

## LABORATORY EXPERIMENTS WITH THE PROTOTYPE TOF-MS

This research culminated in the construction and laboratory testing of a prototype instrument, referred to as the EDU (section 1.4 and Chapter 3). Characterization and testing of the EDU was performed at the SDL IOTF. Because the IOTF currently lacks the ability to simulate a rocket experiment (e.g., ion beam energy too high, no neutral beam), the goal of instrument testing was to ultimately compare results from the laboratory with modeled instrument performance. A model that accurately reproduces laboratory results can be used to make predictions for instrument performance on a rocket flight. With this in mind, ion and neutral experiments were performed with the EDU to measure instrument performance in terms of mass resolution. Further experiments were conducted to investigate the deflection efficiency of the BNG and also to determine the contribution of UV photons to background count rates. Finally, the instrument was operated at elevated pressures under argon backfill to study the effect of pressure on instrument performance, including mass resolution. The experiments presented in this chapter demonstrate the ability of the SDL TOF-MS to make measurements of common ambient species in the MLT.

### 7.1. Equipment and Methods

The IOTF consists of a 24" diameter UHV chamber with an attached Colutron® G-2-D ion gun system. The ion gun produces ions using either an inductively coupled plasma source or a hot cathode discharge source, and is capable of generating ion beams with energies from 1 to 10 keV and energy spreads  $<1$  eV. A Wien filter provides mass selection of ions from the gun. Typical ion beams used for testing the EDU had energies between 10 and 30 eV. An example of an ion beam produced in the IOTF is shown in Figure 7.1. A Faraday cup/electrometer and an MCP/phosphor/CCD camera are used for ion beam diagnostics. For testing and experiments, instruments are mounted in the 24" chamber on a manipulator with two axes of rotation and three degrees of translation. Both the

24" chamber and the ion gun are evacuated with turbo pumps backed by dry scroll pumps. During experiments with the EDU, pressure was monitored with ion and Baratron<sup>®</sup> gauges.

The fully assembled EDU (Chapter 3 and Figure 3.17) was installed on the manipulator in the 24" UHV chamber as shown in Figure 7.2. Electrical leads and connectors from the EDU were insulated with Teflon<sup>™</sup> tubing and connected to feedthroughs in the UHV chamber. During instrument installation, special care was taken to maintain the cleanliness of the instrument and vacuum chamber. Prior to opening the UHV chamber, surfaces near the installation port were wiped clean with a lint-free wipe dampened with IPA, after which a protective sheet of Llumalloy was taped over the port. The chamber was vented with filtered N<sub>2</sub>, and a portable HEPA filter blower was attached to a secondary port on the chamber to produce airflow out of the chamber while the installation port was open.

The reader is referred to section 3.1 for a discussion of the various electrical requirements of the EDU. DC power requirements ranged from a few volts to -2400 V (Figure 3.1).

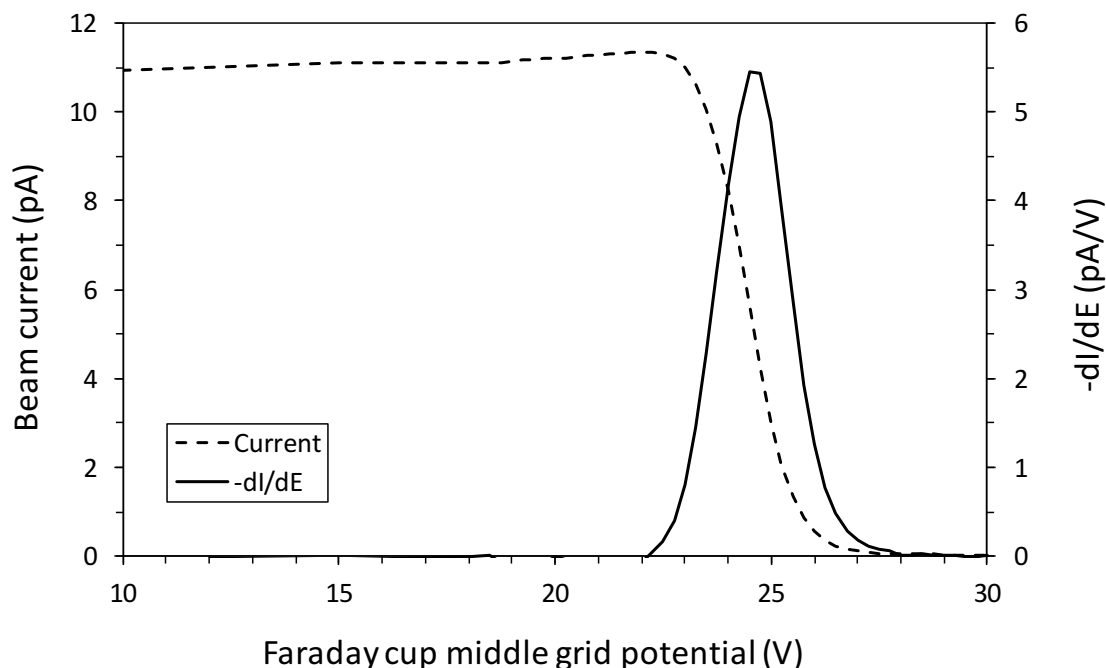


**Figure 7.1.** Example of an ion beam produced in the SDL IOTF. This particular beam had an energy of 24.5 eV with an energy spread of 1.9 eV, measured at FWHM.

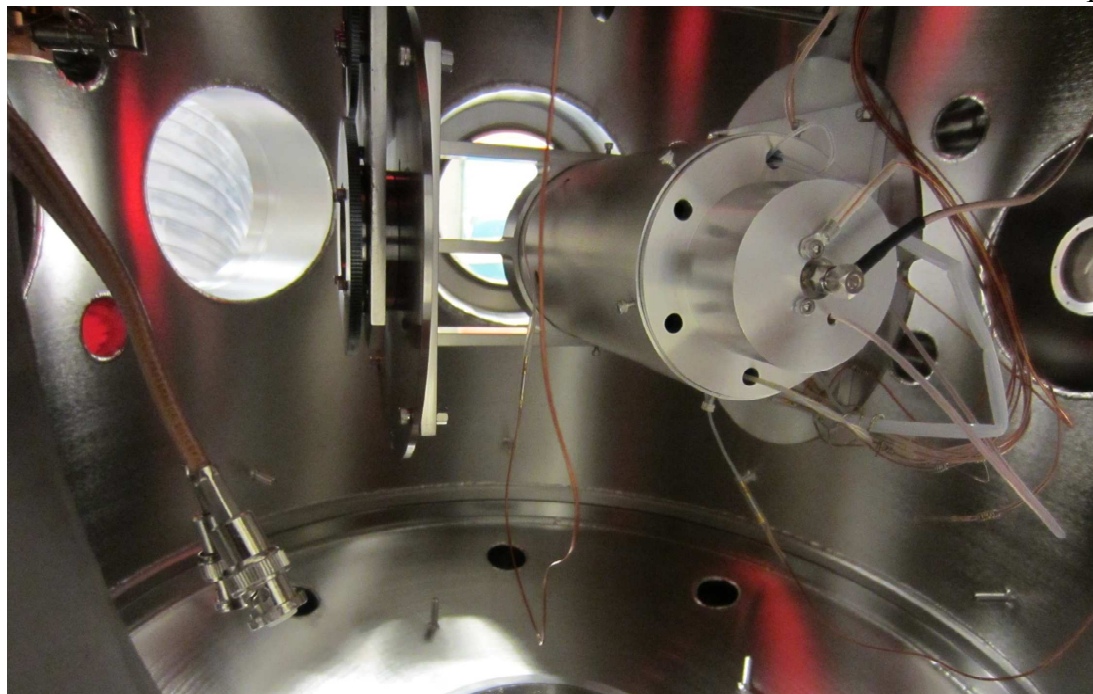


**Figure 7.2.** The EDU (facing away from camera) mounted in the 24" UHV chamber.

These requirements include instrument operating potentials and pulse processing electronics. Commercial laboratory rack-mounted supplies were used wherever possible.

The BNG deflection efficiency was measured experimentally. Count rates were measured for deflection potentials, centered on the acceleration potential, at  $\pm 5$  V increments on the BNG. Results from these experiments were used to determine the BNG offset potentials to apply during experiments with the EDU. These results were also compared to theoretical predictions and simulations of the BNG deflection efficiency previously discussed in section 2.4.

The most commonly employed source of charged particles for experiments with the EDU in ion mode was the ion gun described earlier in this section, using argon as the source gas. In most cases the ion gun was tuned, using a Wien filter, to select  $\text{Ar}^+$  ( $m/z = 40$ ). Once a satisfactory beam was established ( $\text{FWHM} < 2$  eV, as measured with the Faraday cup/electrometer system), the EDU was oriented to maximize the count rate on the MCP detector. On several occasions the gun was operated without applying the velocity

filter, in order to collect spectra containing peaks from multiple species. An ion gauge was also used on several occasions as an ion source; the collection grid on the gauge was biased to expel, rather than collect, ions and the EDU was pointed towards the gauge.

Experiments were also performed with the EDU operating in neutral mode. Many of these experiments were performed under backfill. For these experiments, gas was introduced to the chamber via the ion gun leak valve, but with the ion gun powered off. The performance of the EDU was tested at elevated pressures in neutral mode; argon was used as the backfill gas in an effort to minimize damage to the ionizer cathode by more reactive gases.

Electronic interference problems prevented the EDU from operating in HT mode (section 1.3.3). The source of the interference was traced to the BNG modulation output of the MDB and resulted in large amounts of noise with a frequency of approximately 200 MHz for several hundred ns after each modulation pulse. The noise was orders of magnitude larger than any observed real signal, and attempts to subtract it out were unsuccessful. Because there are multiple BNG modulation pulses for each start pulse in HT mode, the resulting spectrum would have been a collection of noise too large to extract the desired signal.

## 7.2. Results and Discussion

Results from experiments with the EDU are now described and discussed, beginning with the BNG deflection efficiency. The background count rate for the instrument under operating conditions follows. Finally, spectra collected with the EDU are presented. These include both ion and neutral spectra.

### 7.2.1. BNG deflection efficiency

The BNG was characterized in the laboratory to determine the deflection voltages necessary to maximize signal to the EDU. To do this, MCP count rates were recorded for various BNG deflection potentials ( $V_{\text{def}}$ ) and compared to the baseline count rate at  $V_{\text{def}} = 0$  V.

This is plotted as a relative intensity in Figure 7.3 for the EDU operating in ion mode. The higher the ion energy, the higher the deflection potential required to deflect ions, which is seen in Figure 7.3 for ions with energies of 122 and 200 eV. The data shown in Figure 7.3 is representative of all BNG deflection efficiency data collected in ion mode.

The BNG ion deflection with the EDU operating in neutral mode is shown in Figure 7.4. Ambient neutrals in the experimental chamber were ionized by the EDU and accelerated to 238 eV. An important reason for experimentally measuring the BNG deflection efficiency is to determine the deflection potential to apply to maximize the SNR. The MDB (section 3.1.2) outputs deflection potentials of  $\pm 23$  V. This is insufficient to entirely deflect all particles from the MCP in either ion or neutral mode for the acceleration potentials used in the EDU. Any ions that impact the MCP during the beam off state contribute to background in the mass spectra. To determine the optimal deflection potential to apply to the

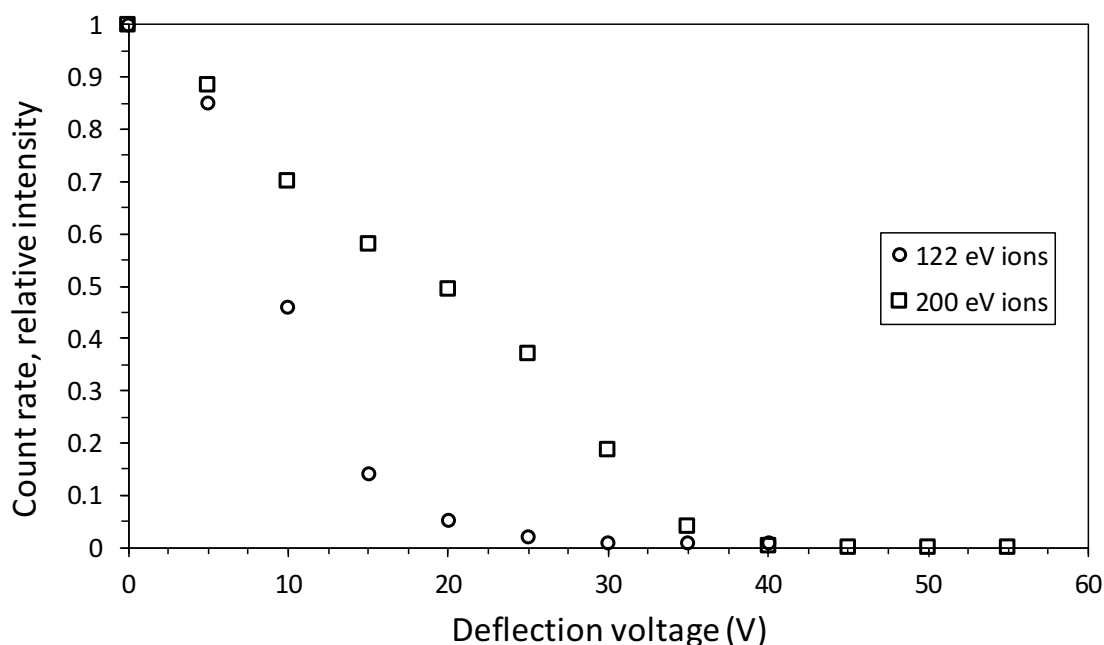


**Figure 7.3.** Relative count rate intensity for several BNG deflection potentials, with the EDU operating in ion mode. The deflection efficiency is obtained by dividing the number of counts at a given  $V_{\text{def}}$  by the number of counts obtained for  $V_{\text{def}} = 0$  V.

BNG, the difference in fraction collected was calculated for  $V_{\text{def}}$  values separated by 25 V. The objective was to maximize the SNR. These values are also plotted in Figure 7.4 as the count rate difference. Here, the optimal deflection potential is  $\pm 40$  V. At this value of  $V_{\text{def}}$ , roughly 40% of ions passing through the BNG in the beam-off state will impact the MCP and contribute to background. In the beam-on state, the BNG will still have  $\pm 15$  V applied and allow roughly 80% of ions to reach the MCP.

The most obvious difference between the count rate curves in Figures 7.3 and 7.4 is their shape. The reason for this is unclear, but may be due to the differences in the acceleration regions between ion and neutral modes. In ion mode, ions enter the instrument and are accelerated by the acceleration grids before reaching the BNG. In neutral mode, ionization appears to be occurring between the acceleration grids and the BNG, with the BNG providing both the acceleration and deflection potentials (see section 3.1.1).

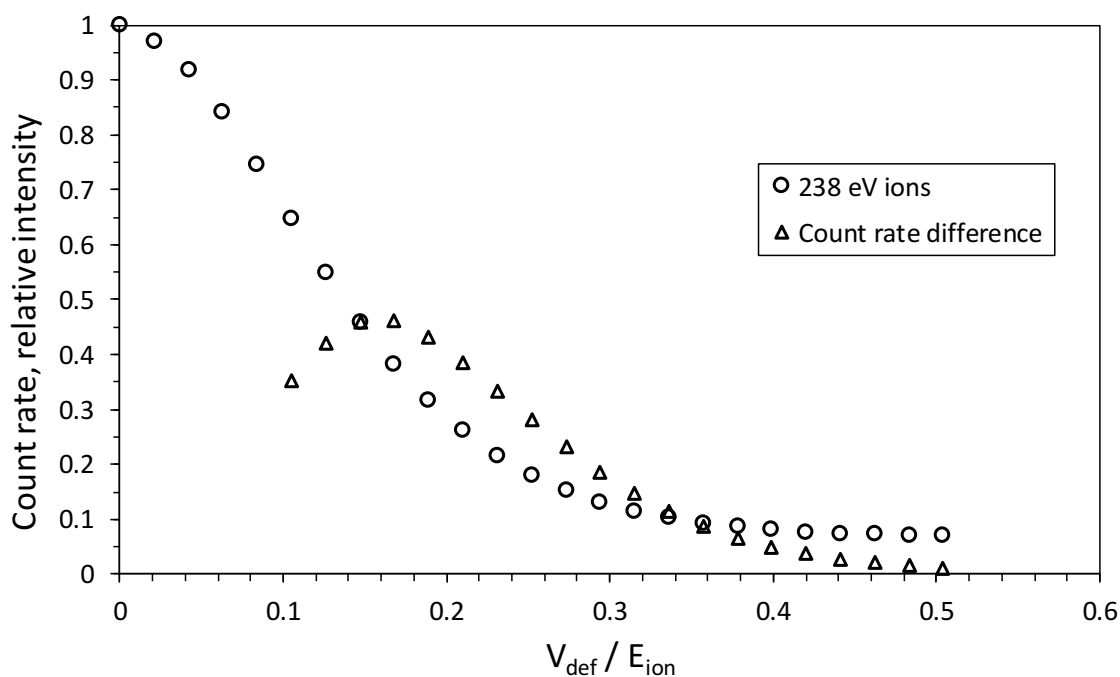


**Figure 7.4.** Relative count rate intensity for  $V_{\text{def}}/E_{\text{ion}}$  ratios up to 0.5, for 238 eV ions, with the EDU operating in neutral mode. The count rate difference is measured by comparing count rates for BNG deflection potentials separated by 25 V.

### 7.2.2. Background Count Rate

With the exception of ion feedback at elevated pressures, background counts in mass spectra taken with the EDU come from two main sources: ions that are insufficiently deflected and stray UV photons. Early in the design phase for the SDL instrument, concern was expressed that ions deflected by the BNG could reflect off of interior instrument surfaces with enough energy to be subsequently detected by the MCP. A combination of two simple experiments showed that ions reflecting from instrument surfaces have a negligible contribution to background. These experiments used 18 eV ions from the ion gun, accelerated to 200 eV inside the instrument. Both experiments were performed within an hour of each other at identical ion gun settings.

The first of these, a BNG deflection efficiency experiment, was similar to those described previously in section 7.2.1. The count rate at increasing values of  $V_{\text{def}}$  is shown in Figure 7.5. The count rate fell below 1% of the maximum value at  $V_{\text{def}} = \pm 40$  V. The count rate then gradually decreased until  $V_{\text{def}} = \pm 80$  V, after which there was no significant change. The second experiment involved operating the EDU as an RPA; both sets of BNG wires were biased together, essentially forming a third grid. Increasing the BNG potential resulted in a decreased count rate, shown in Figure 7.6. As the RPA potential increased, the count rate decreased steadily until at 20 V, it abruptly dropped<sup>1</sup>. There was no statistically significant change in count rate at higher RPA potentials. At this point any background could not come from reflected ions; the retarding potential was sufficiently high to entirely prevent ions from reaching the MCP.

The count rates for high values of  $V_{\text{def}}$  (Figure 7.3) were very similar to the count rates at high RPA values (Figure 7.4). This suggests that ions deflected by the BNG accommo-

---

<sup>1</sup>At first glance it appears that the ions have an extra 20 eV of energy. An acceleration potential of -181 V was used to accelerate 18 eV ions, resulting in a total ion kinetic energy of 200 eV. A potential of at least +200 V, relative to the acceleration potential, was required to fully reject the 200 eV ions. Thus the ion count rate drops to effectively zero at an RPA potential of 20 V.

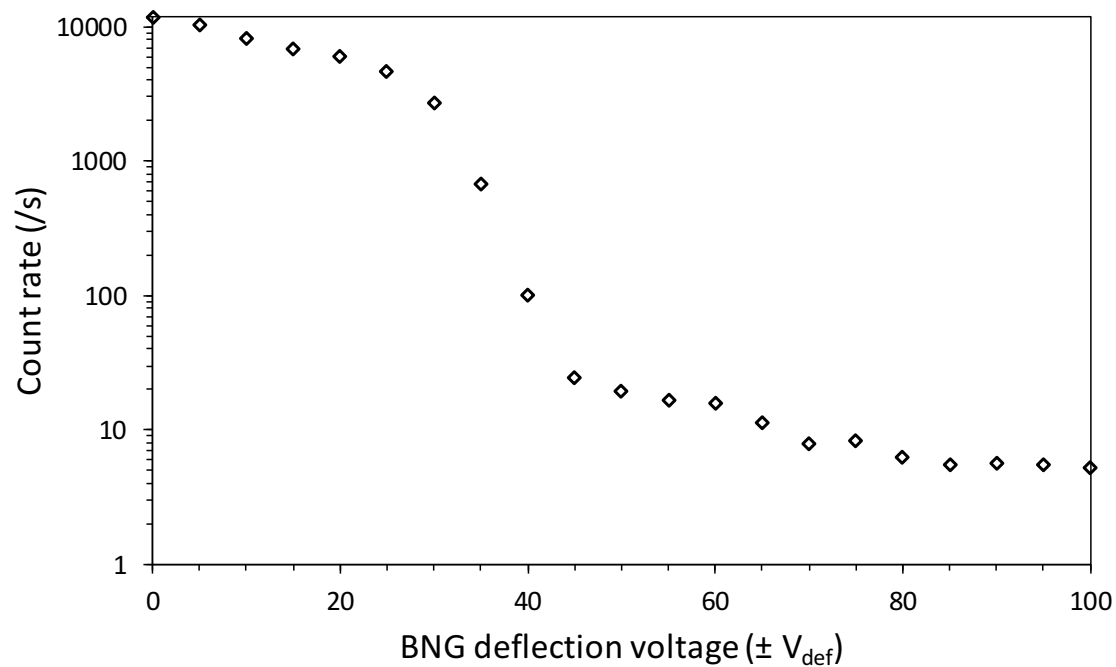


**Figure 7.5.** Count rates at increasing values of  $V_{\text{def}}$  for 200 eV ions.

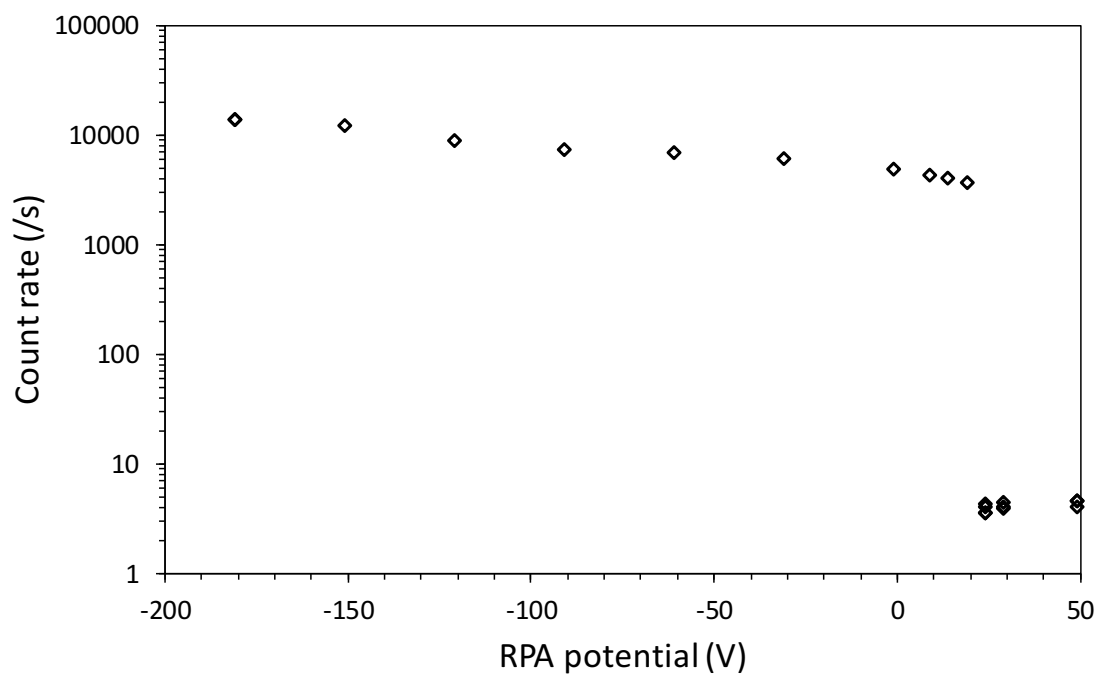


**Figure 7.6.** Count rates with the EDU operating in RPA mode, using 200 eV ions.

dated at a very high efficiency to the interior instrument surfaces, losing the majority of their kinetic energy and/or diffusely reflecting from these surfaces. Stray UV is then the major contributor to background above the point where changing  $V_{\text{def}}$  causes little variation in count rate. The most probable source of these photons in ion mode is UV emission from the ion gun. On a rocket experiment, UV emissions from the ambient atmosphere would be the largest source of background counts, assuming a  $V_{\text{def}}$  large enough to normally deflect all ions from the MCP. Background due to UV could be greatly reduced by employing a reflectron, eliminating direct line-of-sight from the ambient atmosphere to the MCP detector.

Neutral mode results in a significantly higher background than does ion mode. Figure 7.7 shows the same count rate data that is presented in Figure 7.4, but in this case it is plotted against  $V_{\text{def}}$ . The background count rate is much higher in neutral mode than in ion mode and at  $V_{\text{def}} = \pm 120$  V is still decreasing slightly. At  $V_{\text{def}} = \pm 120$  V the count rate is 7% of that measured at  $V_{\text{def}} = 0$  V. (In ion mode, the count rate at  $V_{\text{def}} = \pm 100$  V is 0.05% of that measured at  $V_{\text{def}} = 0$  V.) That the ionization of neutrals takes place inside the instrument, directly in the line-of-sight of the MCP, is likely responsible for the higher background in neutral mode. However, employing the BNG as both the acceleration grid and ion deflector may also result in less efficient ion deflection. A reflectron design would also help decrease background in a neutral TOF-MS by moving the ionization volume out of the line-of-sight of the MCP detector.

### 7.2.3. Spectra

The EDU was mounted in the ion optics chamber November 28, 2011, and two days later it was operated in ion mode to produce the spectrum shown in Figure 7.8. Functional testing of the instrument included operating the instrument in both ion mode and neutral mode. Additionally, the instrument was tested at elevated pressures under argon backfill. A virtual TOF-MS was later coded in MATLAB<sup>®</sup> (Chapter 8) and compared to the laboratory

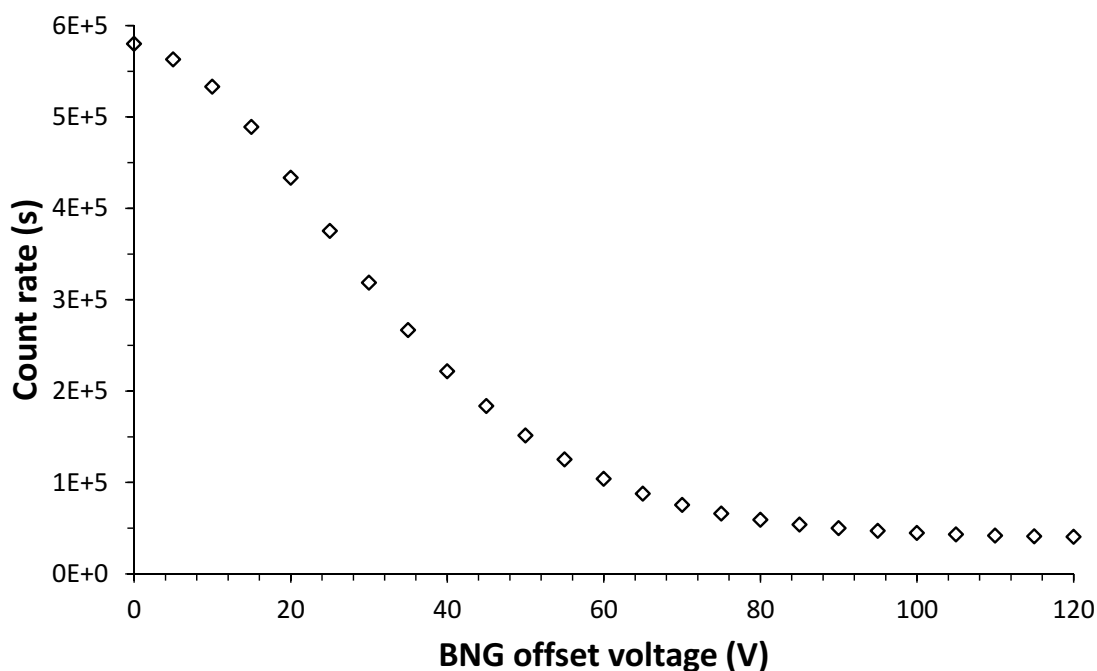


**Figure 7.7.** Count rates at increasing values of the BNG offset voltage ( $V_{\text{def}}$ ) for 238 eV neutrals.

experiments presented in this chapter.

Initially, modulation pulses from the MDB exhibited a large amount of ringing, shown in Figure 3.8, that adversely affected spectra from the EDU. The effect of this ringing is evident in the spectrum shown in Figure 7.8. The MDB was modified and a 150  $\Omega$  resistor was placed in series between each BNG lead and the MDB to remove the ringing (see section 3.1.2). This resulted in an increased modulation pulse rise time, but a more stable modulation waveform. Figure 7.9 shows a typical modulation pulse used to test the EDU after modifying the MDB.

#### 7.2.3.1. Ion Mode

The ion gun was the most frequently used source for operating the EDU in ion mode. The spectrum shown in Figure 7.10 was produced using a 20.6 eV ion beam with an energy spread of 0.75 eV at FWHM. The velocity filter was tuned to select  $m/z$  40, argon. Ions were further accelerated by 179.4 V inside the EDU, yielding a total ion energy of 200 eV.

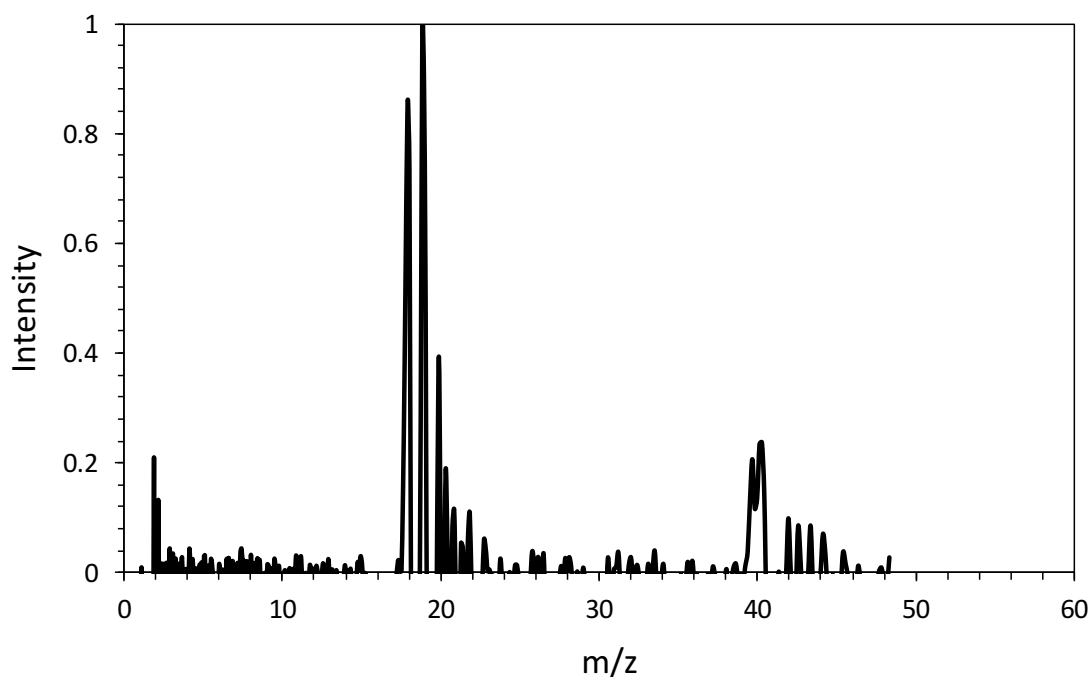


**Figure 7.8.** Early mass spectrum recorded with the EDU. The instrument was operated in ion mode for this spectrum, using the ion gauge in the UHV chamber as the ion source.

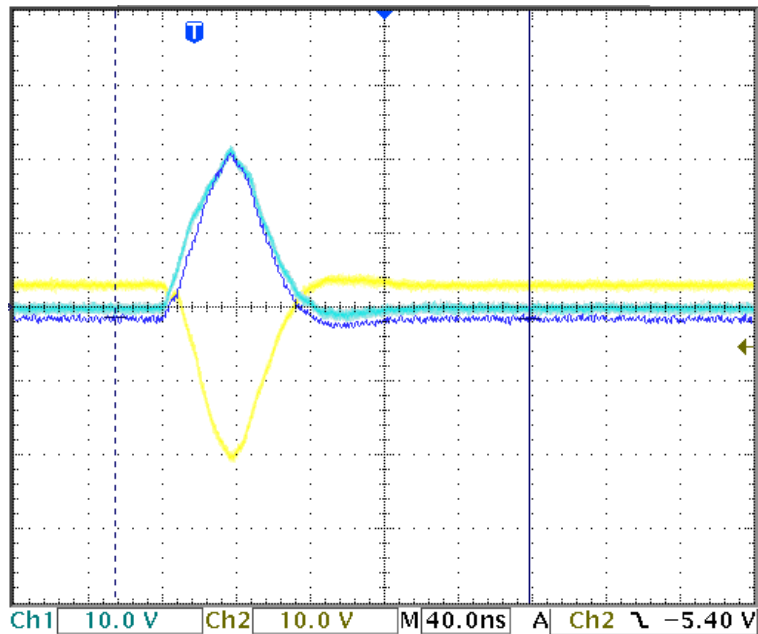


**Figure 7.9.** Modulation waveform most commonly used to drive the BNG during experiments with the EDU. The pulse setting on the MDB is 40 ns, and the waveform was measured at the BNG leads. This waveform was achieved after adding 150  $\Omega$  between each BNG channel and the MDB. Full-scale voltage range is -40 to 40 V and full-scale time range is -200 to 200 ns.

The BNG deflection offset was  $\pm 40$  V, and the pulse width was set to 40 ns (see Figure 7.9). Counts were placed in bins 1.6 ns wide. The argon ( $m/z$  40) peak in Figure 7.10 has a FWHM resolution of 76, sufficient for unit mass resolution. The resolution at 10% of the peak height is 37, which is not quite sufficient for unit mass resolution at this level, but is more than adequate to resolve peaks that are separated by several u.

The mass spectrum in Figure 7.11 shows two different isotopes of argon,  $m/z$  40 and 36, produced using a 4.7 eV ion beam with an energy spread of 1eV at FWHM. Ions were accelerated by  $V_{acc} = 100$  V inside the EDU, resulting in a total kinetic energy of 105 eV. The BNG deflection potential was  $V_{def} = \pm 30$  V. Mass resolution at the  $^{40}\text{Ar}$  peak is 39.8 at FWHM. Because the natural abundance of  $^{36}\text{Ar}$  is only 0.34%, the height of the  $m/z$  36 peak in Figure 7.11 appears to be abnormally high [McLafferty and Tureček, 1993]. However, the ion gun velocity filter was poorly tuned to  $m/z$  40 (tuning was most likely between the two masses, closer to  $m/z$  36), allowing both masses to be present in the ion

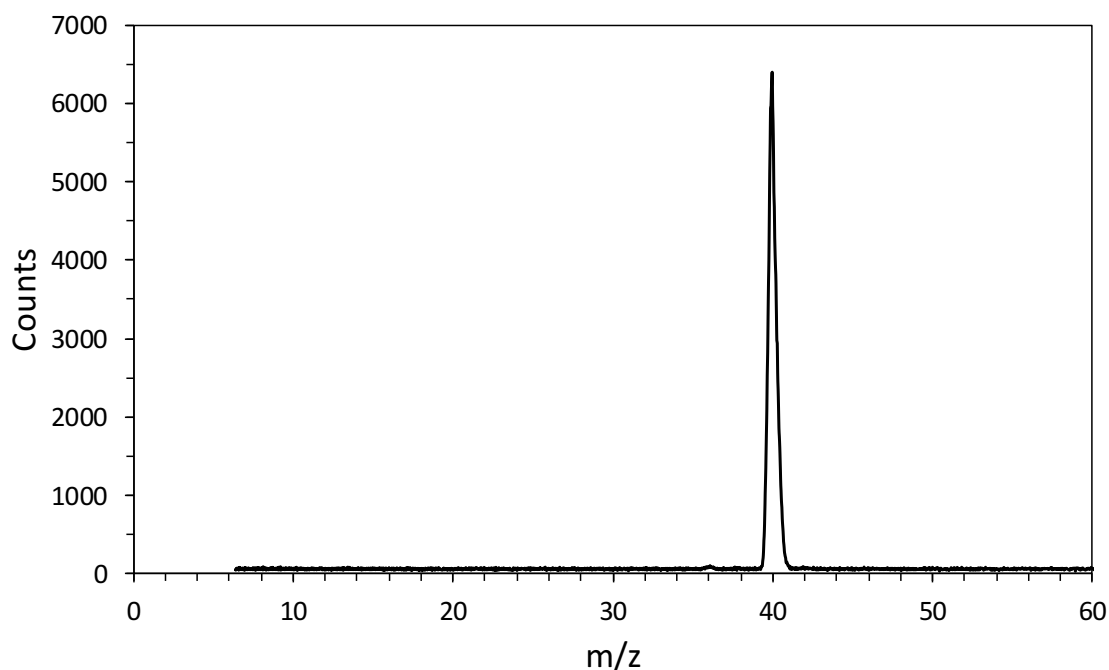


**Figure 7.10.** Mass spectrum of argon taken with the EDU operating in ion mode. FWHM mass resolution is 76 at  $m/z = 40$ .

beam.

The spectrum shown in Figure 7.12 was obtained by using an ion gauge as the ion source. The spectrum includes not only ambient gases from the chamber, but also back-filled gases including argon, helium, and lab air. During this experiment the chamber pressure was  $\sim 10^{-4}$  Torr, corresponding to a mfp about five times the drift length of the EDU. Peaks were identified at least in part by visually monitoring the mass spectrum as different gases were used to backfill the chamber (i.e., the  $\text{He}^+$  peak increased more rapidly while the chamber was under He backfill). Peak shifting and broadening in the spectrum is attributed to hot ions with large energy distributions. Since this spectrum was taken before modifications to the MDB to remove waveform ringing, peak doubling is also present.

The energy spread of sampled particles has a large influence on the achievable mass resolution of a linear TOF-MS and will be discussed further in Chapter 8. In the region of the MLT, ion temperatures are similar to neutral temperatures [Roble, 1995]. Ions sampled

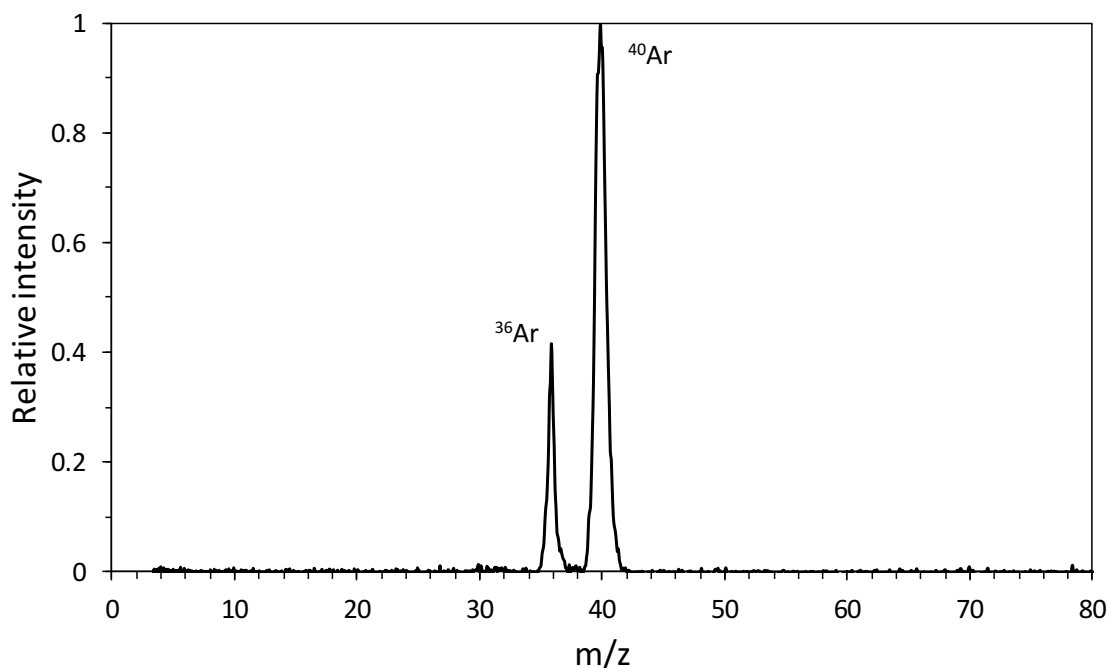


**Figure 7.11.** Mass spectrum of  $^{40}\text{Ar}$  and  $^{36}\text{Ar}$ , resulting from an ion beam with the velocity filter tuned between the two masses. FWHM resolution is 39.8 at  $m/z$  40.

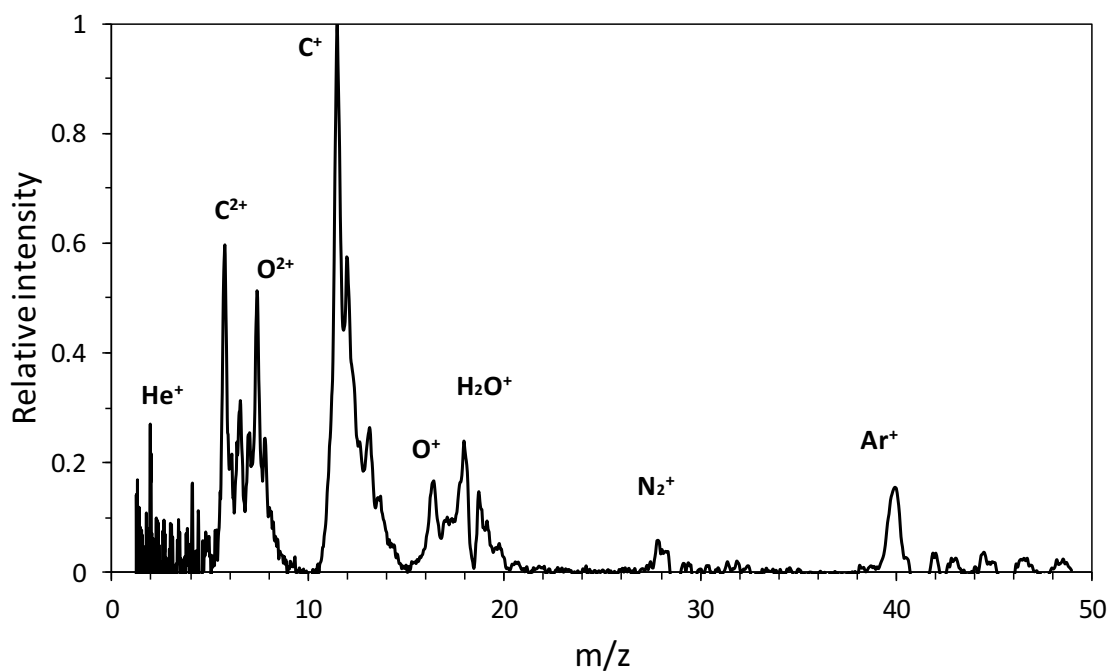


**Figure 7.12.** Mass spectrum collected with the EDU operating in ion mode, using an ion gauge as the ion source. The ion gauge produces “hot” ions with a range of energies, leading to peak spreading and shifting.

by the SDL instrument on a rocket will have an initial energy that is defined by the speed of the rocket relative to the ambient atmosphere, while the energy spread will be related to the velocity distribution of the ambient particles. In the lower regions of the MLT (Figure 1.2) the energy distributions of sampled ions may be similar to or even smaller than those used to produce Figures 7.10 and 7.11. At higher altitudes the energy distributions of ambient ions have the potential to be quite large, due to increased temperatures, which would complicate measurements made with a linear TOF-MS.

The experiments shown here demonstrate the ability of the SDL instrument to successfully operate and produce spectra in ion mode. Using the ion gun to generate well-defined ion beams, spectra were obtained that exhibited unit mass resolution at FWHM up through  $m/z$  40 (Figures 7.10 and 7.11). This covers a large portion of the range of gaseous ions of interest in the MLT. Figure 7.12 was obtained from a poorly defined source, in terms of energy spread, yet peaks from individual species were distinguishable. In this case the

versatility of the instrument was also demonstrated by operating in ion mode at  $10^{-4}$  Torr. Spectra collected in ion mode were later compared to a computer model of the instrument. These experiments provided validation for the model, allowing instrument operating parameters to be further studied as discussed in more detail in Chapter 8.

#### 7.2.3.2. Neutral Mode

Neutral particles must be ionized in order to be measured with a mass spectrometer; in the SDL instrument this is accomplished via EI (section 7.1). Electrical potentials applied to the different instrument components in neutral mode are discussed earlier, in section 3.1. In neutral mode the BNG served as both acceleration grid and the ion gate. Two examples of spectra obtained by operating the EDU in neutral mode are shown in Figures 7.13 and 7.14. To produce the spectrum in Figure 7.13, the BNG was centered on -200 V with  $V_{\text{def}} = \pm 60$  V, resulting in an ion energy of 284 eV. The spectrum in Figure 7.14 was produced with the BNG centered on -150 V, with  $V_{\text{def}} = \pm 40$  V. A bin width of 12.8 ns was used for Figure 7.13, and 3.2 ns for Figure 7.14.

The spectrum shown in Figure 7.13 was obtained at a pressure of  $5 \times 10^{-7}$  Torr under backfill from both  $\text{N}_2$  ( $m/z$  28) and Ar ( $m/z$  40). The peaks at these  $m/z$  values are especially prominent, with additional peaks appearing in the spectrum due to residual gases in the chamber. The cluster of peaks from  $m/z = 12$  to  $m/z = 20$  demonstrates unit mass resolution through this range; peaks at  $m/z$  values of 12, 14, 16, 17, 18, 19, and 20 are clearly visible and distinguishable. Molecular and atomic hydrogen both appear in the spectrum. Other interesting features of this spectrum include peaks from doubly ionized particles, as well as from fragmented molecules. The small peak at  $m/z = 20$  likely corresponds to  $\text{Ar}^{2+}$ , with  $\text{Ar}^+$  having a stronger peak at  $m/z = 40$ . Examples of fragments in Figure 7.13 include H (from  $\text{H}_2$  and  $\text{H}_2\text{O}$ ), C (from  $\text{CO}_2$ ), N (from  $\text{N}_2$ ), O (from  $\text{O}_2$ ), and OH (from  $\text{H}_2\text{O}$ ). The fragments result from EI-induced dissociation.

In contrast to Figure 7.13, which shows multiple peaks, Figure 7.14 has only two promi-

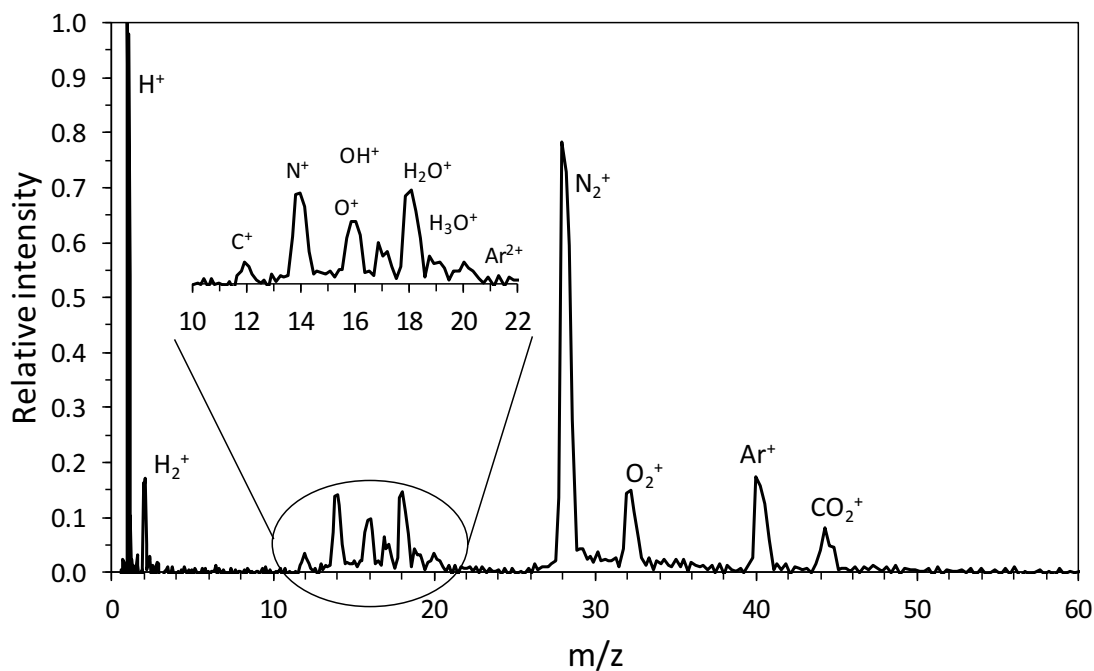


**Figure 7.13.** Mass spectrum produced with the EDU in neutral mode at  $5 \times 10^{-7}$  Torr, under nitrogen and argon backfill. Additional peaks are due to residual gases in the test chamber.

nent peaks. In part, this is because only argon was used as a backfill gas to produce this spectrum. Pressure also plays an important role; the backfill pressure was  $9 \times 10^{-5}$  Torr for the spectrum in Figure 7.14, while it was only in the mid  $10^{-7}$  Torr range for Figure 7.13. The minor peaks, due to residual gases, were simply overwhelmed by the amount of Ar backfill used to produce the spectrum in Figure 7.14, but were present in spectra taken at lower Ar backfill pressures on the same day. The larger peak (at  $m/z$  40) is due to  $\text{Ar}^+$ , and the smaller peak (at  $m/z$  20) is from  $\text{Ar}^{2+}$ . Based on their respective TOFs (4430 ns for  $m/z$  40 and 3130 ns for  $m/z$  20), both peaks in Figure 7.14 correspond to an energy of 238 eV. This suggests that the ionization is taking place between the second acceleration grid and the BNG, as described in section 3.1.1.

These experiments demonstrate the ability of the SDL instrument to operate in neutral mode and detect neutral particles over mass range covering major ambient species of interest in the MLT. The spectrum in Figure 7.13 shows that particles with  $m/z$  values up

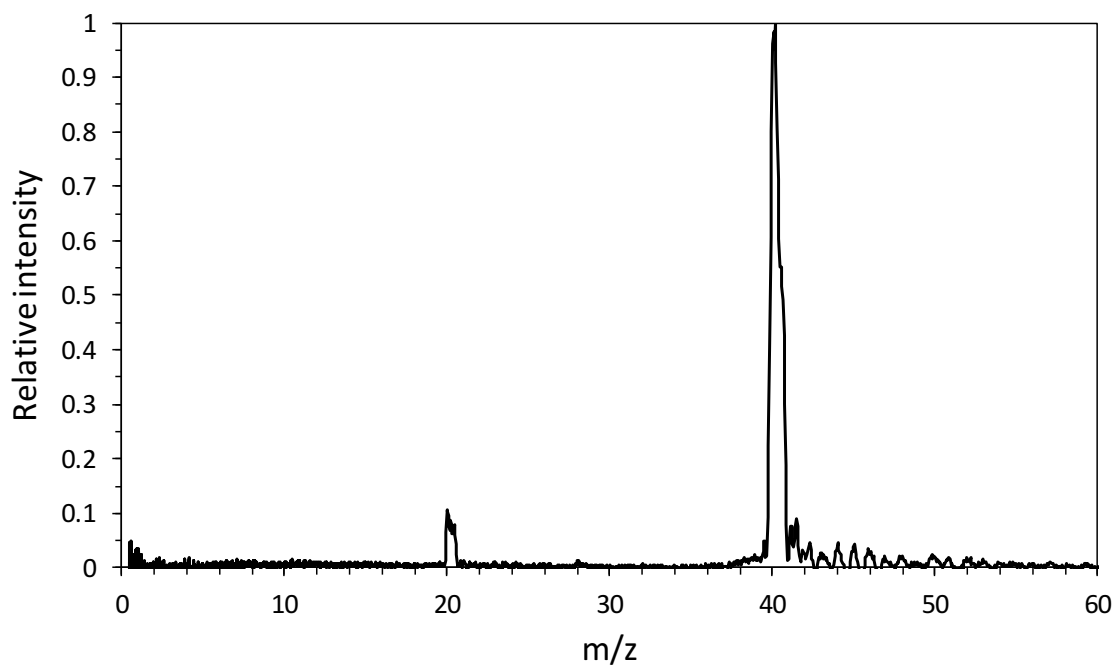


**Figure 7.14.** Mass spectrum produced with the EDU operating in neutral mode at  $9 \times 10^{-5}$ , under argon backfill. The large peak is due to singly ionized argon while the smaller peak is due to doubly ionized argon.

to at least 20 can be distinguished from neighboring particles separated by 1 m/z. Major MLT species that are not represented in Figure 7.13 include m/z 30 (NO) and 48 (O<sub>3</sub>). The resolution demonstrated by the EDU is sufficient to resolve m/z 30 (NO) from both N<sub>2</sub> and O<sub>2</sub>, at least for the peak height levels shown in Figure 7.13, although minor peaks from isotopes of major species (e.g., <sup>30</sup>N<sub>2</sub>) may complicate the measurement. The m/z 48 peak would be far enough from neighboring peaks (CO<sub>2</sub> at m/z 44, for example) that it should be resolved without difficulty. Improvements in the BNG modulation pulse will decrease baseline noise and enhance the definition of ion packets, leading to more improved mass resolution.

#### 7.2.3.3. Resolution

Resolution is a term used in mass spectrometry to describe the ability to distinguish peaks that are separated by a small difference in m/z [*de Hoffmann and Stroobant, 2007*].

In addition to the discussion in this section, resolution is further discussed in section 8.2 from a simulation standpoint. Some factors that affect the resolution of a TOF-MS instrument are drift length, start-pulse width, acceleration potential, bin size, and the energy distribution of sampled ions. One factor affecting resolution that is unique to the EDU is the BNG modulation waveform. Ideally, the modulation pulses would be perfect square waves (infinitesimally small rise/fall times, no ringing); but this is difficult to attain in practice. For an ideal start pulse, the ion flux through the BNG would be nominally uniform during the beam-on state. The BNG modulation waveform used to generate the spectra presented in this chapter is shown in Figure 7.9 and is a triangle wave instead of a square wave. In actuality, the ion flux through the BNG begins at the onset of the start pulse and continues to increase until midway through the pulse, at which point it decreases until the end of the pulse. The rise/fall time of the pulse is approximately 30 ns.

Varying the BNG offset potential ( $V_{\text{def}}$ ) would have very little effect on mass resolution for a perfectly square modulation waveform. But, since the modulation pulses are triangle, not square waves, the BNG offset potential does affect the mass resolution of the EDU. Figure 7.15 shows the effect of  $V_{\text{def}}$  on resolution (measured at FWHM) for argon ions ( $m/z = 40$ ) with energies of 100 and 200 eV, with the EDU operating in ion mode. The ion beam used to produce the data in Figure 7.15 had an energy spread of 0.6 eV at FWHM. In general, mass resolution increases as  $V_{\text{def}}$  increases, with the exception of the data point at  $V_{\text{def}} = 20$  V for the 200 eV ions. The data point in question has an artificially high resolution, due to a secondary peak, which is nearly half as high as the main peak in the spectrum. At this value of  $V_{\text{def}}$ , there is a slight overlap in the BNG modulation pulse, because the pulse amplitude is about 23 V. If the resolution at  $V_{\text{def}}$  is adjusted to compensate for this secondary peak, equivalent to measuring the resolution at 48% of the peak height, then Figure 7.16 more accurately describes the effect of  $V_{\text{def}}$  on mass resolution for the EDU.

The spectrum in Figure 7.17 has a FWHM resolution of 100 (at  $m/z$  40) and represents

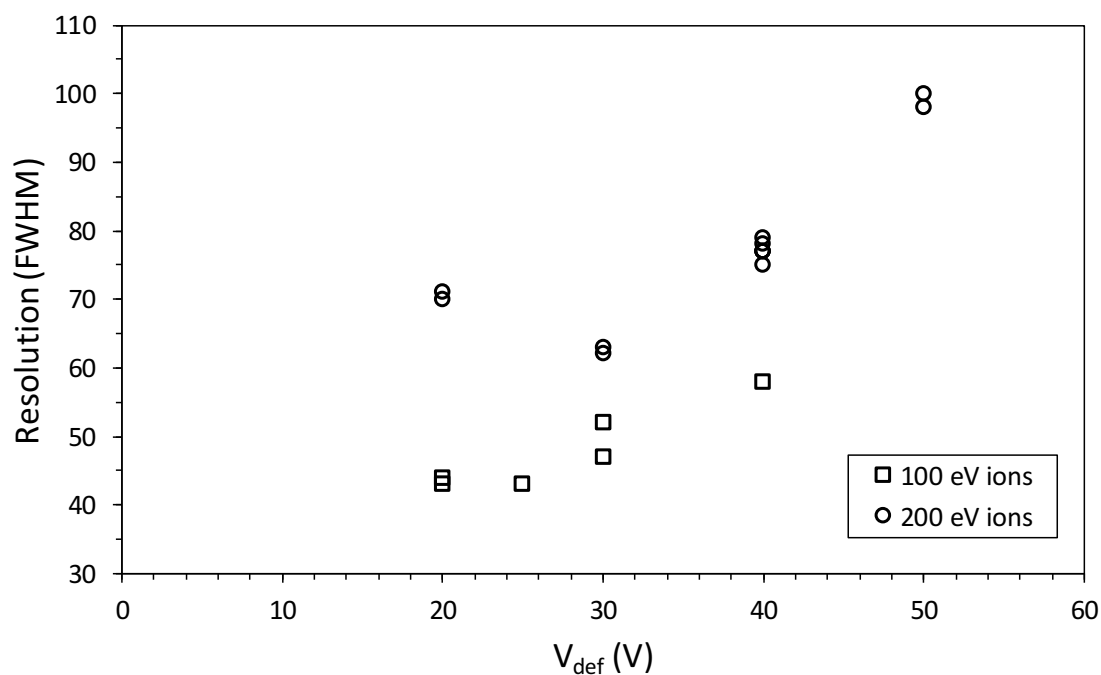


**Figure 7.15.** Effect of BNG deflection offset voltage ( $V_{\text{def}}$ ) on mass resolution. Resolution was measured at FWHM of the  $m/z$  40 peak.

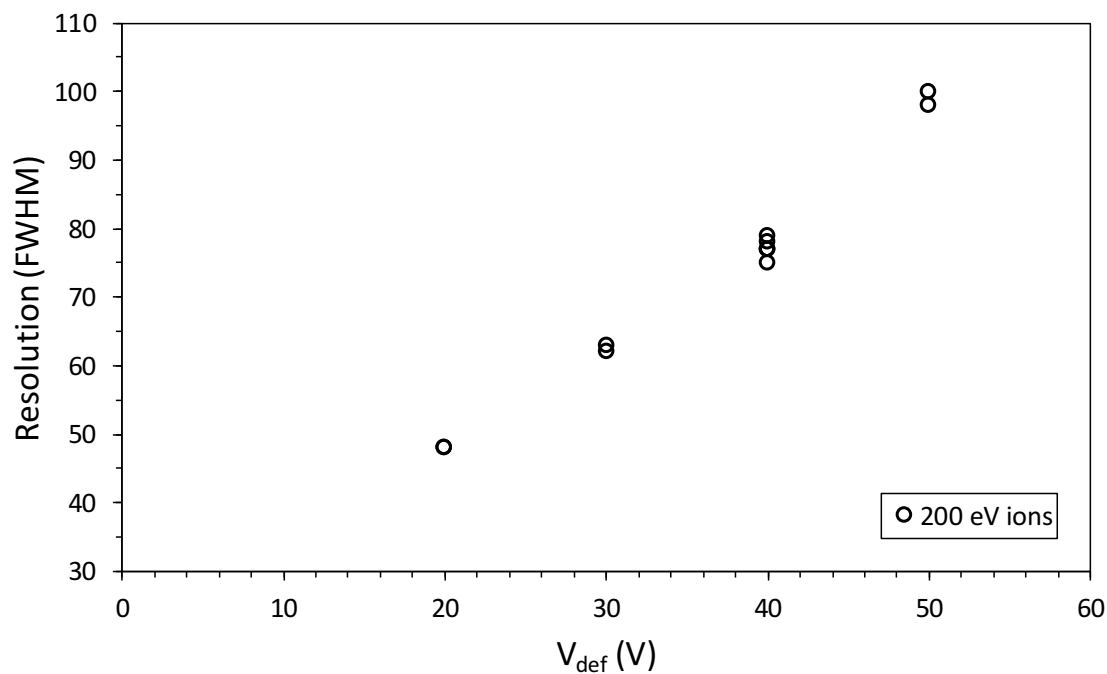


**Figure 7.16.** Effect of BNG deflection offset voltage ( $V_{\text{def}}$ ) on mass resolution of the EDU for ion energies of 200 eV. The data point at  $V_{\text{def}} = 20$  V has been adjusted to compensate for the shape of the  $m/z$  40 peak in the mass spectrum.

the highest-resolution spectrum obtained during laboratory testing of the EDU. The resolution at 10% of the peak height is 44, sufficient to achieve unit mass resolution up through  $m/z$  40 (argon). The spectrum was obtained in ion mode, using a 20.7 eV ion beam with an energy spread of 0.6 eV at FWHM. Ions were accelerated inside the instrument to a total energy of 200 eV. The start pulse width was 40 ns (see Figure 7.9) and  $V_{\text{def}}$  was  $\pm 50$  V.

#### 7.2.3.4. High-pressure Instrument Performance

The most important motivation for the SDL instrument was to develop a TOF-MS capable of operating at pressures likely to be encountered in the MLT (Chapter 1). This is a multipart challenge, involving the operation of an MCP detector at elevated pressures (Chapter 4), as well as mfp considerations for ions transiting the drift region (Chapter 6). With this in mind, an experiment was performed to study the effect of pressure on the mass resolution of the EDU. Mass spectra were collected at pressures ranging from  $3 \times 10^{-7}$  to  $2 \times 10^{-4}$  Torr under argon backfill. The EDU was operated in neutral mode for these ex-

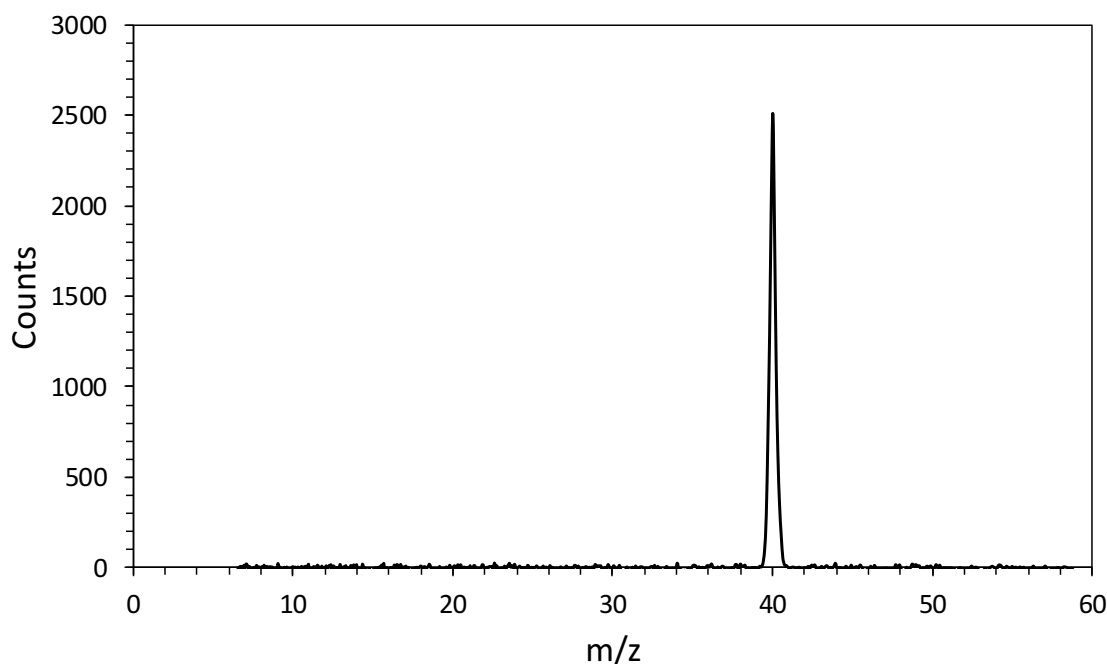


**Figure 7.17.** Highest resolution mass spectrum obtained with the EDU during laboratory testing. FWHM resolution is 100, with a resolution of 44 at 10% of peak height.

periments, with the high-transmission grids held at 100 V. The BNG was centered on -150 V with  $V_{\text{def}} = \pm 40$  V, resulting in ion energies of 238 eV. Resolution was measured at the FWHM level on the argon peak ( $m/z = 40$ ).

Figure 7.18 shows the mass resolution of the  $m/z$  40 peak plotted against the backfill pressure. The mfp limit (see section 6.1.3) is defined here as the pressure below which 90% of ions transit the drift region collision-free. This occurs at a pressure of approximately  $3.5 \times 10^{-5}$  Torr for the EDU, and is denoted in the figure. At pressures below  $10^{-5}$  Torr the resolution exhibits some scatter, ranging between 55 and 59, but has no clear trend. Between  $10^{-5}$  and  $3.5 \times 10^{-5}$  Torr, the resolution begins to degrade. The resolution drops sharply above  $3.5 \times 10^{-5}$  Torr. The MCP HV power supply tripped shortly after collecting the spectrum at  $2 \times 10^{-4}$  Torr, which is the highest pressure at which the EDU has operated.

For resolution measured at the FWHM level for  $m/z$  40, the EDU produced spectra with better than unit mass resolution over the entire range of pressures shown in Figure 7.18. The

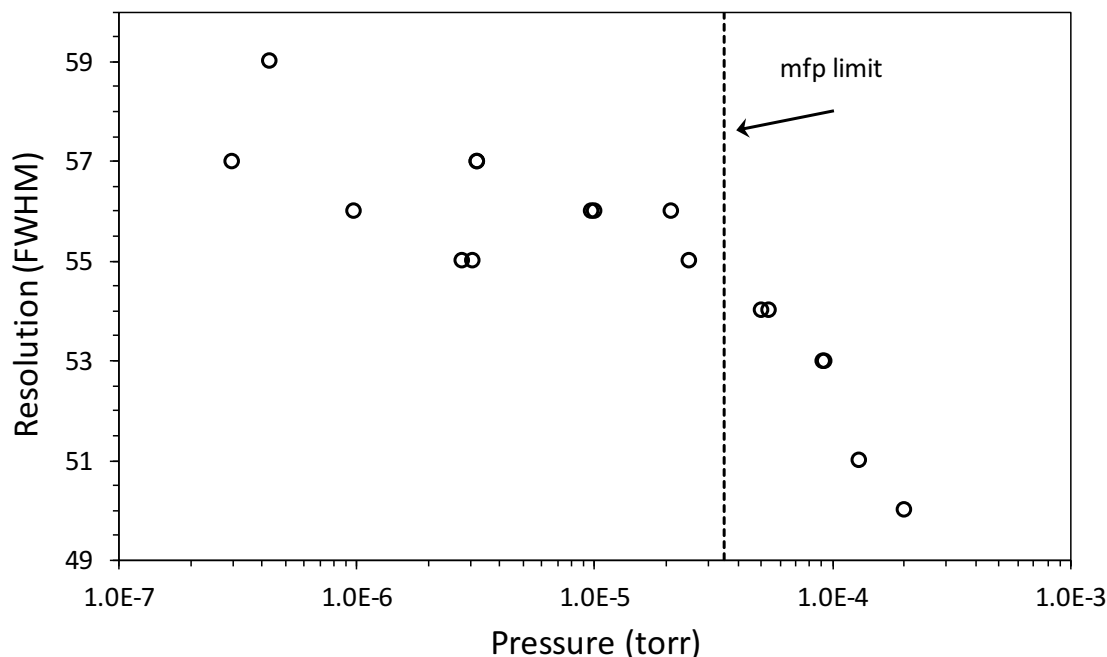


**Figure 7.18.** Pressure effects on mass resolution for the EDU. Based on spectra obtained under argon backfill. Resolution as measured at the FWHM level.

data shown here suggest that for optimal resolution, the EDU should be operated at or below  $10^{-5}$  Torr. This is an order of magnitude above the recommended MCP operating pressure. These experiments also show that, if the resulting resolution degradation is acceptable, the SDL TOF-MS can be operated at pressures between  $10^{-5}$  and  $10^{-4}$  Torr. In neutral mode at least, pressures higher than  $10^{-4}$  Torr should be avoided to prevent MCP discharge events. The pressure effects on mass resolution have not been tested with the EDU in ion mode, although in this mode, the instrument has successfully operated at  $10^{-4}$  Torr. The lower background in ion mode may allow the instrument to operate at even higher pressures.

### 7.3. Conclusions

Experimental results presented in this chapter validate the concept and design of the SDL instrument. The instrument operated as expected in ion mode, producing spectra using both an ion gun and an ion gauge as sources. The instrument also successfully operated in neutral mode, even though the actual instrument settings used differed from what was expected. The EDU routinely generated mass spectra with FWHM resolutions of 50 and higher at  $m/z$  40, even at pressures as high as  $10^{-4}$  Torr. The EDU achieved a maximum mass resolution of 100 (at  $m/z$  40) while operating in ion mode. These important results demonstrate that the SDL TOF-MS is capable of resolving the major gaseous species present in the MLT.

The experiments and results described in this chapter led to modeling efforts (Chapter 8) to study the effects of critical instrument operating parameters on mass resolution. Improvements in further generations of the SDL TOF-MS will enhance instrument performance. For example, improvements in the BNG modulation waveform generator electronics, leading to faster rise and fall times, will improve mass resolution. Likewise, further development of the ionizer to decrease the energy spread in sampled ions will lead to improved mass resolution in neutral mode. Finally, eliminating the electronic interference associated with the BNG modulation pulses will allow the SDL TOF-MS to operate in

HT mode as originally intended. These advancements will improve an instrument that has already demonstrated the ability to resolve major species of interest in the MLT.

## CHAPTER 8

## INSTRUMENT PERFORMANCE MODELING: MASS RESOLUTION

Mass resolution describes the ability to distinguish peaks from species with slightly different masses in a mass spectrum [*de Hoffmann and Stroobant, 2007*]. For example, a mass resolution of 40 means that two adjacent peaks (at least unit mass separation) of  $m/z$  40 or less and with similar heights, can be distinguished. Equation 1.8, repeated here, is the definition of mass resolution for TOF-MS

$$\frac{m}{\Delta m} = \frac{t}{2\Delta t}. \quad (8.1)$$

In equation 8.1  $m$  is the mass at the peak and  $\Delta m$  is the width of the peak at a certain height [*Cotter, 1997*];  $t$  and  $\Delta t$  also represent the peak and its width, but in terms of TOF. Common values at which to measure  $\Delta m$  are 50% (FWHM), 10%, and 5% of the peak height [*Russell and Edmondson, 1997; de Hoffmann and Stroobant, 2007*]. Major factors that affect resolution in TOF-MS instruments are the temporal width of the start pulse, length of the drift region, and the energy spread of sampled ions. Results from sets of three simple simulations performed using Microsoft<sup>®</sup> Excel<sup>®</sup> are given in section 8.1 to illustrate the individual effects of each of these factors. Section 8.2 presents results from more realistic simulations of the SDL TOF-MS. These simulations were performed using MATLAB<sup>®</sup> and consider additional factors including ion energy and bin size of the TOF spectrum. Simulations of the SDL instrument operating *in-situ* in the MLT are presented in section 8.3.

### 8.1. Mass Resolution for TOF-MS in General

This section illustrates the general effects of start-pulse width, drift length, and energy spread on mass resolution. Each factor is considered individually. The particles in each simulation are assumed to have a mass of 40 u, corresponding to argon. Mass resolution

is simulated for ion beam energies ranging from 100 to 300 eV. The simulations calculate the average TOF,  $t_{\text{ave}}$ , of particles in a pulse, as well as the TOFs of the slowest and fastest particles. The TOFs of the earliest and latest arriving particles ( $t_{\text{min}}$  and  $t_{\text{max}}$ ) are used to calculate  $\Delta t$ , and resolution is calculated as  $t/2\Delta t$ , as given in equation 8.1.

### 8.1.1. Effect of Pulse Width on Mass Resolution

Pulse width refers to the temporal length of the ion pulse as it enters the field-free drift region. To investigate the effect of pulse width on mass resolution, simulated ions were given a uniform energy (i.e., zero energy spread), but not necessarily the same start times. The ion start-time distribution was uniform, and pulse widths from 5 ns to 80 ns were simulated. The drift length was 15 cm. There were assumed to be no other factors affecting resolution. The drift time for each ion crossing the drift region is similar to equation 1.4, but with an added time factor,  $t_0$ , to reflect the time relative to the beginning of the start pulse when the ion entered the drift region. This time can be expressed as

$$t = D\sqrt{\frac{m}{2qV}} + t_0. \quad (8.2)$$

If  $t_p$  is the temporal width of the ion pulse, then the average drift time for ions from a single pulse is

$$t_{\text{ave}} = D\sqrt{\frac{m}{2qV}} + \frac{t_p}{2}. \quad (8.3)$$

The minimum and maximum drift times are given by

$$t_{\text{min}} = D\sqrt{\frac{m}{2qV}}, \quad (8.4)$$

and

$$t_{\text{max}} = D\sqrt{\frac{m}{2qV}} + t_p. \quad (8.5)$$

Using equation 8.1,  $\Delta t = t_{\max} - t_{\min} = t_p$ . The resolution for different pulse widths at ion energies ranging from 100 to 300 eV is shown in Figure 8.1. These results show that for a given ion energy, a shorter pulse width yields a higher resolution. This is expected, because the pulse width is reflected in the arrival times of ions at the end of the drift region (see equations 8.4 and 8.5). The effect of shorter pulses on mass resolution is more pronounced at lower ion energies. This is easily seen by considering the limiting case of very low ion energy, leading to a large  $t$  in equation 8.1, while  $\Delta t$  remains the pulse width,  $t_p$ .

### 8.1.2. Effect of Drift Length on Mass Resolution

The effect of the length of the field-free drift region on mass resolution is due to the amount of time that ions spend in the drift region. To investigate this effect a simple simulation with varying drift lengths was performed. The pulse width was 10 ns, and simulated ions had a uniform energy (no energy spread). There were assumed to be no other factors affecting resolution. The average drift time for ions is the same as equation 8.3. The

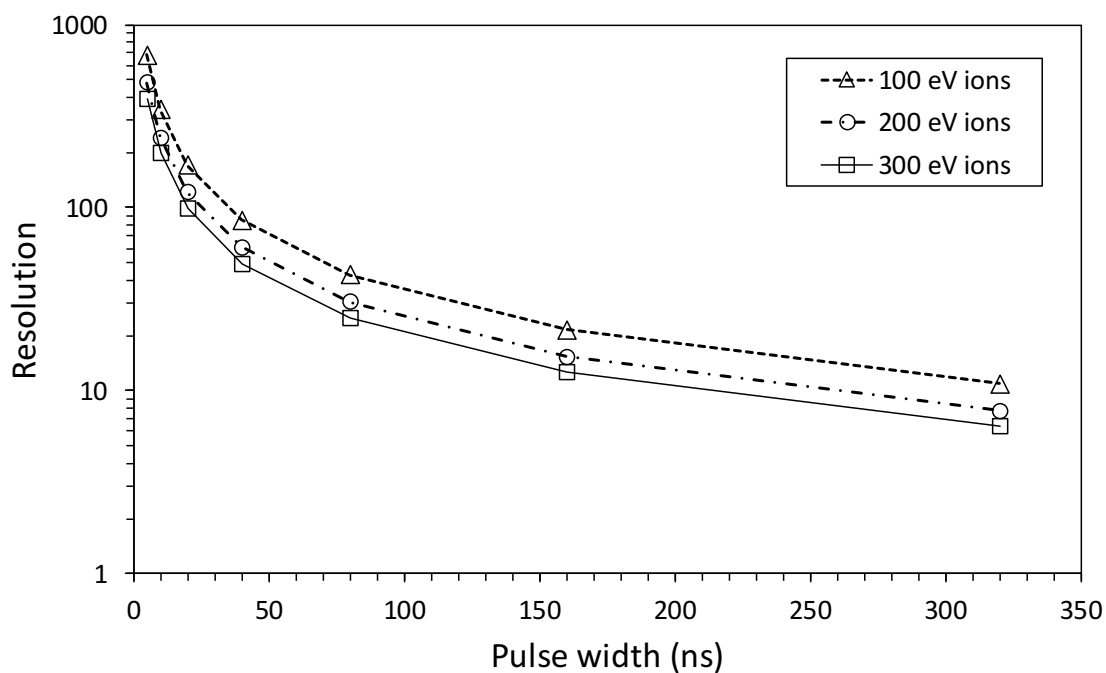


**Figure 8.1.** Effect of pulse width on mass resolution.

minimum and maximum drift times are identical to equations 8.4 and 8.5. Drift lengths from 0.05 to 1.0 m were simulated. The simulation confirms that mass resolution improves with increasing drift length, as shown in Figure 8.2. A longer drift distance results in an increased ion travel time,  $t$ , in equation 1.8. If  $\Delta t$  in equation 1.8 remains constant, then an increase in  $t$  results in improved mass resolution.

### 8.1.3. Energy Spread Effects on Mass Resolution

Energy spread refers to the initial kinetic energy distribution of sampled ions. Ions with less energy require more time to cross the drift region compared to more energetic ions of the same  $m/z$  value. To simulate this effect, infinitesimally small ion pulses were given a uniform (square) energy distribution. The width of the energy distribution was  $\Delta E$  and centered about the mean ion energy,  $E$ . The kinetic energy of particles in the simulation ranged from  $E - \Delta E/2$  to  $E + \Delta E/2$ , where  $E = qV$  in equation 1.4. The length of the

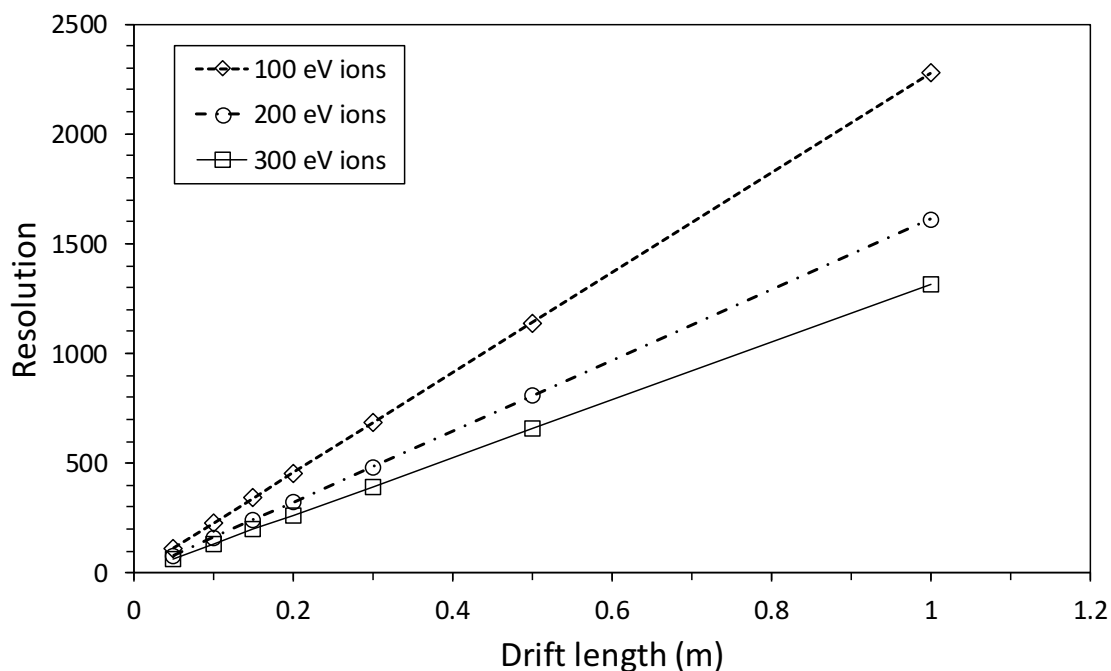


**Figure 8.2.** Effect of drift length on mass resolution.

field-free drift region was 15 cm. The TOF for the fastest particles is given by

$$t_{\min} = D \sqrt{\frac{m}{2(E + \frac{\Delta E}{2})}}, \quad (8.6)$$

and the TOF for the slowest particles is given by

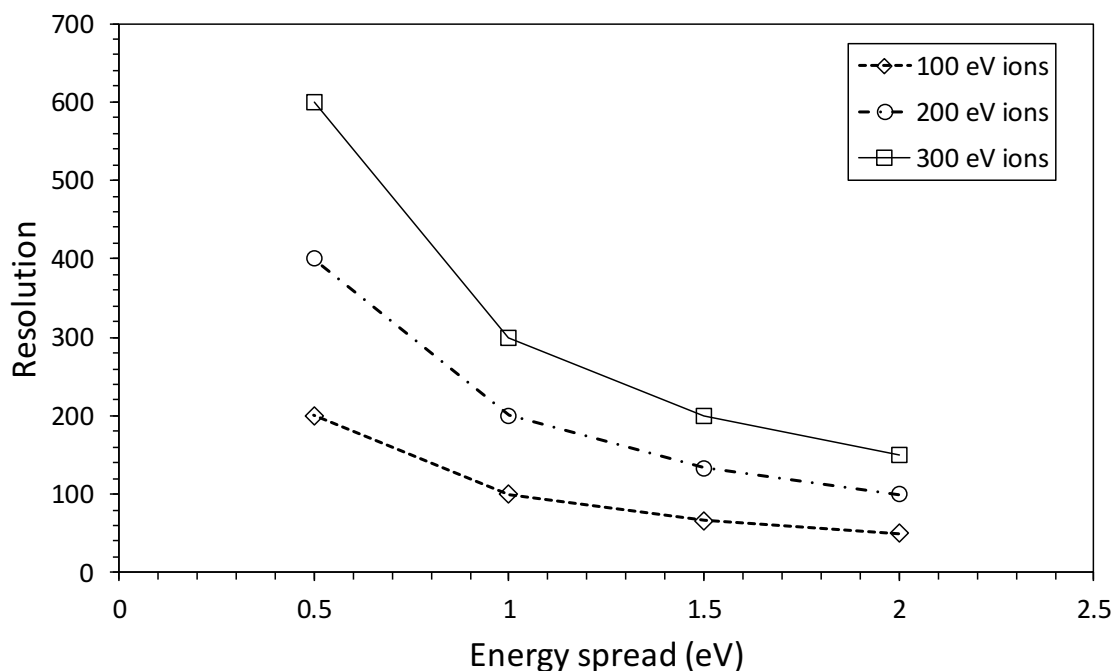
$$t_{\max} = D \sqrt{\frac{m}{2(E - \frac{\Delta E}{2})}}. \quad (8.7)$$

Figure 8.3 shows the simulation results for energy spreads of 0.5 eV, 1.0 eV, 1.5 eV, and 2.0 eV. The highest resolution was achieved for the smallest energy spread, 0.5 eV. This was expected, as smaller initial energy spreads result in a smaller arrival time distribution. Figure 8.3 shows another interesting trend: the energy of the sampled ions also affects resolution. Resolution increases as the ion energy increases. This can be explained by considering that at increasing ion energies, less time is available for ions to be affected by the initial energy spread. Simply stated,  $\Delta t$  in equation 8.1 decreases faster than  $t$ .

#### 8.1.4. Discussion of General Mass Resolution Simulations

Three factors that affect the resolution of a TOF-MS instrument were considered in this section: pulse width, drift length, and energy spread. The effects of each of these factors are shown in Figures 8.1 - 8.3. The combined results of these simulations indicate that the highest mass resolution with a TOF-MS instrument would be achieved by sampling ions with a small energy spread, using a short pulse width, combined with a long drift length.

Figure 8.1 seems to suggest that infinitesimally small ion pulses are best; however, there are some practical considerations to take into account. First, a pulse must have a finite size. Second, pulse widths are electronics limited. Shorter pulses are more difficult to achieve than longer pulses. The start pulses generated by the MDB have a rise/fall time of about 30 ns, which limits the minimum achievable pulse for the EDU. Also, the pulse width does not change the amount of time required for ions to travel through the drift region. Thus,



**Figure 8.3.** Effect of energy spread on mass resolution.

shorter pulses result in a lower instrument duty cycle.

Figure 8.2 shows an improvement in mass resolution as the drift length increases. As a practical matter, the drift length of a TOF-MS instrument must be small enough to allow the instrument to be placed where it will be used. In the case of the SDL instrument, it must fit on a rocket or satellite. Additionally, increasing the drift length raises the probability of collisions between sampled ions and residual gas particles, necessitating a lower pressure to meet the mfp requirement. One way to increase drift length is to employ a reflectron, although the primary purpose of a reflectron is to correct for the kinetic energy spread in sampled ions.

From Figure 8.3, it is obvious that the more uniform the energy of sampled ions, the better the mass resolution. In reality, it is difficult to eliminate the energy spread of sampled ions. Fortunately, the negative effects of energy spread can largely be compensated for by employing a reflectron (see section 1.3.2).

The results presented in this section (8.1) are idealizations: only one factor was varied

in each of the three cases considered. In practice, it is unlikely that any of these resolution-degrading factors can be entirely eliminated. Most likely, several different factors will affect resolution. Potential factors affecting mass resolution include: instrument pressure (mfp considerations), time of particle ionization, ion energy, initial energy spread, ion position at the beginning of a start pulse, and bin size. The challenge is to compensate for these factors and achieve the desired mass resolution in a practicable instrument package.

## 8.2. Resolution Simulations for the SDL TOF-MS

A Monte Carlo model written by the author, using MATLAB<sup>®</sup>, was developed to simulate the SDL TOF-MS. Design and development of the SDL instrument is described in detail in Chapters 2 and 3. Model inputs include: start-pulse width, field-free drift length, ion energy (i.e., acceleration potential), FWHM of the energy spread of simulated particles, and bin size of the TOF spectrum. All of these model inputs are user-adjustable, which allows the user to simulate the effects of different operating parameters on instrument resolution.

The model assigns a random start time,  $t_0$ , to each simulated ion based on the start-pulse width. The rather unrealistic uniform energy distribution used in section 8.1 was replaced with a more realistic normal distribution, which is similar to the ion beam energy profiles observed during laboratory testing of the EDU (see Figure 7.1). Each simulated ion is assigned a random energy corresponding to a normal distribution centered about the user-defined ion energy. The energy spread FWHM is also user defined. The time required for each simulated ion to travel the drift distance is then calculated using

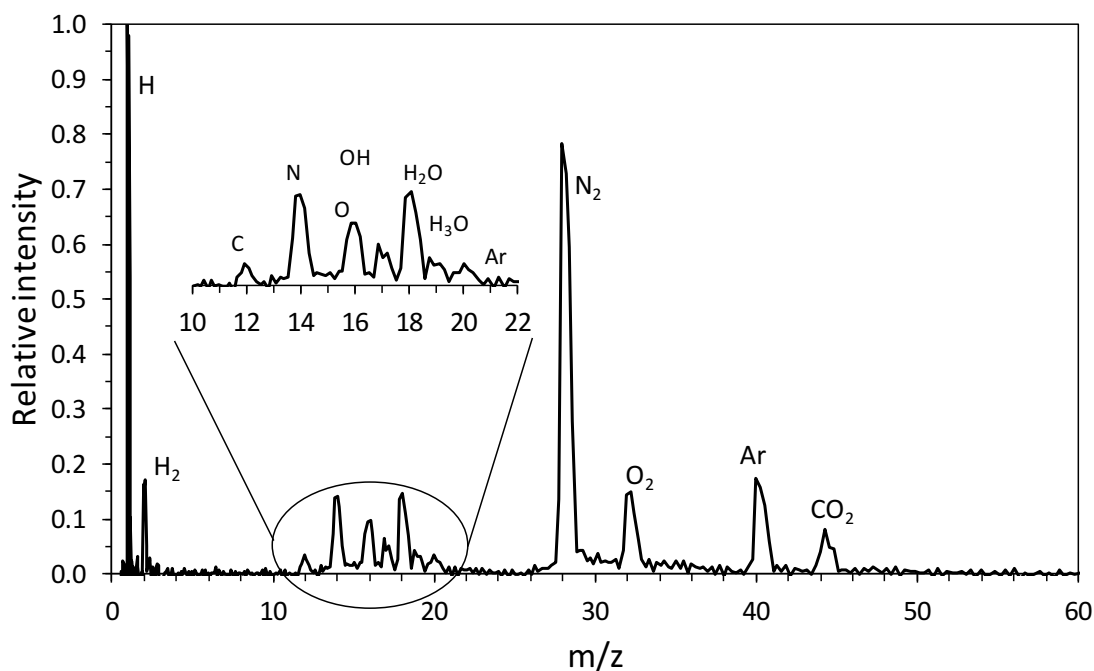
$$t = t_0 + D\sqrt{\frac{m}{2E}}, \quad (8.8)$$

which is similar to equations 1.4 and 8.2, but with  $E = q \cdot V_{acc}$ .  $D$  is the drift length of the simulated instrument and  $m$  is the mass of the simulated particles. As a note, all of the

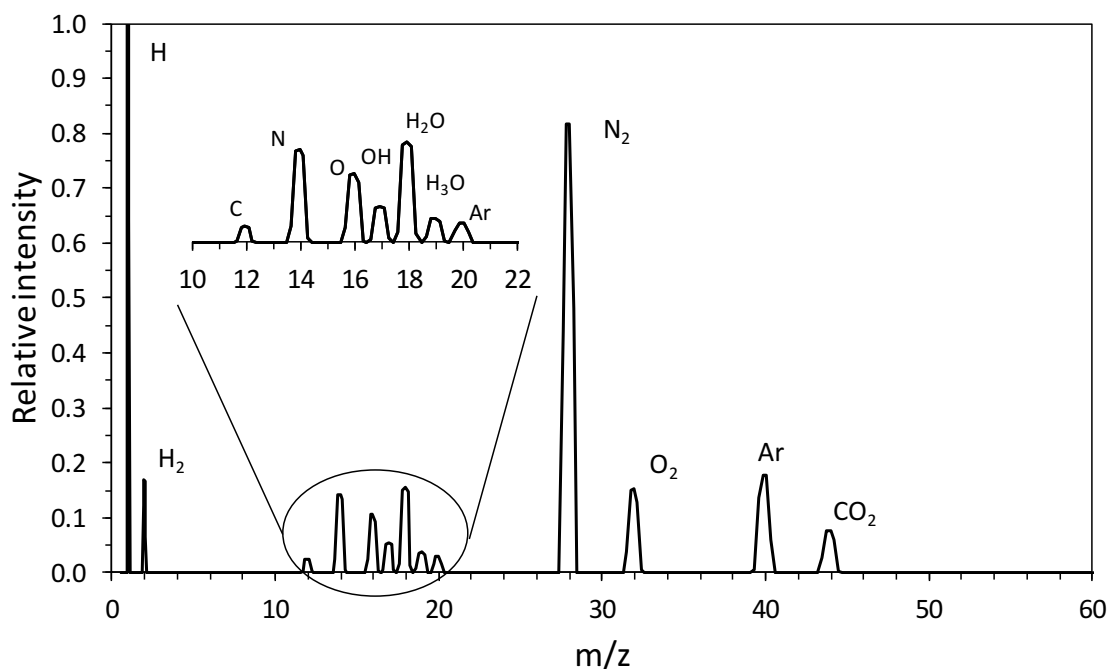
results in sections 8.2.1 - 8.2.5 assumed  $^{40}\text{Ar}$  for simulated ions. After  $t$  is calculated for each ion, the arrival times are binned and the resolution is calculated using equation 1.8.

Figure 8.4 is an actual spectrum obtained with the EDU and is the same spectrum shown in Figure 7.13. For comparison, a spectrum produced using the Monte Carlo methods described above is shown in Figure 8.5.

Additional masses were included in the simulation, with the number of simulated particles being adjusted to match the peak heights in the experimental spectrum. The pulse width (40 ns) and TOF bin width (12.8 ns) settings used to generate Figure 8.4 were also used in the model. The model assumed an ion energy of 283.7 eV, for consistency with the experiment. Instead of defining the energy spread at the FWHM level, the initial ion energy was based on a Maxwell velocity distribution at 290 K to generate the simulated spectrum in Figure 7.13. The simulated and experimental spectrums agree very well qualitatively.



**Figure 8.4.** Neutral mass spectrum collected with the EDU. This is the same as Figure 7.13, and is repeated here for comparison with the simulated mass spectrum in Figure 8.5. Experimental details for this spectrum are given in section 7.2.3.2.



**Figure 8.5.** Simulated mass spectrum, using the Monte Carlo methods described in section 8.2. Compare with Figure 8.4.

Additionally, the FWHM resolution for the  $N_2$  peak ( $m/z$  28) is 40 for the experimental spectrum and 41 for the simulated spectrum. These results validate the Monte Carlo model used here to study the effects of various operating parameters of the SDL TOF-MS.

Convergence of the Monte Carlo model was tested by running the simulation for different numbers of ions; each number of ions was tested 10 times. Simulation parameters were: 200 eV ion energy, 2 eV FWHM energy spread, 20 ns start pulse width, 6 ns bin size, and 15 cm drift length. Mass resolution was measured (at  $m/z$  40) for each simulation run, and an average resolution and standard deviation of the mean resolution was recorded. Figure 8.6 shows the average resolution of 10 model runs for each simulated number of ions. The resolution quickly converges for  $10^4$  simulated ions; there is no significant change in resolution out to  $10^6$  simulated ions. The standard deviation of the mean resolution (10 model runs) for each amount of simulated ions tested is shown in Figure 8.7. The standard deviation of the mean resolution, measured at FWHM (FW10%M), is 0.12 (0.06) for  $10^5$

simulated ions.

The results presented in sections 8.2.1 – 8.2.5 each represent the average resolution for 10 model runs, with each run using  $1 \times 10^5$  simulated ions. Except where otherwise noted, simulated instrument parameters were: ion energy, 200 eV; initial spread in ion energy at FWHM, 1 eV; TOF bin size, 6 ns; drift length, 15 cm; start pulse width, 20 ns. The effects of each of these parameters on instrument resolution were tested with the Monte Carlo simulation. Results are presented at the 50% and 10% level of the  $m/z$  40 peak.

### 8.2.1. Energy Spread

The Monte Carlo model was used to simulate the effects of initial energy spreads ranging from 0.005 to 2 eV, measured at FWHM, on instrument resolution. The energy distributions were normally distributed and centered on an ion energy of 200 eV. Results from these simulations are shown in Figure 8.8. Resolution was expected to improve as the energy spread decreased. Instead, resolution reached a maximum at an energy FWHM value

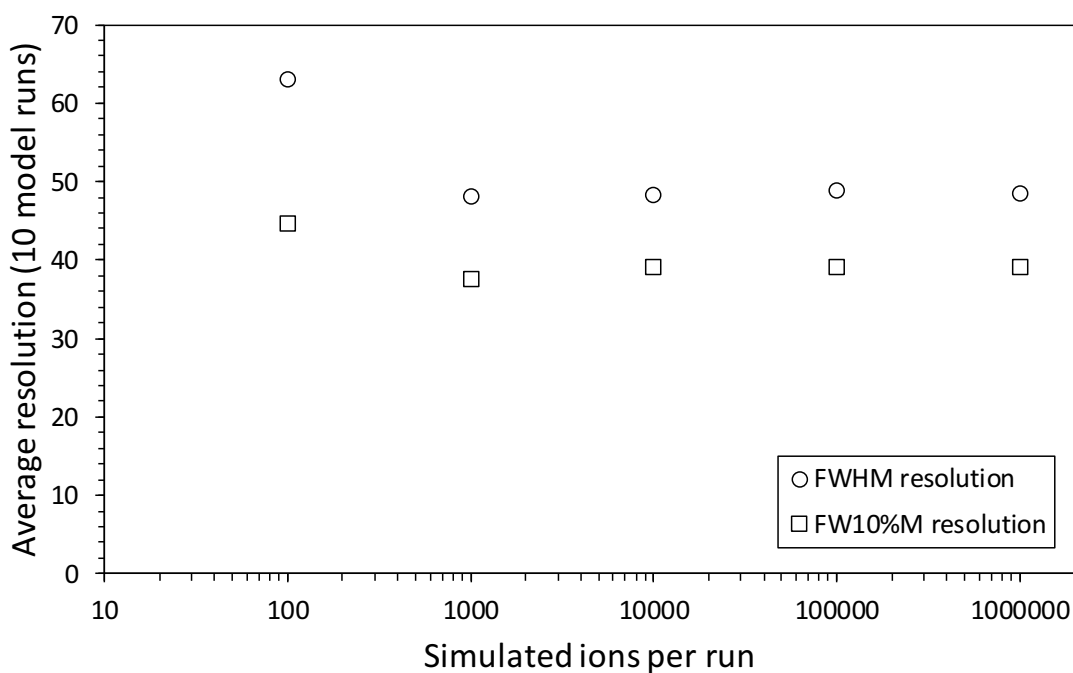


**Figure 8.6.** Convergence testing of the SDL instrument Monte Carlo model: average resolution. Each data point represents the average resolution from 10 runs of the model.

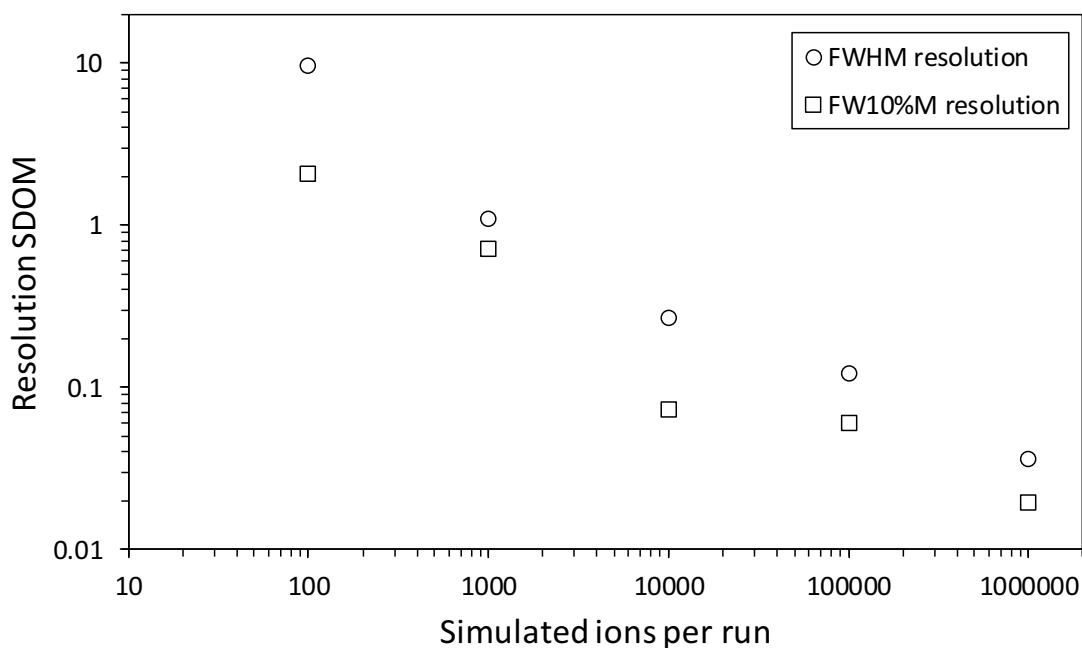


**Figure 8.7.** Convergence testing of the SDL instrument Monte Carlo model: standard deviation. Each data point represents the standard deviation of the mean resolution for 10 model runs.

of about 0.2 eV; no improvement in resolution occurred at lower energy spreads.

Improved resolution was obtained by running the simulation with TOF bins of 3 ns width (results not shown), but the resolution plateau at energy FWHMs lower than 0.2 eV was again observed. Similar results were observed for start-pulse widths of 10 ns and 2 ns, as well as for variations in ion energy (results not shown). In contrast, changing the field-free drift length did affect the onset of the resolution plateau. Employing shorter drift lengths in the simulations caused the resolution plateau to shift toward higher energy FWHMs. For a given drift length, reducing the simulated energy FWHM below a certain amount does not improve resolution. Drift length, therefore, appears to be the driving factor responsible for the location of the resolution plateau observed in Figure 8.8. This is not to say that resolution cannot be improved below a certain energy spread; it can. But below a certain point, energy spread becomes a nonfactor and instrument operating parameters must be adjusted to achieve improved resolution.

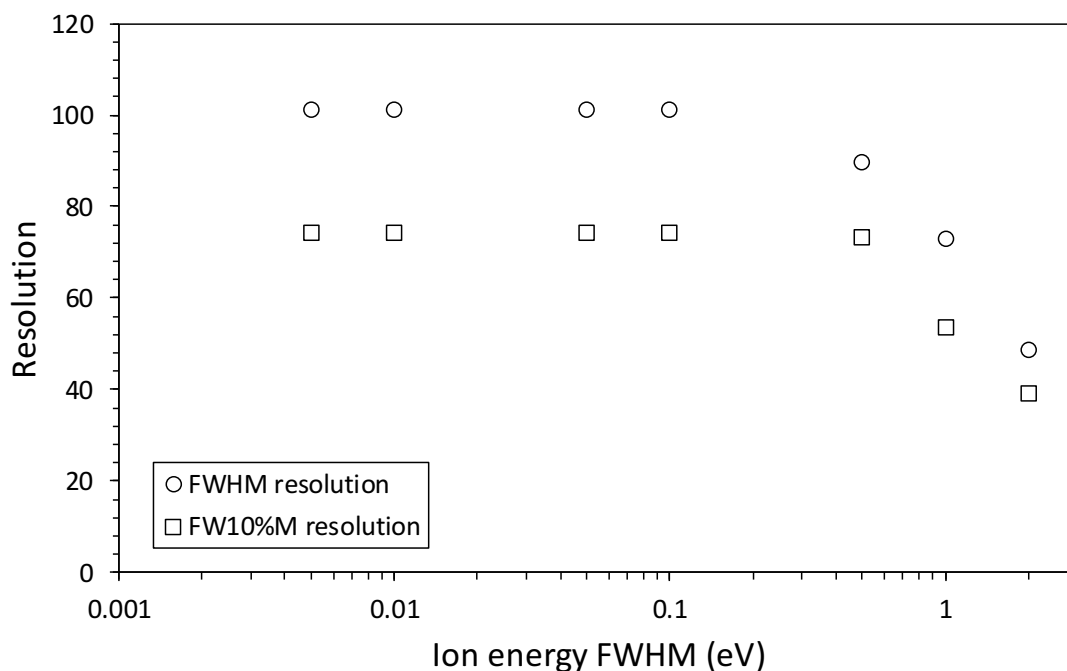


**Figure 8.8.** Simulated effect of ion energy FWHM on mass resolution for the SDL instrument.

### 8.2.2. Start Pulse Width

The effect of the start pulse width on mass resolution for the SDL instrument was also studied with the Monte Carlo model. Results from these simulations are presented in Figure 8.9 and show that shorter start pulses result in higher mass resolution. This was expected; as the start pulse decreases,  $\Delta t$  in equation 8.8 becomes smaller.

Although resolution improves with smaller start pulses, practical considerations must be taken into account. Shorter pulses are more difficult to produce and they result in a lower duty cycle, which has negative implications for instrument sensitivity. Reducing the start pulse width below the TOF bin size does not significantly improve resolution. Regardless of how short the ion pulse, TOFs for individual ions are still recorded in bins with finite size. Energy spread in sampled ions also diminishes the returns from shorter start pulses. For example, two ions that share the same start time,  $t_0$ , but have energies of 199 eV and 201 eV (recall, this simulation assumed an energy spread of 1 eV at FWHM) will differ in

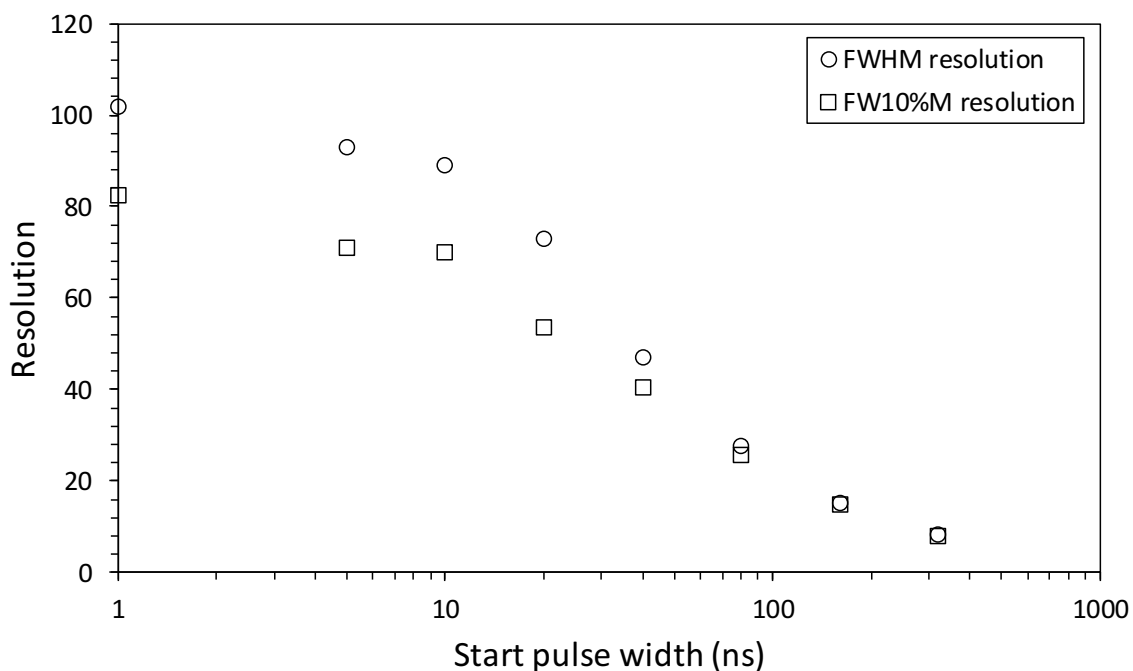


**Figure 8.9.** Simulated effect of start pulse width on mass resolution for the SDL instrument.

TOF by 24 ns. Even ions of 199.5 eV and 200.5 eV, with the same start time, will differ in TOF by 12 ns. Despite this, it should be remembered that shorter start-pulses do not degrade resolution.

### 8.2.3. Drift Length

Instrument performance in terms of mass resolution was simulated for drift lengths ranging from 0.05 to 1.0 m. Results from these simulations (Figure 8.10) display behavior that was unexpected. Instead of resolution continuously improving at increasing drift lengths, as in section 8.1.2, the resolution in Figure 8.10 quickly plateaus at a drift length of about 0.4 m. The energy spread of the simulated ions appears to be responsible for this plateau. The TOF for ions with the average ion energy doubles when the drift length is doubled. The difference in TOFs for two ions starting at the same  $t_0$ , but with different energies, also doubles when the drift length is doubled. The TOF difference for ions with different energies is closely related to  $\Delta t$  in equation 1.8. Examination of equation

1.8 shows that if  $t$  and  $\Delta t$  increase at the same rate, resolution will decrease. In fact, the factor of 2 in the denominator of equation 1.8 means that resolution will improve only if  $t$  increases at least twice as fast as  $\Delta t$ .

The simulation was run again, but with a smaller energy spread of 0.5 eV at FWHM. Results from these simulations (Figure 8.11) again show mass resolution initially improving, but again plateauing between drift lengths of 0.6 and 1.0 m. The simulation was run once more, this time with zero energy spread. These results are shown in Figure 8.12 and are what was initially expected: a linear relationship between mass resolution and drift length. Figure 8.12 represents the idealized case of perfectly uniform ion energy (similar to Figure 8.2). The results in this section show that increasing drift length improves mass resolution, but only to a point that is dependent on the ion energy spread.

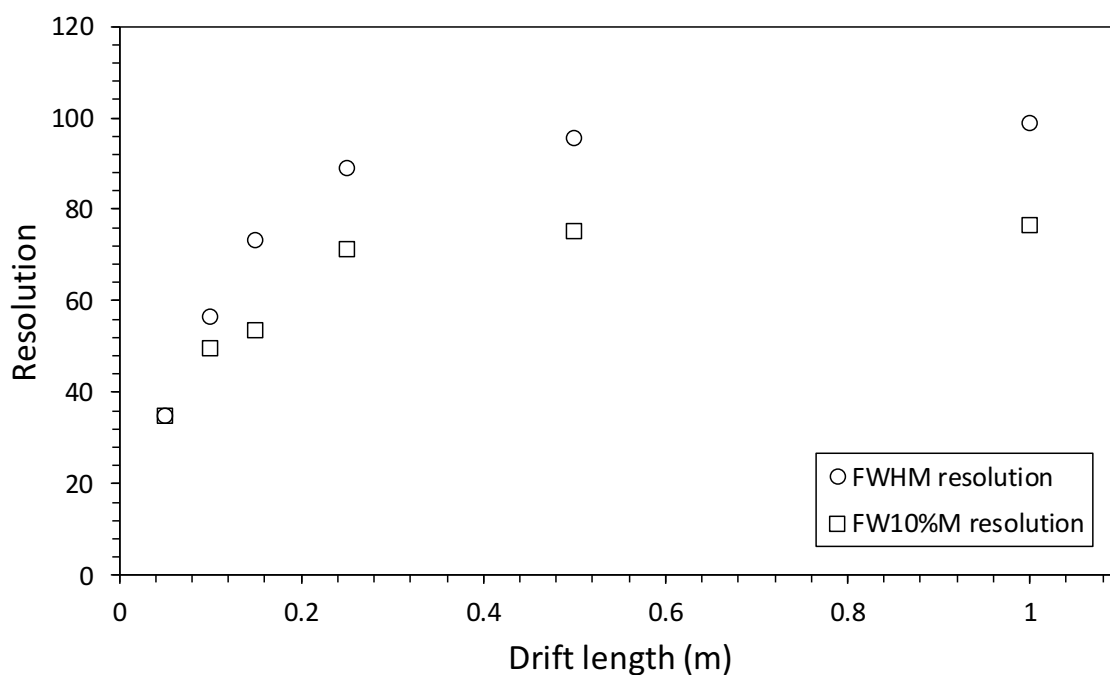


**Figure 8.10.** Simulated effect of drift length on mass resolution for the SDL instrument, for ions with a 1 eV FWHM energy spread.

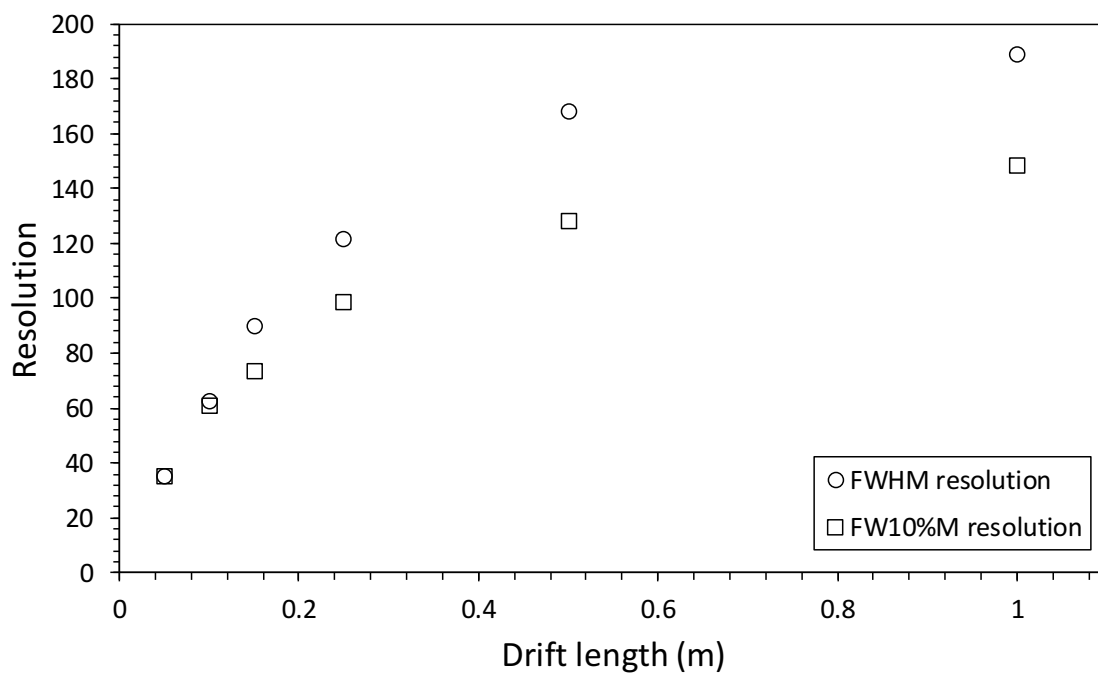


**Figure 8.11.** Simulated effect of drift length on mass resolution for the SDL instrument, with a 0.5 eV FWHM energy spread.

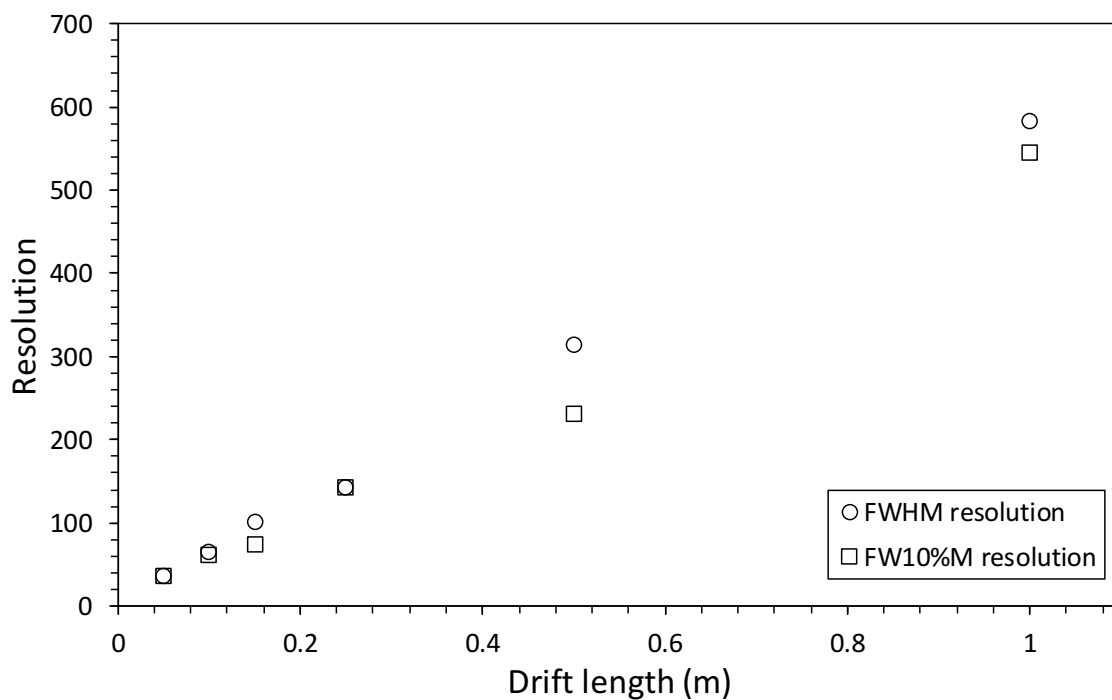


**Figure 8.12.** Simulated effect of drift length on mass resolution for the SDL instrument for monoenergetic ions.

#### 8.2.4. Ion Energy (Acceleration Potential)

The energy of ions in the SDL TOF-MS is determined by the initial ion energy before entering the instrument and the acceleration voltage inside the instrument itself. In the laboratory, while operating the instrument in ion mode, the initial ion energy comes from the ion gun system. In space, the initial energy is due to the speed of ambient particles with respect to the instrument. In both cases, most of the ion energy is ultimately due to the acceleration potential. The Monte Carlo model does not distinguish between the initial ion energy and that gained by the acceleration potential; rather, as used here, ion energy simply refers to the total kinetic energy of sampled ions.

Ion energies from 100 to 350 eV were simulated in order to model the effect of ion energy on mass resolution. Results from these simulations are shown in Figure 8.13. Interestingly, this figure shows mass resolution increasing at ion energies from 100 to 250 eV, where resolution reaches a maximum, and then decreasing at higher energies. At first glance, these results seem counterintuitive; lower ion energies result in larger TOFs which, according to equation 1.8, should improve mass resolution. However, the energy spread effect has a large impact on  $\Delta t$ . As drift time increases, energy spread dominates, resulting in degraded resolution. The effects of energy spread can be reduced by increasing the ion energy. However, after sufficiently increasing the ion energy, the start pulse width becomes the dominating factor affecting  $\Delta t$ . This explains the decline in resolution for ion energies greater than 250 eV in Figure 8.13. Ultimately, energy spread and pulse width effects must be balanced when considering the effects of ion energy on mass resolution.

#### 8.2.5. TOF Bin Size

Section 8.2.1 stated that TOF bin size could affect mass resolution. For experiments performed with the EDU, bin size is determined by the pulse processing electronics (see section 3.1.3) and is user adjustable. To simulate the effect of bin size on mass resolution, Monte Carlo instrument simulations were conducted for bin sizes ranging from 1 to 48 ns.

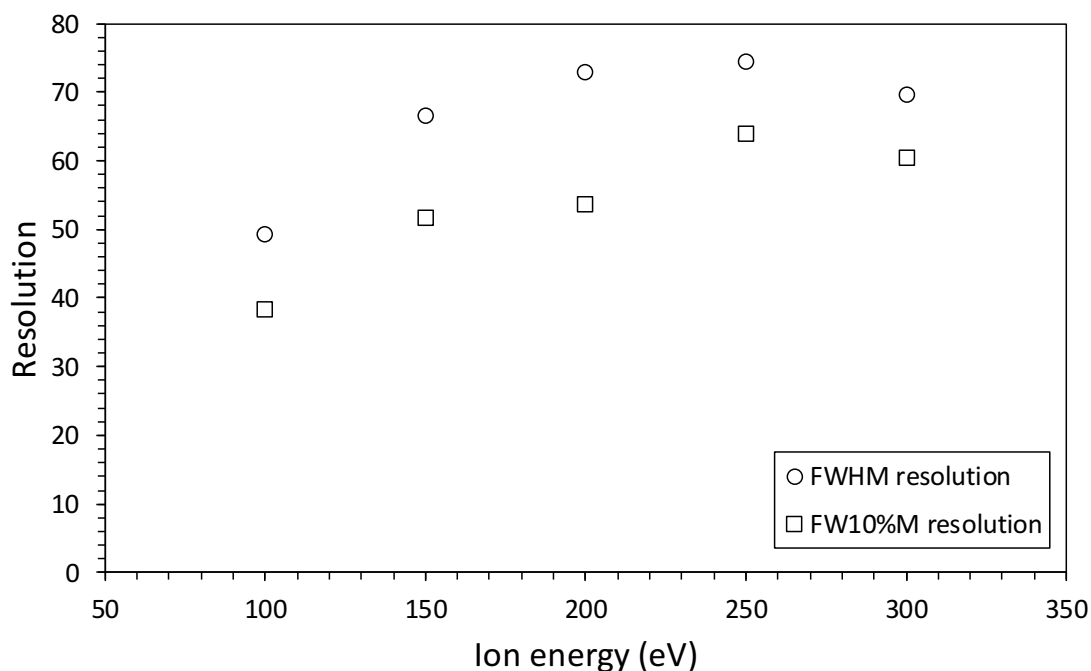


**Figure 8.13.** Simulated effect of ion energy (acceleration potential) on mass resolution for the SDL instrument.

Results from these simulations, which use an energy spread of 1 eV at FWHM, are shown in Figure 8.14 and show mass resolution increasing at smaller bin widths, which was expected. Wider bins increase  $\Delta t$  in equation 1.8 resulting in lower resolution. As a practical consideration, bins must be sufficiently large to collect enough counts to yield meaningful information. Simulations run with a 2 eV energy spread at FWHM (not shown) showed improved resolution only until the bin size reached 3 ns, below which no improvement in resolution was observed. Once again, energy spread can have a significant effect on the maximum achievable mass resolution of the instrument.

### 8.3. Simulations of the SDL Instrument Operating *In-Situ* in the MLT

A virtual TOF-MS, based on the Monte Carlo methods described in section 8.2, was developed by the author to simulate the performance of the SDL instrument in space. In contrast to the laboratory case, where all sampled species have nominally the same kinetic energy, the kinetic energy of particles sampled in space is dependent on their mass and

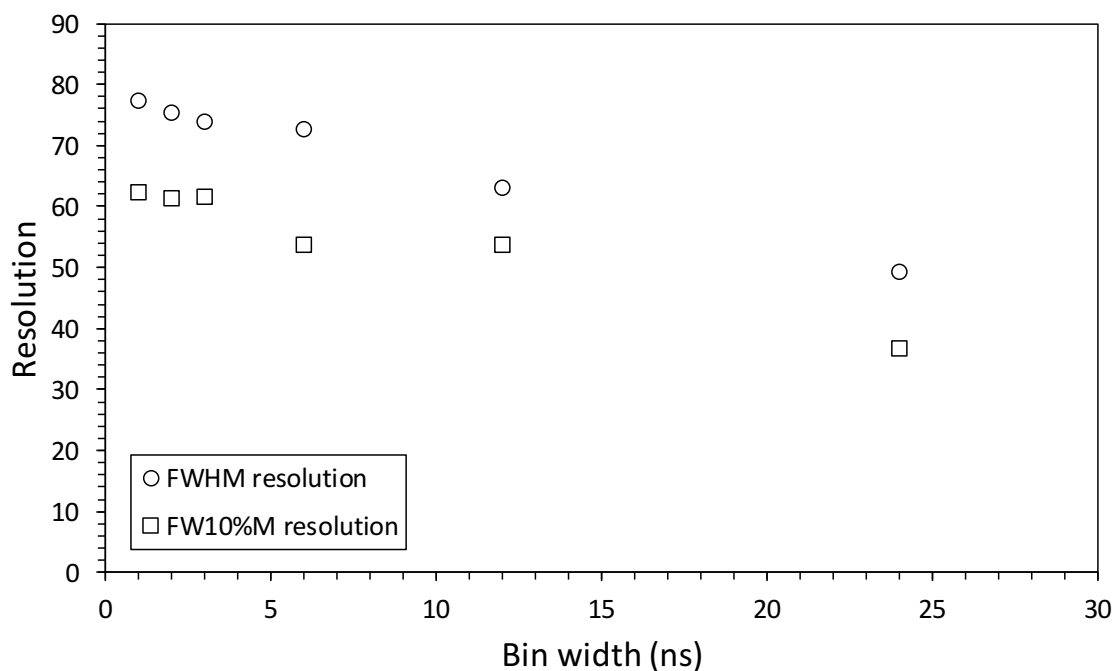


**Figure 8.14.** Simulated effect of bin width on mass resolution for the SDL instrument.

the velocity of the vehicle carrying the instrument. This mass-dependent energy effect is shown in Figure 1.4. The virtual TOF-MS calculates ions' initial energies based on a Maxwellian velocity distribution, equation 2.1, drifting at the vehicle velocity. Both the ambient temperature and vehicle velocity are user adjustable. The acceleration potential used in these simulations was 200 V, and unless otherwise noted, the start pulse width was 40 ns. The resulting TOFs for individual particles were placed in 6.4 ns bins. Simulation results from the virtual TOF-MS are presented here to illustrate the predicted capabilities of the SDL instrument.

An instrument with a mass range up through  $m/z$  48 (ozone) is sufficient to measure the major atmospheric species of interest. Higher masses were included in the simulations simply to demonstrate predicted instrument capabilities. Furthermore, simulated species did not necessarily correspond to realistic atmospheric species; rather, they covered the mass range of interest to demonstrate the resolution capabilities of the SDL TOF-MS. Represented masses were clustered around  $m/z$  values of 2, 17, 29, 47, and 99. Each of these had

$10^6$  simulated particles. To demonstrate resolution capability,  $10^4$  particles were simulated at  $m/z$  values of 1, 16, 28, 46, and 98, while a further  $10^2$  particles were simulated at  $m/z$  values of 3, 18, 30, 48, and 100.

A spectrum generated with the virtual TOF-MS, representing a rocket-borne linear instrument with a 15 cm drift length, is shown in Figure 8.15. The simulated vehicle velocity was 1 km/s and ambient particles were assumed to be thermalized at 500 K. The spectrum shows baseline resolution for simulated species of  $m/z$  30 and lower, with unit mass resolution at 10% of peak height up through  $m/z$  47. This is sufficient to resolve the major atmospheric gases. Resolution degrades quickly at increasing mass, and  $m/z$  98, 99, and 100 are not resolved from each other. The duty cycle for this simulated spectrum is 0.49%. By reducing the mass range to 51, the duty cycle can be increased to 0.73%.

A satellite instrument travels much faster than a sounding rocket, resulting in a broader energy distribution for sampled particles. Figure 8.16 is a spectrum resulting from simulat-

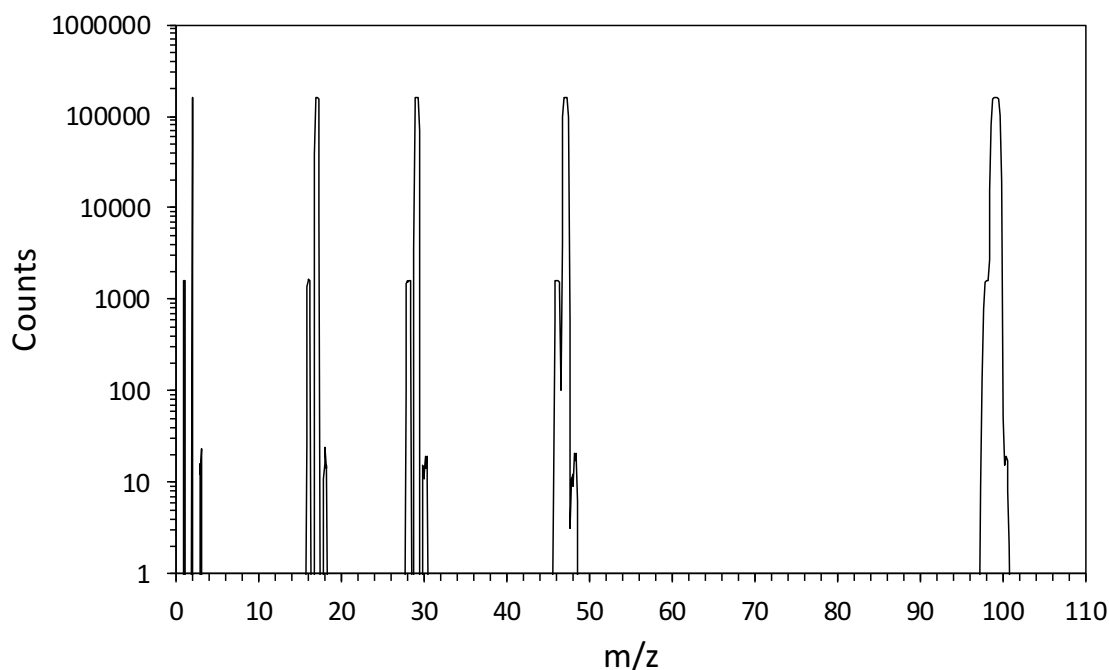


**Figure 8.15.** Simulated spectrum for a linear TOF-MS instrument traveling at 1 km/s, sampling particles thermalized at 500 K.

ing a linear TOF-MS instrument with a 15 cm drift length, traveling at 7.8 km/s, sampling particles thermalized at 1000 K, with a mass range up to  $m/z$  51. Simulated masses 1, 2, and 3 are resolved at the baseline level, while masses 16, 17, and 18 are resolved at the 10% level. By mass 28, it is impossible to distinguish between masses separated by 1 u at any peak level. The duty cycle under these conditions is 0.75%.

The wider velocity distribution at 1000 K, combined with the higher vehicle speed, presents an obvious obstacle to making well-resolved mass spectra in LEO with a linear TOF-MS. The concept of a reflectron, a device used to compensate for energy spread, was introduced in section 1.3.2. The virtual TOF-MS was used to simulate a reflectron instrument with two field-free drift regions,  $D_1$  and  $D_2$ , each with a length of 10 cm. Optimal mass resolution is achieved for the condition  $D_1 + D_2 = 4d$ , where  $d$  is the penetration depth of ions in the reflectron (same as equation 1.18) [Cotter, 1997]. The penetration depth depends on ion energy, which at orbital velocities can vary significantly, being de-

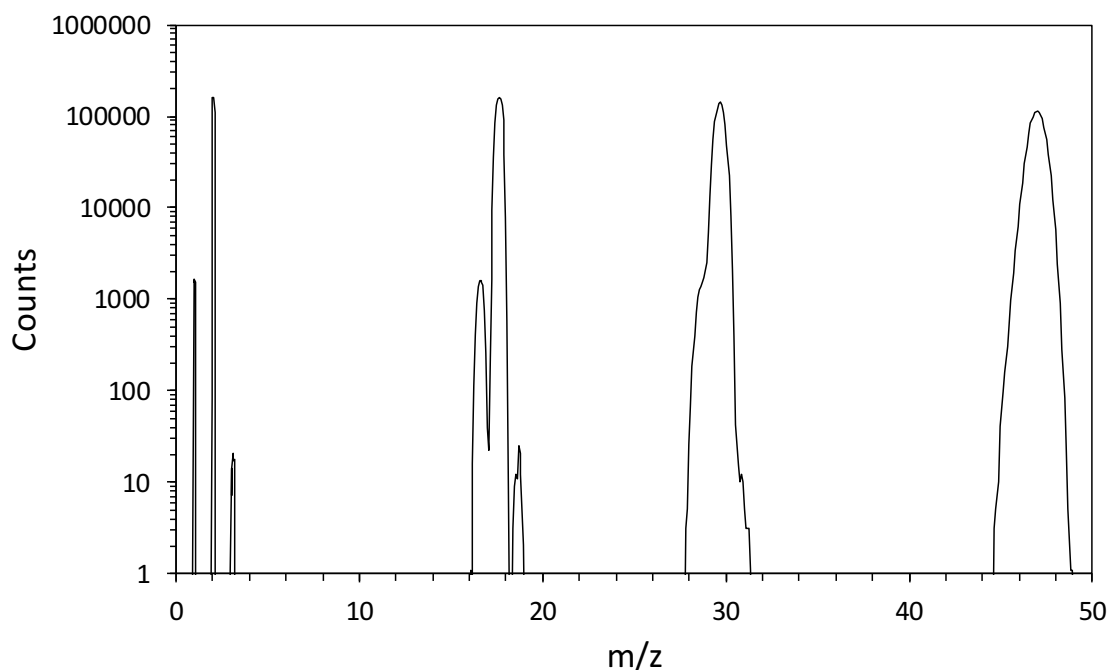


**Figure 8.16.** Simulated spectrum for a linear TOF-MS instrument traveling at 7.8 km/s, sampling particles thermalized at 1000K.

terminated by ion mass (Figure 1.4). At a velocity of 7.8 km/s, for example, a hydrogen ion has an energy of 0.3 eV while an argon ion has an energy of 12.6 eV. An ion of mass 100 u traveling at this speed has an energy of 31.5 eV. Under these conditions, the optimal resolution equation (1.18) can be strictly satisfied for only one mass. In this case the reflectron can be tuned to a specific mass, preferably chosen where energy spread correction is most vital.

The virtual TOF-MS incorporates the option to simulate an RTOF-MS. The reflectron depth and potential are generated by the program, based on a user-selected tuning mass. In the simulations presented here, the most massive simulated species was chosen as the tuning mass. The reflectron potential is determined according to the equation

$$V_r = V_{\text{acc}} + \frac{\text{KE}_{\text{tm}}}{q} + V_b, \quad (8.9)$$

where  $V_{\text{acc}}$  is the acceleration potential,  $\text{KE}_{\text{tm}}$  is the initial kinetic energy of the tuning mass, and  $V_b$  is a buffer voltage to ensure ions (which may be more massive than the tuning mass) reverse direction before reaching the end of the reflectron. The total reflectron depth is then calculated as

$$D = \frac{V_r d}{V_{\text{acc}} + \text{KE}_{\text{tm}}}, \quad (8.10)$$

where  $d$  is the penetration depth in equation 1.18.

An RTOF-MS operating at orbital velocity (7.8 km/s) was simulated with the virtual instrument, and the resulting spectrum is shown in Figure 8.17. The ambient temperature for this simulation was assumed to be 1000 K. The reflectron was tuned to  $m/z$  99, having a depth of 5.22 cm and a voltage of 241.5 V. In stark contrast to the linear instrument (Figure 8.16), the reflectron instrument clearly resolves all simulated masses at the baseline level. The improved resolution comes with a price, however, as the reflectron duty cycle is only 0.21%. By shortening the mass range to  $m/z$  51, while maintaining a 40 ns start pulse width,

the duty cycle can be increased to 0.28%. The energy spread compensation provided by the reflectron allows wider start pulses to be employed. With a start pulse of 120 ns, the reflectron tuned to  $m/z$  47, and mass range up to  $m/z$  51, the simulated reflectron instrument achieves a duty cycle of 0.87% while maintaining baseline resolution. This is a significant improvement over the linear instrument.

#### 8.4. Conclusions

A Monte Carlo model of the SDL TOF-MS was developed to study the effects of critical instrument operating parameters on mass resolution. These parameters included start pulse width, drift length, ion energy, and TOF bin size. Although energy spread is more accurately described as a characteristic of ions that are sampled, and is not technically an instrument operating parameter, its effect on mass resolution was also simulated. All of the simulated operating parameters affected mass resolution. However, one issue surfaced repeatedly: energy spread of the simulated ions. In fact, energy spread was the single greatest

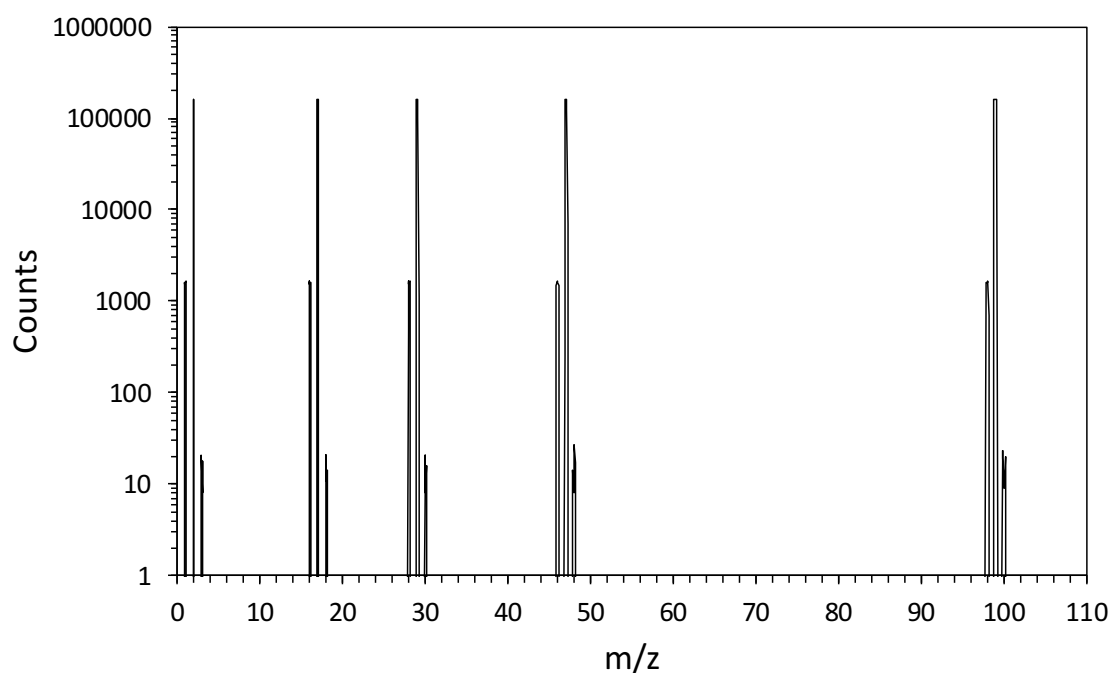


**Figure 8.17.** Simulated spectrum for a reflectron TOF-MS instrument traveling at 7.8 km/s, sampling particles thermalized at 1000 K.

factor limiting instrument resolution in all the simulations presented in this section. The majority of the simulations presented here employed an energy spread of 1 eV at FWHM, which is similar to ion beams produced in the SDL IOTF. Fortunately, the energy spread expected to be encountered on a sounding rocket flight to the MLT is smaller, ranging from 0.2 to 0.5 eV at FWHM, corresponding to a rocket velocity of 1000 m/s and ambient temperatures from 200 to 600 K.

For suborbital missions ( $v \leq 1$  km/s, and ambient temperatures  $\leq 500$  K), a linear TOF-MS offers sufficient resolution to measure the major species of interest (up through  $m/z$  48). However, the increased energy spreads resulting from higher speeds and temperatures severely degrade resolution. A properly designed reflectron can be employed to compensate for the energy spread, making baseline unit mass resolution possible even at orbital velocities. The superior resolution of an RTOF-MS allows a longer start pulse to be used, which in turn helps compensate for the decreased duty cycle that would otherwise occur. This is beneficial from an engineering standpoint, because longer start pulses are easier to generate.

Shorter start pulses improve mass resolution, but require faster electronics and are more difficult to design and build. Below a certain pulse width, improvements in mass resolution are negligible due to the energy spread of sampled ions (see Figure 8.9). That pulse width will be somewhere between 2 and 7 ns for a rocket-borne SDL instrument, which represents the difference in TOF for two ions on either extreme of the energy spread for MLT conditions. This suggests that start pulses shorter than 5 ns will do little to improve mass resolution. Additionally, smaller start pulses decrease the instrument duty cycle, which negatively affects sensitivity. Ideally, the largest pulse possible should be used, while maintaining the necessary resolution. Ultimately, mission requirements and constraints will dictate the instrument operating parameters and whether a linear or reflectron SDL TOF-MS is used.

## CHAPTER 9

## PREDICTED PERFORMANCE: SENSITIVITY AND ACCURACY

Previous chapters of this work have described the design, assembly, operation, and performance modeling of the SDL instrument; the instrument concept has been validated. This chapter presents sensitivity and number density accuracy analyses for the SDL instrument. When referring to instrument performance, sensitivity is a term used to describe the relationship between the amount of analyte and the resulting signal. A sensitivity analysis for the SDL TOF-MS is presented in section 9.1 for both neutral and ion modes of operation. The neutral sensitivity analysis begins with a description of the ion current generated in the ionizer; equations are then developed to relate the ambient neutral density to the MCP count rate. Similar equations are developed for the ion sensitivity analysis to relate the ambient ion density to the MCP count rate.

A number density accuracy analysis is presented in section 9.2 for both ions and neutral particles. This analysis is based on the sensitivity analysis and predicted performance parameters of the SDL instrument. Examples are given, for several different species, to demonstrate how the uncertainty in number density can be calculated. This analysis predicts the accuracy with which the SDL TOF-MS will measure ambient species in the MLT.

### 9.1. Sensitivity Analysis

The sensitivity analysis demonstrates the retrieval of ambient number densities from mass spectra collected with the SDL TOF-MS in the upper atmosphere. This analysis begins with the ion current generated in the ionizer, which can be expressed as

$$I_{\text{ion}} = I_e \sigma N_{\text{ionizer}} l. \quad (9.1)$$

In this equation  $I_e$  is the electron emission current,  $\sigma$  is the ionization cross section (species and energy dependent),  $N_{\text{ionizer}}$  is the number density of neutral particles in the ionizer, and

$l$  is the path length of electrons in the ionizer. The first step is to relate  $I_{\text{ion}}$  to the number density of neutral particles in the ambient atmosphere,  $N_{\text{ambient}}$ . Ignoring bow shock effects, the flux of particles through the aperture of an instrument traveling at speed  $v$  is

$$\Phi_a = N_{\text{ambient}}v. \quad (9.2)$$

The ionizing electrons are assumed to form a 2D sheet, with length  $l$  and width  $w$ , from the cathode to the Faraday cup (sections 1.4 and 3.1.1). The particle flux through the electron sheet can be expressed as

$$\Phi_{\text{ionizer}} = N_{\text{ionizer}}v. \quad (9.3)$$

The number of particles passing through the aperture can be compared to the number of particles passing through the electron sheet by setting

$$\pi r^2 \Phi_a = \alpha l w \Phi_{\text{ionizer}}, \quad (9.4)$$

where  $r$  is the aperture radius and  $\alpha$  is a species-specific factor that relates the fraction of particles that pass through the aperture to the number of particles that pass through the electron sheet. All of the ions that pass through the electron sheet must have previously traveled through the aperture, but not all of the particles that travel through the aperture necessarily pass through the electron sheet. Lighter particles especially, which may have large enough velocity components normal to the aperture plane to miss the electron sheet, have a lower probability of passing through the electron sheet. The factor,  $\alpha$ , is generally close to unity but ultimately depends on instrument geometry, ambient temperature, and  $v$ , and is smaller for lighter species. Substituting in for  $\Phi_a$  and  $\Phi_{\text{ionizer}}$ , equation 9.4 can be expressed

$$N_{\text{ambient}}v\pi r^2 = \alpha N_{\text{ionizer}}vlw. \quad (9.5)$$

Solving for  $N_{\text{ionizer}}l$  gives

$$N_{\text{ionizer}}l = N_{\text{ambient}} \frac{\pi r^2}{\alpha w}. \quad (9.6)$$

Substituting in to equation 9.1 for  $N_{\text{ionizer}}l$  yields

$$I_{\text{ion}} = I_e \sigma N_{\text{ambient}} \frac{\pi r^2}{\alpha w}. \quad (9.7)$$

Dividing both sides of equation 9.7 by the elementary charge,  $q$ , gives the number of neutral particles that have been ionized per second,

$$\frac{N_{\text{ni}}}{\text{s}} = \frac{I_e \sigma N_{\text{ambient}} \pi r^2}{\alpha q w}. \quad (9.8)$$

The count rate,  $R$ , at the detector can be expressed for neutrals as

$$R_{\text{neutrals}} = \frac{I_e \sigma N_{\text{ambient}} \pi r^2}{\alpha q w} F Q, \quad (9.9)$$

where  $F$  is the instrument transmission fraction and  $Q$  is the detector quantum efficiency. Factors that affect  $F$  include mesh transmission coefficients and ion interactions with the BNG and other instrument components.

When the TOF-MS operates in ion mode, the ambient atmosphere acts as the ion source, and all factors relating to the ionizer in equation 9.9 no longer apply. The ion flux through the aperture is the same as equation 9.2 but with  $N_{\text{ambient}}$  representing the number density for ions. Multiplying the ion flux by the aperture area and also by  $FQ$  gives the count rate in ion mode,

$$R_{\text{ions}} = N_{\text{ambient}} v \pi r^2 F Q. \quad (9.10)$$

It should be noted that  $N_{\text{ambient}}$  in equations 9.9 and 9.10 are not the same;  $N_{\text{ambient}}$  in equation 9.9 refers to the ambient *neutral* particle density, while  $N_{\text{ambient}}$  in equation 9.10 refers to the ambient *ion* density. Equations 9.9 and 9.10 can be solved for  $N_{\text{ambient}}$  to find

the ambient number densities for neutrals and ions based on the detector count rate,

$$N_{\text{neutrals}} = \frac{R_{\text{neutrals}} \alpha q w}{I_e \sigma \pi r^2 F Q} \quad (9.11)$$

$$N_{\text{ions}} = \frac{R_{\text{ions}}}{v \pi r^2 F Q}. \quad (9.12)$$

Standard error propagation formulae are used to determine the uncertainty in  $N_{\text{neutrals}}$  and  $N_{\text{ions}}$  [Taylor, 1997]. The uncertainties are added in quadrature for both, yielding

$$\frac{\delta N_{\text{neutrals}}}{N_{\text{neutrals}}} = \sqrt{\left(\frac{\delta R_{\text{neutrals}}}{R_{\text{neutrals}}}\right)^2 + \left(\frac{\delta w}{w}\right)^2 + \left(\frac{\delta I_e}{I_e}\right)^2 + 2\left(\frac{\delta r}{r}\right)^2 + \left(\frac{\delta F}{F}\right)^2 + \left(\frac{\delta Q}{Q}\right)^2} \quad (9.13)$$

$$\frac{\delta N_{\text{ions}}}{N_{\text{ions}}} = \sqrt{\left(\frac{\delta R_{\text{ions}}}{R_{\text{ions}}}\right)^2 + \left(\frac{\delta v}{v}\right)^2 + 2\left(\frac{\delta r}{r}\right)^2 + \left(\frac{\delta F}{F}\right)^2 + \left(\frac{\delta Q}{Q}\right)^2}. \quad (9.14)$$

Uncertainties in  $\sigma$ , the ionization cross section, are assumed to be well known and negligible. The uncertainties  $\delta R_{\text{neutrals}}$  and  $\delta R_{\text{ions}}$  are determined from mass spectra. If the uncertainties due to instrument components are very small or negligible, i.e.,

$$\frac{\delta w}{w} = \frac{\delta I_e}{I_e} = \frac{\delta r}{r} = \frac{\delta F}{F} = \frac{\delta Q}{Q} = \frac{\delta v}{v} \approx 0, \quad (9.15)$$

then the uncertainties in  $N_{\text{ions}}$  and  $N_{\text{neutrals}}$  are due entirely to the count rate uncertainties,  $\delta R_{\text{neutrals}}$  and  $\delta R_{\text{ions}}$ . Equations 9.13 and 9.14 then simplify to

$$\frac{\delta N_{\text{neutrals}}}{N_{\text{neutrals}}} = \sqrt{\left(\frac{\delta R_{\text{neutrals}}}{R_{\text{neutrals}}}\right)^2} = \frac{\delta R_{\text{neutrals}}}{R_{\text{neutrals}}} \quad (9.16)$$

$$\frac{\delta N_{\text{ions}}}{N_{\text{ions}}} = \sqrt{\left(\frac{\delta R_{\text{ions}}}{R_{\text{ions}}}\right)^2} = \frac{\delta R_{\text{ions}}}{R_{\text{ions}}}. \quad (9.17)$$

The count rate,  $R$ , is determined for each  $m/z$  value in a spectrum by knowing the number of counts in the corresponding peak, the duty cycle, and the integration distance

(number of scans required to produce the spectrum). The count rate can be expressed as

$$R = \frac{n}{t}, \quad (9.18)$$

where  $n$  is the number of counts in the peak of interest and  $t$  is the amount of time the instrument is in the beam-on state. The time,  $t$ , can be written as

$$t = t_{\text{tot}}d_c, \quad (9.19)$$

where  $t_{\text{tot}}$  is the total time required to collect a spectrum and  $d_c$  is the instrument duty cycle.

The time required to collect a spectrum can also be expressed as

$$t_{\text{tot}} = \frac{d_i}{v}, \quad (9.20)$$

where  $d_i$  is the integration distance and  $v$  is the velocity of the vehicle carrying the instrument. Using equations 9.19 and 9.20, the count rate in equation 9.18 can be expressed as

$$R = \frac{nv}{d_i d_c}. \quad (9.21)$$

The uncertainty in  $R$  is

$$\frac{\delta R}{R} = \sqrt{\left(\frac{\delta n}{n}\right)^2 + \left(\frac{\delta v}{v}\right)^2 + \left(\frac{\delta d_i}{d_i}\right)^2 + \left(\frac{\delta d_c}{d_c}\right)^2}. \quad (9.22)$$

If the uncertainties in velocity ( $\delta v$ ), integration distance ( $\delta d_i$ ), and duty cycle ( $\delta d_c$ ) are negligible, then

$$\delta R = R \frac{\delta n}{n}. \quad (9.23)$$

In any case,  $\delta v$  and  $\delta d_i$  are related and can be easily ascertained;  $\delta d_c$  should also be small and easily calculated. The main source of uncertainty in  $\delta R$  then is the number of counts

in the peak of interest.

## 9.2. Number Density Accuracy

The predicted performance of the SDL TOF-MS, in terms of number density accuracy, is modeled in this section for both ions and neutrals. The model used here was originally developed by Dr. Erik Syrstad and adapted for this study by the author. Ambient densities used as inputs for the ion number density accuracy analysis were provided by *Mertens* [2011]. Neutral densities were obtained from the MSIS-E-90 reference atmosphere [*Hedin*, 1991], supplemented with additional densities from *Mertens* [2011]. The results presented in this section are for a rocket flight with an apogee of 160 km, with measurements beginning at 85 km for ions and 70 km for neutrals. The model assumes the use of a linear version of the TOF-MS. As such, there is a direct line of sight from the MCP detector to the atmosphere, resulting in background counts from ambient UV emissions. A UV background analysis is performed in section 9.2.1. The count rates used to calculate the number density accuracy are based on the sensitivity analysis in section 9.1; subsequently, an uncertainty analysis is performed based on the predicted number of counts.

The number density accuracy analysis also takes in to account the integration distance, which determines the number of individual scans that are used to form a spectrum. As an example, an instrument traveling at 1000 m/s that requires 8000 ns per scan will be able to perform  $1.25 \times 10^5$  scans in the time it takes to travel 1 km. In this case, an integration distance of 1 km simply means that  $1.25 \times 10^5$  individual scans are summed together to produce one mass spectrum, from which the density for that kilometer of altitude is calculated. A rocket traveling on a ballistic trajectory slows as its altitude increases. Thus, for a constant integration distance, more scans are combined to form a mass spectrum at higher altitudes than at lower altitudes. This is useful because the ambient number density decreases at higher altitudes, leading to less overall signal. However, since the rocket velocity slows with increasing altitude, the number of scans used to form a mass spectrum

increases, helping to offset the negative effects of decreasing number density. This effect can be exploited by using an apogee near the altitude of greatest interest.

### 9.2.1. UV Background Analysis

The UV background analysis presented here was performed by the author and is based on volume emission rates from *Mertens* [2011], at 1 km increments for altitudes from 85 km to 160 km (at Poker Flat, AK), consistent with an IBC III aurora. The approach employed here to estimate the UV background can be applied to any other location and condition as long as the volume emission rate can be estimated. MCP detectors are generally sensitive to UV photons with wavelengths shorter than 1500 Å [*Siegmund et al.*, 1996], so only emissions shorter than 1500 Å were considered in this analysis (1493 Å and 1200 Å in the data set from [*Mertens*, 2011]). The volume emission rates for these two wavelengths are shown in Figure 9.1.

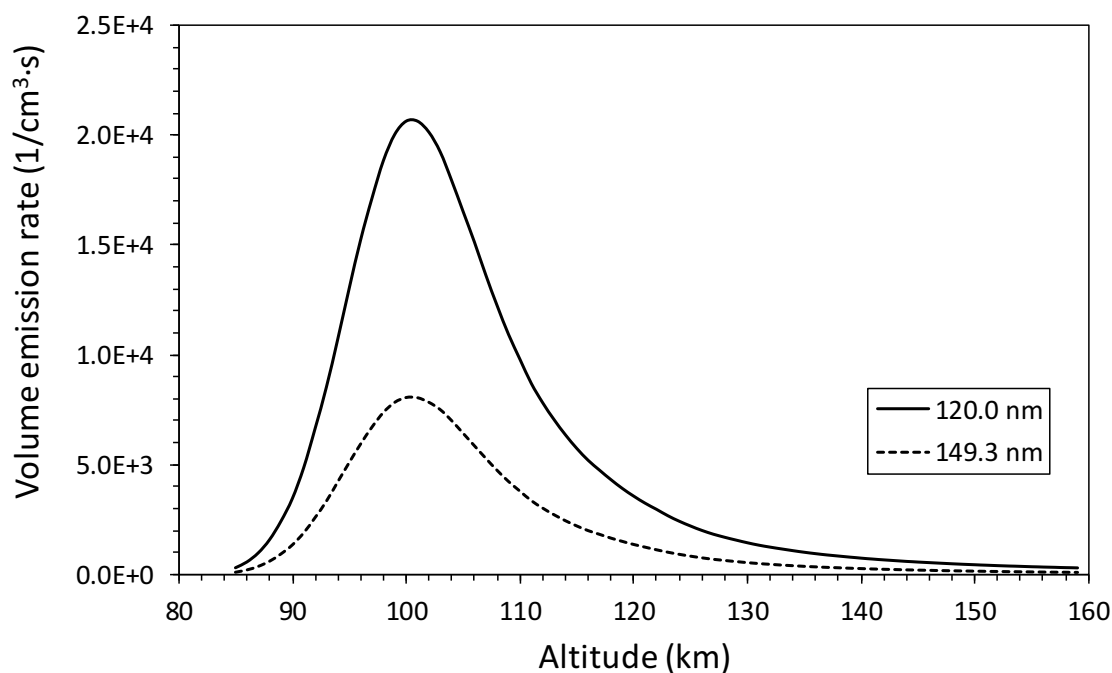


**Figure 9.1.** Volume emission rates for 120.0 and 149.3 nm photons above Poker Flat, AK, consistent with a class IBC III aurora. These emission rates are based on data from *Mertens* [2011].

For this analysis the instrument was assumed to point in the zenith direction for the duration of the rocket flight. The MCP field of view for a linear TOF-MS instrument extends forward from the instrument in the shape of a right circular cone with its apex located at the instrument aperture (Figure 9.2). The cone's divergence is determined by the instrument geometry, specifically: the active area of the MCP detector,  $A_{MCP}$ ; the area of the aperture,  $A_a$ ; and the distance from the MCP to the instrument aperture,  $d_{MCP}$ . This analysis uses the assumption that  $A_a \ll A_{MCP}$ . The emission cone can be divided into slices as shown in Figure 9.2. Since the volume emission rate data is at 1 km intervals, the slices

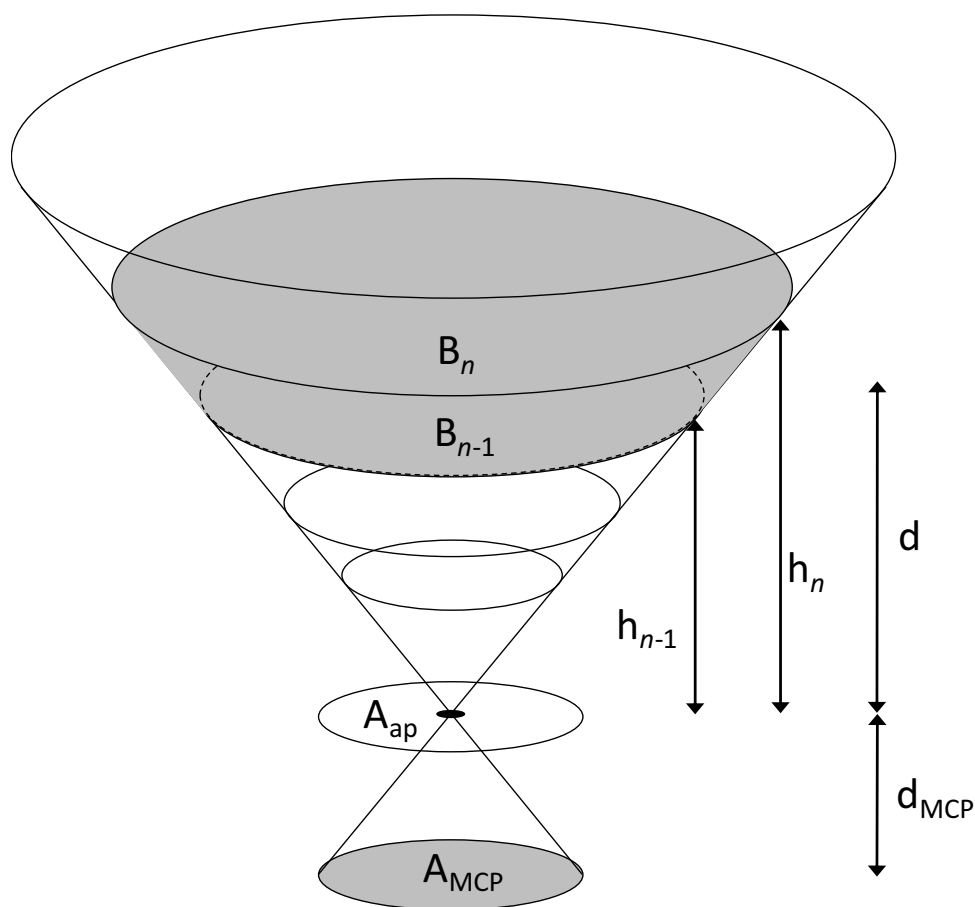


**Figure 9.2.** The UV background emission cone extends in front of the instrument, with its apex located at the instrument aperture. The shape of the cone is determined by the area of the MCP detector,  $A_{MCP}$ , and the distance from the MCP to the instrument aperture  $d_{MCP}$ . Figure is not to scale.

have a depth of 1 km. The slices form a cone (the slice nearest the aperture) and frustums (the remaining slices) with thicknesses  $h_n - h_{n-1} = 1$  km and base areas  $B_{n-1}$  and  $B_n$ , which represent the areas of the flat edges of each slice. Each  $B_n$  is easily calculated as

$$B_n = A_{\text{MCP}} \left( \frac{d_n}{d_{\text{MCP}}} \right)^2, \quad (9.24)$$

where  $B_n$  is the area of the base and  $d_n$  is the distance from the instrument aperture to the base. The volume of each slice is

$$V_n = \frac{h_n B_n - h_{n-1} B_{n-1}}{3}. \quad (9.25)$$

Note that for the first slice  $h_0 = 0$ , and equation 9.25 simplifies to the volume of a cone.

The volume emission rate,  $\epsilon_n$ , is assumed to be constant for each individual slice. For  $d_{\text{MCP}} = 15$  cm and  $r_{\text{MCP}} = 9$  mm, where  $r_{\text{MCP}}$  is the radius of the active area of the MCP, the angle between the edge of the emission cone and a line normal to the surface of the aperture is small, only  $3.4^\circ$ . The apparent area of the instrument aperture as viewed from a point on or near the edge of slice of the emission cone is nearly the same (99.8%) as the apparent area of the aperture as viewed from the center of the same slice. Because of this, all emitted photons are assumed to emanate from the center of the emitting element. The total number of photons emitted from each slice of the emission cone is

$$L_n = V_n \epsilon_n, \quad (9.26)$$

and they are assumed to emit isotropically. This idealized point of emission can be envisioned as lying at the center of a sphere with radius

$$r_n = h_{n-1} + \frac{h_{n-1} + h_n}{2} \quad (9.27)$$

and surface area

$$A_n = 4\pi r_n^2. \quad (9.28)$$

The fraction of photons from the emitting volume that enter the aperture is simply the ratio of the area of the aperture to the area of the emission sphere,

$$E_n = \frac{A_a}{A_n}. \quad (9.29)$$

The background count rate due to UV photons from one emission slice is

$$b_n = L_n \cdot E_n. \quad (9.30)$$

The contribution of photons from each slice of the emitting cone is summed together,

$$\beta_n = \sum_{n_{\text{slices}}} b_n, \quad (9.31)$$

to obtain the total UV background count rate at a given altitude.

A short MATLAB<sup>®</sup> script was written by the author to estimate the MCP background count rate due to UV airglow, based on equations 9.24 - 9.31. The script allows the user to adjust the size of the instrument aperture, as well as the distance from the MCP detector to the aperture. Input for the script is the volume emission rate data ( $\epsilon$ , in units of  $\text{cm}^{-3}\text{s}^{-1}$ ) shown in Figure 9.1. Volume emission rates below 85 km were assumed to be negligible. The volume emission rates were extrapolated from the data up to 300 km, but had a negligible effect on the overall background count rate. Figure 9.3 shows the estimated UV background count rates for the SDL TOF-MS at altitudes from 70 to 160 km, for several different aperture diameters. Instrument parameters for the data presented in Figure 9.3 were  $d_{\text{MCP}} = 15$  cm and  $r_{\text{MCP}} = 9$  mm. These background count rates were used in the number density accuracy predictions presented later in sections 9.2.2 and 9.2.3.

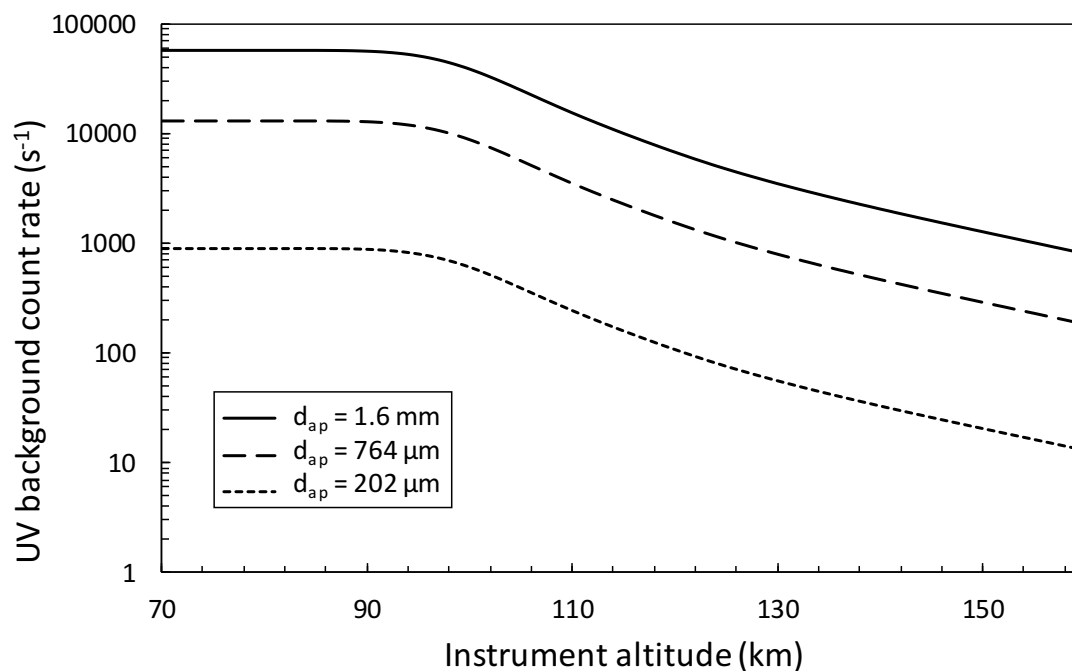


**Figure 9.3.** Estimated background count rate for the SDL TOF-MS at altitudes from 70 - 160 km, due to background UV airglow emissions. Simulated aperture diameters were 1.6 mm, 764  $\mu\text{m}$ , and 202  $\mu\text{m}$ .

### 9.2.2. Number Density Accuracy - Ions

The ion number density accuracy analysis for the SDL instrument was modeled using a set of ion densities from 85 to 160 km. This data was provided by *Mertens* [2011] and is shown in Figure 9.4. The simulated instrument aperture diameter was 764  $\mu\text{m}$ , chosen to limit the count rate at the MCP detector to a maximum of 10 MHz for the species with the highest density in the simulated data (in this case,  $\text{NO}^+$ ). Ion transmission through the instrument was estimated to be 50%, and a quantum efficiency of 0.65 was used for the MCP. A duty cycle of 0.73% and a peak broadening factor of 0.78 were assumed, both based on modeling results from section 8.3. A simulated mass spectrum was created based on these instrument parameters, the ion density data in Figure 9.4, the predicted UV background (Figure 9.3), and an integration distance of 1 km. The number density accuracy analysis is based on the number of counts in each peak in the simulated mass spectrum.

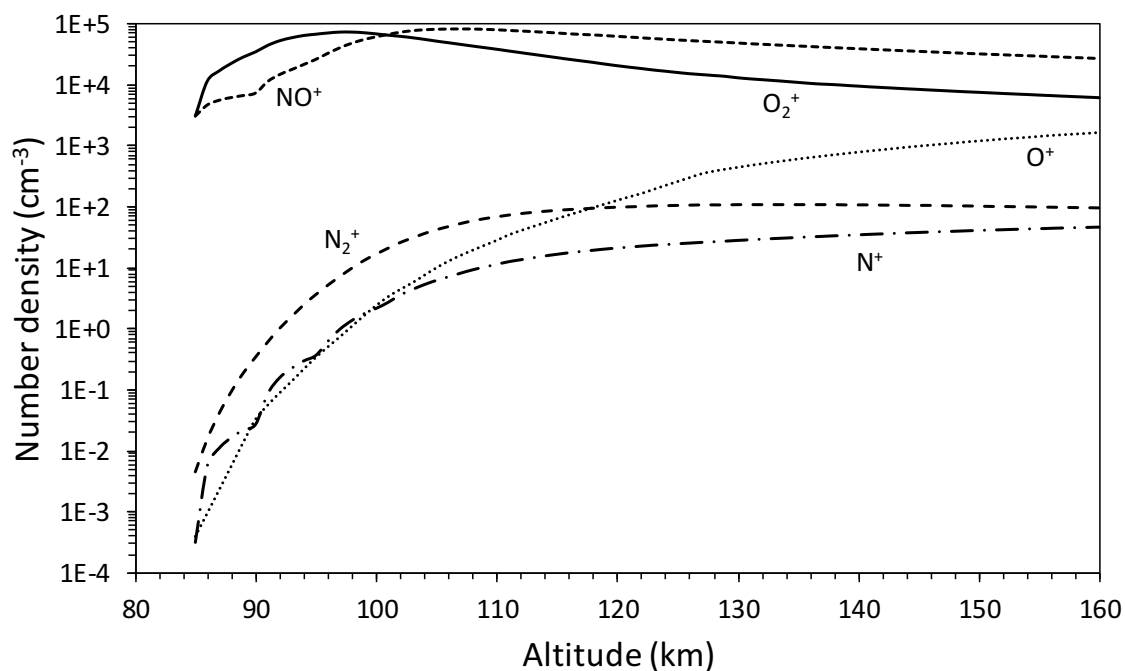


**Figure 9.4.** Ion densities used in the ion number density accuracy analysis. Based on data from *Mertens* [2011].

The predicted number density accuracy is shown in Figure 9.5 for the ambient densities in Figure 9.4. The species with the highest densities ( $O_2^+$  and  $NO^+$ ) have a predicted measurement accuracy better than 3% relative standard deviation above 85 km. The less common ions ( $N^+$ ,  $O^+$ , and  $N_2^+$ ) have a lower predicted measurement accuracy. Above 122 km,  $O^+$  number density measurements with relative standard deviations below 10% are predicted to be possible. Examples follow in sections 9.2.2.1 and 9.2.2.2 ( $O^+$  and  $NO^+$ ) for calculating the relative standard deviations shown in Figure 9.5.

One way to improve the measurement accuracy is to increase the integration distance. This serves to increase the number of counts in each peak, but doing so degrades vertical resolution. Alternatively, the aperture size can be increased to enhance the signal, improving the measurement accuracy for less abundant species while retaining a high vertical resolution. However, this method can saturate the detector for peaks of more abundant species. Another option is to use a lower apogee, which results in lower vehicle speeds and

more scans per integration distance, thus enhancing the measurement accuracy.

### 9.2.2.1. Example: O<sup>+</sup> Density Uncertainty

The uncertainty in the O<sup>+</sup> density is simple and serves well as a first example. Besides UV background counts, the m/z 16 peak in ion mode is due entirely to ambient atomic oxygen ions. The total number of counts in this peak is

$$N_{16} = N_{O^+} + N_{UV}, \quad (9.32)$$

where  $N_{O^+}$  is the number of counts due to O<sup>+</sup> and  $N_{UV}$  is the number UV background counts. According to Poisson counting statistics, the uncertainty in a counting experiment where  $N$  counts are measured is  $\delta N = \sqrt{N}$  [Taylor, 1997]. The uncertainty in the m/z 16

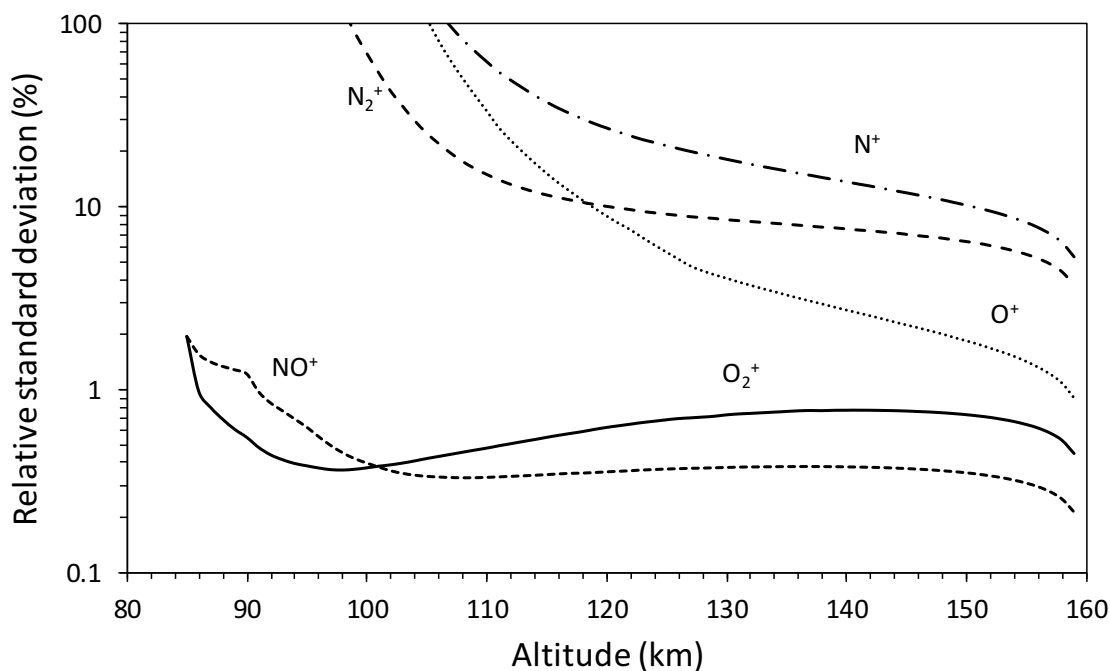


**Figure 9.5.** Modeled number density accuracy for ions. These results assume ambient densities shown in Figure 9.4 and UV background count rates for a 764  $\mu\text{m}$  diameter instrument aperture (Figure 9.3). Integration distance was 1 km. Other simulation parameters given in text.

peak can thus be expressed as

$$\delta N_{16} = \sqrt{N_{16}}. \quad (9.33)$$

The number of counts in the m/z 16 peak due to UV background can be found by looking at an area of the spectrum devoid of peaks. Other sources of background are assumed to be negligible, but can be accounted for, as well, by using this method. The uncertainty in  $N_{UV}$  is

$$\delta N_{UV} = \sqrt{N_{UV}}. \quad (9.34)$$

Equation 9.32 can be rearranged to give the number of counts due to  $O^+$ ,

$$N_{O^+} = N_{16} - N_{UV}. \quad (9.35)$$

The uncertainty  $\delta N_{O^+}$  can be expressed as

$$\delta N_{O^+} = \sqrt{(\delta N_{16})^2 + (\delta N_{UV})^2} = \sqrt{N_{16} + N_{UV}}, \quad (9.36)$$

and the fractional uncertainty in the number of  $O^+$  counts can then be written as

$$\frac{\delta N_{O^+}}{N_{O^+}} = \frac{\sqrt{N_{16} + N_{UV}}}{N_{O^+}}. \quad (9.37)$$

Equation 9.37 can be multiplied by 100 to give the relative standard deviation, or percent uncertainty.

#### 9.2.2.2. Example: $NO^+$ Density Uncertainty

The uncertainty in the  $NO^+$  density provides a more complicated example. The m/z 30 peak has contributions from  $NO^+$ ,  $N_2^+(30)$ , and UV background, and can be expressed as

$$N_{30} = N_{NO^+} + N_{N_2^+(30)} + N_{UV}, \quad (9.38)$$

where  $N_{\text{NO}^+}$  is the number of counts due to  $\text{NO}^+$  and  $N_{\text{N}_2^+(30)}$  is the number of counts due to the 30 u isotopologue of  $\text{N}_2^+$ . The uncertainty in this peak is

$$\delta N_{30} = \sqrt{N_{30}}. \quad (9.39)$$

The number of counts in the m/z 30 peak due to UV background and associated uncertainty are found as described in section 9.2.2.1. Equation 9.38 can be rearranged to give the number of counts due to  $\text{NO}^+$ , as

$$N_{\text{NO}^+} = N_{30} - N_{\text{N}_2^+(30)} - N_{\text{UV}}. \quad (9.40)$$

The uncertainty  $\delta N_{\text{NO}^+}$  can be expressed as

$$\delta N_{\text{NO}^+} = \sqrt{(\delta N_{30})^2 + (\delta N_{\text{N}_2^+(30)})^2 + (\delta N_{\text{UV}})^2}. \quad (9.41)$$

Expressions for the uncertainties  $\delta N_{30}$  and  $\delta N_{\text{UV}}$  are given in equations 9.39 and 9.34. The uncertainty in  $\text{N}_2^+(30)$  must now be found. In this example, it is assumed that  $N_{\text{N}_2^+(28)}$  is already known. The isotopic abundance of  $^{15}\text{N}$  is 0.0037 [McLafferty and Tureček, 1993]. There are three possible combinations of  $\text{N}_2$ , resulting in masses of 28, 29, and 30 u. The isotopic abundances of  $\text{N}_2$  are 0.992614 (28 u), 0.007373 (29 u), and 0.000014 (30 u). The ratio of  $\text{N}_2^+(30)$  to  $\text{N}_2^+(28)$  is

$$\frac{N_{\text{N}_2^+(30)}}{N_{\text{N}_2^+(28)}} = \frac{0.0037^2}{0.9963^2}. \quad (9.42)$$

Equation 9.42 can be solved for  $N_{\text{N}_2^+(30)}$ , giving

$$N_{\text{N}_2^+(30)} = \left( \frac{0.0037^2}{0.9963^2} \right) N_{\text{N}_2^+(28)}. \quad (9.43)$$

The uncertainty of a quantity,  $f$ , of the form  $f = aA$ , where  $a$  has no uncertainty, is  $\delta f^2 = a^2 \cdot \delta A^2$  [Taylor, 1997]. This allows the uncertainty  $\delta N_{N_2^+(30)}$  to be expressed as

$$\delta N_{N_2^+(30)}^2 = \left( \frac{0.0037^2}{0.9963^2} \right)^2 \cdot N_{N_2^+(28)}^2 = 1.902 \times 10^{-10} \cdot \delta N_{N_2^+(28)}^2. \quad (9.44)$$

The uncertainty  $\delta N_{NO^+}$  can now be expressed as

$$\delta N_{NO^+} = \sqrt{N_{30} + 1.902 \times 10^{-10} \cdot \delta N_{N_2^+(28)}^2 + N_{UV}}. \quad (9.45)$$

The fractional uncertainty for  $NO^+$  is expressed as

$$\frac{\delta N_{NO^+}}{N_{NO^+}} = \frac{\sqrt{N_{30} + 1.902 \times 10^{-10} \cdot \delta N_{N_2^+(28)}^2 + N_{UV}}}{N_{NO^+}}. \quad (9.46)$$

Multiplying equation 9.46 by 100 yields the relative standard deviation for  $NO^+$ .

### 9.2.3. Number Density Accuracy - Neutrals

A number density accuracy analysis was also performed for neutrals. This analysis was based on data from an MSIS-E-90 atmosphere [Hedin, 1991], with additional densities from Mertens [2011]. The neutral atmosphere used in this analysis is shown in Figure 9.6. To be measured with a mass spectrometer, neutral particles must first be ionized. The SDL TOF-MS employs EI to ionize neutral particles. EI is considered a hard ionization technique, meaning that many fragment particles are created during the ionization process. Fragmentation complicates the interpretation of neutral mass spectra. This is in contrast to ion mode, where no fragmentation occurs. Additionally, not every neutral particle that enters the ionizer will be ionized; the fraction of particles that are ionized in EI is perhaps as small as 0.001 [de Hoffmann and Stroobant, 2007].

As with the number density accuracy analysis for ions, the first step in the analysis for neutral particles is to calculate an expected mass spectrum based on the neutral densities

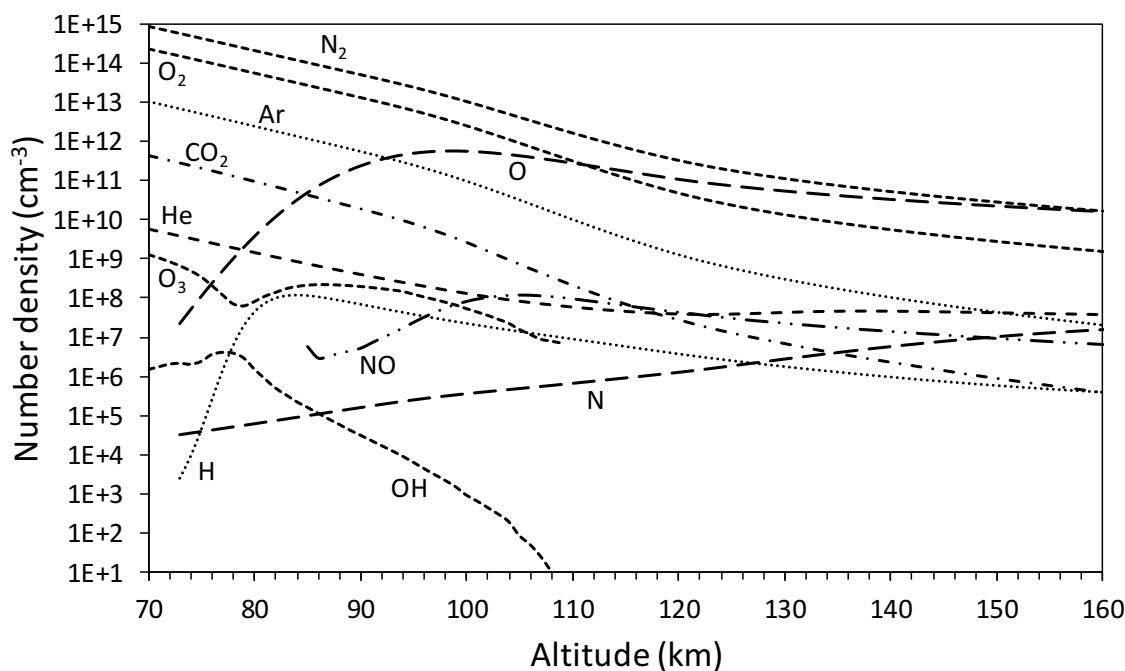


**Figure 9.6.** Densities used in the neutral number density accuracy analysis. Based on data from *Hedin* [1991]; *Mertens* [2011].

and chosen instrument parameters. The ionization process makes this more complicated for neutrals than for ions. Two factors are mainly responsible for this increase in complication: fragmentation and ionization cross section. The fragmentation fraction for many species that fragment during EI can be estimated from *Linstrom and Mallard* [2001]. The dissociation fractions and ionization cross sections used in the neutral particle analysis are shown in Tables 9.1 and 9.2, respectively.

The EI cross section values assume an electron energy of 100 eV. Electron-induced dissociation of parent molecules in the ionizer results in some peaks in the mass spectrum having contributions from two or more atmospheric species. For example, besides contributions from ambient atomic oxygen, the  $m/z$  16 peak will also include oxygen from dissociated OH, NO, O<sub>2</sub>, CO<sub>2</sub>, and O<sub>3</sub>, although contributions from OH and O<sub>3</sub> will be very small over the majority of the altitude range considered here. Table 9.3 lists the main contributors to the major peaks of interest for  $m/z$  values below 50. Examples for calculating the relative

**Table 9.1.** Dissociation Fractions of Molecules Used in the Neutral Number Density Accuracy Analysis [*Linstrom and Mallard, 2001*]

Species	Dissociation Fraction
OH	0.1228
N <sub>2</sub>	0.1204
NO	0.0803
O <sub>2</sub>	0.1803
CO <sub>2</sub>	0.2143
O <sub>3</sub>	0.5634

**Table 9.2.** Electron Ionization Cross Sections Used in the Neutral Number Density Accuracy Analysis [*Sorokin et al., 2000; Linstrom and Mallard, 2001; Joshipura et al., 2001*]

Species	Ionization Cross Section, $\sigma$ (m <sup>2</sup> )
H	$5.46 \times 10^{-21}$
He	$3.60 \times 10^{-21}$
N	$1.58 \times 10^{-20}$
O	$1.40 \times 10^{-20}$
OH	$1.88 \times 10^{-20}$
N <sub>2</sub>	$2.62 \times 10^{-20}$
NO	$2.92 \times 10^{-20}$
O <sub>2</sub>	$2.62 \times 10^{-20}$
Ar	$2.9 \times 10^{-20}$
CO <sub>2</sub>	$3.74 \times 10^{-20}$
O <sub>3</sub>	$3.78 \times 10^{-20}$

standard deviations for He and O, which are representative of the methods used to obtain the number density accuracies presented in this section, are given in sections 9.2.3.1 and 9.2.3.2.

A number density accuracy analysis for atmospheric neutrals is shown in Figure 9.7 for an aperture diameter of 202  $\mu\text{m}$  and an integration distance of 1 km. A duty cycle of

**Table 9.3.** Contributors to Different m/z Peaks in a Mass Spectrum of Neutral Particles in the Upper Atmosphere

m/z	Peak Contributors
1	H (from ambient H and from dissociated OH)
4	He (ambient)
14	N (from ambient N and from dissociated N <sub>2</sub> and NO)
16	O (from ambient O and from dissociated NO, O <sub>2</sub> , CO <sub>2</sub> and O <sub>3</sub> )
17	Ambient OH and <sup>17</sup> O
18	<sup>18</sup> O (from ambient <sup>18</sup> O, dissociated NO, O <sub>2</sub> , CO <sub>2</sub> and O <sub>3</sub> )
28	N <sub>2</sub> (ambient) and CO (from dissociated CO <sub>2</sub> )
29	N <sub>2</sub> (ambient, with one <sup>15</sup> N) and CO ( <sup>13</sup> C or <sup>17</sup> O from dissociated CO <sub>2</sub> )
30	NO (ambient) and N <sub>2</sub> (ambient, with two <sup>15</sup> N atoms)
32	O <sub>2</sub> (ambient) and NO (with one <sup>18</sup> O)
34	<sup>34</sup> O <sub>2</sub> (ambient)
36	<sup>36</sup> Ar (ambient) and <sup>36</sup> O <sub>2</sub> (with two <sup>18</sup> O atoms)
40	Ar (ambient)
44	CO <sub>2</sub> (ambient)
48	O <sub>3</sub> (ambient)

0.73% and a peak broadening factor of 0.78 were used. This analysis assumes an adjustable EI emission current, which allows for a maximum count rate (i.e., just below detector saturation limits) to be maintained for the strongest peak at any given altitude in the flight profile. At lower altitudes the ionizer current is small to avoid saturating the MCP detector. At higher altitudes the number density decreases, and the electron emission current is increased with the intent of maintaining a nominally constant count rate at the most abundant mass peak. As with the number density accuracy analysis for ions, the most abundant neutral particles are measured with the greatest accuracy.

Figure 9.7 shows the estimated accuracy with which neutral densities can be measured with the SDL TOF-MS. The major species (O<sub>2</sub> and N<sub>2</sub>) are predicted to be measureable

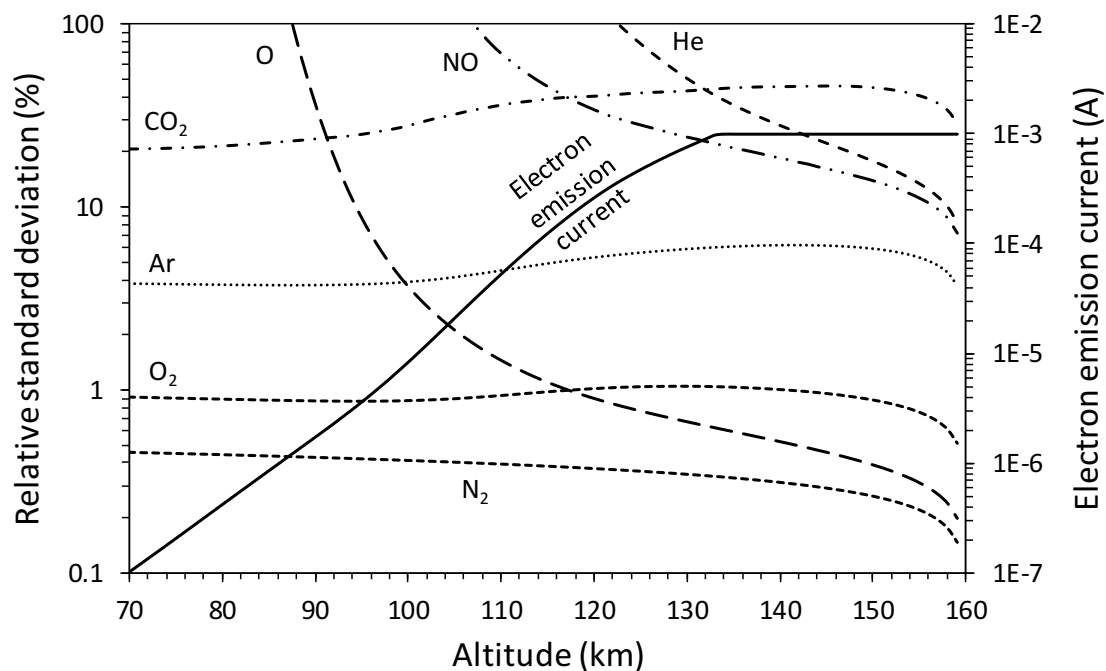


**Figure 9.7.** Results from the neutral number density accuracy analysis for a 202  $\mu\text{m}$  diameter instrument aperture and an integration distance of 1 km. These results assume ambient densities shown in Figure 9.6.

at better than 1% accuracy over the entire simulated flight profile (70 to 160 km). The measurement accuracy for atomic oxygen improves, falling below 1% at approximately 120 km, as its ambient density increases. However, species with small ambient densities are difficult to measure with good accuracy. To improve the measurement of species with lower densities, the SDL TOF-MS can be operated in a saturated variation of neutral mode. In saturation mode, the mass peaks for the most common species are intentionally saturated, and a maximum count rate is maintained for a species with a lower ambient number density. The more abundant species, whose mass peaks are saturated at their most common isotopes, are instead measured from their minor isotope peaks. For example, the electron emission current can be set to maintain a constant count rate at the  $m/z$  29 peak ( $^{29}\text{N}_2$ ) just below the saturation count rate level of the MCP detector. In this case the  $\text{N}_2$  density would be measured from the  $m/z$  29 peak instead of the  $m/z$  28 peak. Other species that are measured at their minor peaks in saturation mode in Figure 9.8 include argon ( $m/z$  36), atomic oxygen

( $m/z$  18), and molecular oxygen ( $m/z$  34).

Results from the neutral number density accuracy analysis for saturation mode are shown in Figure 9.8. Simulation parameters included an aperture diameter of 1600  $\mu\text{m}$ , an integration distance of 1 km, a 0.73% duty cycle, and a peak broadening factor of 0.78. The electron emission current was set to maintain the maximum unsaturated count rate at the  $m/z$  29 peak, resulting in the intentional saturation of the  $m/z$  16, 28, 32, and 40 peaks. The  $m/z$  32 ( $\text{O}_2$ ) peak remained saturated throughout the entire altitude range, so the  $\text{O}_2$  number density accuracy was measured from the  $m/z$  34 ( $^{34}\text{O}_2$ ) peak. Both the  $m/z$  16 and 40 peaks ( $^{16}\text{O}$  and  $^{40}\text{Ar}$ , respectively) were only saturated throughout part of the altitude range; at these altitudes, their number density accuracies were calculated based on the  $^{18}\text{O}$  and  $^{36}\text{Ar}$  isotopes. The curves for both O and Ar show discontinuities where the density accuracy changes from being calculated from the minor isotope to the most abundant isotope.

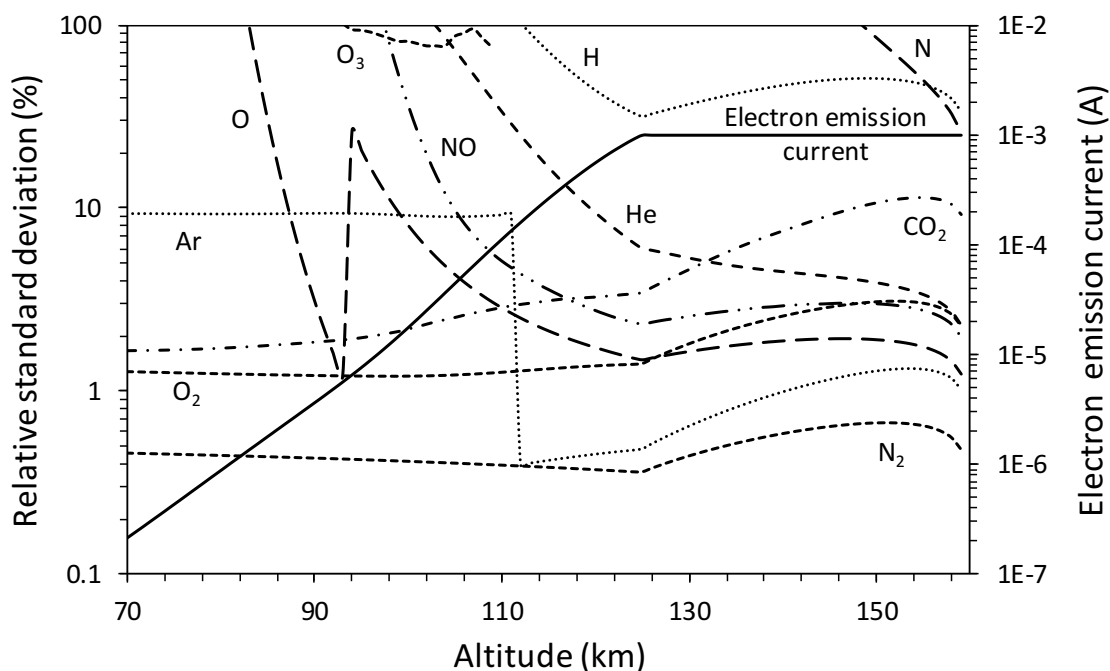


**Figure 9.8.** Results from the neutral number density accuracy analysis for the SDL TOF-MS operating in saturation mode, for a 1600  $\mu\text{m}$  diameter instrument aperture and an integration distance of 1 km. Discontinuities, for example in Ar and O, result from changing the measurement accuracy calculation from a minor to a major isotope of the species.

Saturation mode allows minor atmospheric species to be measured with greater accuracy than in standard operation.

The integration distance, mentioned in section 9.2, determines the number of individual scans that are combined to form a mass spectrum. Figure 9.9 shows the same number density analysis as Figure 9.8, except that the integration distance is 5 km instead of 1 km. The measurement accuracy improves with a longer integration distance but at the expense of vertical resolution. The combination of saturation mode and a longer integration distance may be useful, if not necessary, to measure less common species of interest.

#### 9.2.3.1. Example: He Density Uncertainty

The  $m/z$  4 peak in the neutral number density accuracy analysis has contributions from He and UV. The total number of counts in the  $m/z$  4 peak can be expressed as

$$N_4 = N_{\text{He}} + N_{\text{UV}}, \quad (9.47)$$

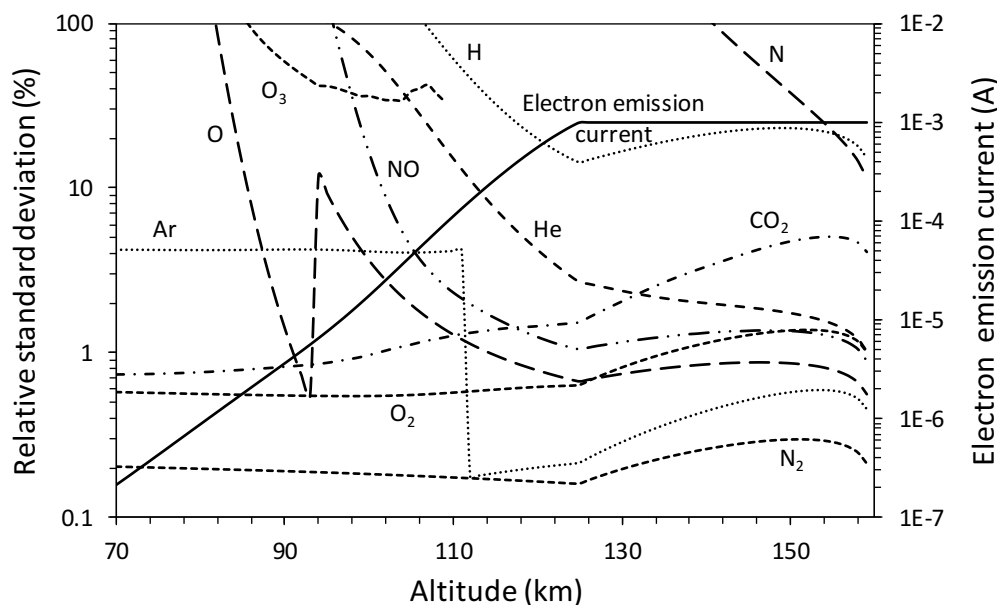


**Figure 9.9.** Results from the neutral number density accuracy analysis for the SDL TOF-MS operating in saturation mode, for a 1600  $\mu\text{m}$  diameter instrument aperture and an integration distance of 5 km. Compare to Figure 9.8, which used an integration distance of 1 km in an otherwise identical analysis.

where  $N_{\text{He}}$  represents the number of counts due to He and  $N_{\text{UV}}$  is the number of counts due to background UV photons. The uncertainty in the m/z 4 peak is

$$\delta N_4 = \sqrt{N_4}. \quad (9.48)$$

The number of counts in the m/z 4 peak due to He, and associated uncertainty is

$$N_{\text{He}} = N_4 - N_{\text{UV}} \quad (9.49)$$

$$\delta N_{\text{He}} = \sqrt{N_4 + N_{\text{UV}}}, \quad (9.50)$$

where  $N_{\text{UV}}$  is found as described in section 9.2.2.1. The fractional uncertainty for He is

$$\frac{\delta N_{\text{He}}}{N_{\text{He}}} = \frac{\sqrt{N_4 + N_{\text{UV}}}}{N_{\text{He}}}. \quad (9.51)$$

Multiplying equation 9.51 by 100 gives the relative standard deviation, or percent uncertainty for the He measurement.

### 9.2.3.2. Example: Atomic Oxygen (O) Density Uncertainty

A more complicated example is the number of counts and associated uncertainty for atomic oxygen (O). Because of EI induced fragmentation, the m/z 16 peak has contributions not only from ambient O and background UV, but also O from dissociated OH, O<sub>2</sub>, NO, CO<sub>2</sub>, and O<sub>3</sub>. The total number of counts in the m/z 16 peak can be expressed as

$$N_{16} = N_{\text{O}} + N_{\text{OH} \rightarrow \text{O}} + N_{\text{O}_2 \rightarrow \text{O}} + N_{\text{NO} \rightarrow \text{O}} + N_{\text{CO}_2 \rightarrow \text{O}} + N_{\text{O}_3 \rightarrow \text{O}} + N_{\text{UV}}, \quad (9.52)$$

where  $N_{\text{O}}$  is the number of counts due to ambient neutral oxygen and  $N_{\text{UV}}$  is the number of counts due to UV background (see section 9.2.2.1). The remaining terms in equation 9.52 represent contributions of dissociated O from the following parent molecules: OH,

O<sub>2</sub>, NO, CO<sub>2</sub>, and O<sub>3</sub>. The concentration of OH is insignificant compared to O at altitudes above about 75 km, ranging from a few percent to less than 0.000001% at altitudes above 100 km; the contribution from  $N_{OH \rightarrow O}$  is small and can be ignored ( $N_{OH \rightarrow O} \approx 0$  in equation 9.52). Similarly, at altitudes above about 80 km the contribution from O<sub>3</sub> can be ignored ( $N_{O_3 \rightarrow O} \approx 0$  in equation 9.52). The number of counts from ambient atomic oxygen (O) can be simplified to

$$N_O = N_{16} - N_{O_2 \rightarrow O} - N_{NO \rightarrow O} - N_{CO_2 \rightarrow O} - N_{UV}. \quad (9.53)$$

The uncertainty in  $N_O$  is given by

$$\delta N_O = \sqrt{(\delta N_{16})^2 + (\delta N_{UV})^2 + (\delta N_{O_2 \rightarrow O})^2 + (\delta N_{NO \rightarrow O})^2 + (\delta N_{CO_2 \rightarrow O})^2}. \quad (9.54)$$

The uncertainties  $\delta N_{16}$  and  $\delta N_{UV}$  are simply

$$\delta N_{16} = \sqrt{N_{16}} \quad (9.55)$$

$$\delta N_{UV} = \sqrt{N_{UV}}. \quad (9.56)$$

The other uncertainty terms in equation 9.54 are more complicated. *Linstrom and Mallard* [2001] contains EI mass spectra for various molecules, including O<sub>2</sub>, NO, and CO<sub>2</sub>, which can be used to estimate the dissociation fractions of each (see also table 9.1). The mass spectrum for O<sub>2</sub> shows a dissociation fraction of 0.180328. The number of O<sub>2</sub> molecules that dissociate can be expressed as

$$N_{O_2 \rightarrow O} = 0.180328 \cdot N_{O_2}. \quad (9.57)$$

The uncertainty  $\delta N_{O_2 \rightarrow O}$  is then expressed as

$$\delta N_{O_2 \rightarrow O} = 0.180328 \cdot \delta N_{O_2}. \quad (9.58)$$

If  $N_{O_2}$  is known (based on the  $m/z$  32 peak for example), then

$$\delta N_{O_2} = \sqrt{N_{O_2}} \quad (9.59)$$

and equation 9.58 can be written

$$\delta N_{O_2 \rightarrow O} = 0.180328 \cdot \sqrt{N_{O_2}}. \quad (9.60)$$

Following a similar process for NO and CO<sub>2</sub> gives

$$\delta N_{NO \rightarrow O} = 0.013393 \cdot \sqrt{N_{NO}} \quad (9.61)$$

$$\delta N_{CO_2 \rightarrow O} = 0.074242 \cdot \sqrt{N_{CO_2}}. \quad (9.62)$$

The total uncertainty for  $N_O$  can then be expressed as

$$\delta N_O = \sqrt{N_{I6} + N_{UV} + 0.0325 \cdot N_{O_2} + 0.000179 \cdot N_{NO} + 0.0055 \cdot N_{CO_2}}. \quad (9.63)$$

At this point the fractional uncertainty and relative standard deviation for atomic oxygen can be easily found by following the same procedure used in sections 9.2.2.1, equation 9.37.

### 9.3. Conclusions

The success of the SDL TOF-MS will ultimately be determined by its ability to make accurate measurements of ambient densities in the upper atmosphere. Sensitivity and number density accuracy analyses were presented in this chapter to demonstrate and predict how, and with what accuracy, ambient densities can be obtained with the SDL instrument. Sensitivity equations were developed for both neutral particles and ions to relate the detector count rate to ambient densities (equations 9.9 and 9.10). The number density accuracy

analysis was based on the sensitivity equations, as well as instrument operating parameters obtained from instrument performance modeling presented in Chapter 8. This also included a UV background analysis. The amount of background due to UV was not a major factor in the scenarios considered here.

Although the number density accuracy analysis presented in this chapter assumed the use of a linear version of the SDL instrument, the performance of a reflectron instrument is expected to be similar. The superior resolution of a reflectron instrument allows the use of longer start pulses, which results in a comparable duty cycle to a linear instrument (Chapter 8). A reflectron has the added advantage of placing the MCP detector out of the direct line of sight of the aperture, eliminating much if not all UV background.

The number density accuracy analyses demonstrated predicted measurement accuracies better than 10% for major neutral species (Ar, N<sub>2</sub>, O<sub>2</sub>, CO<sub>2</sub>) throughout the entire simulated altitude range, from 70 to 160 km. The major ion species NO<sup>+</sup> and O<sub>2</sub><sup>+</sup> are predicted to be measurable at better than 1% throughout most of the altitude range (85 to 160 km). Other minor neutrals and ions should be measurable at better than 10% uncertainty over much of the altitude range. Improved measurement of minor species may be improved by using a larger sampling aperture, to increase the signal from minor species, while intentionally saturating the peaks of major species. Increasing the integration distance improves the measurement accuracy for all species but at the expense of vertical resolution. Lower rocket apogees result in greater number of scans per integration distance, which can also be used to improve measurement accuracy. The results presented here demonstrate the potential of the SDL instrument to successfully make composition measurements in the MLT to expand the current understanding of this region of Earth's atmosphere.

## CHAPTER 10

## SUMMARY, CONCLUSIONS, AND FUTURE WORK

## 10.1. Summary and Conclusions

This dissertation describes the development of a new TOF-MS instrument for making *in-situ* composition measurements of the upper atmosphere, in particular the MLT region. The SDL TOF-MS is compact and adaptable, compatible with both sounding rockets and small satellites. This study integrated modeling and simulations with laboratory experiments to identify operational boundaries and capabilities for this new instrument. Rigorous computer modeling was performed to study the effect of critical instrument operating parameters on instrument performance. A laboratory prototype of this instrument was tested in the laboratory, successfully demonstrating TOF-MS technology under conditions relevant to *in-situ* MLT measurements.

Design of the ion optics for the SDL TOF-MS is presented in Chapter 2. Ions are accelerated by an acceleration grid system, after which they pass through a Bradbury-Nielsen gate. The gate operates in two modes, either deflecting ions away from the instrument axis (beam off) or allowing them to pass through unimpeded (beam on). The gate is the enabling technology for the SDL instrument and produces ion pulses with small temporal and spatial uncertainties. The ion pulses pass through a field-free drift region to reach the MCP detector. To aid in the ion optics design, Monte Carlo models were developed to simulate ion behavior in both the beam on and beam off states; these simulations were used to define instrument parameters prior to the design and construction of the prototype instrument.

The electrical and mechanical design of the prototype instrument are discussed in Chapter 3. Because the goal of this project was to build and test a functional instrument head that could be tested in the existing ion optics facilities at SDL, rack-mounted power supplies and commercial pulse-processing electronics were used wherever possible. A modulation driver board was designed and constructed in house to provide deflection potentials for the

BNG. Results from computer modeling of the ion optics design were incorporated in both the electrical and mechanical design of the instrument. The mechanical design and fabrication of the prototype instrument was also performed at SDL; the assembled instrument was then tested in the SDL IOTF.

The MCP detector used in the SDL TOF-MS was chosen based on previous reports of its performance at elevated pressures. This detector underwent rigorous laboratory testing to study its behavior at pressures extending into the  $10^{-2}$  Torr range. These experiments are described in Chapter 4 and include background count rate and detector discharge experiments under a variety of backfill gases. The detector performed remarkably well; background count rates after scrubbing were  $<10$  cts/s at pressures above 1 mTorr. Other experiments demonstrated the detector's ability to be exposed to pressures above 10 mTorr, with operating voltages applied, before discharging. Additionally, humidity levels as high as 50% (RH) did not noticeably affect detector background or discharge pressure. Finally, the TOF-MS was successfully operated at  $2 \times 10^{-4}$  Torr under argon backfill, to produce a mass spectrum in neutral mode. These experiments demonstrate the stability of the MCP detector at pressures relevant to MLT conditions.

A new getter-based pumping system, consisting of barium loaded TGs, has been considered for use in the SDL TOF-MS. Experiments to determine the capabilities of this new system are presented in Chapter 5. These experiments resulted in a pumping speed database, covering a range of pressures from  $5 \times 10^{-5}$  Torr to  $5 \times 10^{-2}$  Torr and quantities of gas sorbed up to 0.4 Torr·L. The results are consistent with pumping speeds quoted by the manufacturer. The database was incorporated in a computer model to simulate instrument pressure for the SDL TOF-MS on a sounding rocket. Besides providing pumping for rocket-borne instruments, TGs may also be employed as a low cost method for maintaining vacuum conditions for pressure-sensitive instruments during shipping or launch preparations.

Chapter 6 presents bow shock and instrument pressure modeling of the SDL instru-

ment. DSMC modeling confirmed that the bow shock is a major obstacle to making accurate composition measurements in the MLT below 120 km. Cryogenically freezing out the bow shock is the only proven method for eliminating bow shock effects at these altitudes. Above 120 km, composition measurements can likely be made without employing cryogenics. Bow shock modeling results were incorporated in an instrument pressure computer model to evaluate the effectiveness of three potential pumping scenarios on a rocket-borne SDL TOF-MS: a miniature turbo pump with a constant 4 L/s pumping speed; TGs, with pumping speeds based on laboratory experiments; and no active pumping at all. The miniature turbo pump was found to be the most effective of the three methods at providing suitable instrument operating pressures. Simulations suggested that TGs combined with an appropriate aperture size could extend the measurement range of the SDL TOF-MS to lower altitudes by 10 to 20 km, compared to an unpumped instrument.

This work culminated in the construction of a functional laboratory prototype of the SDL instrument. The subject of Chapter 7 is the characterization of this instrument in the SDL IOTF. Experiments were performed to determine ion deflection capabilities of the BNG. Results from these experiments were used to optimize the BNG deflection potential for collecting mass spectra. The instrument successfully operated in both ion and neutral modes and was used to produce spectra with unit mass resolution at  $m/z$  40. Spectra from multiple experiments are presented in the text. The EDU was also successfully operated at a maximum pressure of  $2 \times 10^{-4}$  Torr, in neutral mode. The maximum resolution achieved to date is 100 (at  $m/z$  40), recorded in ion mode. The results from characterization of the prototype instrument validate the SDL TOF-MS concept. Additionally, the instrument has demonstrated the necessary mass resolution to measure major MLT gas species.

Chapter 8 describes a computer model of the SDL instrument and results from simulations performed to study the effects of different instrument operating parameters on mass resolution. The model has good qualitative agreement with spectra obtained in the laboratory with the SDL instrument. The most important factor affecting mass resolution was

found to be the energy spread of sampled particles. The model was also used to simulate the performance of both a rocket-borne and a satellite-mounted instrument. Simulations of a rocket-borne linear instrument produced spectra with sufficient mass resolution to distinguish the major atmospheric species at  $m/z$  values as high as 47; however, beyond this the mass resolution deteriorated significantly. A linear design was found to be insufficient to obtain unit mass resolution for a satellite-mounted instrument. The high speed of a satellite, combined with the large energy spread of ambient particles in LEO, require a reflectron version of the SDL TOF-MS. Simulations of a reflectron instrument in LEO produced spectra with unit mass resolution at  $m/z$  values as high as 100. The superior mass resolving capabilities of a reflectron instrument allow a much longer ion pulse to be used than for a linear instrument, resulting in similar duty cycles for both. The effects of critical instrument operating parameters can be quickly explored with the computer model. This model is being used in current space science proposals.

An instrument sensitivity analysis for the SDL TOF-MS is presented in Chapter 9. This analysis, performed for both ions and neutrals, relates ambient densities to detector count rates. The sensitivity analysis was used to predict the accuracy at which number density measurements in the MLT can be made with the SDL instrument. The SDL instrument is expected to be able to measure the more abundant species (Ar, N<sub>2</sub>, O<sub>2</sub>, CO<sub>2</sub>) in the MLT with a 10% uncertainty or better. The uncertainty is higher for minor species. Ionizer emission current, aperture size, apogee, and integration distance can be adjusted to improve measurement uncertainties and meet the science goals and sensitivity needs of each mission.

## 10.2. Future Work

Future work on the SDL TOF-MS will concentrate on two main areas of development: electronics and instrument design. Instrument components requiring DC voltages will require a flight-compatible power supply. Pulse processing electronics will be developed to

replace the commercial electronics used during testing of the prototype instrument. A BNG modulation drive with improved pulse rise and fall times and reduced ringing will result in ion pulses with high spatial and temporal definition. Elimination of the noise currently interfering with the pulse processing electronics will allow the instrument to be operated in HT mode.

Instrument design efforts will focus on the incorporation of a reflectron in the SDL instrument. Only single stage reflectrons have been considered in this dissertation; other reflectron options include dual stage, quadratic, and gridless designs. These may offer superior energy focusing while occupying less space, to reduce the overall size of the instrument. Rigorous SIMION<sup>®</sup> modeling will be required to optimize the mechanical design of the reflectron. A prototype SDL RTOF-MS instrument can then be constructed and merged with the improved electronics. Efforts are underway at SDL to develop a neutral beam source to complement the existing ion optics facility. A supersonic neutral beam will allow the SDL instrument to be characterized under conditions relevant to LEO.

The last published data from an ion mass spectrometer in the mesopause region is more than 20 years old [*Balsiger et al.*, 1996; *Dickson et al.*, 2013]. The SDL TOF-MS was designed specifically with the MLT region in mind. The instrument has the proven capability of measuring both major and minor atmospheric species, resolving neighboring mass peaks when present in laboratory experiments (Figure 7.13). Continued work on the electronics and instrument design will improve instrument performance. The instrument is small and adaptable, and is well suited for use as either a sounding rocket or small satellite payload. The ultimate goal for the SDL TOF-MS is to use the instrument to make accurate composition measurements in the Earth's upper atmosphere.

## REFERENCES

- Aikin, A. C., A. E. Hedin, D. J. Kendig, and S. Drake (1993), Thermospheric molecular oxygen measurements using the ultraviolet spectrometer on the Solar Maximum Mission Spacecraft, *J. Geophys. Res.*, *98*(A10), 17,607–17,613, doi:10.1029/93JA01468.
- AlfaVakuo (2016), AlfaVakuo e.U. Home, Online, accessed 2016-08-26. <http://alfavakuo.eu/>.
- Alpers, M., T. Blix, S. Kirkwood, D. Krankowsky, F.-J. Lübken, S. Lutz, and U. von Zahn (1993), First simultaneous measurements of neutral and ionized iron densities in the upper mesosphere, *J. Geophys. Res.*, *98*(A1), 275–283, doi:10.1029/92JA01665.
- Alvatec (2014), Alvatec tube getters, Online, accessed 2014-08-09. [http://www.alvatec.com/files/5713/4797/2242/tube-getter-intern-ausdruck\\_gh.pdf](http://www.alvatec.com/files/5713/4797/2242/tube-getter-intern-ausdruck_gh.pdf).
- Amyx, K., Z. Sternovsky, S. Knappmiller, S. Robertson, M. Horanyi, and J. Gumbel (2008), In-situ measurement of smoke particles in the wintertime polar mesosphere between 80 and 85 km altitude, *J. Atmos. Sol. Terr. Phys.*, *70*(1), 61 – 70, doi:10.1016/j.jastp.2007.09.013.
- Arnold, F., J. Kissel, D. Krankowsky, H. Wieder, and J. Zähringer (1971), Negative ions in the lower ionosphere: A mass-spectrometric measurement, *J. Atmos. Terr. Phys.*, *33*(8), 1169 – 1175, doi:10.1016/0021-9169(71)90104-8.
- ASTM Standard F798-97 (Reapproved 2002), Standard practice for determining getting rate, sorption capacity, and gas content of nonevaporable getters in the molecular flow regime, ASTM International, West Conshohocken, PA, doi:10.1520/F0798-97R02.
- Balsiger, F., E. Kopp, M. Friedrich, K. M. Torkar, and U. Wälchli (1993), Small-scale structure of  $O_2^+$  and proton hydrates in a noctilucent cloud and polar mesospheric summer echo of August 9/10 1991 above Kiruna, *Geophys. Res. Lett.*, *20*(20), 2315–2318, doi:10.1029/93GL02819.
- Balsiger, F., E. Kopp, M. Friedrich, K. M. Torkar, U. Wälchli, and G. Witt (1996), Positive ion depletion in a noctilucent cloud, *Geophys. Res. Lett.*, *23*(1), 93–96, doi:10.1029/95GL03608.
- Balsiger, H., P. Eberhardt, J. Geiss, and E. Kopp (1971), A mass spectrometer for the simultaneous measurement of the neutral and the ion composition of the upper atmosphere, *Rev. Sci. Instrum.*, *42*(4), 475–476, doi:10.1063/1.1685134.
- Barjatya, A., and C. M. Swenson (2006), Observations of triboelectric charging effects on Langmuir-type probes in dusty plasma, *J. Geophys. Res.*, *111*(A10), doi:10.1029/2006JA011806, A10302.

- Beig, G., J. Scheer, M. G. Mlynczak, and P. Keckhut (2008), Overview of the temperature response in the mesosphere and lower thermosphere to solar activity, *Rev. Geophys.*, 46(3), doi:10.1029/2007RG000236, RG3002.
- Bird, G. A. (1988), Aerodynamic effects on atmospheric composition measurements from rocket vehicles in the thermosphere, *Planet. Space Sci.*, 36(9), 921 – 926, doi:10.1016/0032-0633(88)90099-2.
- Bird, G. A. (2005), The DS2V/3V program suite for DSMC calculations, *AIP Conference Proceedings*, 762(1), 541–546, doi:10.1063/1.1941592.
- Björn, L. G., et al. (1985), Heavy ionospheric ions in the formation process of noctilucent clouds, *J. Geophys. Res.*, 90(D5), 7985–7998, doi:10.1029/JD090iD05p07985.
- Bloomer, R. N. (1957a), Barium getters and oxygen, *Brit. J. Appl. Phys.*, 8(1), 40.
- Bloomer, R. N. (1957b), The oxidation of evaporated barium films (getters), *Brit. J. Appl. Phys.*, 8(8), 321.
- Boedeker Plastics (2016), PEEK (polyetheretherketone Specifications, Online, accessed 2016-07-14. [http://www.boedeker.com/peek\\_p.htm](http://www.boedeker.com/peek_p.htm).
- Boyd, I. D. (2009a), Direct simulation Monte Carlo for atmospheric entry. 1. Theoretical basis and physical models, NATO RTO report EN-AVT-162, pp. 16(1)–1 – 16(1)–28.
- Boyd, I. D. (2009b), Direct simulation Monte Carlo for atmospheric entry. 2. Code development and application results, NATO RTO report EN-AVT-162, pp. 16(2)–1 – 16(2)–28.
- Bradbury, N. E., and R. A. Nielsen (1936), Absolute values of the electron mobility in hydrogen, *Phys. Rev.*, 49, 388–393, doi:10.1103/PhysRev.49.388.
- Brasseur, G. P., and S. Solomon (2005), *Aeronomy of the Middle Atmosphere: Chemistry and Physics of the Stratosphere and Mesosphere*, Springer, Dordrecht, The Netherlands.
- Brock, A., N. Rodriguez, and R. N. Zare (1998), Hadamard transform time-of-flight mass spectrometry, *Anal. Chem.*, 70(18), 3735–3741, doi:10.1021/ac9804036.
- Brock, A., N. Rodriguez, and R. N. Zare (2000), Characterization of a Hadamard transform time-of-flight mass spectrometer, *Rev. Sci. Instrum.*, 71(3), 1306–1318, doi:10.1063/1.1150456.
- Brown, R. F., D. M. Trayer, and M. R. Busby (1970), Condensation of 300-2500 k gases on surfaces at cryogenic temperatures, *J. Vac. Sci. Technol.*, 7(1), 241–246, doi:10.1116/1.1315808.

- Chambers, A. (2005), *Modern Vacuum Physics*, CRC Press, New York, NY.
- Clemesha, B. R. (1995), Sporadic neutral metal layers in the mesosphere and lower thermosphere, *J. Atmos. Terr. Phys.*, 57(7), 725 – 736, doi:10.1016/0021-9169(94)00049-T.
- Cochran, R. F., B. N. Laprade, R. Prunier, L. Erickson, and W. Dunn (2005), Performance characteristics of detectors operated in harsh environments, in *The HEMS 2005 Conference*.
- Cotter, R. J. (1997), *Time-of-Flight Mass Spectrometry: Instrumentation and Applications in Biological Research*, American Chemical Society, Washington DC.
- Creare (2014), Creare, Online, accessed 2014-08-01. <http://www.creare.com/products/minivac.html>.
- Creare (2016), Fluid and Thermal Systems, Online, accessed 2016-08-05. <http://www.creare.com/r-d-services/fluid-and-thermal-systems/#1461890148303-309ffc9-8502>.
- Dahl, D. A. (2000), Simion for the personal computer in reflection, *Int. J. Mass Spectrom.*, 200(1 - 3), 3 – 25, doi:10.1016/S1387-3806(00)00305-5.
- de Hoffmann, E., and V. Stroobant (2007), *Mass Spectrometry: Principles and Applications*, John Wiley & Sons, Ltd., Chichester, UK.
- Dengg, F. (2011), Alvatec GmbH, Personal communication.
- Dickson, S., M. Gausa, S. Robertson, and Z. Sternovsky (2013), Channel electron multiplier operated on a sounding rocket without a cryogenic vacuum pump from 120 to 80 km altitude, *J. Atmos. Sol. Terr. Phys.*, 95 - 96, 51 – 58, doi:10.1016/j.jastp.2013.01.003.
- Espy, P. J., G. O. L. Jones, G. R. Swenson, J. Tang, and M. J. Taylor (2004), Seasonal variations of the gravity wave momentum flux in the Antarctic mesosphere and lower thermosphere, *J. Geophys. Res.*, 109(D23), doi:10.1029/2003JD004446, D23109.
- Fernández, F. M., J. M. Vadillo, F. Engelke, J. R. Kimmel, R. N. Zare, N. Rodriguez, M. Wetterhall, and K. Markides (2001), Effect of sequence length, sequence frequency, and data acquisition rate on the performance of a Hadamard transform time-of-flight mass spectrometer, *J. Am. Soc. Mass Spectrom.*, 12(12), 1302 – 1311, doi:10.1016/S1044-0305(01)00322-1.
- Fernández, F. M., J. M. Vadillo, J. R. Kimmel, M. Wetterhall, K. Markides, N. Rodriguez, and R. N. Zare (2002), Hadamard transform time-of-flight mass spectrometry: A high-speed detector for capillary-format separations, *Anal. Chem.*, 74(7), 1611–1617, doi:10.1021/ac015673u.

- Ferrario, B. (1996), Chemical pumping in vacuum technology, *Vacuum*, 47(4), 363 – 370, doi:10.1016/0042-207X(95)00252-9.
- Franke, S. J., X. Chu, A. Z. Liu, and W. K. Hocking (2005), Comparison of meteor radar and Na Doppler lidar measurements of winds in the mesopause region above Maui, Hawaii, *J. Geophys. Res.*, 110(D9), doi:10.1029/2003JD004486, D09S02.
- Gadsden, M. (1982), Noctilucent clouds, *Space Sci. Rev.*, 33(3), 279–334, doi:10.1007/BF00196999.
- Gadsden, M., and W. Schröder (1989), *Noctilucent Clouds*, Springer, Berlin, FRG, doi:10.1007/978-3-642-48626-5\_1.
- Gao, L., A. Sugiarto, J. D. Harper, R. G. Cooks, and Z. Ouyang (2008), Design and characterization of a multisource hand-held tandem mass spectrometer, *Anal. Chem.*, 80(19), 7198–7205, doi:10.1021/ac801275x.
- Gardner, C. S., D. G. Voelz, C. F. Sechrist, and A. C. Segal (1986), Lidar studies of the nighttime sodium layer over Urbana, Illinois: 1. Seasonal and nocturnal variations, *J. Geophys. Res.*, 91(A12), 13,659–13,673, doi:10.1029/JA091iA12p13659.
- Gelinas, L. J., K. A. Lynch, M. C. Kelley, R. L. Collins, M. Widholm, E. MacDonald, J. Ulwick, and P. Mace (2005), Mesospheric charged dust layer: Implications for neutral chemistry, *J. Geophys. Res.*, 110(A1), doi:10.1029/2004JA010503, A01310.
- Goldberg, R. A., et al. (2001), Dropps: A study of the polar summer mesosphere with rocket, radar and lidar, *Geophys. Res. Lett.*, 28(8), 1407–1410, doi:10.1029/2000GL012415.
- Gordley, L. L., et al. (2009), The solar occultation for ice experiment, *J. Atmos. Sol. Terr. Phys.*, 71(3 - 4), 300 – 315, doi:10.1016/j.jastp.2008.07.012.
- Grebowsky, J. M., and D. Bilitza (2000), Sounding rocket data base of E- and D-region ion composition, *Adv. Space Res.*, 25(1), 183 – 192, doi:10.1016/S0273-1177(99)00916-3.
- Griffiths, B. (2012), Kore Technology Ltd, Personal communication.
- Guilhaus, M. (1995), Principles and instrumentation in time-of-flight mass spectrometry, *J. Mass Spectrom.*, 30(11), 1519–1532, doi:10.1002/jms.1190301102.
- Gumbel, J. (2001a), Aerodynamic influences on atmospheric in situ measurements from sounding rockets, *J. Geophys. Res.*, 106(A6), 10,553–10,563, doi:10.1029/2000JA900166.
- Gumbel, J. (2001b), Rarefied gas flows through meshes and implications for atmospheric

- measurements, *Ann. Geophys.*, 19(5), 563–569, doi:10.5194/angeo-19-563-2001.
- Gumbel, J., M. Rapp, and C. Unckell (1999), Aerodynamic aspects of rocket-borne in situ studies, in *European Rocket and Balloon Programs and Related Research*, vol. 437, p. 459.
- Hargreaves, J. K. (1979), *The Upper Atmosphere and Solar Terrestrial Relations: An Introduction to the Aerospace Environment*, Van Nostrand Reinhold, New York, NY.
- Hargreaves, J. K. (1992), *The Solar-Terrestrial Environment*, Cambridge Atmospheric and Space Science Series, Cambridge University Press, New York, NY.
- Harwit, M., and N. Sloane (1979), *Hadamard Transform Optics*, Academic Press, New York, NY.
- Hays, P. B., V. J. Abreu, M. E. Dobbs, D. A. Gell, H. J. Grassl, and W. R. Skinner (1993), The high-resolution doppler imager on the Upper Atmosphere Research Satellite, *J. Geophys. Res.*, 98(D6), 10,713–10,723, doi:10.1029/93JD00409.
- Hedin, A. E. (1987), MSIS-86 Thermospheric Model, *J. Geophys. Res.*, 92(A5), 4649–4662, doi:10.1029/JA092iA05p04649.
- Hedin, A. E. (1991), Extension of the MSIS Thermosphere Model into the middle and lower atmosphere, *J. Geophys. Res.*, 96(A2), 1159–1172, doi:10.1029/90JA02125.
- Hedin, J., J. Gumbel, T. Waldemarsson, and F. Giovane (2007a), The aerodynamics of the MAGIC meteoric smoke sampler, *Adv. Space Res.*, 40(6), 818 – 824, doi:10.1016/j.asr.2007.06.046.
- Hedin, J., J. Gumbel, and M. Rapp (2007b), On the efficiency of rocket-borne particle detection in the mesosphere, *Atmos. Chem. Phys.*, 7(14), 3701–3711, doi:10.5194/acp-7-3701-2007.
- Hedin, J., J. Gumbel, J. Stegman, and G. Witt (2009), Use of O<sub>2</sub> airglow for calibrating direct atomic oxygen measurements from sounding rockets, *Atmos. Meas. Tech.*, 2(2), 801–812, doi:10.5194/amt-2-801-2009.
- Hernandez, G. (1976), Lower-thermosphere temperatures determined from the line profiles of the O I 17,924-K (5577 Å) emission in the night sky, 1. Long-term behavior, *J. Geophys. Res.*, 81(28), 5165–5172, doi:10.1029/JA081i028p05165.
- Hoffman, D., B. Singh, and J. H. Thomas (1997), *Handbook of Vacuum Science and Technology*, Academic Press, San Diego, CA.
- Höffner, J., and F.-J. Lübken (2007), Potassium lidar temperatures and densities in the

- mesopause region at Spitsbergen (78°N), *J. Geophys. Res.*, *112*(D20), doi:10.1029/2007JD008612, d20114.
- Horányi, M., J. Gumbel, G. Witt, and S. Robertson (1999), Simulation of rocket-borne particle measurements in the mesosphere, *Geophys. Res. Lett.*, *26*(11), 1537–1540, doi:10.1029/1999GL900298.
- Hu, X., Z. Yan, S. Guo, Y. Cheng, and J. Gong (2011), Sodium fluorescence doppler lidar to measure atmospheric temperature in the mesopause region, *Chin. Sci. Bull.*, *56*(4), 417–423, doi:10.1007/s11434-010-4306-x.
- Hunten, D. M., R. P. Turco, and O. B. Toon (1980), Smoke and dust particles of meteoric origin in the mesosphere and stratosphere, *J. Atmos. Sci.*, *37*(6), 1342–1357, doi:10.1175/1520-0469(1980)037<1342:SADPOM>2.0.CO;2.
- Immel, T. J., et al. (2012), The Ionospheric Connection Explorer-A pioneering research mission for space physics and aeronomy., in *AGU Fall Meeting Abstracts*, vol. 1, p. 06.
- Immel, T. J., et al. (2013), ICON: The Ionospheric Connection Explorer-NASA's next space physics and aeronomy mission, in *AGU Fall Meeting Abstracts*, vol. 1, p. 03.
- Istomin, V. G. (1963), Ions of extra-terrestrial origin in the earth's ionosphere, *Planet. Space Sci.*, *11*(2), 173 – 174, doi:10.1016/0032-0633(63)90140-5.
- Johannessen, A., and D. Krankowsky (1972), Positive-ion composition measurement in the upper mesosphere and lower thermosphere at a high latitude during summer, *J. Geophys. Res.*, *77*(16), 2888–2901, doi:10.1029/JA077i016p02888.
- Johnson, C. Y. (1961), Aeronomic parameters from mass spectrometry, *Ann. Geophys.*, *17*, 118.
- Johnson, C. Y., and J. P. Heppner (1956), Daytime measurement of positive and negative ion composition to 131 km by rocket-borne spectrometer, *J. Geophys. Res.*, *61*(3), 575–575, doi:10.1029/JZ061i003p00575.
- Joshi, K. N., M. Vinodkumar, and U. M. Patel (2001), Electron impact total cross sections of CH<sub>x</sub>, NH<sub>x</sub> and OH radicals vis-à-vis their parent molecules, *J. Phys B*, *34*(4), 509, doi:10.1088/0953-4075/34/4/301.
- Kasprzak, W. T., D. Krankowsky, and A. O. Nier (1968), A study of day-night variations in the neutral composition of the lower thermosphere, *J. Geophys. Res.*, *73*(21), 6765–6782, doi:10.1029/JA073i021p06765.
- Kayser, D. C., L. H. Johnson, W. E. Potter, and A. O. Nier (1979), Theory of the fly-through mode for neutral mass spectrometers, *Space Sci. Instrum.*, *4*, 339–350.

- Killeen, T. L., et al. (1999), Timed Doppler interferometer (TIDI), *Proc. SPIE Int. Soc. Opt. Eng.*, 3756, 289–301, doi:10.1117/12.366383.
- Kimmel, J. R., F. M. Fernández, and R. N. Zare (2003), Effects of modulation defects on Hadamard transform time-of-flight mass spectrometry (HT-TOFMS), *J. Am. Soc. Mass Spectrom.*, 14(3), 278 – 286, doi:10.1016/S1044-0305(03)00006-0.
- Kline-Schoder, B. (2011), Creare, Personal communication.
- Knappmiller, S., S. Robertson, Z. Sternovsky, and M. Friedrich (2008), A rocket-borne mass analyzer for charged aerosol particles in the mesosphere, *Rev. Sci. Instrum.*, 79(10), 104502, doi:10.1063/1.2999580.
- Kopp, E., P. Eberhardt, U. Herrmann, and L. G. Björn (1985), Positive ion composition of the high-latitude summer D region with noctilucent clouds, *J. Geophys. Res.*, 90(D7), 13,041–13,053, doi:10.1029/JD090iD07p13041.
- Koppelaar, D. W., C. J. Barinaga, M. B. Denton, R. P. Sperline, G. M. Hieftje, G. D. Schilling, F. J. Andrade, J. H. Barnes, and I. IV (2005), MS Detectors, *Anal. Chem.*, 77(21), 418 A–427 A, doi:10.1021/ac053495p.
- Kore Technology Limited (2015), Some of your more Frequently Asked Questions regarding Photonis Scientific detectors, Online, accessed 2015-06-26. <http://www.kore.co.uk/mcp-faq.htm#2>.
- Krankowsky, D., F. Arnold, V. H. Friedrich, and D. Offermann (1979), Neutral atmospheric composition measurements during the Western European Winter Anomaly Campaign 1975/76, *J. Atmos. Terr. Phys.*, 41(10), 1085 – 1090, doi:http://dx.doi.org/10.1016/0021-9169(79)90084-9.
- Krueger, D. A., C.-Y. She, and T. Yuan (2015), Retrieving mesopause temperature and line-of-sight wind from full-diurnal-cycle Na lidar observations, *Appl. Opt.*, 54(32), 9469–9489, doi:10.1364/AO.54.009469.
- Lafferty, J. (1998), *Foundations of Vacuum Science and Technology*, Wiley, New York, NY.
- Lake, L. R., and A. O. Nier (1973), Loss of atomic oxygen in mass spectrometer ion sources, *J. Geophys. Res.*, 78(10), 1645–1653, doi:10.1029/JA078i010p01645.
- Laprade, B. N., and R. F. Cochran (2006), Performance characterization of high pressure electron multipliers under poor vacuum conditions, in *54 th ASMS Conference Proceedings*.
- Laprade, B. N., R. F. Cochran, R. Prunier, and R. Leffingwell (2006), Progress in the development of a high gain atmospheric pressure ion detector, in *Pittcon 2006 Conference*.

- Lehmacher, G. A., T. D. Scott, M. F. Larsen, S. G. Bilén, C. L. Croskey, J. D. Mitchell, M. Rapp, F.-J. Lübken, and R. L. Collins (2011), The turbopause experiment: atmospheric stability and turbulent structure spanning the turbopause altitude, *Ann. Geophys.*, 29(12), 2327–2339, doi:10.5194/angeo-29-2327-2011.
- Lehmacher, G. A., T. M. Gaulden, M. F. Larsen, and J. D. Craven (2013), Multiple neutral density measurements in the lower thermosphere with cold-cathode ionization gauges, *J. Atmos. Sol. Terr. Phys.*, 92, 137 – 144, doi:10.1016/j.jastp.2012.11.002.
- Lide, D. R. (2005), *CRC Handbook of Chemistry and Physics, 86th Edition*, CRC Press LLC, New York, NY.
- Lieberman, M., and A. Lichtenberg (2005), *Principles of Plasma Discharges and Materials Processing*, Wiley, Hoboken, NJ, doi:10.1002/0471724254.
- Linstrom, P. J., and W. G. Mallard (2001), *NIST Chemistry WebBook; NIST Standard Reference Database No. 69*, National Institute of Standards and Technology, Gaithersburg, MD, <http://webbook.nist.gov/chemistry/>.
- Livesey, R. G. (2001), Method for calculation of gas flow in the whole pressure regime through ducts of any length, *J. Vac. Sci. Technol. A*, 19(4), 1674–1678, doi:10.1116/1.1345895.
- Londer, H., G. R. Myneni, P. Adderley, G. Bartlok, W. Knapp, D. Schleussner, and E. Ogris (2007), New high capacity getter for vacuum insulated mobile LH<sub>2</sub> storage tank systems, *Vacuum*, 82(4), 431 – 434, doi:10.1016/j.vacuum.2007.07.063.
- López-Puertas, M., M. Á. López-Valverde, R. R. Garcia, and R. G. Roble (2000), A review of CO<sub>2</sub> and CO abundances in the middle atmosphere, in *Atmospheric Science Across the Stratopause*, edited by D. E. Siskind, S. D. Eckermann, and M. E. Summers, pp. 83–100, AGU, Washington, D. C., doi:10.1029/GM123p0083.
- Lumpe, J. D., L. E. Floyd, L. C. Herring, S. T. Gibson, and B. R. Lewis (2007), Measurements of thermospheric molecular oxygen from the Solar Ultraviolet Spectral Irradiance Monitor, *J. Geophys. Res.*, 112(D16), doi:10.1029/2006JD008076, d16308.
- Mahaffy, P. R., et al. (2012), The sample analysis at mars investigation and instrument suite, *Space Science Reviews*, 170(1), 401–478, doi:10.1007/s11214-012-9879-z.
- Maier, E. J. R. (1969), Sounding rocket measurements of ion composition and charged particle temperatures in the topside ionosphere, *J. Geophys. Res.*, 74(3), 815–823, doi:10.1029/JA074i003p00815.
- Mamyrin, B. A. (2001), Time-of-flight mass spectrometry (concepts, achievements, and prospects), *Int. J. Mass Spectrom.*, 206(3), 251 – 266, doi:10.1016/S1387-3806(00

00392-4.

- Manura, D. J., and D. A. Dahl (2011), *SIMION Version 8.0/8.1 User Manual*, Scientific Instrument Services, Inc., Ringoes, NJ.
- Martin, A. P., J. V. Vallerga, J. B. McPhate, and O. H. W. Siegmund (2003), Further scrubbing and quantum efficiency results of the HST-COS far-ultraviolet detector, in Future EUV/UV and Visible Space Astrophysics Missions and Instrumentation, *Proc. SPIE*, 4854, 526–531, doi:10.1117/12.460033.
- McDade, I. C. (1998), The photochemistry of the MLT oxygen airglow emissions and the expected influences of tidal perturbations, *Adv. Space Res.*, 21(6), 787 – 794, doi: 10.1016/S0273-1177(97)00674-1.
- McLafferty, F. W., and F. Tureček (1993), *Interpretation of Mass Spectra*, University Science Books, Sausalito, CA.
- Meadows, E. B., and J. W. Townsend (1956), Neutral gas composition of the upper atmosphere by a rocket-borne mass spectrometer, *J. Geophys. Res.*, 61(3), 576–577, doi: 10.1029/JZ061i003p00576.
- Meriwether, J. W. (1989), A review of the photochemistry of selected nightglow emissions from the mesopause, *J. Geophys. Res.*, 94(D12), 14,629–14,646, doi:10.1029/JD094iD12p14629.
- Mertens, C. (2011), NASA, Personal communication.
- Mertens, C. J., M. G. Mlynczak, M. Lopez-Puertas, P. P. Wintersteiner, R. H. Picard, J. R. Winick, L. L. Gordley, and J. M. Russell III (2003), Retrieval of kinetic temperature and carbon dioxide abundance from nonlocal thermodynamic equilibrium limb emission measurements made by the SABER experiment on the TIMED satellite, in Remote Sensing of Clouds and the Atmosphere VII, *Proc. SPIE*, 4882, 162–171, doi: 10.1117/12.463358.
- MKS (2015), Analog 600 Series Selection Guide, Online, accessed 2015-05-16. <http://www.mksinst.com/docs/ur/600analogseries-ds.pdf>.
- Mlynczak, M., et al. (2003), The natural thermostat of nitric oxide emission at 5.3  $\mu\text{m}$  in the thermosphere observed during the solar storms of April 2002, *Geophys. Res. Lett.*, 30(21), doi:10.1029/2003GL017693, 2100.
- Mlynczak, M., G. Diskin, G. Sachse, C. Mertens, E. Syrstad, L. Qian, and S. Solomon (2012), Measurement of carbon dioxide in the mesosphere and lower thermosphere, in *Next-Generation Suborbital Researchers Conference 2012*.

- Mlynczak, M. G. (2011), What is the temperature and carbon dioxide concentration in the mesosphere?, in *AGU Fall Meeting Abstracts*, vol. 1, p. 04.
- Molina, M. J., and F. S. Rowland (1974), Stratospheric sink for chlorofluoromethanes: chlorine atomic-catalysed destruction of ozone, *Nature*, *249*(5460), 810–812.
- Mozer, F. S., and P. Bruston (1967), Electric field measurements in the auroral ionosphere, *J. Geophys. Res.*, *72*(3), 1109–1114, doi:10.1029/JZ072i003p01109.
- Narcisi, R., A. Bailey, G. Federico, and L. Wlodyka (1983), Positive and negative ion composition measurements in the D- and E-regions during the 26 February 1979 solar eclipse, *J. Atmos. Terr. Phys.*, *45*(7), 461 – 478, doi:10.1016/S0021-9169(83)81107-6.
- Narcisi, R. S., and A. D. Bailey (1965), Mass spectrometric measurements of positive ions at altitudes from 64 to 112 kilometers, *J. Geophys. Res.*, *70*(15), 3687–3700, doi:10.1029/JZ070i015p03687.
- Netolicky, W. (2012), Photonis USA, Inc., Personal communication.
- Nier, A. O. (1977), Planetary atmospheres with mass spectrometers carried on high-speed probes or satellites, *AIAA Prog. Astronaut. Aeronaut.*, *51*, 1255–1275.
- Nier, A. O., J. H. Hoffman, C. Y. Johnson, and J. C. Holmes (1964), Neutral composition of the atmosphere in the 100- to 200-kilometer range, *J. Geophys. Res.*, *69*(5), 979–989, doi:10.1029/JZ069i005p00979.
- Nier, A. O., W. E. Potter, D. C. Kayser, and R. G. Finstad (1974), The measurement of chemically reactive atmospheric constituents by mass spectrometers carried on high-speed spacecraft, *Geophys. Res. Lett.*, *1*(5), 197–200, doi:10.1029/GL001i005p00197.
- Nier, A. O., W. E. Potter, and D. C. Kayser (1976), Atomic and molecular oxygen densities in the lower thermosphere, *J. Geophys. Res.*, *81*(1), 17–24, doi:10.1029/JA081i001p00017.
- Nussbaumer, V., K. H. Fricke, M. Langer, W. Singer, and U. von Zahn (1996), First simultaneous and common volume observations of noctilucent clouds and polar mesosphere summer echoes by lidar and radar, *J. Geophys. Res.*, *101*(D14), 19,161–19,167, doi:10.1029/96JD01213.
- Offermann, D. (1972), On the atomic oxygen measurements by rocket-borne mass spectrometers, *J. Geophys. Res.*, *77*(31), 6284–6286, doi:10.1029/JA077i031p06284.
- Offermann, D., and A. Drescher (1973), Atomic oxygen densities in the lower thermosphere as derived from in situ 5577-Å night airglow and mass spectrometer measurements, *J. Geophys. Res.*, *78*(28), 6690–6700, doi:10.1029/JA078i028p06690.

- Offermann, D., and T. G. Scholz (1973), Functional tests of a cryo-cooled mass spectrometer ion source in a supersonic wind tunnel, *Rev. Sci. Instrum.*, 44(11), 1573–1577, doi:10.1063/1.1686003.
- Offermann, D., and H. Tatarczyk (1973), A cryo-cooled mass spectrometer ion source for atmospheric composition measurements at supersonic rocket velocities, *Rev. Sci. Instrum.*, 44(11), 1569–1572, doi:10.1063/1.1686002.
- Offermann, D., and H. Trinks (1971), A rocket borne mass spectrometer with helium cooled ion source, *Rev. Sci. Instrum.*, 42(12), 1836–1843, doi:10.1063/1.1685018.
- Offermann, D., and U. von Zahn (1971), Atomic oxygen and carbon dioxide in the lower thermosphere, *J. Geophys. Res.*, 76(10), 2520–2522, doi:10.1029/JA076i010p02520.
- Offermann, D., V. Friedrich, P. Ross, and U. V. Zahn (1981), Neutral gas composition measurements between 80 and 120 km, *Planet. Space Sci.*, 29(7), 747 – 764, doi:10.1016/0032-0633(81)90046-5.
- Ouyang, Z., and R. G. Cooks (2009), Miniature mass spectrometers, *Annu. Rev. Anal. Chem.*, 2(1), 187–214, doi:10.1146/annurev-anchem-060908-155229.
- Pfaff, R., et al. (2001), Rocket probe observations of electric field irregularities in the polar summer mesosphere, *Geophys. Res. Lett.*, 28(8), 1431–1434, doi:10.1029/2000GL012677.
- Phan, T. (2010), Alvatec GmbH, Personal communication.
- Philbrick, C. R., F. J. Schmidlin, K. U. Grossmann, G. Lange, D. Offermann, K. D. Baker, D. Krankowsky, and U. von Zahn (1985), Density and temperature structure over northern Europe, *J. Atmos. Terr. Phys.*, 47(1), 159 – 172, doi:10.1016/0021-9169(85)90131-X.
- Photonis (2015a), AP-TOF, Online, accessed 2015-06-19. <http://www.photonis.com/en/ism/48-advanced-performance-tof-detector.html>.
- Photonis (2015b), MCP (Chevron) Start-up procedure, Online, accessed 2015-06-17. <http://www.photonis.com/en/content/20-ism-product-documentation>.
- Picone, J. M., A. E. Hedin, D. P. Drob, and A. C. Aikin (2002), NRLMSISE-00 empirical model of the atmosphere: Statistical comparisons and scientific issues, *J. Geophys. Res.*, 107(A12), SIA 15–1–SIA 15–16, doi:10.1029/2002JA009430.
- Pisacane, V. L. (2008), *The Space Environment and Its Effects on Space Systems*, American Institute of Aeronautics and Astronautics, Reston, VA, doi:<http://dx.doi.org/10.2514/4.862533>.

- Plane, J. M. C., et al. (2014), A combined rocket-borne and ground-based study of the sodium layer and charged dust in the upper mesosphere, *J. Atmos. Sol. Terr. Phys.*, *118, Part B*, 151 – 160, doi:10.1016/j.jastp.2013.11.008.
- Plane, J. M. C., W. Feng, and E. C. M. Dawkins (2015), The mesosphere and metals: Chemistry and changes, *Chem. Rev.*, *115*(10), 4497–4541, doi:10.1021/cr500501m.
- Pomerantz, W., I. Beerer, K. Stephens, J. Griffith, W. Persall, and J. Tizard (2012), Opportunities for geoscience research onboard Virgin Galactic's SpaceShipTwo, in *AGU Fall Meeting Abstracts*, vol. 1, p. 02.
- Rager, J. P., and J. F. Renaud (1974), The use of a microchannel electron multiplier in spectroscopic instrumentation, involving frequent vacuum breaking, *Rev. Sci. Instrum.*, *45*(7), 922–926, doi:10.1063/1.1686769.
- Raizada, S., C. M. Brum, C. A. Tepley, J. Lautenbach, J. S. Friedman, J. D. Mathews, F. T. Djuth, and C. Kerr (2015), First simultaneous measurements of Na and K thermospheric layers along with TILs from Arecibo, *Geophys. Res. Lett.*, *42*(23), 10,106–10,112, doi: 10.1002/2015GL066714.
- Rapp, M., J. Gumbel, and F.-J. Lübken (2001), Absolute density measurements in the middle atmosphere, *Ann. Geophys.*, *19*(5), 571–580, doi:10.5194/angeo-19-571-2001.
- Rapp, M., I. Strelnikova, and J. Gumbel (2007), Meteoric smoke particles: Evidence from rocket and radar techniques, *Adv. Space Res.*, *40*(6), 809 – 817, doi:10.1016/j.asr.2006.11.021.
- Robertson, S., et al. (2009), Mass analysis of charged aerosol particles in NLC and PMSE during the ECOMA/MASS campaign, *Ann. Geophys.*, *27*(3), 1213–1232, doi:10.5194/angeo-27-1213-2009.
- Robertson, S., S. Dickson, M. Horányi, Z. Sternovsky, M. Friedrich, D. Janches, L. Megner, and B. Williams (2014), Detection of meteoric smoke particles in the mesosphere by a rocket-borne mass spectrometer, *J. Atmos. Sol. Terr. Phys.*, *118, Part B*, 161 – 179, doi: 10.1016/j.jastp.2013.07.007.
- Roble, R. G. (1995), Energetics of the mesosphere and thermosphere, in *The Upper Mesosphere and Lower Thermosphere: A Review of Experiment and Theory*, edited by R. M. Johnson and T. L. Killeen, pp. 1–21, AGU, Washington, D. C., doi:10.1029/GM087p0001.
- Russell, D. H., and R. D. Edmondson (1997), High-resolution mass spectrometry and accurate mass measurements with emphasis on the characterization of peptides and proteins by matrix-assisted laser desorption/ionization time-of-flight mass spectrometry, *J. of Mass Spectrom.*, *32*(3), 263–276, doi:10.1002/(SICI)1096-9888(199703)32:3<263::

AID-JMS501>3.0.CO;2-1.

Russell III, J. M., M. G. Mlynczak, L. L. Gordley, J. J. Tansock, Jr., and R. W. Esplin (1999), Overview of the SABER experiment and preliminary calibration results, *Proc. SPIE*, 3756, 277–288, doi:10.1117/12.366382.

Russell III, J. M., et al. (2009), The aeronomy of ice in the mesosphere (AIM) mission: Overview and early science results, *J. Atmos. Sol. Terr. Phys.*, 71(3 - 4), 289 – 299, doi:10.1016/j.jastp.2008.08.011.

Sandel, B. R., A. L. Broadfoot, and D. E. Shemansky (1977), Microchannel plate life tests, *Appl. Opt.*, 16(5), 1435–1437, doi:10.1364/AO.16.001435.

Sanderson, W. (2010–2016), Space Dynamics Laboratory, Personal communication.

Sargoytchev, S. I., S. Brown, B. H. Solheim, Y.-M. Cho, G. G. Shepherd, and M. J. López-González (2004), Spectral airglow temperature imager (SATI): a ground-based instrument for the monitoring of mesosphere temperature, *Appl. Opt.*, 43(30), 5712–5721, doi:10.1364/AO.43.005712.

Schaefer, E. J. (1969), Composition and temperature of the neutral tropic lower thermosphere, *J. Geophys. Res.*, 74(14), 3488–3498, doi:10.1029/JA074i014p03488.

Schuerch, S., M. Schaer, K. O. Boernsen, and U. P. Schlunegger (1994), Enhanced mass resolution in matrix-assisted laser desorption/ionization linear time-of-flight mass spectrometry, *Biol. Mass Spectrom.*, 23(11), 695–700, doi:10.1002/bms.1200231108.

Schulte, P., and F. Arnold (1992), Detection of upper atmospheric negatively charged microclusters by a rocket-borne mass spectrometer, *Geophys. Res. Lett.*, 19(23), 2297–2300, doi:10.1029/92GL02631.

Seedhouse, E. (2012), *Astronauts For Hire: The Emergence of a Commercial Astronaut Corps*, Springer US, Boston, MA, doi:10.1007/978-1-4614-0520-7\_6.

Seedhouse, E. (2016), *XCOR, Developing the Next Generation Spaceplane*, Springer-Praxis Books, Chichester, UK, doi:10.1007/978-3-319-26112-6\_6.

Sharp, W. E. (1980), Absolute concentrations of O(<sup>3</sup>P) in the lower thermosphere at night, *Geophys. Res. Lett.*, 7(7), 485–488, doi:10.1029/GL007i007p00485.

Siegmund, O. H. W. (1989), Preconditioning of microchannel plate stacks, *Proc. SPIE*, 1072, 111–118, doi:10.1117/12.952545.

Siegmund, O. H. W., and J. M. Stock (1991), Performance of low-resistance microchannel-plate stacks, *Proc. SPIE*, 1549, 81–89, doi:10.1117/12.48329.

- Siegmund, O. H. W., J. Vallerga, and B. Wargelin (1988), Background events in microchannel plates, *IEEE Trans. Nucl. Sci.*, 35(1), 524–528, doi:10.1109/23.12778.
- Siegmund, O. H. W., et al. (1994), Delay-line detectors for the UVCS and SUMER instruments on the SOHO satellite, *Proc. SPIE*, 2280, 89–100, doi:10.1117/12.186839.
- Siegmund, O. H. W., M. A. Gummin, T. Ravinett, S. R. Jelinsky, and M. L. Edgar (1996), Performance of small-pore microchannel plates, *Proc. SPIE*, 2808, 98–106, doi:10.1117/12.255986.
- Smith, C. P., Jr, and E. C. Pressly (1959), *Upper Atmosphere Research Report Number 21. Summary of Upper Atmosphere Rocket Research Firings*, US Naval Research Laboratory, Washington, D. C., <http://www.dtic.mil/docs/citations/ADB957191>.
- Smith, H. T. (2013), Commercial suborbital reusable launch vehicles: ushering in a new era for turbopause exploration, in *AGU Fall Meeting Abstracts*, vol. 1, p. 08.
- Sorokin, A. A., L. A. Shmaenok, S. V. Bobashev, B. Möbus, M. Richter, and G. Ulm (2000), Measurements of electron-impact ionization cross sections of argon, krypton, and xenon by comparison with photoionization, *Phys. Rev. A*, 61, 022,723, doi:10.1103/PhysRevA.61.022723.
- Sounding Rocket Working Group, National Aeronautics and Space Administration (2003), Findings & Concerns, Online, accessed 2016-06-09. [http://rscience.gsfc.nasa.gov/mt\\_03\\_jan\\_find.html](http://rscience.gsfc.nasa.gov/mt_03_jan_find.html).
- Stebel, K., V. Barabash, S. Kirkwood, J. Siebert, and K. H. Fricke (2000), Polar mesosphere summer echoes and noctilucent clouds: Simultaneous and common-volume observations by radar, lidar and CCD camera, *Geophys. Res. Lett.*, 27(5), 661–664, doi:10.1029/1999GL010844.
- SteinWeg, A., D. Krankowsky, P. Lämmerzahl, and B. Anweiler (1992), Metal ion layers in the auroral lower E-region measured by mass spectrometers, *J. Atmos. Terr. Phys.*, 54(6), 703 – 714, doi:10.1016/0021-9169(92)90108-W.
- Stephan, A. W., T. J. Immel, G. S. Bust, and J. Edlstein (2013), Measurement of the daytime F-region ionosphere from ICON, in *AGU Fall Meeting Abstracts*, vol. 1, p. 2136.
- Störmer, C. (1946), Frequency of 12,330 measured heights of aurora from southern Norway in the years 1911 - 1944, *Terr. Magn. Atmos. Electr.*, 51(4), 501–504, doi:10.1029/TE051i004p00501.
- Strelnikov, B., M. Rapp, T. A. Blix, N. Engler, J. Höffner, J. Lautenbach, F.-J. Lübken, B. Smiley, and M. Friedrich (2006), In situ observations of small scale neutral and plasma

- dynamics in the mesosphere/lower thermosphere at 79°N, *Adv. Space Res.*, 38(11), 2388 – 2393, doi:10.1016/j.asr.2005.03.097.
- Strelnikova, I., et al. (2009), Measurements of meteor smoke particles during the ECOMA-2006 campaign: 2. Results, *J. Atmos. Sol. Terr. Phys.*, 71(3 - 4), 486 – 496, doi:10.1016/j.jastp.2008.07.011.
- Stuhlinger, E. (2001), Enabling technology for space transportation, in *The Century of Space Science*, edited by J. A. M. Bleeker, J. Geiss, and M. C. E. Huber, pp. 59–114, Springer, Dordrecht, The Netherlands, doi:10.1007/978-94-010-0320-9\_3.
- Summers, M. E. (2011), Observations of the mesosphere/lower thermosphere with the next generation of reusable suborbital vehicles, in *AGU Fall Meeting Abstracts*, vol. 1, p. 09.
- Summers, M. E., R. R. Conway, C. R. Englert, D. E. Siskind, M. H. Stevens, J. M. Russell, L. L. Gordley, and M. J. McHugh (2001), Discovery of a water vapor layer in the Arctic summer mesosphere: Implications for polar mesospheric clouds, *Geophys. Res. Lett.*, 28(18), 3601–3604, doi:10.1029/2001GL013217.
- Swenson, G. R., and A. Z. Liu (1998), A model for calculating acoustic gravity wave energy and momentum flux in the mesosphere from OH airglow, *Geophys. Res. Lett.*, 25(4), 477–480, doi:10.1029/98GL00132.
- Swenson, G. R., and S. B. Mende (1994), OH emission and gravity waves (including a breaking wave) in all-sky imagery from Bear Lake, UT, *Geophys. Res. Lett.*, 21(20), 2239–2242, doi:10.1029/94GL02112.
- Taylor, J. R. (1997), *An Introduction to Error Analysis: The Study of Uncertainties in Physical Measurements*, A Series of Books in Physics, University Science Books, Sausalito, CA.
- Taylor, M. J., M. A. Hapgood, and P. Rothwell (1987), Observations of gravity wave propagation in the OI (557.7 nm), Na (589.2 nm) and the near infrared OH nightglow emissions, *Planet. Space Sci.*, 35(4), 413 – 427, doi:10.1016/0032-0633(87)90098-5.
- Taylor, M. J., A. P. van Eyken, H. Rishbeth, G. Witt, N. Witt, and M. A. Clilverd (1989), Simultaneous observations of noctilucent clouds and polar mesospheric radar echoes: Evidence of non-correlation, *Planet. Space Sci.*, 37(8), 1013 – 1020, doi:10.1016/0032-0633(89)90056-1.
- Taylor, M. J., M. Gadsden, R. P. Lowe, M. S. Zalcik, and J. Brausch (2002), Mesospheric cloud observations at unusually low latitudes, *J. Atmos. Sol. Terr. Phys.*, 64(8 - 11), 991 – 999, doi:10.1016/S1364-6826(02)00053-6.
- Taylor, M. J., et al. (2009), Coordinated optical and radar image measurements of noctilu-

- cent clouds and polar mesospheric summer echoes, *J. Atmos. Sol. Terr. Phys.*, 71(6 - 7), 675 – 687, doi:10.1016/j.jastp.2008.12.005.
- Thomas, S. W., and A. Behnke (1993), Microchannel plate intensifier gain uniformity improvement in sealed tubes by selective scrubbing, *Proc. SPIE*, 1801, 820–827, doi: 10.1117/12.145841.
- Thurairajah, B., S. M. Bailey, E. A. Syrstad, C. S. Fish, D. E. Siskind, and J. M. Russell (2013), Mass spectrometer sounding of the turbopause region on commercial vehicles, in *AGU Fall Meeting Abstracts*, vol. 1, p. 1992.
- Timothy, J. G. (1981), Curved-channel microchannel array plates, *Rev. Sci. Instrum.*, 52(8), 1131–1142, doi:10.1063/1.1136749.
- Townsend, J. W. (1952), Radiofrequency mass spectrometer for upper air research, *Rev. Sci. Instrum.*, 23(10), 538–541, doi:10.1063/1.1746079.
- Trapp, O., J. R. Kimmel, O. K. Yoon, I. A. Zuleta, F. M. Fernández, and R. N. Zare (2004), Continuous two-channel time-of-flight mass spectrometric detection of electrosprayed ions, *Angew. Chem. Int. Ed.*, 43(47), 6541–6544, doi:10.1002/anie.200461240.
- Trinks, H., and U. von Zahn (1975), The ESRO 4 gas analyzer, *Rev. Sci. Instrum.*, 46(2), 213–217, doi:10.1063/1.1134170.
- Trinks, H., D. Offermann, U. von Zahn, and C. Steinhauer (1978), Neutral composition measurements between 90- and 220-km altitude by rocket-borne mass spectrometer, *J. Geophys. Res.*, 83(A5), 2169–2176, doi:10.1029/JA083iA05p02169.
- Turco, R. P., O. B. Toon, R. C. Whitten, R. G. Keesee, and D. Hollenbach (1982), Noctilucent clouds: Simulation studies of their genesis, properties and global influences, *Planet. Space Sci.*, 30(11), 1147 – 1181, doi:10.1016/0032-0633(82)90126-X.
- Turnbull, J. C. (1977), Barium, strontium, and calcium as getters in electron tubes, *J. Vac. Sci. Technol.*, 14(1), 636–639, doi:10.1116/1.569166.
- Verhoeven, J., and H. van Doveren (1982), Interactions of residual gases with a barium getter film as measured by AES and XPS, *J. Vac. Sci. Technol.*, 20(1), 64–74, doi:10.1116/1.571310.
- Viggiano, A. A., and D. E. Hunton (1999), Airborne mass spectrometers: four decades of atmospheric and space research at the Air Force Research Laboratory, *J. Mass Spectrom.*, 34(11), 1107–1129, doi:10.1002/(SICI)1096-9888(199911)34:11<1107::AID-JMS880>3.0.CO;2-I.
- von Zahn, U. (1963), Monopole spectrometer, a new electric field mass spectrometer, *Rev.*

- Sci. Instrum.*, 34(1), 1–4, doi:10.1063/1.1718110.
- von Zahn, U. (1967), Mass spectrometric measurements of atomic oxygen in the upper atmosphere: A critical review, *J. Geophys. Res.*, 72(23), 5933–5937, doi:10.1029/JZ072i023p05933.
- von Zahn, U., and J. Gross (1969), Mass spectrometric investigation of the thermosphere at high latitudes, *J. Geophys. Res.*, 74(16), 4055–4063, doi:10.1029/JA074i016p04055.
- von Zahn, U., and T. L. Hansen (1988), Sudden neutral sodium layers: a strong link to sporadic E layers, *J. Atmos. Terr. Phys.*, 50(2), 93 – 104, doi:10.1016/0021-9169(88)90047-5.
- von Zahn, U., and J. Höffner (1996), Mesopause temperature profiling by potassium lidar, *Geophys. Res. Lett.*, 23(2), 141–144, doi:10.1029/95GL03688.
- von Zahn, U., F.-J. Lübken, and C. Pütz (1990), BUGATTI experiments: Mass spectrometric studies of lower thermosphere eddy mixing and turbulence, *J. Geophys. Res.*, 95(D6), 7443–7465, doi:10.1029/JD095iD06p07443.
- Wagener, S. (1951), Efficiency and mechanism of barium getters at low pressures, *Brit. J. Appl. Phys.*, 2(5), 132.
- Whitehead, J. D. (1970), Production and prediction of sporadic E, *Rev. Geophys.*, 8(1), 65–144, doi:10.1029/RG008i001p00065.
- Wickwar, V. B., M. J. Taylor, J. P. Herron, and B. A. Martineau (2002), Visual and lidar observations of noctilucent clouds above Logan, Utah, at 41.7°N, *J. Geophys. Res.*, 107(D7), ACL 2–1–ACL 2–6, doi:10.1029/2001JD001180.
- Wikipedia (2015), Barium — Wikipedia, The Free Encyclopedia, Online, accessed 2015-05-20. <http://en.wikipedia.org/wiki/Barium>.
- Wiza, J. L. (1979), Microchannel plate detectors, *Nucl. Instrum. Meth.*, 162(1), 587 – 601, doi:10.1016/0029-554X(79)90734-1.
- Yi, F., S. Zhang, C. Yu, Y. Zhang, Y. He, F. Liu, K. Huang, C. Huang, and Y. Tan (2013), Simultaneous and common-volume three-lidar observations of sporadic metal layers in the mesopause region, *J. Atmos. Sol. Terr. Phys.*, 102, 172 – 184, doi:10.1016/j.jastp.2013.05.013.
- Yoon, O. K., I. A. Zuleta, J. R. Kimmel, M. D. Robbins, and R. N. Zare (2005), Duty cycle and modulation efficiency of two-channel hadamard transform time-of-flight mass spectrometry, *J. Am. Soc. Mass Spectrom.*, 16(11), 1888 – 1901, doi:10.1016/j.jasms.2005.07.025.

- Yoon, O. K., I. A. Zuleta, M. D. Robbins, G. K. Barbula, and R. N. Zare (2007), Simple template-based method to produce Bradbury-Nielsen gates, *J. Am. Soc. Mass Spectrom.*, *18*(11), 1901 – 1908, doi:10.1016/j.jasms.2007.07.030.
- Yoon, O. K., I. A. Zuleta, M. D. Robbins, G. K. Barbula, and R. N. Zare (2008), Erratum to: Simple template-based method to produce Bradbury-Nielsen gates, *J. Am. Soc. Mass Spectrom.*, *19*(12), 1948–1948, doi:10.1016/j.jasms.2008.08.013.
- Young, J. M., C. Y. Johnson, and J. C. Holmes (1967), Positive ion composition of a temperate-latitude sporadic E layer as observed during a rocket flight, *J. Geophys. Res.*, *72*(5), 1473–1479, doi:10.1029/JZ072i005p01473.
- Zare, R. N., F. M. Fernández, and J. R. Kimmel (2003), Hadamard transform time-of-flight mass spectrometry: More signal, more of the time, *Angew. Chem. Int. Ed.*, *42*(1), 30–35, doi:10.1002/anie.200390047.
- Zbinden, P., M. Hidalgo, P. Eberhahdt, and J. Geiss (1975), Mass spectrometer measurements of the positive ion composition in the D- and E-regions of the ionosphere, *Planet. Space Sci.*, *23*(12), 1621 – 1642, doi:10.1016/0032-0633(75)90090-2.

APPENDICES

## APPENDIX A

## TG EXPERIMENT VOLUME CALCULATIONS

An experiment to evaluate TG pumping speed was described in Chapter 5. Volume calculations for the experimental chamber used in these experiments are presented here. The chamber was constructed from CF vacuum components and included crosses, nipples, valves, and gauges. Volume calculations for some of these components was straightforward (e.g., crosses and nipples), but difficult for irregularly shaped components (e.g., valves and gauges). Two nearly identical experimental setups, designated (a) and (b), were used for the TG experiments. The only difference between the two setups was an additional 2 3/4" CF nipple in setup (a). Volume calculations and accompanying uncertainties for the TG experimental test chamber were made by carefully measuring the volumes of the individual components of the experimental setup and estimating their uncertainties. The volumes and associated uncertainty of each component are included in the following analysis. Errors were calculated according to standard error propagation techniques (see for example, *Taylor* [1997]). A set of Mitutoyo micrometers, accurate to 0.01 mm, was used to make most of the measurements in this appendix. However, in the following analysis the uncertainty is often estimated to be larger than 0.01 mm to reflect the inherent difficulty of making measurements using hand tools. Other methods of measurement were used in a few instances, and will be noted where appropriate. Calculations were made using Mathcad Prime®.

## A.1. CF Nipple

Test volume (a) used two 2 3/4" CF nipples, while test volume (b) used one. This, and the necessary difference in the number of 2 3/4" CF gaskets used, was the only difference between the two test setups. The nipples were identical and had a length of  $125 \pm 3$  mm and an inner diameter of  $34.8 \pm 0.5$  mm. The nipple volume was calculated as a cylinder with diameter,  $d_n$ , and length,  $l_n$ . The uncertainties in  $d_n$  and  $l_n$  were added in quadrature. For test volume (a), which used two nipples, the total nipple volume was calculated to

be  $V_{na} = 2V_n = 238 \pm 9$  mL. For test volume (b) the nipple volume was calculated to be  $V_{nb} = V_n = 119 \pm 4$  mL.

### A.2. CF Four-Way Cross

Both test volumes employed two 2 3/4" CF four-way crosses. Their volumes were measured by mechanical engineering student Lisa Phillips, using Solid Edge<sup>®</sup> and a solid model of a four-way cross. The volume of each cross was calculated to be  $V_{cross} = 12.9$  in<sup>3</sup>, with an estimated uncertainty of 0.5 in<sup>3</sup>. The total volume of crosses in the experimental setup was expressed as

$$V_c = 2 \cdot V_{cross}, \quad (\text{A.1})$$

with an uncertainty of

$$\delta V_c = 2 \cdot \delta V_{cross}. \quad (\text{A.2})$$

The total cross volume in the experimental setup was calculated to be  $V_c = 414 \pm 16$  mL.

### A.3. Right-Angle Pneumatic Valve

One right-angle pneumatic valve was used in each experimental setup. The vacuum volume of the valve consisted of two cylindrical portions. The first cylindrical portion was measured to have a length of  $l_{RAvalve1} = 43.3 \pm 0.5$  mm and a diameter of  $d_{RAvalve1} = 32.2 \pm 0.5$  mm. This portion,  $V_{RAvalve1}$ , was calculated as the volume of a cylinder of diameter,  $d_{RAvalve1}$ , and length,  $l_{RAvalve1}$ . Errors in  $d_{RAvalve1}$  and  $l_{RAvalve1}$  were added in quadrature to calculate the uncertainty in  $V_{RAvalve1}$ . The second cylindrical portion had a length of  $l_{RAvalve2} = 5.3 \pm 0.5$  mm and a diameter of  $d_{RAvalve2} = 34.7 \pm 0.5$  mm. This portion,  $V_{RAvalve2}$ , was calculated as the volume of a cylinder of diameter,  $d_{RAvalve2}$ , and length,  $l_{RAvalve2}$ . Errors in  $d_{RAvalve2}$  and  $l_{RAvalve2}$  were added in quadrature to calculate the uncertainty in  $V_{RAvalve2}$ . The total volume of the right angle valve was the sum of the two portions, expressed as

$$V_{RAv} = V_{RAvalve1} + V_{RAvalve2}, \quad (\text{A.3})$$

yielding a volume of  $V_{RAv} = 40 \pm 1$  mL.

#### A.4. Baratron<sup>®</sup> Capacitance Manometer

The experimental chamber in each setup was separated into two subvolumes, with a Baratron<sup>®</sup> capacitance manometer attached to each subvolume. The vacuum volume of each Baratron<sup>®</sup> was found on the manufacturer's website [MKS, 2015]. The vacuum volume of each Baratron<sup>®</sup> was  $6.3 \pm 2$  mL, giving each setup a total Baratron<sup>®</sup> volume of  $V_B = 12.6 \pm 4$  mL. The uncertainty reflects the ambiguity as to whether the quoted volume included the fittings on the Baratrons<sup>®</sup>.

#### A.5. Conical Adapter, 2 3/4" CF to Mini CF

Each experimental setup used two conical adapters (2 3/4" CF to mini CF). The shape of the conical adapters can be broken down into three smaller volumes: two cylindrical sections and a conical portion with the top of the cone missing. The measured dimensions of the cylindrical portions are given in Table A.1. The volumes of the cylindrical portions were calculated with their corresponding lengths and diameters, with the errors in length and diameter adding in quadrature.

Calculating the volume of the conical portion was more complicated. First, the total height of the adapter was measured to be  $h_{CA_{total}} = 79.5 \pm 1$  mm. The height of the conical portion was then calculated to be

$$h_2 = h_{tot} - l_{CA1} - l_{CA2}. \quad (\text{A.4})$$

**Table A.1.** Dimensions for the Cylindrical Portions of the Conical Adapter

Cylindrical portion	Length (mm)	Diameter (mm)	Volume (ml)
1	$l_{CA1} = 24 \pm 2$	$d_{CA1} = 15.9 \pm 0.5$	$4.8 \pm 0.5$
2	$l_{CA2} = 12.5 \pm 2$	$d_{CA2} = 34.9 \pm 0.5$	$12 \pm 2$

The volume of the conical portion of the conical adapter can be described as a large cone less the volume of the top of the larger cone. Referring to Figure A.1, the larger cone has the volume ( $V_{\text{large}}$ ) of a cone of height,  $h_{\text{large}}$ , and radius at the base of  $R_{\text{CA2}}$ , where  $R_{\text{CA2}} = d_{\text{CA2}}/2$ . In Figure A.1,

$$h_{\text{large}} = h_2 + h_s. \quad (\text{A.5})$$

The smaller cone has height,  $h_s$ , and a radius,  $r$ , where  $r = d_{\text{CA1}}/2$ . The relation

$$\frac{h_s}{r_{\text{CA1}}} = \frac{h_{\text{large}}}{R_{\text{CA2}} - r_{\text{CA1}}} \quad (\text{A.6})$$

can be used to find  $h_s$ , which can be expressed as

$$h_s = \frac{r_{\text{CA1}} h_2}{r_{\text{CA3}} - r_{\text{CA1}}}. \quad (\text{A.7})$$

$h_s$  and  $r$  can then be used to calculate the volume,  $V_{\text{small}}$ , of the small cone. The volume of the conical portion of the adapter,  $V_{\text{CA3}}$ , can now be expressed as the difference between the large cone and small cone

$$V_{\text{CA3}} = V_{\text{large}} - V_{\text{small}}. \quad (\text{A.8})$$

The volume of the conical portion of the adapter was calculated to be  $V_{\text{CA3}} = 23 \pm 2$  mL.

The total volume of the conical adapter was calculated as the sum of the three sections,

$$V_{\text{conical.adapter}} = V_{\text{CA1}} + V_{\text{CA2}} + V_{\text{CA3}}, \quad (\text{A.9})$$

with the uncertainties for each portion adding in quadrature. Each setup used two conical adapters, for a total volume of

$$V_{\text{CA}} = 2 \cdot V_{\text{conical.adapter}}. \quad (\text{A.10})$$

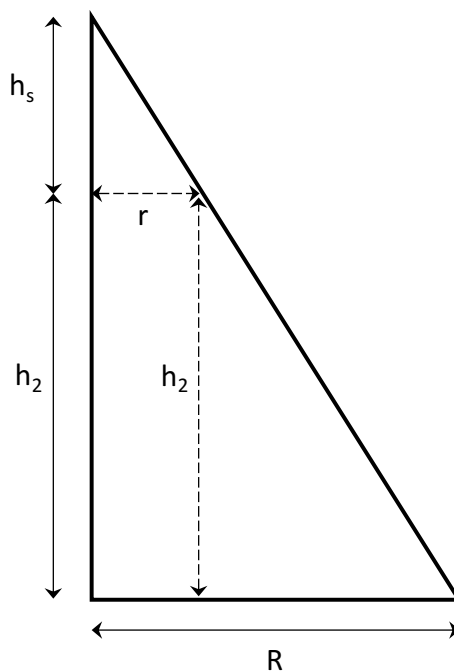


**Figure A.1.** Diagram for calculating the volume of the conical adapter. The conical portion of the adapter can be described as a cone with a base of radius,  $R$ , and height,  $h_2$ . Shown is a cross section of half the cone.

The total conical adapter volume in each setup was calculated to be  $V_{CA} = 79 \pm 6$  mL.

#### A.6. Electrical/Thermocouple Feedthrough

The volume of the electrical/thermocouple feedthrough had a significantly larger fractional uncertainty than most of the other components of the experimental test volume. The several wires and connectors of the feedthrough are considered in a later section. The total volume the feedthrough contributed to the experimental setup is small, so its uncertainty did not significantly affect the overall volume measurements. Measurements for this piece were made with a set of micrometers. The flange (sized for a mini-CF fitting, 1.33" diameter) was smaller than the interior of the feedthrough, making it difficult to measure the interior dimensions. The wall thickness of the feedthrough at the flange was assumed to be the same as the wall thickness for the rest of the feedthrough. The total length (or depth) of the volume of the feedthrough exposed to vacuum was measured to be  $l_{ft,tot} = 30 \pm 2$  mm. The

outer diameter of the feedthrough flange (designated portion 1 of the feedthrough) was measured to be  $d_{o1} = 19 \pm 0.5$  mm and the inner diameter was measured to be  $d_{i1} = 15.9 \pm 0.5$  mm. The wall thickness was then calculated to be  $T_{\text{wall}} = 1.6 \pm 0.4$  mm, as

$$T_{\text{wall}} = \frac{d_{o1} - d_{i1}}{2}. \quad (\text{A.11})$$

The length of the larger-diameter inner portion of the feedthrough was designated as portion 2 and was measured to be  $l_{\text{ft},2} = 11 \pm 2$  mm. Portion 2 had an outer diameter of  $d_{o2} = 25.5 \pm 0.5$  mm. The inner diameter of portion 2 was calculated by considering the outer diameter and the wall thickness,

$$d_{\text{ft},2} = d_{o2} - T_{\text{wall}}. \quad (\text{A.12})$$

The length of portion 1 of the feedthrough was calculated to be

$$l_{\text{ft},1} = l_{\text{ft,tot}} - l_{\text{ft},2}, \quad (\text{A.13})$$

and the diameter was

$$d_{\text{ft},1} = d_{i1}. \quad (\text{A.14})$$

Portion 1 was calculated as the volume of a cylinder with diameter,  $d_{i1}$ , and length,  $l_{\text{ft},1}$ . Portion 2 was calculated as the volume of a cylinder with diameter,  $d_{\text{ft},2}$ , and length,  $l_{\text{ft},2}$ . The total volume of the electrical/thermocouple feedthrough is the sum of the two portions,

$$V_{\text{ft}} = V_{\text{ft},1} + V_{\text{ft},2}, \quad (\text{A.15})$$

and was calculated to be  $V_{\text{ft}} = 8 \pm 1$  mL.

### A.7. Zero-Length Adapter

The experimental setup included one 2 3/4" CF to mini-CF zero length adapter. The diameter and length of the zero-length adapter were measured with micrometers and found to be  $d_{zla} = 15.8 \pm 0.5$  mm and  $l_{zla} = 13.8 \pm 2$  mm, respectively. The adapter was calculated as the volume of a cylinder of diameter,  $d_{zla}$ , and length,  $l_{zla}$ , giving  $V_{zla} = 2.7 \pm 0.4$  mL.

### A.8. Gaskets

The individual components used in the TG experimental apparatus were separated by copper gaskets, which served to create seals between different vacuum components. The seal is created by a knife edge in each piece biting into the copper gasket. Experimental setup (a) used eight 2 3/4" gaskets while experimental setup (b) used seven. The gaskets used to attach the gate valve to the experimental apparatus are not considered here due to the method used to find the volume of the gate valve, discussed later. Two mini-CF gaskets were used in each setup, but their contribution to the total volume was negligible (less than 1 mL). Measurements were made using micrometers. The height of the volume enclosed by a gasket was measured to be  $h_g = 2.6 \pm 1.0$  mm. The diameter of the enclosed volume,  $d_g$ , was measured to be  $d_g = 36.8 \pm 0.5$  mm. The volume enclosed by a gasket was calculated as a cylinder with height,  $h_g$ , and diameter,  $d_g$ , with the errors adding in quadrature. The total volume of all the gaskets combined was

$$V_g = n_{\text{gasket}} \cdot V_{\text{gasket}}, \quad (\text{A.16})$$

and was calculated to be  $V_g = 22 \pm 9$  mL for setup (a) and  $V_g = 19 \pm 7$  mL for setup (b).

### A.9. Gate Valve

The gate valve used in the experiment had an internal volume that was impossible to determine by making measurements with a pair of micrometers; an alternative approach was employed. With the gate valve in the open position, a 2 3/4" CF blank was attached to

one side of the gate. The interior volume of the gate valve was then filled with IPA, chosen in order to maintain cleanliness inside the valve. The IPA inside the gate valve was then poured into a graduated cylinder and measured to be  $V_{gv} = 455 \pm 40$  mL.

#### A.10. Leak Valve

The vacuum portion of the leak valve used in the experimental setup consisted of two adjacent cylindrical portions. The total height of the vacuum volume of the leak valve was measured to be  $h_{lv.total} = 20.9 \pm 0.5$  mm. The height of the first portion was measured to be  $h_{lv.1} = 2.4 \pm 0.5$  mm, and the diameter was measured to be  $d_{lv.1} = 38.1 \pm 0.5$  mm. The volume of the first portion of the leak valve was calculated as a cylinder with height,  $h_{lv.1}$ , and diameter,  $d_{lv.1}$ , yielding a volume of  $V_{lv.1} = 2.7362 \pm 0.5746$  mL. The height of the second portion of the leak valve was calculated as

$$h_{lv.2} = h_{lv.total} - h_{lv.1}, \quad (\text{A.17})$$

and the diameter of the second portion was measured to be  $d_{lv.2} = 34.5 \pm 0.5$  mm. The second portion of the leak valve was calculated as the volume of a cylinder of height,  $h_{lv.2}$ , and diameter,  $d_{lv.2}$ , giving  $V_{lv.2} = 17.2942 \pm 0.8296$  mL. The total volume of the leak valve was the sum

$$V_{lv} = V_{lv.1} + V_{lv.2}, \quad (\text{A.18})$$

and was found to be  $V_{lv} = 20 \pm 1$  mL.

#### A.11. Ion Gauge

The ion gauge volume was measured by filling an old burned out ion gauge, similar to the one used in the TG experiments, with water. The water in the ion gauge was then emptied into a graduated cylinder and measured to have a volume  $V_{IG} = 264 \pm 5$  mL.

### A.12. Electrical/Thermocouple Feedthrough Wires

Several wires and connectors were attached to the electrical/thermocouple feedthrough. Although small, the volume taken up by these wires and connectors was measured and taken into account. This volume was subtracted from the total vacuum volume. The diameter of the feedthrough wires was measured to be  $d_{fw} = 1.3 \pm 0.1$  mm. The two electrical feedthrough wires were approximately the same length,  $l_{efw} = 150 \pm 20$  mm. The lengths of the two thermocouple wires were  $l_{tfw1} = 130 \pm 20$  mm and  $l_{tfw2} = 110 \pm 20$  mm. Each thermocouple wire had a small connector which was measured to have length  $l_{ta} = 30 \pm 1$  mm, width  $w_{ta} = 3 \pm 0.2$  mm, and thickness  $t_{ta} = 0.9 \pm 0.1$  mm. The volume of each electrical feedthrough wire,  $V_{efw}$ , was calculated as the volume of a cylinder with length,  $l_{efw}$ , and diameter,  $d_{fw}$ . Errors were added in quadrature. The total volume of the two electrical feedthrough wires was given by

$$V_{efw.tot} = 2 \cdot V_{efw} \quad (\text{A.19})$$

The thermocouple connector volume was calculated using

$$V_{ta} = l_{ta} \cdot w_{ta} \cdot t_{ta}, \quad (\text{A.20})$$

with the errors adding in quadrature. The volumes of the thermocouple feedthrough wires were calculated as the volume of cylinders of diameter,  $d_{fw}$ , and lengths,  $l_{tfw1}$ , and  $l_{tfw2}$ . Each thermocouple feedthrough wire, including connector, had a volume given by

$$V_{t1} = V_{tfw1} + V_{ta}, \quad (\text{A.21})$$

$$V_{t2} = V_{tfw2} + V_{ta}, \quad (\text{A.22})$$

with associated errors added in quadrature.

Each electrical and thermocouple wire was attached at the base of the feedthrough with

a cylindrically shaped feedthrough connector. The actual connectors were very difficult to access, so a similar connector from a different feedthrough was measured. The diameter and length of the connector were measured to be  $d_{fc} = 5.5 \pm 0.5$  mm and  $l_{fc} = 15.4 \pm 0.5$  mm. The connector volume was calculated as the volume of a cylinder with diameter,  $d_{fc}$ , and length,  $l_{fc}$ . The total volume of all the wires and associated connectors in the feedthrough was given by

$$V_{fw} = V_{efw} + V_{tfw1} + V_{tfw2} + 4 \cdot V_{fc}, \quad (\text{A.23})$$

with the errors adding in quadrature, and was calculated to be  $V_{fw} = 2.3 \pm 0.3$  mL.

### A.13. TG Mount

A mount held the TG to the feedthrough during backfill experiments and comprised two pieces. Piece one was irregularly shaped and was measured by immersing it in a graduated cylinder filled with water and observing the subsequent change in volume, yielding  $V_{gtm1} = 2.0 \pm 0.5$  mL. Piece two was a disc with a hole in the middle and was measured using micrometers. The inner and outer diameters of piece two were  $d_{gtm2i} = 15.8 \pm 0.5$  mm and  $d_{gtm2o} = 31.8 \pm 0.5$  mm. The height of piece two was measured to be  $h_{gtm2} = 1.0 \pm 0.1$  mm. The volume of piece two was calculated as the volume of a cylinder of height,  $h_{gtm2}$ , and diameter,  $d_{gtm2o}$ , less the volume of a cylinder with the same height and diameter,  $d_{gtm2i}$ , given by

$$V_{gtm2} = \pi \cdot \left[ \left( \frac{d_{gtm2o}}{2} \right)^2 - \left( \frac{d_{gtm2i}}{2} \right)^2 \right] \cdot h_{gtm2}. \quad (\text{A.24})$$

The total volume of the TG mounts was then the sum of the two pieces,

$$V_{gtm} = V_{gtm1} + V_{gtm2}, \quad (\text{A.25})$$

and was calculated to be  $V_{gtm} = 2.6 \pm 0.5$  mL.

#### A.14. Tubegetter

The volume of the TG was calculated based on micrometer measurements, as well as stated dimensions on parts drawings from the manufacturer. The volume of barium in the tube was estimated from the amount of barium in the tube and the density of barium. It was not known if there was any more material inside the tube.

The inner and outer TG diameters were measured to be  $d_{gti} = 11 \pm 0.5$  mm and  $d_{gto} = 12 \pm 0.5$  mm respectively. The length of the TG was taken from parts drawings provided by the manufacturer and was  $l_{gt} = 110 \pm 5$  mm [Phan, 2010]. The TG barium load was  $m_{Ba} = 3$  g. The density of barium is  $\rho_{Ba} = 3.62$  gm/cm<sup>3</sup> [Wikipedia, 2015; Lide, 2005]. The volume of barium in the TG was found using

$$V_{Ba} = \frac{m_{Ba}}{\rho_{Ba}}, \quad (\text{A.26})$$

and was calculated to be  $V_{Ba} = 0.8 \pm 0.3$  mL, where the uncertainty was an estimate. The TG tube volume was calculated as the volume of a cylinder of length,  $l_{gt}$ , and diameter,  $d_{gto}$ , less the volume of a cylinder with the same height and diameter,  $d_{gti}$ , given by

$$V_{gt} = \pi \cdot \left[ \left( \frac{d_{gto}}{2} \right)^2 - \left( \frac{d_{gti}}{2} \right)^2 \right] \cdot l_{gt}. \quad (\text{A.27})$$

The total volume of the TG (including the barium load) was given by

$$V_{gtt} = V_{gt} + V_{Ba}, \quad (\text{A.28})$$

and was calculated to be  $V_{gtt} = 3 \pm 1$  mL.

#### A.15. Miscellaneous

A miscellaneous volume was introduced to estimate the small amount of material that was in the TG experimental test volume, but which was very difficult, if not impossible,

to find the volume. These materials included the heating wire used to activate the TG, ceramic sleeving used to electrically insulate the TG from the heating wire, insulation on the feedthrough wires, and any material unaccounted for inside the TG. This miscellaneous volume was estimated to be  $V_{misc} = 2 \pm 1$  mL.

#### A.16. Total Experimental Volume

The total experimental volume for the TG experiments can be expressed as

$$V = V_n + V_c + V_{RAV} + V_B + V_{CA} + V_{ft} + V_{zla} \quad (\text{A.29})$$

$$+ V_g + V_{gv} + V_{lv} + V_{IG} - V_{fw} - V_{gtm} - V_{gtt} - V_{misc},$$

with the errors for each term adding in quadrature. The total volume was calculated to be  $V_a = 1.55$  mL  $\pm 3\%$  for experimental setup (a) and  $V_b = 1.42$  mL  $\pm 3\%$  for experimental setup (b). A miscalculation led to a value of  $V_a = 1.53$  L for setup (a) being used during the analysis of the TG backfill experimental data. Because the difference between the used and actual values of  $V_a$  was small, the TG pumping speed calculations were left as done and not revisited. The variations in calculated TG pumping speeds were so large that the used value of  $V_a$  was inconsequential (see Figure 5.14).

#### A.17. Alternative Volume Measurement Method

The astute reader may question why two different experimental volumes were employed to conduct TG backfill experiments. The answer lies in a previous attempt to determine the volume of the TG experimental apparatus. This method, though elegant on paper, was difficult to implement in practice, but is explained here.

The experimental apparatus (section 5.1.1, Figure 5.1) consisted of two volumes ( $V_1$  and  $V_2$ ) separated by a gate valve. The volume  $V_1$  was unknown and  $V_2$  consisted of known and unknown subvolumes. With the gate valve separating volumes  $V_1$  and  $V_2$  closed, the pressure in  $V_1$  can be changed relative to the pressure in  $V_2$ . If the gate valve is then opened,

the pressure will equilibrate between the two volumes. This can be expressed as

$$P_{1i}V_1 + P_{2i}V_2 = P_f(V_1 + V_2). \quad (\text{A.30})$$

$V_2$  can be changed by a known amount and the experiment repeated. Applying equation A.30 to both of these experiments yields

$$P_{11i}V_1 + P_{21i}V_{21} = P_{1f}(V_1 + V_{21}), \quad (\text{A.31})$$

$$P_{12i}V_1 + P_{22i}V_{22} = P_{2f}(V_1 + V_{22}), \quad (\text{A.32})$$

where  $V_2$  in equation A.30 is equal to  $V_{21}$  for the first experiment and  $V_{22}$  for the second experiment.  $P_{11i}$  and  $P_{21i}$  are the initial pressures in volumes  $V_1$  and  $V_{21}$ , respectively, for the first experiment and  $P_{1f}$  is the final pressure after opening the gate valve.  $P_{12i}$  and  $P_{22i}$  are the initial pressures in volumes  $V_1$  and  $V_{22}$ , respectively, for the second experiment and  $P_{2f}$  is the final pressure after opening the gate valve. Volumes  $V_{21}$  and  $V_{22}$  can be expressed in terms of their unknown and known portions

$$V_{21} = V_{2u} + V_{21k}, \quad (\text{A.33})$$

$$V_{22} = V_{2u} + V_{22k}, \quad (\text{A.34})$$

where the subscript u stands for unknown and the subscript k is for the known portion of  $V_2$ . Equations A.33 and A.34 can be used to express equations A.31 and A.32 as

$$P_{11i}V_1 + P_{21i}(V_{2u} + V_{21k}) = P_{1f}(V_1 + V_{2u} + V_{21k}), \quad (\text{A.35})$$

$$P_{12i}V_1 + P_{22i}(V_{2u} + V_{22k}) = P_{2f}(V_1 + V_{2u} + V_{22k}). \quad (\text{A.36})$$

There are now two equations (A.35 and A.36) and two unknowns ( $V_1$  and  $V_{2u}$ ). Solving

equation A.35 for  $V_1$  and substituting into equation A.36 allows  $V_{2u}$  to be expressed as

$$V_{2u} = \frac{(P_{2f} - P_{22i})(P_{11i} - P_{1f})V_{22k} - (P_{1f} - P_{21i})(P_{12i} - P_{2f})V_{21k}}{(P_{1f} - P_{21i})(P_{12i} - P_{2f}) - (P_{2f} - P_{22i})(P_{11i} - P_{1f})}. \quad (\text{A.37})$$

Equation A.37 can then be substituted back in to equation A.35 and solved for  $V_1$  to give

$$V_1 = \frac{(P_{1f} - P_{21i})(P_{2f} - P_{22i})(V_{22k} - V_{21k})}{(P_{1f} - P_{11i})(P_{2f} - P_{22i}) - (P_{1f} - P_{21i})(P_{2f} - P_{12i})}. \quad (\text{A.38})$$

Equations A.37 and A.38 can then be used to calculate the volume(s) of the test setup. Measuring the TG experimental volume by this method was attempted but yielded results with too much variation to be useful. Hence, the first method described was used to determine the experimental volumes for the TG backfill experiments.

## APPENDIX B

## TG EXPERIMENTS: SUPPLEMENTAL FIGURES

Data from experiments with five TGs were combined to find the average TG pumping speed, over a range of noninert gas partial pressure and quantity of gas sorbed, shown in Figure 5.12. This appendix contains plots generated from individual TG experiments, as a supplement to the plots shown in Chapter 5. Figures B.1 through B.4 show the range of noninert gas partial pressure and quantity of gas sorbed during individual backfill experiments for four TGs. Figures B.5 through B.8 show the pumping speed versus noninert gas partial pressure for four TGs. Figures B.9 through B.12 show the pumping speed versus quantity of gas sorbed for four TGs.

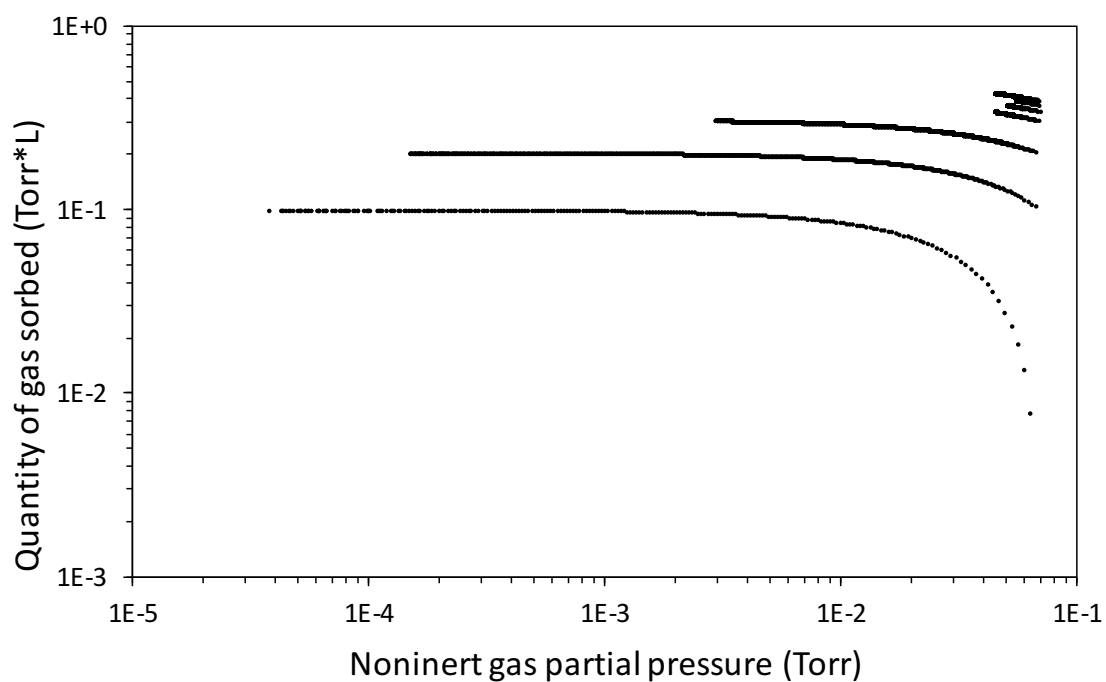


**Figure B.1.** Range of noninert gas partial pressure and quantity of gas sorbed during backfill experiments with TG 10382-6.

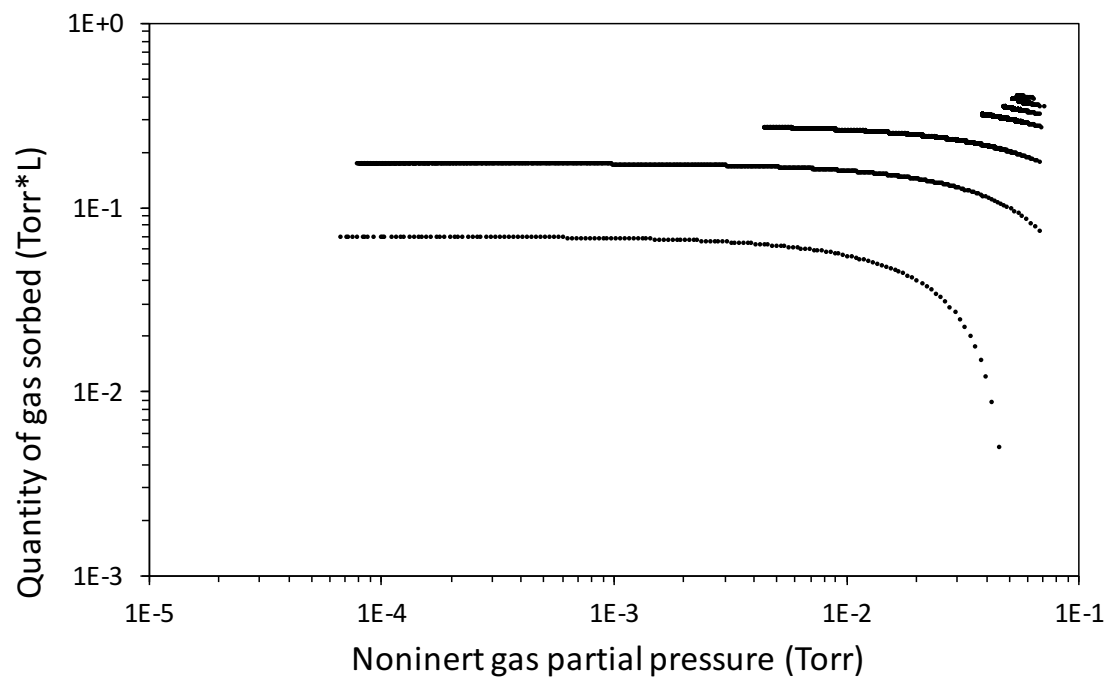


**Figure B.2.** Range of noninert gas partial pressure and quantity of gas sorbed during backfill experiments with TG 10384-1.

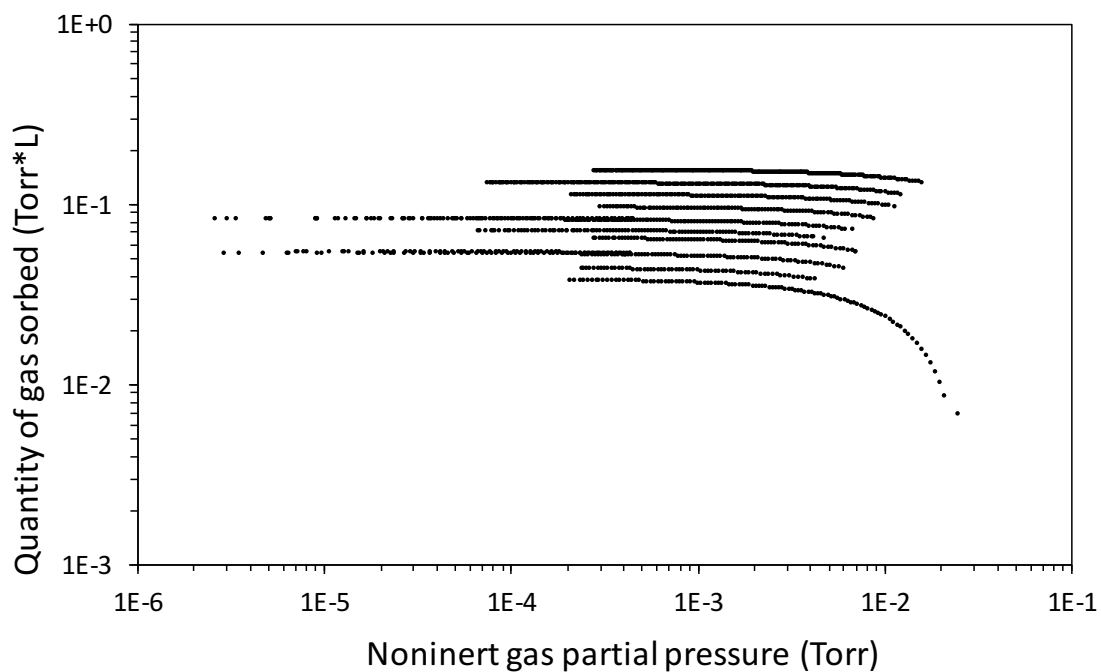


**Figure B.3.** Range of noninert gas partial pressure and quantity of gas sorbed during backfill experiments with TG 10384-2.

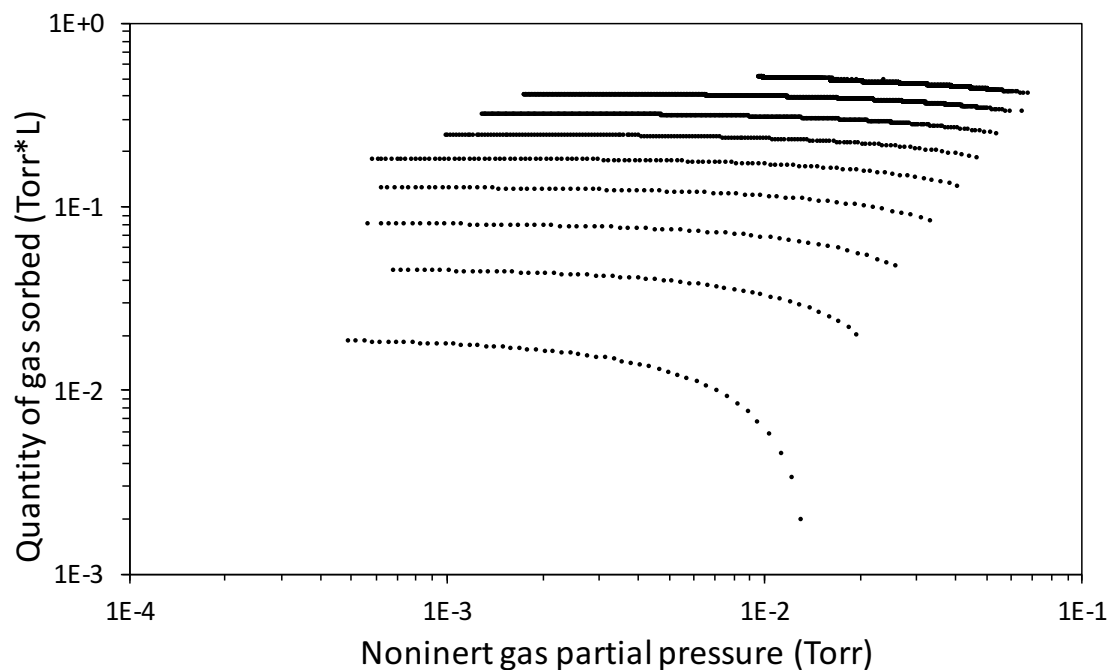


**Figure B.4.** Range of noninert gas partial pressure and quantity of gas sorbed during backfill experiments with TG 10384-3.

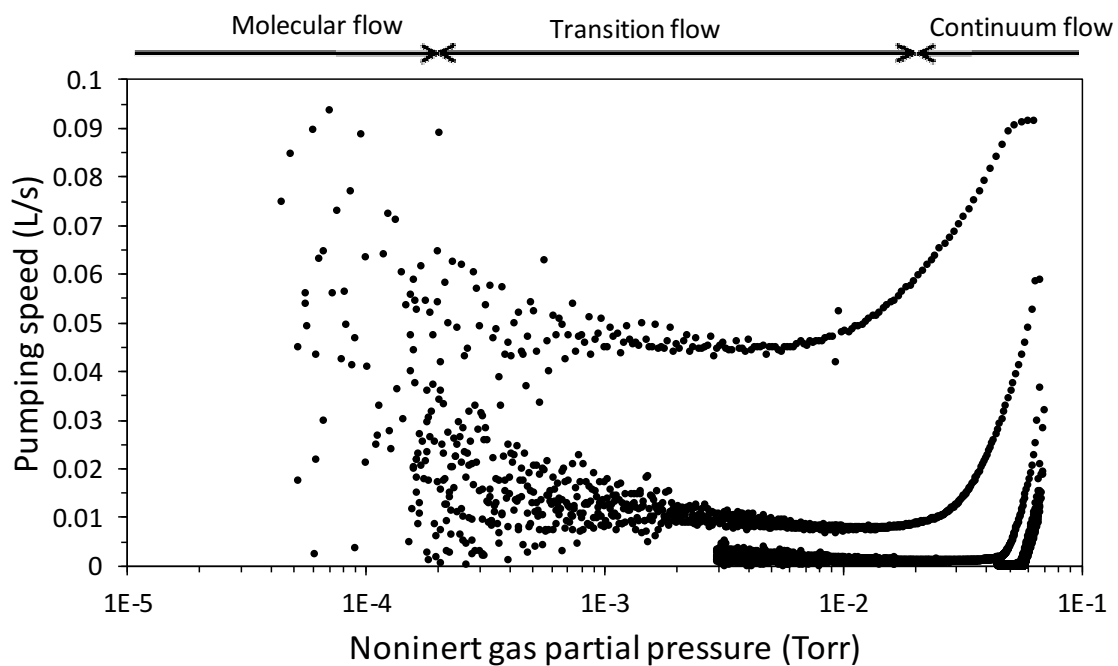


**Figure B.5.** Pumping speed versus noninert gas partial pressure during experiments with TG 10382-6. Approximate flow regime boundaries are noted.

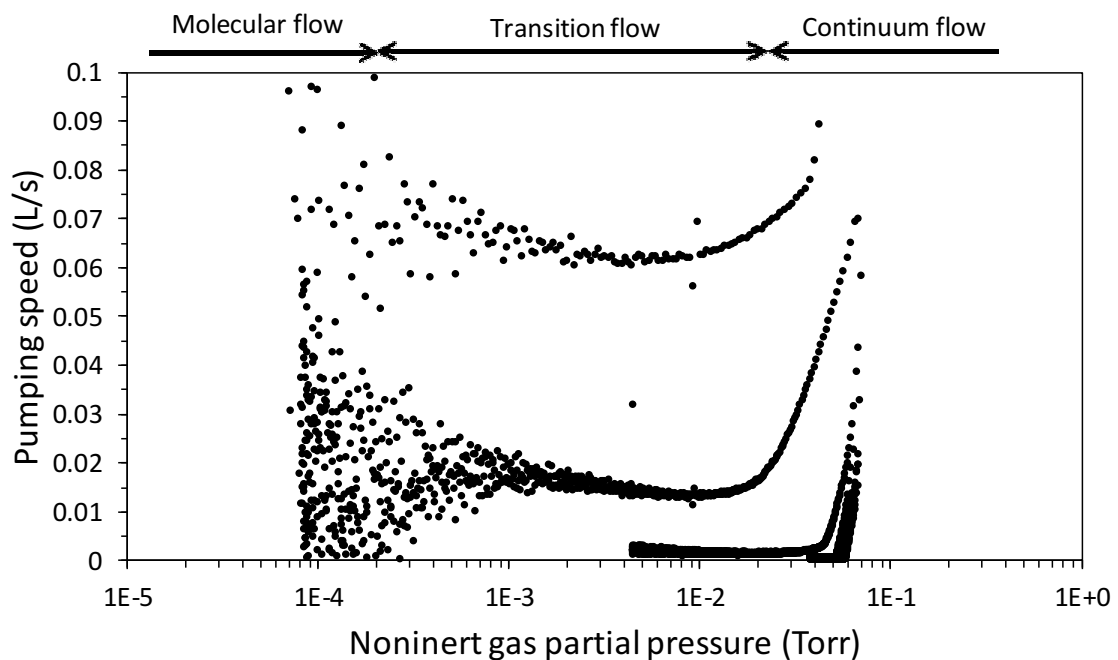


**Figure B.6.** Pumping speed versus noninert gas partial pressure during experiments with TG 10384-1. Approximate flow regime boundaries are noted.

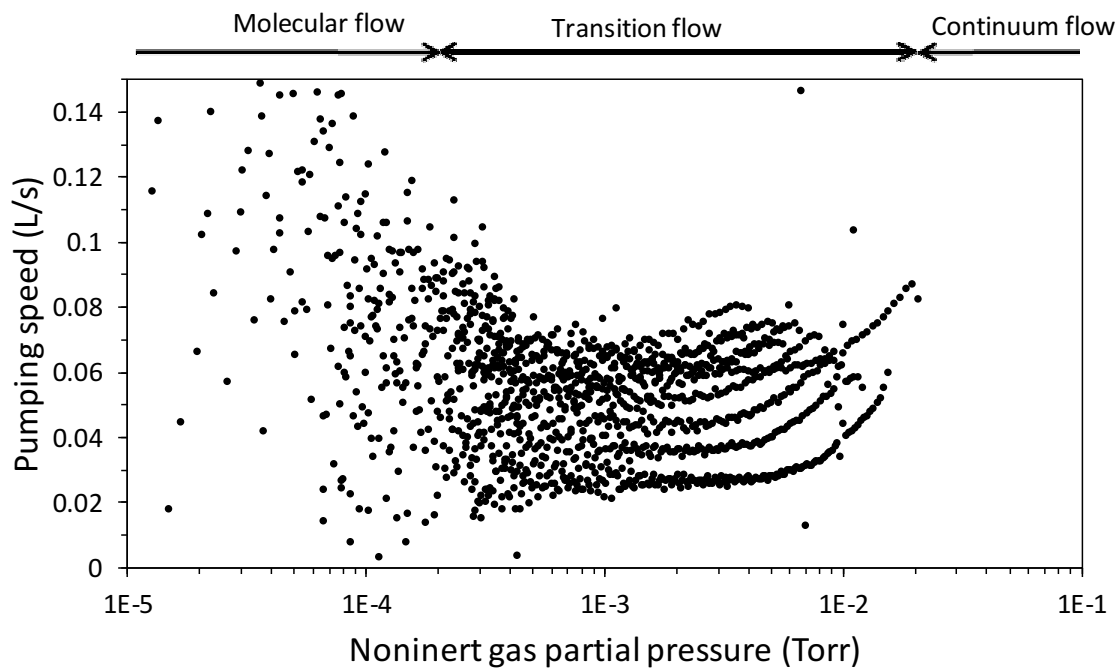


**Figure B.7.** Pumping speed versus noninert gas partial pressure during experiments with TG 10384-2. Approximate flow regime boundaries are noted.

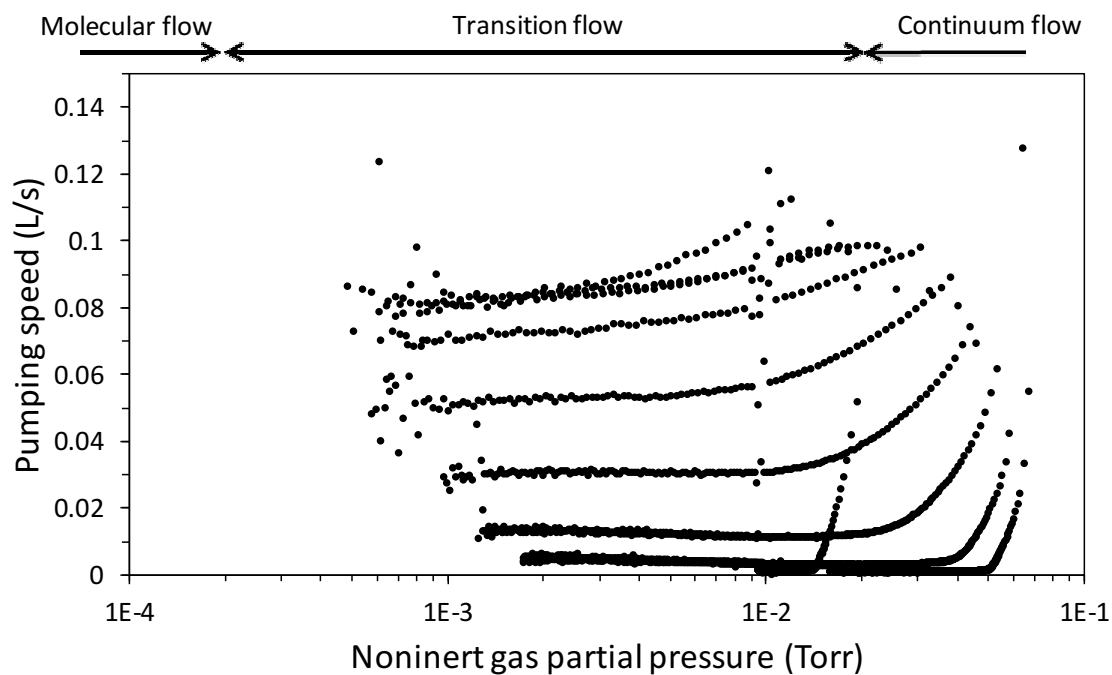


**Figure B.8.** Pumping speed versus noninert gas partial pressure during experiments with TG 10384-3. Approximate flow regime boundaries are noted.

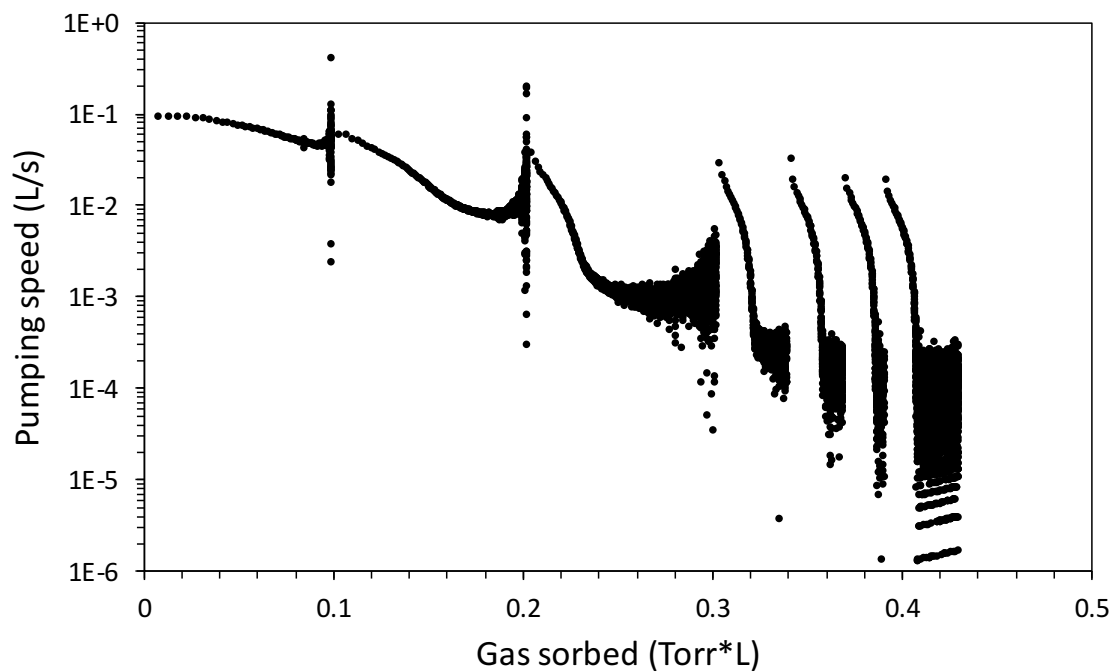


**Figure B.9.** Pumping speed versus quantity of gas sorbed for TG 10382-6.

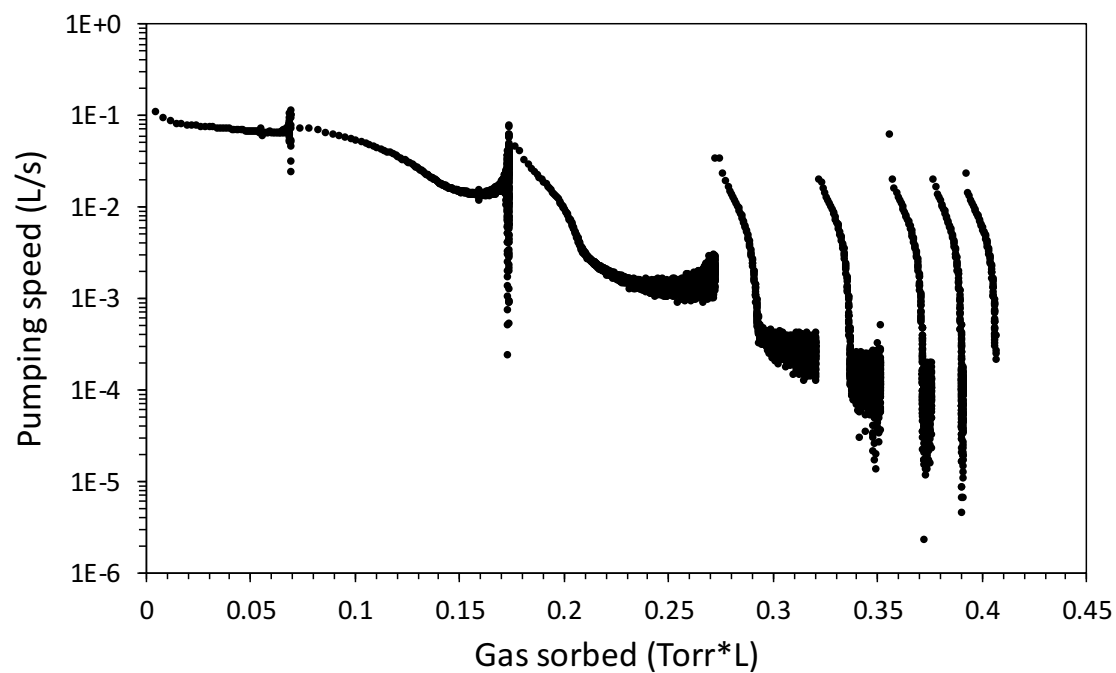


**Figure B.10.** Pumping speed versus quantity of gas sorbed for TG 10384-1.

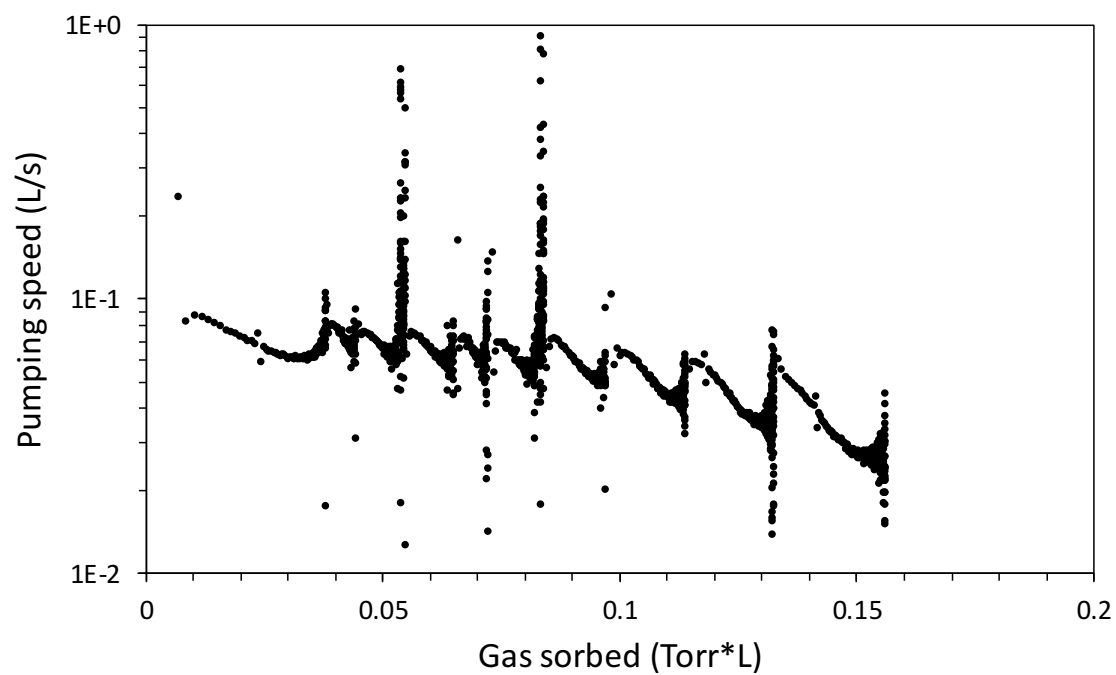


**Figure B.11.** Pumping speed versus quantity of gas sorbed for TG 10384-2.

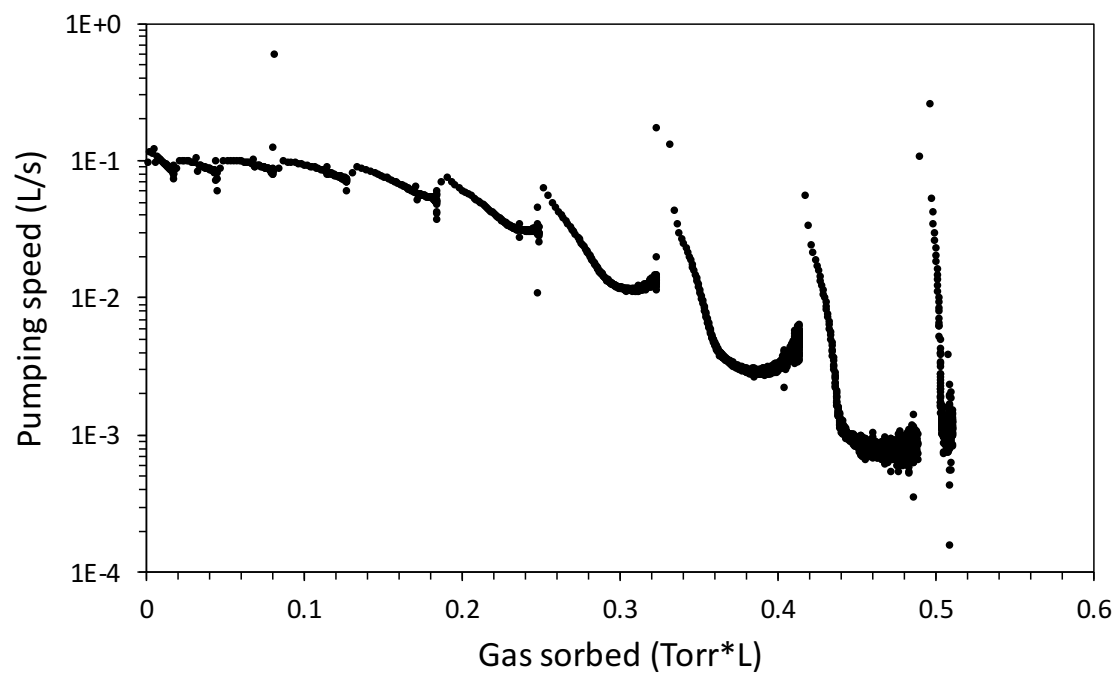


**Figure B.12.** Pumping speed versus quantity of gas sorbed for TG 10384-3.

## APPENDIX C

## PERMISSION TO INCLUDE FIGURE

September 16, 2016

E. Addison Everett  
651 E 600 N Apt 1  
Logan, UT 84321

Dear Mr. Laprade,

I am in the process of preparing my dissertation in the Physics department at Utah State University. I hope to complete my degree program in December of this year.

I am requesting your permission to include the attached material as shown. I will include acknowledgements and/or appropriate citations to your work as shown in a special appendix. The bibliographic citation will appear at the end of the manuscript as shown. Please advise me of any changes you require.

Please indicate your approval of this request by signing in the space provided, attaching any other form or instruction necessary to confirm permission. If you have any questions, please call me at the number below.

I hope you will be able to reply immediately. If you are not the copyright holder, please forward my request to the appropriate person or institution.

Thank you for your cooperation,



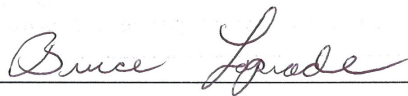
E. Addison Everett  
(435) 868-7515

---

I hereby give permission to E. Addison Everett to reprint **Slide 18** from the following material in his dissertation.

Cochran, R. F., B. N. Laprade, R. Prunier, L. Erickson, and W. Dunn (2005), Performance characteristics of detectors operated in harsh environments, in *The HEMS 2005 Conference*.

Signed: \_\_\_\_\_



9/19/16

## CURRICULUM VITAE

E. ADDISON EVERETT  
e.a.everett@aggiemail.usu.edu

www.linkedin.com/in/eaddisoneverett  
(435) 868-7515

---

**RESEARCH  
INTERESTS**

Spacecraft instrumentation, particle detection, instrument performance modeling/simulation, Monte-Carlo simulations, instrument development, time-of-flight mass spectrometry.

**EDUCATION****Utah State University (USU), Logan, Utah**

Ph.D., Physics, expected by May 2017 (defended May 2016).

Dissertation: *Design and Characterization of a Time-of-Flight Mass Spectrometer for Composition Measurements in the Upper Atmosphere.*

Ph.D. Advisor: Dr. Michael J Taylor.

B.S., Physics, May 2005.

**SCHOLARSHIPS &  
FELLOWSHIPS**

**Keith Taylor Fellowship**  
USU Physics Department, 2013.

**Adams Scholarship for Extraordinary Teaching Effort**  
USU Physics Department, 2009.

**HONORS &  
AWARDS**

**Outstanding Graduate Teaching Assistant**  
USU Physics Department, April 2014.

**1<sup>st</sup> Place Poster Award**  
Intermountain Graduate Research Symposium, April 2011.

**Outstanding Student Paper Award**  
American Geophysical Union Fall Meeting, December 2010.

**RESEARCH  
EXPERIENCE**

**Graduate Research Assistant**, Space Dynamics  
Laboratory,  
June 2009 – Present.

Design and characterization of a new time-of-flight mass spectrometer for space applications. Included laboratory experimentation with laboratory prototype and individual instrument subassemblies. Developed multiple computer models to simulate instrument performance.

**Graduate Research Assistant**, USU Nanophotonics  
Laboratory,

January 2006 – December 2008,

Assisted with the growth and characterization of InGaAs quantum dots using molecular beam epitaxy and scanning tunneling microscopy.

**TEACHING  
EXPERIENCE**

**Recitation Instructor**, USU Physics Department,  
August 2012 – May 2015,  
Physics for Scientists and Engineers I & II (PHYS 2200,  
2210, 2220).

**Laboratory Instructor**, USU Physics Department,  
January 2006 – December 2006, August 2012 – May 2015,  
Introductory Physics Laboratory I & II (PHYS 2215,  
2225).

**Tutor**, USU Physics Department,  
August 2012 – May 2015,  
Physics Learning Center.

**Instructor**, USU Physics Department,  
January 2007 – May 2009,  
Introduction to Computer Methods in Physics (PHYS  
2500).

**Laboratory Assistant**, USU Physics Department,  
August 2005 – January 2009,  
Intermediate and Advanced Physics Undergraduate  
Laboratory (PHYS 3870, 3880).

**PUBLICATIONS &  
PRESENTATIONS**

A Rocket-Borne Axially Sampling Time-of-Flight Mass Spectrometer for Investigation of the Upper Atmosphere, E. A. Everett and E. A. Syrstad, Poster, AGU Fall Meeting, December 2013 (Poster).

A New Mass Spectrometer for the Upper Atmosphere, E. Addison Everett, Utah State University Physics Colloquium, October 2013 (Talk).

Carrier capture dynamics of single InGaAs/GaAs quantum-dot layers, K. N. Chauhan, D. M. Riffe, E. A. Everett, D. J. Kim, H. Yang, and F. K. Shen, *Journal of Applied Physics*, 113, 203710 (2013).

Characterization of an Axially Sampling Time-of-Flight Mass Spectrometer for Upper Atmospheric Measurements, ASMS Annual Conference, May 2012 (Poster).

A New Mass Spectrometer for Upper Atmospheric Measurements in the Auroral Region, E. A. Everett, J. S. Dyer, M. Watson, W. Sanderson, S. Schicker, D. Work, C. J. Mertens, S. M. Bailey, and E. A. Syrstad, AGU Fall Meeting, December 2011 (Poster).

An Axial Time-of-Flight Mass Spectrometer for Upper Atmospheric Measurements, E. A. Everett, W. Sanderson, D. Allen, J. S. Dyer, M. Watson, and E. A. Syrstad, ASMS Annual Conference, June 2011 (Poster).

Design and Analysis of a Getter-Based Vacuum Pumping System for a Rocket-Borne Mass Spectrometer, E. A. Everett, E. A. Syrstad, and J. S. Dyer, Poster, AGU Fall Meeting, December 2010 (Poster).

Growth of nanodots on a strained GaAs epilayer using scanning tunneling microscope, Joseph Abel, Dong Jun Kim, E. Addison Everett, and Haeyeon Yang, *Journal of Crystal Growth* 310 (2008).

Annealing induced transition of flat strained InGaAs epilayers into three-dimensional islands, D. J. Kim, E. A. Everett, and H. Yang, *Journal of Applied Physics* 101 106106 (2007).

**PUBLICATIONS &  
PRESENTATIONS,  
continued**

Effects of As<sub>4</sub> flux on morphology of InGaAs quantum dots and the critical thickness, Nicholas Lambert, E. Addison Everett, Dong Jun Kim, and Haeyeon Yang, NAMBE Conference, 9 October 2006 (Poster).

One dimensional array of QDs for a single InGaAs layer deposition on a smooth (001) surface of GaAs substrate, Joseph Abel, Dong Jun Kim, E. Addison Everett, and Haeyeon Yang, NAMBE Conference, 9 October 2006 (Poster).

Study on energetics of self-assembled quantum dot using molecular beam epitaxy and scanning tunneling microscopy, Richard Wilson, Dong Jun Kim, E. Addison Everett, and Haeyeon Yang, 2006 Four Corners Section of the APS Fall Meeting, 6 October 2006 (Poster).

Variation and effects of As<sub>4</sub> flux on morphology of InGaAs quantum dots, E. Addison Everett, Dong Jun Kim, and Haeyeon Yang, 2006 Four Corners Section of the APS Fall Meeting, 6 October 2006 (Talk).